Molecular dynamics simulations of silicate and borate glasses and melts: Structure, diffusion dynamics and vibrational properties

Dissertation
zur Erlangung des Grades
"Doktor
der Naturwissenschaften"
am Fachbereich Physik, Mathematik und Informatik
der Johannes Gutenberg-Universität
in Mainz

Christoph Scherer

geb. in Zweibrücken (Rheinland-Pfalz)
Mainz, im April 2015

Datum der mündlichen Prüfung: 06.07.2015

"My friends and I have been thinking another year had come gone
And so we started drinking and singing new years songs.
Like Auld Lang Syne, There Comes a Time, and Prince's 1999...
But none of those songs seem to do it for us, at the time...

This year a lot of things have come to pass
Raise a glass, raise a glass
Some made us cry some made us laugh
Raise a glass, raise a glass

Next year will be better
The old year is gone forever
Thank god it's over, thank god it's over
Thank god it's over, it's over now
Thank god it's over, thank god it's over
Thank god it's over, it's over now

To all are friends and those we've left behind
Sing Auld Lang Syne, sing Auld Lang Syne
Thou you're gone you're never far from mind
Auld Lang Syne, sing Auld Lang Syne

Let bygones be bygones
Bye-bye gone we're moving on
Thank god it's over, thank god it's over
Thank god it's over, it's over now
Thank god it's over, thank god it's over
Thank god it's over, it's over now

This year many things have come to pass
Raise a glass, raise a glass
Some things really kicked our ass
Raise a glass, raise a glass

Come raise your spirits
Sing loud so the dead will hear it
Thank god it's over, thank god it's over
Thank god it's over, it's over now
Thank god it's over, thank god it's over
Thank god it's over, it's over now
Thank god it's over, thank god it's over
Thank god it's over, it's over now
Thank god it's over, thank god it's over
Thank god it's over, it's over now"

Jim'S Big Ego - New Lang Syne (Thank God It's Over)

Molecular dynamics simulations of silicate and borate glasses and melts: Structure, diffusion dynamics and vibrational properties

In this work, computer simulations of the model glass formers SiO_2 and B_2O_3 are presented, using the techniques of classical molecular dynamics (MD) simulations and quantum mechanical calculations, based on density functional theory (DFT). The latter limits the system size to about $100 - 200$ atoms. SiO_2 and B_2O_3 are the two most important network formers for industrial applications of oxide glasses.

In case of SiO_2, classical MD simulations are carried out, employing two different classical potentials: the well studied BKS potential and the CHIK potential. In agreement with previous results, it is found that small systems (as small as 165 atoms) show all characteristic features of glassy dynamics, the main finite size effect is a dynamical slowing down and the temperature dependence of the self-diffusion constants shows an Arrhenius behavior at low temperatures. Glass samples are generated by means of a quench from the melt with classical MD simulations and a subsequent structural relaxation with DFT forces. The latter mainly reduces the mean Si-O-Si angle by about $4° - 6°$. After the relaxation, the glass configurations of the BKS and the CHIK potential show no significant structural differences. In addition, the structural properties are in good agreement to the ones of a full ab initio quench from the melt and to experimental results from neutron and X-ray scattering. A special focus is on the study of vibrational properties, as they give access to low-temperature thermodynamic properties. Therefore, a comparison of the calculated vibrational spectrum $g(\nu)$ with the experimental one is a good test for the quality of a glass structure. The vibrational spectra are calculated by the so-called "frozen phonon" method, employing classical and quantum mechanical forces. In accordance to previous work, the DFT curves show excellent agreement with experimental results of inelastic neutron scattering. The same is observed, regarding the heat capacity at constant volume $C_V(T)$.

These glass configurations after the structural relaxation are the basis for calculations of the linear thermal expansion coefficients $\alpha_L(T)$, employing the quasi-harmonic approximation. The striking observation is a change of sign of $\alpha_L(T)$, both, using quantum mechanical (DFT) and classical forces for all but one examined glass configuration. To my knowledge this has not been reported before. The temperature range of negative thermal expansion is below about 130 K to 160 K (DFT forces) and 290 K to 325 K (classical forces). At temperatures below about 200 K, the DFT curves show a very good agreement with experimental results.

There is strong experimental evidence that in vitreous B_2O_3, about $60\% - 80\%$ of the boron atoms are located in planar, 3-membered boroxol rings. Having this in mind, ab initio MD simulations of the glass melt are carried out, showing an increased amount of 3-membered rings at 2300 K. The liquid trajectory at 2300 K is the basis for the development of a new classical interaction potential by extending the structural fitting procedure used for the development of the CHIK potential. The inclusion of 3-body angular terms leads to a significantly improved agreement of the liquid properties of the classical MD and ab initio MD simulations. In the course of this, a new angular potential type is introduced that is smoothly switched on and off, depending on the

inter-atomic distances. It is implemented as a new pair style of the LAMMPS software package. Again, glass samples are generated by quenches from the melt with classical MD simulations and a subsequent quantum mechanical relaxation, comparing two different parametrizations of the new potential type and the original parameter set before the fitting procedure. In addition, 4 full ab initio quenches are conducted. In all cases, the mean B-O and O-O distances are in good agreement with experimental results from neutron diffraction. The glass structures of the new 3-body potentials show an improvement, in terms of a slightly smaller mean B-B distance and the occurrence of some boroxol rings, compared to the ones of the original parameter set. However, the mean boroxol ring fraction is still quite small ($f = 2.5 \pm 1.1\%$ to $f = 8 \pm 2.3\%$). The ab initio quenches show a slightly larger mean boroxol ring fractions of $f = 5 \pm 5\%$ (quench from 3600 K) and $f = 15 \pm 5\%$ (quench from 2300 K). In agreement with previous work, this demonstrates that the occurrence of boroxol rings is a particularly sensitive measure of the quality of a classical force field and that the very high quench rates in computer experiments prevent the emergence of boroxol ring fractions comparable to the experimental one. The DFT vibrational spectra $g(\nu)$ show an acceptable agreement with results from inelastic neutron scattering. The peak height of the boroxol ring signature depends on the value of f.

Summarizing the above results, a quench from the melt with a classical MD simulation and a subsequent structural relaxation can lead to a glass configuration comparable to the one of a full ab initio quench, given a suitable classical force field. No general statement can be given, which method leads to a glass structure that is in better agreement with the one obtained in a real laboratory experiment.

Molekulardynamiksimulationen von Silikat- und Boratgläsern: Struktur, Diffusionsdynamik und Vibrationseigensschaften

In dieser Arbeit werden Computersimulationen der Modellglasbildner SiO_2 und B_2O_3 vorgestellt, mittels klassischer Molekulardynamik(MD)-Simulationen und quantenmechanischer Rechnungen, basierend auf der Dichtefunktionaltheorie (DFT). Letzteres limitiert die Systemgröße auf in etwa $100 - 200$ Atome. SiO_2 und B_2O_3 sind die beiden wichtigsten Netzwerkbildner für industrielle Anwendungen oxidischer Gläser.

Im Falle von SiO_2 werden klassische MD-Simulationen mit zwei verschiedenen klassischen Potentialen durchgeführt: Dem gut untersuchten BKS und dem CHIK Potential. In Übereinstimmung mit bisherigen Ergebnissen zeigen auch kleine Systeme (ca. 165 Atome) alle charakteristischen Merkmale glasiger Dynamik, der vorwiegende "Finite Size Effekt" ist eine Verlangsamung der Dynamik und die Diffusionskonstanten weisen ein Arrheniusverhalten in der Temperaturabhängigkeit bei niedrigen Temperaturen auf. Glaskonfigurationen werden durch einen Quench aus der Schmelze mit klassischen MD Simulationen und einer nachfolgenden strukturellen Relaxation mit DFT Kräften generiert. Letzteres verringert im Wesentlichen den mittleren Si-O-Si Winkel um etwa $4° - 6°$. Nach der Relaxation weisen die Glasproben des BKS Potential und des CHIK Potentials keine signifikanten strukturellen Unterschiede auf. Des Weiteren stimmen die strukturellen Eigenschaften gut mit denen eines Ab Initio Quenches und mit experimentellen Ergebnissen von Röntgen- und Neutronenstreuung überein. Ein besonderer Fokus liegt auf den Vibrationseigenschaften, da diese die Berechnung der Niedertemperatur-Thermodynamik ermöglichen. Daher ist ein Vergleich des berechneten mit dem experimentellen Vibrationsspektrums $g(\nu)$ ein guter Test für die Qualität einer Glasstruktur. Die Vibrationsspektren werden unter Verwendung von klassischen und quantenmechanischen Kräften mit der sogenannten "Frozen Phonon"-Methode berechnet. In Analogie zu bisherigen Arbeiten zeigen die DFT-Kurven eine hervorragende Übereinstimmung mit experimentellen Ergebnissen inelastischer Neutronenstreuung. Entsprechendes gilt für die Wärmekapazität bei konstantem Volumen $C_{\mathrm{V}}(T)$.

Diese Glaskonfigurationen nach der strukturellen Relaxation sind Basis für Berechnung der linearen thermischen Ausdehnungskoeffizienten $\alpha_{\mathrm{L}}(T)$ in quasiharmonischer Näherung. Bemerkenswert ist die Beobachtung eines Vorzeichenwechsels in $\alpha_{\mathrm{L}}(T)$ sowohl im Falle von quantenmechanischen (DFT) als auch von klassischen Kräften bei allen außer einer Glaskonfiguration, was meines Wissens bis jetzt noch nicht berichtet wurde. Der Temperaturbereich der negativen thermischen Ausdehnung reicht von 0 K bis hin zu etwa 130 K und 160 K (DFT Kräfte) und bis hin zu etwa 90 K und 325 K (klassische Kräfte). Bei Temperaturen unter 200 K zeigen die DFT-Kurven eine sehr gute Übereinstimmung mit experimentellen Daten.

Es gibt starke experimentelle Belege dafür, dass sich in purem B_2O_3-Glas etwa $60\% - 80\%$ der Boratome in planaren Boroxolringen mit je 3 Bor- und 3 Sauerstoffatomen befinden. Dies vorweg geschickt, werden Ab Initio MD Simulationen der Glasschmelze durchgeführt, welche bei 2300 K eine vermehrte Anzahl von Dreiringen aufweisen. Die Flüssig-Trajektorie bei 2300 K dient als Grundlage für die Entwicklung eines neuen klassischen Wechselwirkungspotentials, basierend auf

einer erweiterten Version der strukturellen Fitprozedur, welche dem CHIK Potential zugrunde liegt. Die Einbeziehung von Dreikörper-Winkeltermen führt zu einer signifikant verbesserten Übereinstimmung der Eigenschaften von klassischen MD und Ab Initio MD Simulationen. Ein neuer Typ Winkelpotential wird eingeführt, bei welchem die Wechselwirkungen kontinuierlich ein- und ausgeschaltet werden abhängig vom interatomaren Abstand. Dieser wird als neuer Pair Style des LAMMPS Softwarepakets implementiert. Wiederum werden Glaskonfigurationen generiert durch Quenches aus der Schmelze mit klassischen MD Simulationen und nachfolgender quantenmechanischer Relaxation. Zwei unterschiedliche Parametrisierungen des neuen Potentialtyps werden mit den Originalparametern vor der Fitprozedur verglichen. Des Weiteren werden 4 Ab Initio Quenches durchgeführt. In allen Fällen stimmen die mittleren B-O und O-O Abstände gut mit experimentellen Daten aus Neutronenstreuung überein. Die Glasstrukturen des neuen Dreikörperpotentials zeigen eine Verbesserung im Vergleich zu den Originalparametern bezüglich leicht kleinerer mittlerer B-B Abstände und des Vorkommens von Boroxolringen. Allerdings ist der mittlere Anteil von Boroxolringen immer noch recht klein ($f = 2.5 \pm 1.1\%$ - $f = 8 \pm 2.3\%$). Die Ab Initio Quenches weisen leicht größere mittlere Anteile von Boroxolringen auf: $f = 5 \pm 5\%$ (Quench von 3600 K) und $f = 15 \pm 5\%$ (Quench von 2300 K). In Übereinstimmung mit bisherigen Arbeiten demonstriert dies, dass das Auftreten von Boroxolringen ein besonders sensitives Maß für die Qualität eines klassischen Kraftfelds ist und dass sehr hohe Quenchraten in Computerexperimenten das Entstehen von Boroxolringen in einer Größenordnung, wie sie im Experiment beobachtet wird, verhindern. Die DFT-Vibrationsspektren $g(\nu)$ zeigen eine akzeptable Übereinstimmung mit den Ergebnissen inelastischer Neutronenstreuung. Die Peakhöhe der Boroxolring-Signatur hängt von f ab.

Durch einem Quench aus der Schmelze mittels klassischer MD Simulation und nachfolgender struktureller Relaxation kann eine Glasstruktur generiert werden, die vergleichbar ist mit der eines Ab Initio Quenches, wenn man ein zweckmäßiges klassisches Kraftfeld verwendet. Es kann keine generelle Aussage getroffen werden, welche Methode zu einer Glasstruktur führt, welche besser mit der eines echten Laborexperiments übereinstimmt.

Contents

List of Figures

List of Tables

Chapter 1

Introduction

In the year 1893, the first laboratory borosilicate glass was introduced onto the market by the "Glastechnisches Laboratorium Schott & Genossen Jena", which nowadays is the "Schott AG". Since 1887 borosilicate glasses, containing the glass former B_2O_3, as well as the glass former SiO_2, have been developed by Otto Schott and patented in 1891 [1]. In 1938 the name DURAN® was introduced for the marketing of laboratory borosilicate glass. DURAN® has the chemical composition in weight percent of 81 % SiO_2, 13 % B_2O_3, 4 % Na_2O+K_2O and 2 % Al_2O_3 [2]. This was a great progress with respect to the alkaline silicate (soda-lime) or lead silicate glasses, as borosilicate glasses have an improved chemical resistance, mechanical strength, heat resistance and thermal shock resistance. The latter is connected to a significantly lower coefficient of thermal expansion. Regarding these properties, pure SiO_2 glass, or vitreous silica, shows even superior behavior. However, it is very hard and expensive to process, due to its very high glass transition temperature of $T_g \simeq 1475\,\mathrm{K}$ [3]. Adding glass modifiers, like alkaline oxides, alkaline earth oxides and aluminum oxide, significantly reduces the glass transition temperature and leads to glasses that are easy and cheap to process [4]. However, the before mentioned properties are significantly deteriorated, making these glasses unusable, for example, as laboratory glasses. Adding the glass former B_2O_3 (boric acid, $T_g \simeq 526\,\mathrm{K}$ [5]) and reducing the amount of glass modifiers, helps in producing a glass, which shows a significant improvement of the relevant properties, in combination with a significantly lower glass transition temperature than pure SiO_2.

This substantiates the interest in the model glass former SiO_2, as well as the model glass former B_2O_3. Regarding glasses with different components, as the aforementioned borosilicate glasses, the exact glass structure is still not known in many cases. Furthermore, the dependence of the properties of a glass on its composition is still hard to predict. In practice, glass development goes along with conducting a series of test melts with a slight variation of the glass compositions and a subsequent interpolation of the glass properties, one is interested in. Therefore, a better understanding of the glass structure on an atomistic level and the prediction of resulting glass properties is desirable.

The first model of oxide glasses was proposed by Zachariasen's random network theory [6]. In this model, the glass consists of a three-dimensional random network built up by glass formers and modified by glass modifiers, following certain rules. However, it turns out that the degree of randomness varies from glass to glass. Some glasses are closer to Zachariasen's picture, whereas others show a more microcrystalline structure [4]. Nowadays, computer simulations are an important tool in the modeling of oxide glasses on an atomistic level. For instance, classical molecular dynamics (MD) [7] or Monte Carlo (MC) [8] simulations can be carried out. Here, typical system sizes are of the order of 1000 to a few 100000 atoms and time scales up to the order of microseconds are accessible. However, the inter-atomic forces are described on the basis of empirical force fields, which are less accurate than a full quantum-mechanical description. The latter can be accomplished on the basis of density functional theory (DFT) [9], limiting the system sizes to about 100 - 200 atoms and the accessible time scales to the order of picoseconds. In principle, both techniques can be combined, which, for example, has already been successfully done in case of the model glass former SiO_2 [10, 11]. Here, the glass structure is generated by means of a classical MD simulation, with a subsequent structural relaxation by means of a quantum-mechanical calculation and a computation of the vibrational properties based on quantum-mechanical forces. This method requires a suitable classical force field to generate a realistic glass structure in the first place.

The work presented in this thesis follows this direction. Due to the aforementioned reasons, the model glass formers SiO_2 and B_2O_3 are examined and glass structures are generated by means of cooling down a glass melt with classical MD simulations, followed by a subsequent quantum-mechanical relaxation (see chapters 4 and 6). In case of SiO_2, two different classical force fields are employed. In case of B_2O_3, a new classical force field is developed, based on the liquid structure at high temperatures extracted from a quantum-mechanical (DFT) calculation. The structural properties of the generated glasses are compared to experimental results. In addition, special focus is placed on the vibrational properties, as the latter give access to the low-temperature thermodynamics. It turns out that a realistic glass structure, in combination with quantum-mechanical forces, leads to a vibrational density of states comparable to the experimental one and a good accordance of the specific heat with respect to temperature. The thermal expansion also shows a good agreement with experimental results in the low-temperature regime. This is demonstrated in case of SiO_2 in chapter 5. Here, a change of sign of the linear expansion coefficient and a range of negative thermal expansion at low temperatures is observed, in agreement to experimental results. To my knowledge, this has not been reported before in case of DFT calculations of vitreous silica.

Chapter 2

Simulation of real glass formers?

2.1 The glass transition - phenomenology

Glass is a non-equilibrium state of matter. At temperatures below the solid-liquid phase transition the equilibrium configuration is a crystalline structure and the corresponding phase depends on the ambient conditions. However, many liquids can form a glass if they are cooled fast enough to avoid crystallization. In this way, a so-called supercooled phase can be reached at temperatures below the melting temperature T_m of the corresponding crystalline structure. In a glass forming liquid the distinction of two typical timescales becomes necessary when cooling the system down [12]. The atom trajectories are constituted of frequent collisions with the neighboring particles. This rattling motion happens on a very short timescale of typically about $10 - 100\,\mathrm{fs}$ in oxide glasses. After several collisions, an atom can break out of the cage of the surrounding particles and change its relative position. This diffusive motion is typically a collective phenomenon and occurs on longer timescales than the rattling motion. This structural relaxation time or α-relaxation time τ_α [13] increases by many orders of magnitude, when cooling the system down and at some point the glass transition temperature T_g is reached. In Fig. 2.1 this two-step relaxation process and the increase of the α-relaxation time by orders of magnitude is impressively demonstrated by means of photon-correlation spectroscopy of the "strong" network forming glass former B_2O_3 at different temperatures [14]. In contrast to the crystallization transition, this is not a phase transition in the sense of the Ehrenfest classification [15], but a kinetic transition. The glass transition temperature T_g is the temperature at which the system falls out of equilibrium and no stress relaxation is possible anymore on the timescale of the experiment. Therefore, there is no unique definition of T_g, but it depends on the experiment. One way of measuring T_g is the increase of the heat capacity C_p from a solid-like to a liquid-like value by means of scanning calorimetry [16]. This is connected to the fact that the configurational contribution to the specific heat decreases to zero at temperatures below T_g [17] and leads to one possible definition of T_g as the onset temperature of the jump in heat capacity at a heating rate of $10\,\mathrm{K/min}$ [18]. At the glass transition temperature T_g defined in this way, the structural

relaxation time is about 100 s. Another common definition of T_g is the temperature at which the shear viscosity η of the glass forming system is equal to 10^{13} Poise $= 10^{12}$ Pa/s [13].

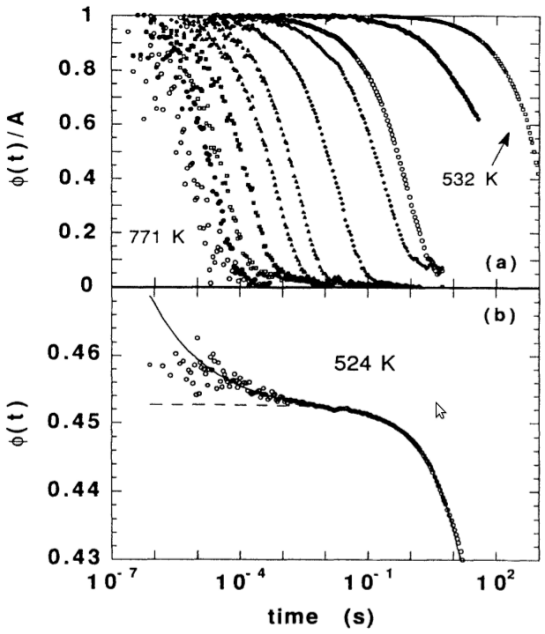

FIGURE 2.1: Structural relaxation functions $\Phi(t)/A$ and $\Phi(t)$ of B_2O_3 above T_g and just below T_g, measured by photon-correlation spectroscopy. Reprinted figure with permission from [14], http://dx.doi.org/10.1103/PhysRevLett.71.2260. Copyright (2015) by the American Physical Society.

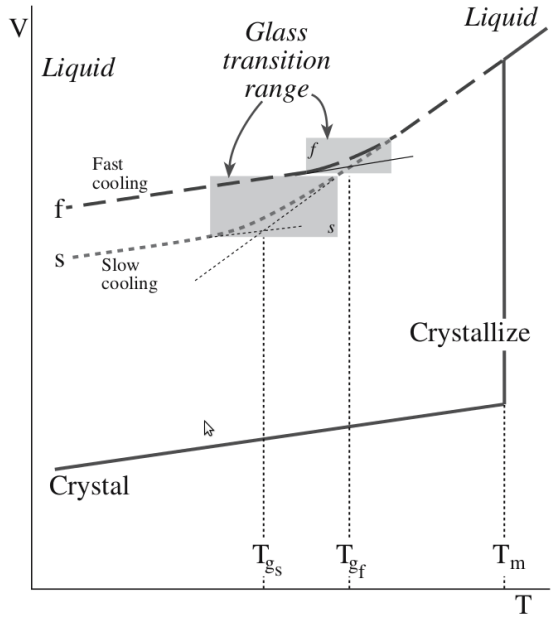

FIGURE 2.2: Schematic V-T diagram of a glass forming liquid. Figure reprinted from [19], page 380. With permission of Springer Science +Business Media.

A consequence of the kinetic nature of the glass transition is the dependence of the glass properties on the cooling rate. This is schematically shown in Fig. 2.2, taken from [19]. So, for example, a higher cooling rate often leads to a lower glass density. When generating glass structures by means of computer simulations, the cooling rates are typically higher by many orders of magnitude compared to values reached in real experimental setups. In classical molecular dynamics simulations, the lowest cooling rates are of the order of $\Gamma = 10^{11}$ K/s to $\Gamma = 10^{10}$ K/s. Even in the latter case, the glass melt is cooled from about 2300 K to room temperature in approximately 0.2 μs. In quantum mechanical simulations, the cooling rates are even higher by about three orders of magnitude. The consequence is that effects of different cooling rates are visible in the generated glass structures [20, 21] and the systems fall out of equilibrium at a much higher temperatures than in real experiments and, thus, the glass transition temperatures are not comparable. In addition to other general limitations of a computer model, one has to keep in mind this difference in the cooling history, when examining glass structures generated by computer simulations.

In different glass forming systems, the temperature dependence of the structural relaxation time τ_α can have a different functional form. A convenient way of demonstrating this feature is plotting the shear viscosities η or the relaxation times τ_α with respect to T/T_g in the so-called

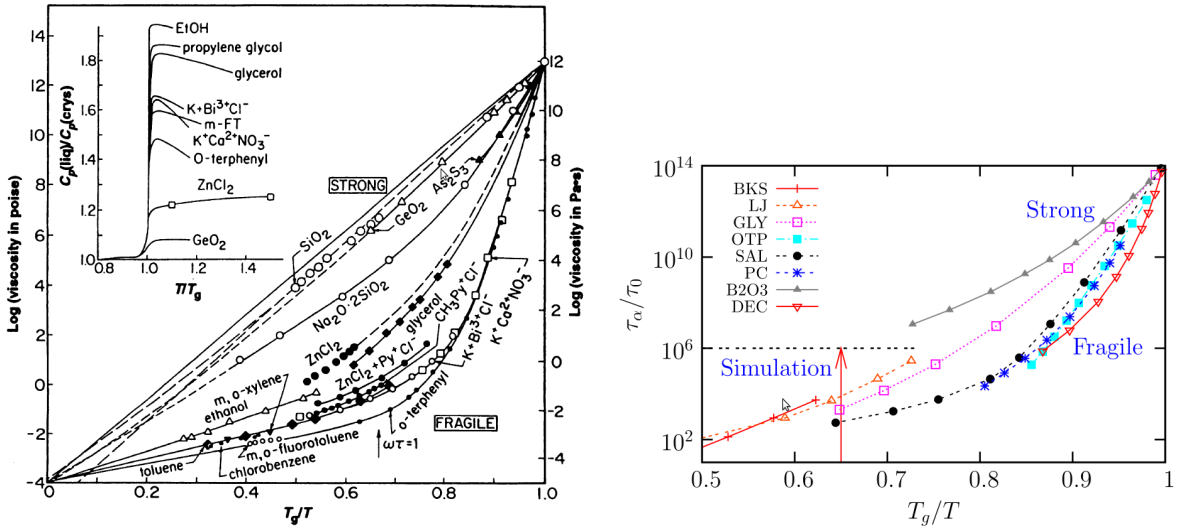

FIGURE 2.3: Angell plots of the shear viscosity η and structural relaxation time τ_α with respect to T_g/T for different glass forming systems, including computer simulations of SiO_2 with the BKS potential [22]. Figure from [12], http://dx.doi.org/10.1126/science.267.5206.1924. Reprinted with permission from AAAS. Reprinted figure with permission from [13], http://dx.doi.org/10.1103/RevModPhys.83.587. Copyright (2015) by the American Physical Society.

Angell plot [12]. Here, the definition of T_g according to $\eta = 10^{13}$ Poise is employed. In Fig. 2.3, examples for different glass forming systems are shown, including computer simulations of SiO_2 with the BKS potential [22]. The "strong" glass formers, like, for example, SiO_2, GeO_2 and B_2O_3 show an Arrhenius-like behavior of $\eta(T)$ or $\tau_\alpha(T)$ over the whole temperature range, whereas the "fragile" glass formers show a super-Arrhenius behavior with a dramatic change of η or τ_α in the glass transition range. Here, the relaxation times increase faster than exponentially with decreasing temperature. This behavior can be modeled by means of a Vogel-Fulcher-Tammann-law [15]:

$$\eta(T) = \eta_0 \exp\left[\frac{B}{T - T_0}\right]. \tag{2.1}$$

This functional form diverges at the Vogel-temperature T_0. The temperature T_0 is close to the so-called Kauzmann temperature T_K [23], at which the excess entropy of a fluid with respect to the corresponding crystalline structure $\triangle S = S - S_{\text{cryst}}$ can be extrapolated to zero. A small value B/T_0 leads to a strong curvature of $\eta(T)$ and the super-Arrhenius behavior of $\eta(T)$ or $\tau_\alpha(T)$ in case of the so-called "fragile" glass formers. In the limit of $T_0 \to 0$, equation (2.1) shows the Arrhenius dependence. Therefore, a large value of B/T_0 leads to a good description of the so-called "strong" glass formers. However, the Vogel-Fulcher-Tammann law does not have a solid theoretical foundation [15]. Another functional form with a more solid theoretical foundation is predicted by Mode-Coupling Theory [24]:

$$\eta\,(T) = \eta_0\ (T - T_\mathrm{c})^{-\gamma}\,. \tag{2.2}$$

Here, T_c is the critical temperature, corresponding to the transition temperature of the system to an ideal glass and γ is a critical exponent. The parameters T_c and γ depend on the material and can be calculated.

Another matter of fact, clearly visible in Fig. 2.3, is that the timescales accessible by computer simulations only allow the calculation of equilibrium properties at higher temperatures than the ones accessible in experiments. A way to overcome this gap is to extrapolate different properties to lower temperatures if the temperature dependence is known. At least for rather strong glass formers, many properties should show an Arrhenius-like temperature dependence and therefore an extrapolation is possible in some cases.

2.2 Vibrational properties, structure and anomalies of oxide glasses

As already described in the introduction, oxide glasses consist of network formers and network modifiers. The most important network formers for industrial applications are silicon oxide SiO_2 and boron oxide B_2O_3. Other oxides that are capable of forming a three-dimensional network are, for example, water H_2O and germanium oxide GeO_2.

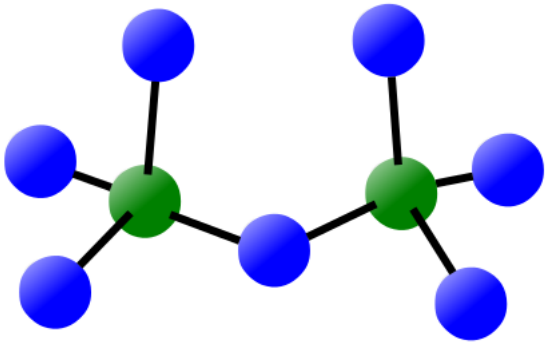

FIGURE 2.4: Illustration of two connected SiO_4 tetrahedra.

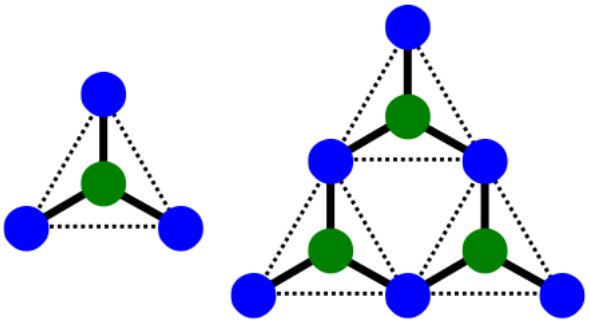

FIGURE 2.5: Illustration of BO_3 triangle and boroxol ring.

All network formers are capable of building a stable three dimensional network. In each case, the glassy network consists of basic building blocks that are connected via bridging oxygen atoms. In the case of SiO_2, the basic building block of the glass structure is a tetrahedron consisting of a silicon atom surrounded by four oxygen atoms: SiO_4. This is illustrated in Fig. 2.4. In the case of B_2O_3, the basic building block is a plane triangular structure consisting of a boron atom surrounded by three oxygen atoms: BO_3 (see Fig. 2.5). These glassy networks show no long-range order, but there is an intermediate or medium range structure. A way to describe

the intermediate range structure is the notation of ring sizes n. Here, n is the number of Si-O or B-O pairs that are linearly connected in a way that the first and last oxygen atom are identical.

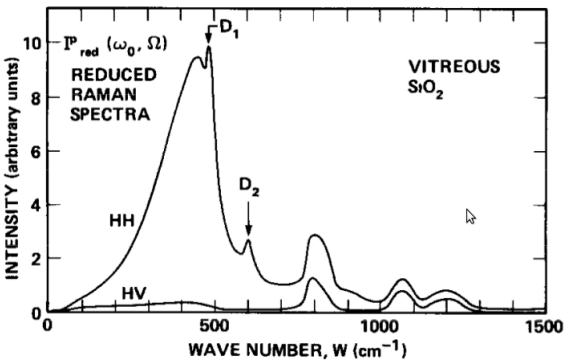

FIGURE 2.6: Raman spectrum of vitreous SiO_2. Reprinted from [25], http://dx.doi.org/10.1016/0038-1098(82)90329-5, with permission from Elsevier.

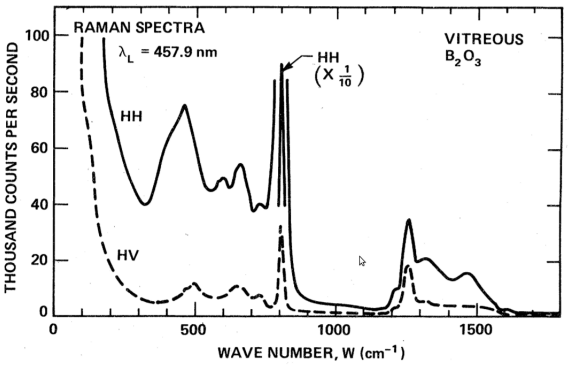

FIGURE 2.7: Raman spectrum of vitreous B_2O_3. Reprinted figure with permission from [26], http://dx.doi.org/10.1103/PhysRevB.22.3983. Copyright (2015) by the American Physical Society.

The vibrational spectrum of oxide glasses gives valuable information on the glass structure. In combination with different structural models, conclusions also on the intermediate range order can be drawn. There are different experimental techniques that give insight into the vibrational properties, for example Raman spectroscopy and inelastic neutron scattering. However, the intensities of the Raman spectrum are highly influenced by the Raman coupling factors. In Fig. 2.6, for example, a Raman spectrum of vitreous SiO_2 is shown. Generally, the high frequency part of the spectrum is connected to vibrational modes that are spatially more localized and the low frequency part is connected to less localized vibrational modes. So, for example, the modes in the frequency range from about $1000\,\mathrm{cm}^{-1} \mathrel{\hat{=}} 30.0\,\mathrm{THz}$ to $1200\,\mathrm{cm}^{-1} \mathrel{\hat{=}} 36\,\mathrm{THz}$ are connected to Si-O bond-stretching motions. In addition to the rather broad vibrational bands, distinct sharp peaks are visible. These sharp peaks are connected to certain structural features. The so-called D1 and D2 lines in the vibrational spectrum of SiO_2 at approximately $495\,\mathrm{cm}^{-1} \mathrel{\hat{=}} 14.8\,\mathrm{THz}$ and $606\,\mathrm{cm}^{-1} \mathrel{\hat{=}} 18.2\,\mathrm{THz}$ are connected to the breathing motion of four-membered ($n = 4$) and three-membered ($n = 3$) rings [27, 28]. In the vibrational spectrum $g(\nu)$ of B_2O_3, the most prominent feature is the sharp peak at about $808\,\mathrm{cm}^{-1} \mathrel{\hat{=}} 24.2\,\mathrm{THz}$. This feature is most pronounced in the Raman spectrum (see Fig. 2.7), due to the Raman coupling factors, but also visible in inelastic neutron scattering [29, 30]. This is connected to the breathing mode of oxygens in a three-membered ring ($n = 3$). A planar ring consisting of 3 boron and 3 oxygen atoms is called boroxol ring, when the participating boron atoms are all 3-fold coordinated with respect to the oxygen atoms and the oxygen atoms are all 2-fold coordinated with respect to the boron atoms [31]. This is illustrated in Fig. 2.5. The high intensity of this peak in the vibrational spectrum in combination with NMR measurements leads to the conclusion that about $60\% - 80\%$ of the boron atoms are localized within such boroxol rings. As a consequence, pure B_2O_3 glass can be seen as a network of BO_3 triangles and B_3O_6 rings.

The above mentioned oxide glasses have rather striking thermo-mechanical properties. For example, vitreous SiO_2 shows a change of sign of the the linear expansion coefficient $\alpha_L(T)$ and a range of negative thermal expansion near the absolute zero at temperatures below about 200 K [32, 33]. In addition, a density maximum occurs in the molten state at approximately 1823 K [34].

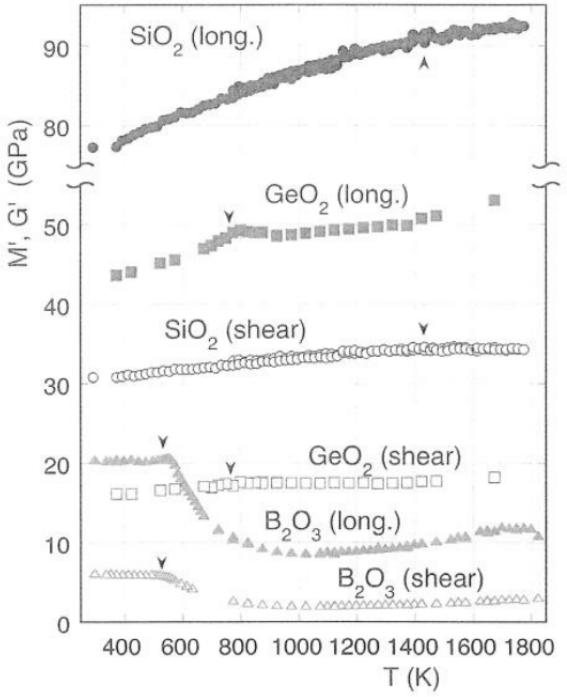

FIGURE 2.8: Longitudinal (M) and shear (G) elastic moduli of SiO_2, B_2O_3 and GeO_2 glass with respect to temperature. Reprinted from [35] with permission from the Society of Glass Technology.

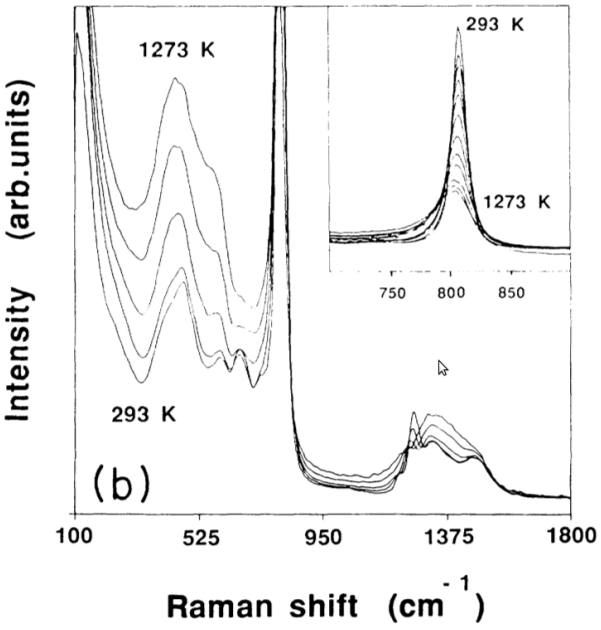

FIGURE 2.9: Raman spectrum of vitreous B_2O_3 at different temperatures. Reprinted figure with permission from [36], http://dx.doi.org/10.1103/PhysRevB.45.12797. Copyright (2015) by the American Physical Society.

Also SiO_2, as well as B_2O_3 and GeO_2, show an increase of the elastic moduli with increasing temperature in certain temperature regimes [35, 37]. For SiO_2, the elastic moduli increase steadily over the whole temperature range displayed in Fig. 2.8. In the case of GeO_2, they show a steady increase with a small cusp at about the glass transition temperature. B_2O_3 shows first a sharp decrease around the glass transition temperature, whereas in the melt at high temperatures, the elastic moduli show a steady increase. This means that the effect of the glass transition is most pronounced for the most fragile of the three glasses, namely B_2O_3. Here, the decay of the elastic moduli is connected to the dissolution of boroxol rings. In fact, Raman spectroscopy at different temperatures below and above the glass transition range shows a strong decrease of the full width at half maximum (FWHM) and the Raman intensity of the peak at around $808\,\mathrm{cm}^{-1} \mathrel{\hat{=}} 24.2\,\mathrm{THz}$ [36] (see Fig. 2.9). In contrast to the immediate drop of the elastic moduli at about the glass transition temperature in the case of B_2O_3, the steady increase of the moduli, in all cases, is connected to topological changes of the network structure without changing the ring sizes. For example in SiO_2, the steady increase is attributed to spontaneous Si-O-Si bond rotations similar to the phase transformation from α- to β-cristobalite [38], which

both show a structure with six-membered rings ($n = 6$). The α-cristobalite has a higher density and less symmetric six-membered rings, whereas β-cristobalite has a lower density and six-membered rings with a higher symmetry. In vitreous SiO_2, the dominant ring size is $n = 6$, as well, and the so-called amorphous-amorphous transition leads to a structure with a lower density and, at the same time, higher elastic moduli.

2.3 Modeling of oxide glasses

The modeling of oxide glasses can be performed in different ways. A simple approach for modeling the glass structure is the construction of ball and stick models [39]. More sophisticated models can be developed by means of computer simulations. To perform computer simulations of oxide glasses on an atomistic level, two different things have to be considered: On the one hand, the interactions of the atoms have to be specified. On the other hand, an initial configuration of the atoms has to be generated and the atom positions have to be updated in a specified manner in each simulation step. A common update scheme of the atoms is the technique of classical molecular dynamics simulations [40]. Here, the particles, in principle, follow trajectories according to Newton's laws of motion of classical mechanics. In addition, the implementation of a thermostat is necessary to perform simulations at a specific temperature. The technique of classical molecular dynamics simulations is described in detail in section 3.1. In classical mechanics, the interactions between particles are described by classical forces. It is convenient to model the atomic interactions by conservative forces which can be derived from a classical potential $V(\{\mathbf{r}_i(t)\})$ depending on the positions of all atoms of the system. The concrete mathematical form of the interaction potential $V(\{\mathbf{r}_i(t)\})$ can be arbitrarily complex. The chemical bonds between the atomic constituents of oxide glasses have an ionic and a directional covalent character. Therefore, a typical potential consists of a long-range electrostatic term and short-range terms. The electrostatic term is composed of 2-body pairwise interactions as the electrostatic force between two atoms only depends on their charge and the distance between them. Specific difficulties, arising from the long-range nature of this interaction, and common ways of implementation techniques are discussed in section 3.1. The short-range interactions typically are only active within a certain cutoff radius r_c of a few angstroms Å ($1\,\text{Å} = 10^{-10}\,\text{m}$) and consist of a repulsive term, originating from the Pauli exclusion principle of the electrons in the atomic shells, and different attractive terms (see section 3.5). Often, van der Waals interactions are used for this purpose. A common addition are further attractive contributions to model the covalent character of inter-atomic bonds. The short-range potential $V(\{\mathbf{r}_i(t)\})$ has to include 3-body interactions, in addition to pairwise interactions, if the directional character of the covalent bonds should be included into the model. In this case, the forces on the atoms not only depend on the pairwise distances between them, but also on the magnitude of angles between distinct triples of atoms. Typical functional forms are given in section 3.5. This makes the implementation more difficult. However, especially in glasses containing boron oxide B_2O_3, the directional term is found to be important to get an acceptable model of the glass structure

(see chapter 6). In the case of SiO_2, it is possible to simulate good model glasses only using 2-body interactions (see chapter 4).

More sophisticated simulation techniques include quantum mechanical interactions between atoms. In principle, the atomic nuclei and the surrounding electrons have to be mathematically described within the framework of quantum mechanics by means of a total wave function $|\Psi(\{\mathbf{r}_i\};\{\mathbf{x}_i\})\rangle$ depending on all degrees of freedom of the system, by solving the many-body Schrödinger equation with the interaction potential $V(\{\mathbf{r}_i\};\{\mathbf{x}_i\})$. Here, $\{\mathbf{x}_i\}$ stands for the degrees of freedom of the n electrons and $\{\mathbf{r}_i\}$ for the degrees of freedom of the N nuclei. Often, it is sufficient to treat only the electrons quantum mechanically and the atomic nuclei as classical particles. This simplification is called Born-Oppenheimer approximation [41] and is justified by the fact that the electronic mass m_e is of the order 10^{-4} of the mass of an atomic nucleus. However, treating all electronic degrees of freedom quantum mechanically is still a many-body problem which is mathematically to complex to solve computationally with present computer technology. Further simplifications have to be made, leading to the density functional theory (DFT). The basic idea of DFT is that any property of the system can be expressed as a functional of the ground state density of the electrons $n_0(\mathbf{x})$ and that the electronic density $n(\mathbf{x})$ that minimizes the functional of the total energy $E[n(\mathbf{x})]$ is the ground state density $n_0(\mathbf{x})$. These are implications of the two Hohenberg-Kohn theorems [9]. Another implication is that it is possible to introduce a system of fictive non-interacting electrons, described by one-particle Schroedinger equations with only 1-body interactions $V_S(\mathbf{x}_i)$, such, that the electronic density $n(\mathbf{x})$ of the system is unchanged. An additional simplification is to treat only the valence electrons of a system explicitly and replace the effects of the core electrons by a pseudopotential. The formalism of DFT is described in detail in section 3.2. DFT is a powerful technique that is broadly used nowadays to simulate different kinds of systems as the interactions between the atoms of the system are quite realistic, despite the simplifications made. Also no empirical forces have to be used. As already described in section 2.1, this technique is computationally much more demanding and requires much smaller system sizes of about 100 - 200 atoms and much faster cooling rates.

Therefore, a useful scheme to generate good glass structures on the computer could be to equilibrate a system at high temperatures with a classical molecular dynamics simulation and after a quench down to room temperature or 0 K switch off the classical force field and continue the computer simulation with a DFT calculation. This combination of classical and quantum mechanical simulation has already been successfully applied, for example, in case of the model glass former SiO_2 [10, 11]. A crucial requirement for the application of this technique is a reliable interaction potential or force field for the classical MD simulation. Once a glass structure has been generated, a comparison of the vibrational spectrum or phonon density of states $g(\nu)$ with experimental results is a good test for the quality of the structure as a good glass structure, in combination with DFT forces, can lead to a realistic $g(\nu)$. Here, $\nu = \omega/2\pi$ is the vibrational frequency. By thermal occupation of $g(\nu)$ or the respective eigenmodes with eigenfrequencies ν_n, the thermodynamic properties of heat capacity at constant volume $C_V(T)$, entropy $S(T)$ and Helmholtz free energy $F(T)$ can be calculated (see section 3.4). The calculation of $F(T)$ at

different system densities gives also access to the linear expansion coefficients $\alpha_L(T) = \frac{1}{L}\left(\frac{\partial L}{\partial T}\right)_p$ (see chapter 5). Especially, $C_V(T)$ and $\alpha_L(T)$ can be directly compared to experimental results.

2.4 Themes of this work

As mentioned before, the quality of a classical force field is an important issue when examining glass melts and generating glass structures by classical MD simulations. For glasses containing SiO_2, a widely used interaction potential is the BKS potential, established by Beest, Kramer and Van Santen in 1990 [22]. The parameters are derived by an iterative process of parameter fitting to microscopic ab initio data of small clusters and optimizing the values to reproduce the experimental unit-cell dimensions and elastic constants of quartz. The BKS potential is an interaction potential only containing 2-body terms. In large scale MD simulations [42], the structural properties, like the static structure factor, are found to be in quite good agreement with experimental results. However, the effective phonon density of states $g(\nu)$ shows discrepancies to the experimental one for low and intermediate frequencies [20]. By employing a new fitting scheme for potential parameters, the properties of the BKS potential could be improved [43]. Here, the potential parameters have been fitted according to the structural properties of a quantum mechanical molecular dynamics simulation of liquid SiO_2, starting with the parameter set from the BKS potential. However, the vibrational spectrum $g(\nu)$ of the new CHIK potential still shows significant differences to the experimental one. As already mentioned in section 2.3, in addition to a realistic structure of the glass or vitreous liquid, it is also necessary to use realistic forces to calculate a realistic $g(\nu)$. In most cases, this can only be achieved by means of a quantum mechanical calculation. Due to the success of the new fitting method [43] in improving the structural properties of liquid and vitreous SiO_2, one theme of this work is the application of this structure-matching scheme to the model glass former B_2O_3. As described in section 2.2, the structure of glasses, containing boron oxide is rather complex and so far, no force field was able to generate a glass structure with a sufficiently high amount of atoms contained in boroxol rings when quenched from the melt. Promising existing potentials are all rather complicated and, for example, include coordination-dependent terms [44, 45], 4-body terms [46, 47], charge-transfer terms [48] or polarization effects [49, 50]. An overview over existing classical force fields of B_2O_3 is given in section 6.1. Regarding this matter, one goal of this work is to test how the structure matching scheme [43] in combination with a simple 2- or 3- body model potential, can lead to a competitive interaction potential and how this scheme could be extended to multi-component glasses.

As already explained in section 2.3, the general course of action in this work is to generate glass structures by quenches from the melt with classical MD simulations and subsequent quantum mechanical relaxations. The latter restrict the examined system sizes to about 100 - 200 atoms. These glass configurations are compared to glass structures, generated by full ab initio quenches, and to experimental results. In chapter 4, these methods are employed in case of the model glass former SiO_2. Here, classical simulations are carried out with the BKS [22] potential and the

CHIK [43] potential. A system size of 165 atoms turns out to be a reasonable choice. In addition to the structural and vibrational properties of the quenched glasses, the structural and dynamical properties of the glass melts are studied (see section 4.1), including the comparison of different system sizes and the temperature dependence of the self-diffusion constants. In principle, the properties of the BKS and the CHIK potential have been compared before [43, 51]. However, to my knowledge, it has not been studied before if structural differences are visible in the glass configurations after the classical quench and the subsequent quantum mechanical relaxation. The respective glass structures are examined in section 4.2. In section 4.3, the vibrational properties are calculated and compared to experimental results. In chapter 5, the thermal expansion of these model glass structures is calculated using the so-called quasi-harmonic approximation, based on the vibrational spectra at different system densities. Classical and quantum mechanical forces are employed and the linear expansion coefficients $\alpha_{\mathrm{L}}(T)$ are compared to experimental results. To my knowledge, the calculation of the thermal expansion of vitreous silica by ab initio methods has not been reported before. In chapter 6, the model glass former B_2O_3 is studied. On the one hand, a set of new force field parameters is fitted, based on the liquid trajectory of an ab initio MD simulation at 2300 K (see section 6.3). On the other hand, the properties of liquid B_2O_3 are studied by means of ab initio MD simulations at different temperatures and compared to the ones of the new classical parameter sets (see sections 6.2 and 6.4). These simulations are carried out at a system size of 150 atoms and a constant system density. Additionally, classical MD simulations of 1200 atoms at $p = 0$ external pressure are conducted. In all cases, the dependence of different properties on temperature are examined, as the internal pressure (150 atom simulations at constant density), the system density ρ (1200 atom simulations at constant external pressure), the self-diffusion constants, the mean B-O-B angles, the mean coordination numbers and the ring sizes. Finally, a set of glass structures is generated in the way described above. The structural and vibrational properties of the glass structures, according to the new parameter set, the original parameter set before the fitting procedure and 4 independent full ab initio quenches are compared to each other and to experimental results (see sections 6.5 and 6.6), both, using classical and quantum mechanical forces.

Chapter 3

Simulation techniques and analysis

3.1 Classical MD simulations

3.1.1 Basic concept

Basic idea of molecular dynamics (MD) simulations

There are different ways to sample the equilibrium properties of a classical many-body system. One way are classical Monte Carlo (MC) simulations [52]. Here, the positions of the particles are updated in a stochastic manner, depending on a sequence of random numbers. Another approach is the one of classical molecular dynamics (MD) simulations. Here, in principle, the classical equations of motion are solved [40]:

$$M_i \, \ddot{\mathbf{r}}_i = -\nabla_{\mathbf{r}_i} V = \mathbf{F}_i. \tag{3.1}$$

This allows to follow the real-time trajectory of the particles and to compute time dependent quantities of the system, such as time correlation functions. The interaction-potential $V = V\left(\{\mathbf{r}_i\left(t\right)\}\right)$ can be written as a series of different 1-, 2- and many-body contributions:

$$V = \sum_{i=1}^{N} V_1\left(\mathbf{r}_i\right) + \frac{1}{2!} \sum_{i,j\neq i=1}^{N} V_2\left(\mathbf{r}_{ij}\right) + \frac{1}{3!} \sum_{i,j\neq i,k\neq i=1}^{N} V_3\left(\mathbf{r}_{ij}, \mathbf{r}_{ik}\right) + \ldots, \quad \mathbf{r}_{ij} = \mathbf{r}_i - \mathbf{r}_j. \tag{3.2}$$

In principle, it can contain up to N-body terms. If no external fields are applied, it is convenient to chose $V_1 = 0$. In general, equation 3.1 can not be solved analytically, but has to be integrated numerically. The most naive algorithm would be to just make a Taylor-expansion up to a specific order:

$$\mathbf{r}_i(t+\delta t) = \mathbf{r}_i(t) + \mathbf{v}_i(t)\,\delta t + \frac{\mathbf{F}_i(t)}{2\,M_i}\,\delta t^2, \quad \mathbf{F}_i(t) = -\nabla_{\mathbf{r}_i} V(\{\mathbf{r}_i(t)\}), \tag{3.3}$$

$$\mathbf{v}_i(t+\delta t) = \mathbf{v}_i(t) + \frac{\mathbf{F}_i(t)}{M_i}\,\delta t, \tag{3.4}$$

This Euler algorithm has some severe drawbacks [7]: It is not time-reversible, meaning that $\mathbf{r}_i(t+\delta t) - \mathbf{v}_i(t+\delta t)\,\delta t + \frac{\mathbf{F}_i(t+\delta t)}{2\,M_i}\,\delta t^2 \neq \mathbf{r}_i(t)$. Furthermore, it is not symplectic, meaning the volume in phase space is not preserved. This can result in a long-term energy drift, which is, of course, unfavorable. A time-reversible and symplectic form of the numerical integration scheme can be achieved by adding the second-order Taylor expansion of $\mathbf{r}_i(t)$ with negative sign to the one, according to equation (3.3). This leads to the Verlet algorithm [53] for the update of the particle positions:

$$\mathbf{r}_i(t+\delta t) = 2\,\mathbf{r}_i(t) - \mathbf{r}_i(t-\delta t) + \frac{\mathbf{F}_i(t)}{2\,M_i}\,\delta t^2. \tag{3.5}$$

In this algorithm, the velocities are not included explicitly to compute the trajectories. However, they are needed to calculate the kinetic energy and the total energy of the system

$$E_{\text{kin}}(t) = \sum_{i=1}^{N} \frac{\mathbf{v}_i(t)^2}{2\,M_i}, \quad E_{\text{tot}}(t) = E_{\text{kin}}(t) + V(\{\mathbf{r}_i(t)\}) \tag{3.6}$$

The velocities can be obtained by means of the particle positions at times $t+\delta t$ and $t-\delta t$:

$$\mathbf{v}_i(t) = \frac{\mathbf{r}_i(t+\delta t) - \mathbf{r}_i(t-\delta t)}{2\delta t}, \tag{3.7}$$

meaning they can only be calculated when the particle positions at $\mathbf{r}_i(t+\delta t)$ are known. This drawback can be overcome by using the velocity Verlet algorithm [54]. Here, the particle positions are updated, according to equation (3.3) and the velocities are update in the following way:

$$\mathbf{v}_i(t+\delta t) = \mathbf{v}_i(t) + \frac{\mathbf{F}_i(t) + \mathbf{F}_i(t+\delta t)}{2\,M_i}\,\delta t. \tag{3.8}$$

In fact, this algorithm is equivalent to the Verlet algorithm (equation (3.5)). This can be seen by substituting $\mathbf{v}_i(t) = \mathbf{v}_i(t-\delta t) + \frac{\delta t}{2\,M_i}\left[\mathbf{F}_i(t-\delta t) + \mathbf{F}_i(t)\right]$ (equation (3.8) evaluated at $t-\delta t$) into equation (3.3). Usually this algorithm is implemented in the following way:

- Update the particle positions according to equation 3.3.

- Update the velocities according to: $\mathbf{v}_i\left(t+\frac{1}{2}\delta t\right)=\mathbf{v}_i\left(t\right)+\frac{\mathbf{F}_i(t)}{M_i}\,\frac{1}{2}\delta t$.
- Calculate the inter-particle forces according to the particle positions $\mathbf{r}_i\left(t+\delta t\right)$: $\mathbf{F}_i\left(t+\delta t\right)=-\nabla_{\mathbf{r}_i}V\left(\mathbf{r}_i\left(t+\delta t\right),..,\mathbf{r}_N\left(t+\delta t\right)\right)$.
- Update the velocities according to: $\mathbf{v}_i\left(t+\delta t\right)=\mathbf{v}_i\left(t+\frac{1}{2}\delta t\right)+\frac{\mathbf{F}_i(t+\delta t)}{M_i}\,\frac{1}{2}\delta t$.

Integrating the equations of motion (3.1), using one of the above integration schemes, leads to the statistical sampling of the system in the microcanonical (NVE) ensemble, meaning the total energy of the system (see equation (3.6)) is conserved. In the limit of $\delta t\to 0$ this is exactly the case, meaning the Hamiltonian

$$H=\sum_{i=1}^{N}\frac{\mathbf{p}_i^2}{2\,M_i}+V\left(\{\mathbf{r}_i\}\right), \tag{3.9}$$

which is the Legendre transform of the Lagrangian

$$\mathcal{L}=\sum_{i=1}^{N}\frac{M_i\left(\frac{\partial\mathbf{r}_i}{\partial t}\right)^2}{2}-V\left(\{\mathbf{r}_i\}\right), \tag{3.10}$$

is a conserved quantity. In practice, the total energy fluctuates around the mean value during a simulation run. This is connected to the fact that the discretized equations of motion with finite δt have a different conserved quantity, called shadow Hamiltonian [55]. The leading corrections to the functional form of equation (3.9) are of the order δt^2. Therefore, the amplitude of the total energy fluctuations $\delta E_{\text{tot}}=|E_{\text{tot}}-\langle E_{\text{tot}}\rangle|$ should be proportional to the time step squared $(\delta t)^2$:

$$|E_{\text{tot}}-\langle E_{\text{tot}}\rangle|\propto(\delta t)^2\,. \tag{3.11}$$

This relation is tested in case of the model glass formers SiO_2 and B_2O_3 in subsection 4.1.1 and section 6.4.

More details of molecular dynamics (MD) simulations

In a MC, as well as an MD simulation, the typical number of particles N is of the order of a few 10000 to 100000. In practice, they are confined in a finite simulation box with box length L_{Box}. When studying the bulk properties of the system, one is not interested in the effects due to the surface of the system. As the surface area scales with $N^{1/3}$, surface effects become

irrelevant, when studying macroscopic systems of the order of $N > 10^{23}$ atoms. To avoid surface effects, the concept of periodic boundary conditions is introduced [40]. Here, the simulation box is surrounded by its own replicas. When a particle moves in the original box, its periodic image moves in the same way and when a particle leaves the original box through one of the walls, an image particle enters through the opposite one. This is illustrated in Fig. 3.1. This implies that only the coordinates of the atoms in the original box have to be stored during the simulation run. In addition, the number of times is counted that an atom passes one of the walls in each direction. With this information the so-called unwrapped atom coordinates $\mathbf{r}_{i,\mathrm{u.}}$ can be calculated. These are important to study, for example, the diffusive properties of the system, as $\mathbf{r}_{i,\mathrm{u.}}(t) - \mathbf{r}_{i,\mathrm{u.}}(0)$ is the total distance that atom i moved in time t.

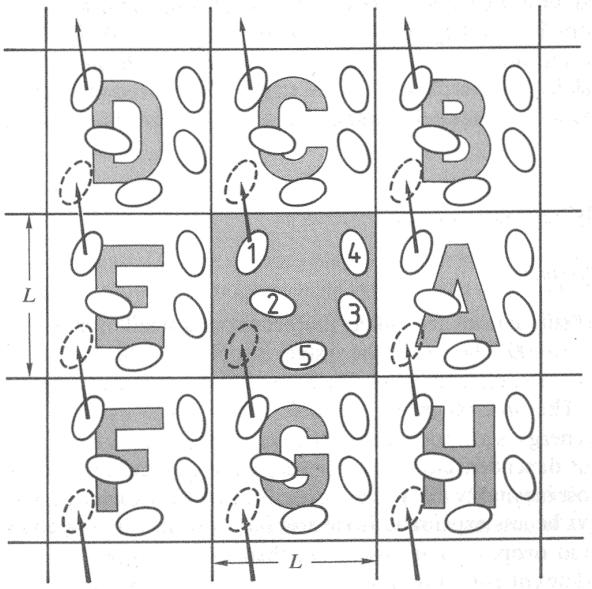

FIGURE 3.1: Illustration of periodic boundary conditions. Figure reprinted from [40], page 24. With permission of Oxford University Press.

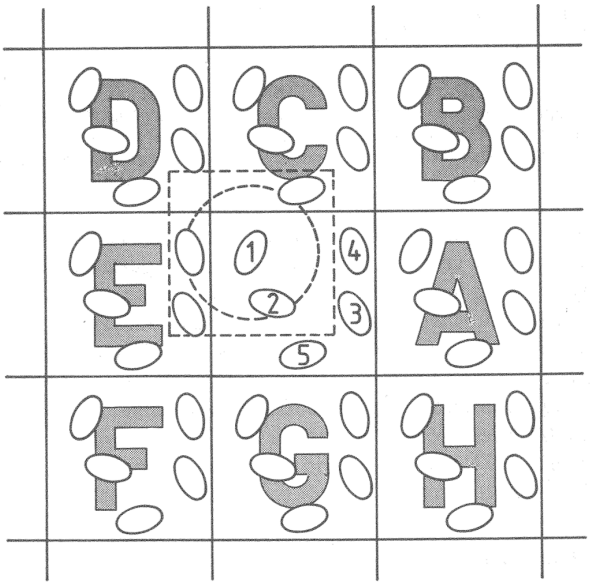

FIGURE 3.2: Illustration of minimum image convention. Figure reprinted from [40], page 28. With permission of Oxford University Press.

The method of periodic boundary conditions preserves the total momentum and energy. However, long-wavelength fluctuations with a wavelength longer than the length of the simulation box L_{Box} are suppressed. Also, depending on the interaction potential $V(\{\mathbf{r}_i(t)\})$, a particle can interact with its own image, leading to unwanted effects. This means that the summations in equation (3.2) not only run over the particles $1, \ldots, N$ within the original simulation box, but also over all relevant image particles. To avoid this, usually, the minimal image convention is applied for short-range interactions. This states, that an atom interacts with all atoms that lie within the closest periodic image of the $N-1$ other atoms in the system [40]. This is illustrated in Fig. 3.2.

As stated above, in a classical molecular dynamics simulation, the forces on the atoms are computed by the derivatives of the interaction potential (see equation (3.1)):

$$\mathbf{F}_i = -\nabla_{\mathbf{r}_i} V\left(\{\mathbf{r}_i\left(t\right)\}\right). \tag{3.12}$$

As already stated above, the total interaction potential (see equation (3.2)) can contain short-range and long-range interactions. Normally, the number of contributions to the total potential energy of the system, according to the individual 2- and 3- body terms of the interaction potential $V_2\left(\mathbf{r}_{ij}\right)$ and $V_3\left(\mathbf{r}_{ij}, \mathbf{r}_{ik}\right)$, increases with increasing inter-particle distances $r_{ij} = |\mathbf{r}_{ij}|$. This is the case, as the number of particles at a distance r_{ij} increases asymptotically with r_{ij}^{d-1}, when d is the dimension of the system [7]. Therefore, interactions are classified as short-range interactions when the respective potential term decreases faster than r_{ij}^{-d} and vice versa. In section 3.5, examples of typical short-range 2-body and 3-body potentials are given. To fulfill the minimum image convention, it is necessary to truncate all short-range parts of the potential at a specific cutoff radius $r_\mathrm{c} < {}^{L_\mathrm{Box}}/_2$. Usually, the potential term has already decayed to a value close to 0 at inter-particle distances of $r_{ij} = r_\mathrm{c}$. However, it is convenient to shift the short-range potential to zero at $r_{ij} = r_\mathrm{c}$ by subtracting the numerical value at the cutoff radius $V\left(r_\mathrm{c}\right)$. This guarantees an overall continuous potential $V\left(\{\mathbf{r}_i\left(t\right)\}\right)$. However, it is still not differentiable at the cutoff r_c. According to equation (3.12), the forces between atoms at inter-atomic distances of $r_{ij} = r_\mathrm{c}$ would be proportional to delta-distributions: $\mathbf{F}_i \propto \delta\left(\mathbf{r}_{ij}\right)$. To avoid this, the short-range potential can be multiplied with a smoothing function after shifting it to zero at $r_{ij} = r_\mathrm{c}$. In this work, the functional form of

$$G\left(r\right) = \exp\left[-\frac{d}{\left(r - r_\mathrm{c}\right)^2}\right] \tag{3.13}$$

is chosen, leading to a short-range potential of

$$V^{\mathrm{S,Shifted+Smoothed}} = \left(V^\mathrm{S}\left(r\right) - V^\mathrm{S}\left(r_\mathrm{c}\right)\right) G\left(r\right). \tag{3.14}$$

In subsection 4.1.1 and section 6.4, the effect of the smoothing on the long term energy drift and the fluctuations of the total energy δE_tot is studied in the case of SiO_2 and B_2O_3.

The most prominent example of a long-range interaction is the Coulomb interaction. Of course, this plays an important role in the modeling of oxide glasses. In case of periodic boundary conditions, the summations of the 2-body terms in equation (3.2) would run over infinite numbers of particles, leading to:

$$V = \frac{1}{2} \sum_{\mathbf{n}\in\mathbb{Z}^3} \sum_{i,j=1, i\neq j \text{for } \mathbf{n}=\mathbf{0}}^{N} V^{\text{Coul}} \left(\mathbf{r}_{ij} + \mathbf{n}\, L_{\text{Box}}\right) = \frac{1}{2} \sum_{\mathbf{n}\in\mathbb{Z}^3} \sum_{i,j=1, i\neq j \text{for } \mathbf{n}=\mathbf{0}}^{N} \frac{C_{\text{Coul}}\, q_i\, q_j}{\left|\mathbf{r}_{ij} + \mathbf{n}\, L_{\text{Box}}\right|}. \quad (3.15)$$

The proportionality constant C_{Coul} depends on the units used in the simulation. In case of $[E] = \text{eV}$, $[q] = \text{e}$ and $[r] = \text{Å}$, the value is $C_{\text{Coul}} = 14.399644846\,\text{eV}\,\text{Å}$. In equation (3.15), an infinite summation over all $\mathbf{n} \in \mathbb{Z}^3$ has to be carried out. Here, the standard method for the numerical treatment of this problem is presented, the Ewald summation [56]. Following the description of [57], a potential decaying with $\frac{1}{r}$ can be re-written as:

$$\frac{1}{r} = \frac{1}{r} - \frac{2}{\sqrt{\pi}} \int_0^{g_{\text{ew}}} dt\, \exp\left[-r^2\, t^2\right] + \frac{2}{\sqrt{\pi}} \int_0^{g_{\text{ew}}} dt\, \exp\left[-r^2\, t^2\right] \quad (3.16)$$

$$\Leftrightarrow \frac{1}{r} = \frac{\text{erfc}\left(g_{\text{ew}}\, r\right)}{r} + \frac{2}{\sqrt{\pi}} \int_0^{g_{\text{ew}}} dt\, \exp\left[-r^2\, t^2\right]. \quad (3.17)$$

Here, $\text{erfc}\,(x)$ is the complementary error function $\text{erfc}\,(x) = \frac{2}{\sqrt{\pi}} \int_x^{\infty} dt\, \exp\left[-t^2\right]$. It has the property that it is fast decaying to zero with increasing x. Putting this into equation (3.15) the sum can be split into two parts:

$$V = V^{\text{S}} + V^{\text{L}} \quad (3.18)$$

$$V^{\text{S}} := \frac{1}{2} \sum_{\mathbf{n}\in\mathbb{Z}^3} \sum_{i,j=1, i\neq j \text{for } \mathbf{n}=\mathbf{0}}^{N} V^{\text{CS}} \left(\left|\mathbf{r}_{ij} + \mathbf{n}\, L_{\text{Box}}\right|\right) \quad (3.19)$$

$$\Leftrightarrow V^{\text{S}} = \frac{1}{2} \sum_{\mathbf{n}\in\mathbb{Z}^3} \sum_{i,j=1, i\neq j \text{for } \mathbf{n}=\mathbf{0}}^{N} \frac{C_{\text{Coul}}\, q_i\, q_j}{\left|\mathbf{r}_{ij} + \mathbf{n}\, L_{\text{Box}}\right|} \text{erfc}\left(g_{\text{ew}}\, \left|\mathbf{r}_{ij} + \mathbf{n}\, L_{\text{Box}}\right|\right) \quad (3.20)$$

$$V^{\text{L}} := \frac{1}{2} \sum_{\mathbf{n}\in\mathbb{Z}^3} \sum_{i,j=1, i\neq j \text{for } \mathbf{n}=\mathbf{0}}^{N} \frac{2\, C_{\text{Coul}}\, q_i\, q_j}{\sqrt{\pi}} \int_0^{g_{\text{ew}}} dt\, \exp\left[-\left|\mathbf{r}_{ij} + \mathbf{n}\, L_{\text{Box}}\right|^2\, t^2\right]. \quad (3.21)$$

Due to the properties of $\text{erfc}\,(x)$, the 2-body term $V^{\text{CS}}(r)$ in equation (3.20) is a short-range interaction and can be cut off at an appropriate cutoff r_{c}^{ew}, according to the minimum image convention. When adding the terms for $\mathbf{n} = \mathbf{0}$ to $i = j = 0$ in equation (3.21), the long-range part of the potential, V^{L}, becomes a periodic function expanded in a Fourier series. For $\hat{f}$ being the Fourier transform of f

$$\hat{f}\,(\mathbf{k}) = \int_{\mathbb{R}^3} d\mathbf{x}\, f\,(\mathbf{x})\, \exp\left[-i\mathbf{k}\cdot\mathbf{x}\right], \quad f\,(\mathbf{x}) = \frac{1}{(2\pi)^3} \int_{\mathbb{R}^3} d\mathbf{k}\, \hat{f}\,(\mathbf{k})\, \exp\left[i\mathbf{k}\cdot\mathbf{x}\right], \quad (3.22)$$

the Poisson summation formula holds [58]:

$$\sum_{\mathbf{n}\in\mathbb{Z}^3} f(\mathbf{n}) = \sum_{\mathbf{n}\in\mathbb{Z}^3} \hat{f}(2\pi\mathbf{n}) = \sum_{\mathbf{k}\in\frac{2\pi\,\mathbf{n}}{L_{\text{Box}}}} \hat{f}(\mathbf{k}\,L_{\text{Box}})\,. \tag{3.23}$$

This in mind, the term V^{L} in equation (3.21) can be reformulated:

$$V^{\text{L}} = \frac{1}{2}\sum_{i,j=1}^{N} \frac{2\,C_{\text{Coul}}\,q_i\,q_j}{\sqrt{\pi}} \int_0^{g_{\text{ew}}} dt \sum_{\mathbf{k}\in\frac{2\pi\,\mathbf{n}}{L_{\text{Box}}}\setminus\mathbf{k}\equiv\mathbf{0}} \int_{\mathbb{R}^3} d\mathbf{n}\, \exp\left[-\left|\mathbf{r}_{ij}+\mathbf{n}\,L_{\text{Box}}\right|^2 t^2 - L_{\text{Box}}\,\mathbf{k}\cdot\mathbf{n}\right] - V^{\text{L}}_{\text{self}}. \tag{3.24}$$

The solution of the integrals leads to [40]:

$$V^{\text{L}} = \frac{1}{2\pi L^3_{\text{Box}}} \sum_{\mathbf{k}\in\frac{2\pi\,\mathbf{n}}{L_{\text{Box}}}\setminus\mathbf{k}\equiv\mathbf{0}} \frac{(2\pi)^2\,\exp\left[-\left(\frac{k}{2\,g_{\text{ew}}}\right)^2\right]}{\mathbf{k}^2} \sum_{i,j=1}^{N} C_{\text{Coul}}\,q_i\,q_j\,\exp\left[i\mathbf{k}\cdot\mathbf{r}_{ij}\right] - V^{L}_{self}. \tag{3.25}$$

The self term $V^{\text{L}}_{\text{self}}$ in equations (3.24) and (3.25) contains the terms for $\mathbf{n}=\mathbf{0}$ to $i=j=0$ that have been added to V^{L} before. It can be calculated in the limit of $\epsilon_i := r_{ij} \to 0$:

$$V^{\text{L}}_{\text{self}} = \frac{1}{2}\sum_{i=1}^{N} \frac{2\,C_{\text{Coul}}\,q_i^2}{\sqrt{\pi}} \lim_{\epsilon_i\to 0} \int_0^{g_{\text{ew}}} dt\,\exp\left[-\epsilon_i^2 t^2\right] \tag{3.26}$$

$$\Leftrightarrow V^{\text{L}}_{\text{self}} = \frac{1}{2}\sum_{i=1}^{N} C_{\text{Coul}}\,q_i^2 \lim_{\epsilon_i\to 0} \frac{1-\text{erfc}\,(g_{\text{ew}}\,\epsilon_i)}{\epsilon_i} \simeq \frac{g_{\text{ew}}}{\sqrt{\pi}} \sum_{i=1}^{N} C_{\text{Coul}}\,q_i^2, \tag{3.27}$$

as $\text{erfc}\,(x) = 1 - \frac{2}{\sqrt{\pi}}x + \mathcal{O}\left(x^3\right)$.

The exclusion of $\mathbf{k}\equiv\mathbf{0}$ in equations (3.24) and (3.25) is a direct consequence of the conditional convergence of the Ewald sum. This assumption is consistent with a situation, where the periodic system (the original simulation box with its infinite periodic images) is embedded in a medium with infinite dielectric constant, meaning an ideal conductor [7].

In practice, the complementary error function can be approximated as

$$\operatorname{erfc}(x) = \operatorname{tp}(x)\, \exp\left[-x^2\right] + \epsilon(x), \quad |\epsilon(x)| \leq 1.5 \cdot 10^{-7}.$$

Here, $\operatorname{tp}(x)$ is a polynomial of the order 5 in $(1 + 0.3275911\, x)^{-1}$ [59].

As $\lim_{x\to\infty} {}^{\operatorname{erfc}(x)}/_{x} = {}^{\exp(-x^2)}/_{x^2}$, the error, due to the cutting off of the short-range term V^{CS} at $r_{\mathrm{c}}^{\mathrm{ew}}$, scales as ${}^{\exp\left[-(g_{\mathrm{ew}}\, r_{\mathrm{c}}^{\mathrm{ew}})^2\right]}/_{(g_{\mathrm{ew}}\, r_{\mathrm{c}}^{\mathrm{ew}})^2}$ (see equations (3.19) and (3.20)). According to equation (3.25), the cutoff error in reciprocal space is ${}^{\exp\left[-\left(\frac{k_{\mathrm{c}}}{2\, g_{\mathrm{ew}}}\right)^2\right]}/_{\left(\frac{k_{\mathrm{c}}}{2\, g_{\mathrm{ew}}}\right)^2}$. In practice, the choice of the real space cutoff and the cutoff error determines the parameters g_{ew} and k_{c} and therefore the number of k-vectors included in the summation.

As stated above, the numerical integration of equation (3.1) leads to the trajectories in the NVE ensemble. When calculating the statistical average of certain quantities, the ensemble average is equal to the time average of this quantity with respect to particular simulation times t, where the atom configurations $\mathbf{r}_i(t)$ are uncorrelated to the previous ones. It should be mentioned that the exact trajectory of the individual atoms is not important for the statistical sampling and the accurate prediction of an atomic trajectory is not possible for longer simulation times, due to the Lyapunov instability. It states that the difference between two different particle trajectories diverges as $|\Delta\mathbf{r}(t)| \propto \epsilon \exp[\lambda t]$, when the initial conditions are disturbed by a small amount ϵ [7].

Techniques to speed up simulations

As explained above, all short-range interactions are cut off at a certain cutoff distance r_{c} (or $r_{\mathrm{c}}^{\mathrm{ew}}$). This means that particles with larger minimum image distances do not interact. This motivates the utilization of Verlet neighbor lists [40] for each atom in the simulation box. This list contains all neighboring atoms within a first neighbor distance less than the cutoff distance plus a so-called skin distance r_{skin}. Interactions between the atoms are only calculated for atoms contained in the neighbor list, reducing the computational cost significantly. In an ideal case the computational costs scale like $\mathcal{O}(N)$ instead of $\mathcal{O}\left(N^2\right)$.

Nowadays, it is convenient to run a simulation program on more than one processor in parallel. There are different schemes for parallelization of a computer program. The parallelization of the LAMMPS software package [60, 61], used for all classical MD simulations in this work, is based on the Message Passing Interface (MPI) standard [62]. Here, the program is started on N_{proc} processors in parallel. Each of the processes carries out a part of the simulation and communicates with the other processes in terms of messages. Input and output is only done by one process. In case of classical MD simulations and the LAMMPS software package, a domain decomposition is applied. Here, the simulation box is divided into a 3-dimensional grid of N_{proc} domains. Each processor calculates the interactions and integrates the equations of motion for the atoms within its domain. Therefore, the positions of all atoms in the Verlet neighbor lists have to be known. Atoms, contained in the neighbor list that are not located in the respective

domain, are called ghost or halo atoms. These position have to be stored, as well, in every of the N_{proc} processes and are updated after the positions of the original atoms are updated. In an ideal case, the parallelization on N_{proc} processors should speed up the simulation by a factor of N_{proc}. However, the speedup is usually less pronounced due to communication times and an unequal load balancing on each processor. The speedup in case of a 165 system of the model glass former SiO_2 is tested in subsection 4.1.1.

Calculating temperature and pressure

The standard method to measure the instantaneous temperature in a classical MD simulation is to employ the kinetic energy of the atoms (see equation (3.6)). In case of a 3-dimensional system the relation between the kinetic energy and the temperature is

$$T := \frac{2}{3\,N\,k_{\text{B}}\,E_{\text{kin}}}, \quad E_{\text{kin}} = \sum_{i=1}^{N} \frac{\mathbf{v}_i^2}{2\,M_i}. \tag{3.28}$$

Using the instantaneous values of $\mathbf{v}_i\,(t)$, the temperature at the simulation time t can be calculated.

The virial of a N particle system in a simulation box of volume V is defined as cite:

$$\mathcal{V} := -\frac{1}{2} \sum_{i=1}^{N} \langle \mathbf{r}_i \cdot \mathbf{F}_{\text{tot},i} \rangle\,, \quad \mathbf{F}_{\text{tot},i} = \mathbf{F}_i + \mathbf{F}_{\text{ext},i}. \tag{3.29}$$

Here, $\mathbf{F}_{\text{tot},i}$ is the total force on each particle due to the internal interactions with the other particles of the system, $\mathbf{F}_i = -\nabla_{\mathbf{r}_i} V$, and external contributions $\mathbf{F}_{\text{ext},i}$, due to the collisions with the confining simulation box. Following the description in [51], the external virial, resulting from $\mathbf{F}_{\text{ext},i}$, is connected to the internal pressure of the system as:

$$\frac{3}{2}\,p_{\text{int}}\,V = \mathcal{V}_{\text{ext}} = -\frac{1}{2} \sum_{i=1}^{N} \langle \mathbf{r}_i \cdot \mathbf{F}_{\text{ext},i} \rangle\,. \tag{3.30}$$

Combination of equations (3.28), (3.29) and (3.29) with the virial theorem [63]

$$\langle E_{\text{kin}} \rangle = \mathcal{V}, \tag{3.31}$$

leads to

$$\langle E_{\text{kin}} \rangle = -\frac{1}{2} \sum_{i=1}^{N} \langle \mathbf{r}_i \cdot \mathbf{F}_i \rangle + \frac{3}{2} p_{\text{int}} V \tag{3.32}$$

$$p_{\text{int}} = \frac{N k_{\text{B}} T}{V} + \frac{1}{3V} \sum_{i=1}^{N} (\mathbf{r}_i \cdot \mathbf{F}_i) . \tag{3.33}$$

Using the instantaneous value of $\mathbf{r}_i(t) \cdot \mathbf{F}_i(t)$, the internal pressure of the system at the simulation time t can be calculated.

The above description can be extended to the non-isotropic case, leading to:

$$S_{\text{int},\alpha\beta} = \frac{1}{V} \sum_{i=1}^{N} M_i v_{i,\alpha} v_{i,\beta} + \frac{1}{V} \sum_{i=1}^{N} (r_{i,\alpha} F_{i,\beta}) , \quad \alpha, \beta \in \{1, 2, 3\} . \tag{3.34}$$

Here, $S_{\text{int},\alpha\beta}$ is the internal stress tensor.

3.1.2 MD sampling in different statistical ensembles

It is possible to conduct molecular dynamics simulations in others than the microcanonical ensemble. This can be achieved by employing thermostats and barostats, resembling the coupling of the system to an external bath.

To simulate in the canonical ensemble, different kinds of thermostats can be used. The idea of the Nosé thermostat [64] is to introduce an additional degree of freedom in the Lagrangian of the system $\mathcal{L}$ and the corresponding Hamiltonian of the system (see equations (3.10) and (3.9)). In the following, the formulations of the Nosé and Nosé-Hoover thermostat of [65] are employed. The Lagrangian, proposed by Nosé in [64], and the corresponding Hamiltonian are:

$$\mathcal{L}_{\text{Nosé}} = \sum_{i=1}^{N} \frac{M_i s^2 \left(\frac{\partial \mathbf{r}_i}{\partial t'}\right)^2}{2} - V(\{\mathbf{r}_i\}) + \frac{Q \left(\frac{\partial s}{\partial t'}\right)^2}{2} - g\, k_{\text{B}} T \ln(s) , \tag{3.35}$$

$$H_{\text{Nosé}} = \sum_{i=1}^{N} \frac{\mathbf{p}_i'^2}{2 M_i s^2} + V(\{\mathbf{r}_i\}) + \frac{p_{\text{s}}^2}{2Q} + g\, k_{\text{B}} T \ln(s) . \tag{3.36}$$

Here, a virtual time t' is introduced. The respective equations of motion are:

$$\frac{\partial \mathbf{r}_i}{\partial t'} = \frac{\mathbf{p}_i'}{M_i s^2}, \quad \frac{\partial \mathbf{p}_i'}{\partial t'} = -\nabla_{\mathbf{r}_i} V, \tag{3.37}$$

$$\frac{\partial s}{\partial t'} = \frac{p_\mathrm{s}}{Q}, \quad \frac{\partial p_\mathrm{s}}{\partial t'} = \frac{1}{s}\left(\sum_{i=1}^{N} \frac{\mathbf{p}_i'^2}{M_i s^2} - g\, k_\mathrm{B} T\right). \tag{3.38}$$

The corresponding equations of motion for the variable pairs $\left\{\mathbf{r}_i, \mathbf{p}_i = \mathbf{p}_i'/s\right\}$ in real time $t = t'/s$ are:

$$\frac{\partial \mathbf{r}_i}{\partial t} = s\frac{\partial \mathbf{r}_i}{\partial t'} = \frac{\mathbf{p}_i'}{M_i s} = \frac{\mathbf{p}_i}{M_i}, \tag{3.39}$$

$$\frac{\partial \mathbf{p}_i}{\partial t} = s\frac{\partial}{\partial t'}\left(\frac{\mathbf{p}_i'}{s}\right) = \frac{\partial \mathbf{p}_i'}{\partial t'} - \frac{1}{s}\frac{\partial s}{\partial t'}\mathbf{p}_i' = -\nabla_{\mathbf{r}_i} V - \frac{1}{s}\frac{\partial s}{\partial t}\mathbf{p}_i, \tag{3.40}$$

$$\frac{\partial s}{\partial t} = s\frac{\partial s}{\partial t'} = s\frac{p_\mathrm{s}}{Q}, \tag{3.41}$$

$$\frac{\partial p_\mathrm{s}}{\partial t} = s\frac{\partial p_\mathrm{s}}{\partial t'} = \sum_{i=1}^{N} \frac{\mathbf{p}_i^2}{M_i} - g\, k_\mathrm{B} T. \tag{3.42}$$

The microcanonical partition function of the system described by $H_\text{Nosé}$ is:

$$\Omega = \int \prod_{i=1}^{N} \mathbf{dp}_i' \mathbf{dr}_i dp_\mathrm{s} ds\, \delta\left(H_\text{Nosé}\left(\left\{\mathbf{r}_i, \mathbf{p}_i'\right\}, p_\mathrm{s}, s\right) - E\right) \tag{3.43}$$

$$\Leftrightarrow \Omega = \int \prod_{i=1}^{N} \mathbf{dp}_i \mathbf{dr}_i dp_\mathrm{s} ds\, s^{3N}\, \delta\left(H_\text{Nosé}\left(\{\mathbf{r}_i, \mathbf{p}_i\}, p_\mathrm{s}, s\right) - E\right). \tag{3.44}$$

Applying the identity

$$\delta\left(f\left(s\right)\right) = \frac{\delta\left(s - s_0\right)}{\left|f'\left(s_0\right)\right|}, \quad f\left(s_0\right) = 0, \tag{3.45}$$

to equation (3.44), leads to:

$$\Omega = \int \prod_{i=1}^{N} \mathbf{dp}_i \mathbf{dr}_i dp_\mathrm{s} ds\, s^{3N} \frac{\delta\left(s - \exp\left[\frac{E - \frac{\mathbf{p}_i^2}{2M_i} - V(\{\mathbf{r}_i\}) - \frac{p_\mathrm{s}^2}{2Q}}{g\, k_\mathrm{B} T}\right]\right)}{\frac{g\, k_\mathrm{B} T}{s}}. \tag{3.46}$$

By choosing $g = (3N + 1)$, equation (3.46) is the partition function of the canonical ensemble, coupled to a heat bath with the temperature T:

$$\Omega = \int \prod_{i=1}^{N} \mathbf{dp}_i \mathbf{dr}_i \, \exp\left[\frac{-\frac{\mathbf{p}_i^2}{2M_i} - V\left(\{\mathbf{r}_i\}\right)}{k_\mathrm{B}T}\right] \int dp_\mathrm{s} \, \frac{\exp\left[\frac{E - \frac{p_\mathrm{s}^2}{2Q}}{k_\mathrm{B}T}\right]}{(3N+1)\; k_\mathrm{B}T}. \tag{3.47}$$

The second term can be regarded as a constant.

As proposed by Hoover [66], one can simplify the equations of motion (equations (3.39) to (3.42)) by introducing a new variable:

$$\xi := \frac{1}{s}\frac{\partial s}{\partial t} = \frac{p_\mathrm{s}}{Q} =: \frac{p_\epsilon}{Q}. \tag{3.48}$$

This leads to the following equations of motion:

$$\frac{\partial \mathbf{r}_i}{\partial t} = \frac{\mathbf{p}_i}{M_i}, \quad \frac{\partial \mathbf{p}_i}{\partial t} = -\nabla_{\mathbf{r}_i} V - \xi\, \mathbf{p}_i, \quad \frac{\partial \xi}{\partial t} = \frac{1}{Q}\left(\sum_{i=1}^{N} \frac{\mathbf{p}_i^2}{M_i} - g\, k_\mathrm{B}T\right). \tag{3.49}$$

The term $\xi\, \mathbf{p}_i = {}^{p_\xi \mathbf{p}_i}/_{Q}$ in equation (3.49) can be interpreted as a friction term. The magnitude depends on the difference between the instantaneous temperature of the system and the temperature of the external heat bath T. In this way, the temperature of the system is controlled. The Nosé-Hoover thermostat has a resonance frequency of $\omega^2 = {}^{g\, k_\mathrm{B}T}/_{Q}$. By changing the so-called mass term Q, this resonance frequency or the timespan in which the temperature is relaxed to the target temperature T can be controlled.

In a similar way, simulations in an isothermal-isobaric (NpT) ensemble can be conducted, introducing an additional degree of freedom. Following the description of [67], in this case the conserved quantity for a system in 3-dimensions is:

$$H_\mathrm{NpT} = \sum_{i=1}^{N} \frac{\mathbf{p}_i^2}{2M_i} + V\left(\{\mathbf{r}_i\}\right) + \frac{p_\xi^2}{2Q} + (3N+1)\; k_\mathrm{B}T\, \xi + \frac{p_\epsilon^2}{2W_\mathrm{g}} + p\, V. \tag{3.50}$$

According to [67], the corresponding equations of motion are:

$$\frac{\partial \mathbf{r}_i}{\partial t} = \frac{\mathbf{p}_i}{M_i} + \frac{p_\epsilon}{W_\mathrm{g}}\mathbf{r}_i, \quad \frac{\partial \mathbf{p}_i}{\partial t} = -\nabla_{\mathbf{r}_i} V\left(\{\mathbf{r}_i\}\right) - \left(1 + \frac{1}{N}\right)\frac{p_\epsilon}{W_\mathrm{g}}\mathbf{p}_i - \frac{p_\xi}{Q}\mathbf{p}_i, \tag{3.51}$$

$$\frac{\partial V}{\partial t} = \frac{3Vp_\epsilon}{W_\mathrm{g}}, \quad \frac{\partial p_\epsilon}{\partial t} = 3V\left(p_\mathrm{int} - p\right) + \frac{1}{N}\sum_{i=1}^{N}\frac{\mathbf{p}_i^2}{M_i} - \frac{p_\xi p_\epsilon}{Q} \tag{3.52}$$

$$\xi = \frac{p_\xi}{Q}, \quad \frac{\partial p_\xi}{\partial t} = \sum_{i=1}^{N}\frac{\mathbf{p}_i^2}{M_i} + \frac{p_\epsilon^2}{W_\mathrm{g}} - (3N+1)\,k_\mathrm{B}T. \tag{3.53}$$

These equations, in principle, generate the isothermal-isobaric partition function at external temperature T and pressure p. Here, the volume of the simulation box V is allowed to change as well and p_int is the internal pressure of the system (see equation (3.33)). As above, the frequency of the barostat can be controlled by altering the mass term W_g.

In [68], a set of equations of motion are given that allow the shape of the simulation box to fluctuate as well, due to an arbitrary external stress, following the ideas of [69]. In addition to the latter, a chain of $k = 1, \ldots, M$ Nosé-Hoover thermostats is coupled to the system, to simulate the system at arbitrary external temperature as well. As described above, the frequencies of the fluctuations can be controlled by changing the mass terms W_g and Q_k, $k = 1, \ldots, M$. The implementation in the LAMMPS software package [60, 61], used for all classical MD simulations in this work, is based on the formulations of [68].

3.2 Density functional theory

In this section, an overview over the basic concepts is given, describing a quantum mechanical many-body system in terms of density functional theory (DFT).

3.2.1 Basic concepts of quantum mechanics

In principle, a system of N atoms and n electrons located at positions $\{\mathbf{r}_i\}$ and $\{\mathbf{x}_i\}$ is described by a many-body Schrödinger equation. When the Hamiltonian $\hat{\mathcal{H}}$ does not depend on time explicitly, which is the case for the system of N atoms and n electrons in absence of time-dependent external potentials, the time-independent Schrödinger equation is given as:

$$\hat{\mathcal{H}}\left|\Psi\left(\{\mathbf{r}_i\};\{\mathbf{x}_i\}\right)\right\rangle = E\left|\Psi\left(\{\mathbf{r}_i\};\{\mathbf{x}_i\}\right)\right\rangle, \tag{3.54}$$

with the many-body Hamiltonian

$$\hat{\mathcal{H}} = \hat{\mathrm{T}}_\mathrm{N} + \hat{\mathrm{T}}_\mathrm{e} + \hat{\mathrm{V}}_\mathrm{NN} + \hat{\mathrm{V}}_\mathrm{Ne} + \hat{\mathrm{V}}_\mathrm{ee}. \tag{3.55}$$

In the whole section 3.2, atomic units are used, meaning $\mathrm{e}^2 = \hbar = m_\mathrm{e} = 1$. The different terms in equation (3.55) are the operators of the kinetic energy of the N nuclei and n electrons,

$$\hat{\mathrm{T}}_\mathrm{N} = \sum_{i=1}^{N} \frac{-\nabla^2_{\mathbf{r}_i}}{2\,M_i}, \quad \hat{\mathrm{T}}_\mathrm{e} = \sum_{i=1}^{n} \frac{-\nabla^2_{\mathbf{x}_i}}{2}, \tag{3.56}$$

and the potential energy operators for the nuclei-nuclei, nuclei-electron and electron-electron interaction:

$$\hat{\mathrm{V}}_\mathrm{NN} = \frac{1}{2} \sum_{i,j\neq i=1}^{N} \frac{Z_i\,Z_j}{|\mathbf{r}_i - \mathbf{r}_j|}, \quad \hat{\mathrm{V}}_\mathrm{Ne} = \sum_{i=1}^{N}\sum_{j=1}^{n} \frac{Z_i}{|\mathbf{r}_i - \mathbf{x}_j|}, \quad \hat{\mathrm{V}}_\mathrm{ee} = \frac{1}{2} \sum_{i,j\neq i=1}^{n} \frac{1}{|\mathbf{x}_i - \mathbf{x}_j|}. \tag{3.57}$$

Here, M_i are the masses and Z_i the charge numbers of the nuclei. Equation (3.54) is analytically not solvable.

Equation (3.54), in combination with equation (3.55), can be reduced to the Schrödinger equation only for the electronic degrees of freedom, applying the Born-Oppenheimer approximation [41]. This states that because of the difference between the masses of the nuclei and the electrons of about 4 orders of magnitude, it is an excellent approximation to separate the total wave function $|\Psi(\{\mathbf{r}_i\};\{\mathbf{x}_i\})\rangle$ into a product of the wave function of the nuclei and the one of the electrons:

$$|\Psi(\{\mathbf{r}_i\};\{\mathbf{x}_i\})\rangle \simeq |\Phi(\{\mathbf{r}_i\}\rangle\ |\Psi\{\mathbf{x}_i\})\rangle\,. \tag{3.58}$$

Furthermore, it is assumed that, at room temperature, the electrons are always in the ground state. This is a reasonable assumption as the typical energies of electronic excitations are of the order of several eV which is much greater than the thermal energy of an electron at $300\,K$ of about $0.026\,\mathrm{eV}$. Following the formulations in [70], the energy eigenvalues E of equation (3.54) can be written as

$$E_\mathrm{total}(\{\mathbf{r}_i\}) = V_\mathrm{NN}(\{\mathbf{r}_i\}) + E_\mathrm{elec}(\{\mathbf{r}_i\})\,. \tag{3.59}$$

This means that quantum mechanical many-body problem is reduced to the one of n electrons in an external potential, due to the N nuclei at fixed positions $\{\mathbf{r}_i\}$, leading to

$$\hat{\mathcal{H}} \left|\Psi\left(\{\mathbf{x}_i\}\right)\right\rangle = E_{\text{elec}}\left(\{\mathbf{r}_i\}\right) \left|\Psi\left(\{\mathbf{x}_i\}\right)\right\rangle, \quad \hat{\mathcal{H}} = \hat{\mathrm{T}}_{\mathrm{e}} + \hat{\mathrm{V}}_{\text{ext}} + \hat{\mathrm{V}}_{\mathrm{ee}}, \tag{3.60}$$

and the potential energy of the N nuclei $V_{\mathrm{NN}}\left(\{\mathbf{r}_i\}\right)$ is just treated as a constant energy term. In the case of absent additional external fields, the potential operator $\hat{\mathrm{V}}_{\text{ext}} = \sum_{j=1}^{n} v_{\text{ext}}\left(\mathbf{x}_j\right)$ is the one due to the nuclei-electron interaction $\hat{\mathrm{V}}_{\mathrm{Ne}}$ in equation (3.57). Here, $\hat{\mathrm{V}}_{\text{ext}}$ is a one-body operator with respect to the electron positions $\{\mathbf{x}_i\}$ with

$$v_{\text{ext}}\left(\mathbf{x}_j\right) = \sum_{i=1}^{N} \frac{Z_i}{\left|\mathbf{r}_i - \mathbf{x}_j\right|} \tag{3.61}$$

in the case of $\hat{\mathrm{V}}_{\text{ext}} = \hat{\mathrm{V}}_{\mathrm{Ne}}$. In the following, the notation of the eigenvalue $E_{\text{elec}}\left(\{\mathbf{r}_i\}\right)$ is replaced by E again, in the sense of being the energy eigenvalue of the n electron system for a fixed set of nuclei positions $\{\mathbf{r}_i\}$.

The ground state energy, according to equation (3.60), satisfies the variational principle

$$E = \min_{\Psi} \left\langle \Psi \left| \hat{\mathcal{H}} \right| \Psi \right\rangle, \tag{3.62}$$

minimizing over all antisymmetric n-body wave functions $|\Psi\rangle$. This is the basis for the Hartree-Fock (HF) approximation, where the many-body wave function $|\Psi\rangle$ is approximated by an anti-symmetrized product of single-particle wave functions [71], based on the so-called Slater determinant [72].

The one-particle density, which is defined as expectation value of the density operator $\hat{n}\left(\mathbf{x}\right) = \sum_{i=1}^{n} \delta\left(\mathbf{x} - \mathbf{x}_i\right)$, is given as:

$$n\left(\mathbf{x}\right) = \left\langle \Psi \left| \hat{n}\left(\mathbf{x}\right) \right| \Psi \right\rangle = n \sum_{\sigma_1} \cdots \sum_{\sigma_n} \int \mathbf{dx}_2 \ldots \mathbf{dx}_n \left|\Psi\left(\mathbf{x}\,\sigma_1, \mathbf{x}_2\,\sigma_2, \ldots, \mathbf{x}_n\,\sigma_n\right)\right|^2. \tag{3.63}$$

Here, the spin degrees of freedom $\{\sigma_i\}$ are explicitly included that have been omitted in the above equations and it is assumed that $|\Psi\rangle$ is normalized to $|\Psi|^2 = 1$. The one-particle density is a much simpler quantity than the many-body wave function $|\Psi\rangle$ and $n\left(\mathbf{x}\right)\mathbf{dx}$ gives the probability to find any electron in a volume element $\mathbf{dx}$ around $\mathbf{x}$.

3.2.2 Hohenberg-Kohn theorems

The basis for the description of the many-body system of n electrons in terms of the one-particle density (see equation (3.63)) are the two Hohenberg-Kohn theorems [9]. Following the description in [73], they can be written as:

Theorem I

The ground state one-particle density $n(\mathbf{x})$ of a many body-system (see equation (3.60)) uniquely determines the external potential $\hat{\mathrm{V}}_{\mathrm{ext}}$ up to a constant.

This implies that any property of the system can be written as a function of the ground state density $n_0(\mathbf{x})$, because by determining $\hat{\mathrm{V}}_{\mathrm{ext}}$, the Hamiltonian $\hat{\mathcal{H}}$ in equation (3.60) is fixed up to a constant. This means that also the wave functions $|\Psi\rangle$ are, in principle, uniquely determined.

Theorem II

The energy functional in equation (3.62) can be written as a functional $E[n(\mathbf{x})]$ of the one-particle density $n(\mathbf{x})$ for any external potential $\hat{\mathrm{V}}_{\mathrm{ext}}$. The global minimum of this functional is the ground state energy and the density $n(\mathbf{x})$ that minimizes the functional is the ground state density $n_0(\mathbf{x})$.

This implies that the functional $E[n(\mathbf{x})]$ by itself determines the ground state energy and ground state density. Following [70], the variational problem can be formulated in two steps. In the first step,

$$F[n(\mathbf{x})] = \min_{\Psi \to n} \left\langle \Psi \left| \hat{T} + \hat{V}_{\mathrm{ee}} \right| \Psi \right\rangle \tag{3.64}$$

is minimized. This has to be understood as a minimization over all antisymmetric wave functions yielding a given density $n(\mathbf{x})$. In the second step,

$$E[n] = \min_{n} \left(F[n] + \int \mathbf{dx}\, n(\mathbf{x})\; v_{\mathrm{ext}}(\mathbf{x}) \right) \tag{3.65}$$

is minimized over all reasonable densities fulfilling $n(\mathbf{x}) \geq 0$, $\int \mathbf{dx}\, n(\mathbf{x}) = N$, with $v_{\mathrm{ext}}(\mathbf{x})$, according to equation (3.61).

3.2.3 Kohn-Sham equations

The main statement of the two Hohenberg-Kohn theorems (see subsection 3.2.2) is that any system property can be expressed in terms of the one-particle density $n(\mathbf{x})$. Due to Kohn

and Sham [74], one can replace the complex many-body system of interacting electrons with a set of fictive non-interacting electrons in some effective local potentials $v_{s,\sigma}(\mathbf{x})$. Following the descriptions in [70] and [73], the so-called Kohn-Sham (KS) system can be described by:

$$\left(-\frac{1}{2}\nabla_{\mathbf{x}}^2 + v_{s,\sigma}(\mathbf{x})\right)\phi_{i,\sigma}(\mathbf{x}) = \epsilon_{i,\sigma}\,\phi_{i,\sigma}(\mathbf{x})\,. \tag{3.66}$$

Here, the spin variables $\sigma \in \{\uparrow,\downarrow\}$ are introduced explicitly. Depending on the type of system, it makes sense to treat the two different spin states separately, leading to more accurate approximations for systems with an odd number of electrons. Consequently, all considered quantities are functionals of the spin up and down densities $n_\sigma(\mathbf{x})$, $\sigma \in \{\uparrow,\downarrow\}$, separately. As in the Hartree-Fock case, the wave function of the KS system is usually an anti-symmetrized product of the orbitals or eigenstates $\phi_{i,\sigma}(\mathbf{x})$ of the $n = n_\uparrow + n_\downarrow$ electrons of the system. In the ground state, usually all of the $n_\uparrow$ and $n_\downarrow$ eigenstates are occupied and the total ground state density can be written as

$$n(\mathbf{x}) = \sum_\sigma n_\sigma(\mathbf{x}) = \sum_\sigma \sum_{i=1}^{n_\sigma} |\phi_i(\mathbf{x})|^2\,. \tag{3.67}$$

The local potential has to be chosen in a way that the ground state density of the KS system is equal to the ground state density of the fully interacting system. The relation between the energy terms of the KS system and the real electrons in equation (3.60) is the following:

$$E = \mathrm{T_e} + \mathrm{V_{ext}} + \mathrm{V_{ee}} = \mathrm{T_s} + \mathrm{U} + \mathrm{V_{ext}} + \mathrm{E_{xc}} = \mathrm{T_s} + \mathrm{V_s}, \tag{3.68}$$

with

$$\mathrm{V_{ext}} = \sum_{\sigma=\uparrow,\downarrow} \int \mathbf{dx}\, n_\sigma(\mathbf{x})\; v_{\mathrm{ext}}(\mathbf{x})\,, \quad \mathrm{V_s} = \sum_{\sigma=\uparrow,\downarrow} \int \mathbf{dx}\, n_\sigma(\mathbf{x})\; v_{\mathrm{s}}(\mathbf{x})\,. \tag{3.69}$$

Here,

$$\mathrm{T_s} = -\frac{1}{2}\sum_{\sigma=\uparrow,\downarrow}\sum_{i=1}^{n_\sigma}\left\langle \phi_{i,\sigma}\left|\nabla_{\mathbf{x}}^2\right|\phi_{i,\sigma}\right\rangle = \frac{1}{2}\sum_{\sigma=\uparrow,\downarrow}\sum_{i=1}^{n_\sigma}\int \mathbf{dx}\,|\nabla_{\mathbf{x}}\phi_{i,\sigma}(\mathbf{x})|^2 > 0 \tag{3.70}$$

is the kinetic energy of the KS eigenstates and

$$\mathrm{U} = \frac{1}{2} \sum_{\sigma,\sigma'=\uparrow,\downarrow} \int \mathbf{dx} \int \mathbf{dx}' \frac{n_\sigma(\mathbf{x})\, n_{\sigma'}\left(\mathbf{x}'\right)}{|\mathbf{x}-\mathbf{x}'|} > 0 \tag{3.71}$$

is the electrostatic or Hartree repulsive self-energy, according to the one-particle densities of charged electrons $n_\sigma(\mathbf{x})$, $\sigma \in \{\uparrow,\downarrow\}$.

Equations (3.67) and (3.70) allow the calculation of the functional derivatives of $\mathrm{T_s}$ and $n_\sigma(\mathbf{x})$ with respect to the KS eigenstates $\phi_{i,\sigma}$:

$$\frac{\delta n_\sigma(\mathbf{x})}{\delta \phi_{i,\sigma}(\mathbf{x})} = \phi_{i,\sigma}(\mathbf{x}), \quad \frac{\delta \mathrm{T_s}}{\delta \phi_{i,\sigma}(\mathbf{x})} = -\frac{1}{2} \nabla^2_{\mathbf{x}} \phi_{i,\sigma}(\mathbf{x}). \tag{3.72}$$

The set of KS eigenstates that minimize $E = \mathrm{T_s}+\mathrm{U}+\mathrm{V_{ext}}+\mathrm{E_{xc}}$, according to equation (3.68), can be obtained employing a variational principle. Using equation (3.72) this leads to the following expression:

$$\frac{\delta E}{\delta \phi_{i,\sigma}(\mathbf{x})} = \frac{\delta \mathrm{T_s}}{\delta \phi_{i,\sigma}(\mathbf{x})} + \left[\frac{\delta U}{\delta n_\sigma(\mathbf{x})} + \frac{\delta V_{\mathrm{ext}}}{\delta n_\sigma(\mathbf{x})} + \frac{\delta \mathrm{E_{xc}}}{\delta n_\sigma(\mathbf{x})}\right] \frac{\delta n_\sigma(\mathbf{x})}{\delta \phi_{i,\sigma}(\mathbf{x})} = 0 \tag{3.73}$$

$$\Leftrightarrow \frac{\delta E}{\delta \phi_{i,\sigma}(\mathbf{x})} = -\frac{1}{2} \nabla^2_{\mathbf{x}} \phi_{i,\sigma}(\mathbf{x}) + \left[\frac{\delta U}{\delta n_\sigma(\mathbf{x})} + \frac{\delta V_{\mathrm{ext}}}{\delta n_\sigma(\mathbf{x})} + \frac{\delta \mathrm{E_{xc}}}{\delta n_\sigma(\mathbf{x})}\right] \phi_{i,\sigma}(\mathbf{x}) = 0. \tag{3.74}$$

Using equations (3.68), (3.69) and (3.71), this leads to the one-electron Schrödinger equations of the KS system (3.66) with

$$v_{\mathrm{s}}(\mathbf{x}) = v_{\mathrm{ext}}(\mathbf{x}) + u(\mathbf{x}) + \frac{\delta \mathrm{E_{xc}}}{\delta n_\sigma(\mathbf{x})} \tag{3.75}$$

and

$$u(\mathbf{x}) = \sum_{\sigma=\uparrow,\downarrow} \int \mathbf{dx}' \frac{n_\sigma\left(\mathbf{x}'\right)}{|\mathbf{x}-\mathbf{x}'|}. \tag{3.76}$$

This implies that the exact ground state energy E and ground state density $n_{0,\sigma}(\mathbf{x})$ could be calculated, if the so-called exchange-correlation functional $\mathrm{E_{xc}}$ was known. In practice, the

computation works by an initial guess of the density $n_\sigma(\mathbf{x})$. Then, the potential term $v_\mathrm{s}(\mathbf{x})$ is calculated, according to equation (3.75). Subsequently, the KS equations (3.66) are solved and a new density is obtained from the resulting $\phi_{i,\sigma}(\mathbf{x})$ (see equation (3.67)). The procedure is iterated until the differences in $n_\sigma(\mathbf{x})$ are lower than a desired cutoff value.

This means that the KS equations, in principle, allow for an exact solution of the complex many-body problem, limited by the numerical accuracy of the iteration process. The approximative nature of the Kohn-Sham approach is caused by the guess of a suitable exchange-correlation functional

$$\mathrm{E_{xc}} = \mathrm{E_x} + \mathrm{E_c}. \tag{3.77}$$

The exchange part $\mathrm{E_x}$ of the exchange-correlation energy is given by

$$\mathrm{E_x} = -\frac{1}{2}\sum_{\sigma,i,j}\int \mathbf{dx}\int \mathbf{dx}'\,\frac{\phi^*_{i,\sigma}(\mathbf{x})\,\phi^*_{j,\sigma}\left(\mathbf{x}'\right)\phi_{i,\sigma}\left(\mathbf{x}'\right)\phi^*_{j,\sigma}(\mathbf{x})}{|\mathbf{x}-\mathbf{x}'|}. \tag{3.78}$$

According to [70], this is the energy contribution due to $\hat{\mathrm{V}}_\mathrm{ee}$ (see equation (3.57)), evaluated in terms of the KS eigenstates $\phi_{i,\sigma}$ minus the respective the Hartree energy (see equation (3.71)). This means, $\mathrm{E_x}$ follows exactly the same anti-symmetrized product of the Hartree-Fock method [71], based on the Slater determinant [72]. The correlation part $\mathrm{E_c}$, in principle, is everything else needed to make equation (3.68) exact. This can be understood as the remaining differences between the non-interacting KS electrons and the interacting real electrons with correlation effects. However, no general formulation of $\mathrm{E_c}$ can be found.

At this point it should be stated that the KS eigenstates $\phi_{i,\sigma}(\mathbf{x})$ have no physical meaning at all [75], but in many cases their interpretation as real electronic states works quite well.

As explained in subsection 3.1.1, the set of atoms is located in a simulation box with periodic boundary conditions and surrounding replicas of the latter. In this sense, the system can be viewed as a crystalline structure with the unit cell being the simulation box. According to Bloch's theorem [76], the one-electron wave functions, which are solutions of the stationary Schrödinger equation with a periodic potential $V(\mathbf{x}) = V(\mathbf{x}+\mathbf{R})$ ($\mathbf{R} \in \{\mathbf{n}\,L_\mathrm{Box}\}$, $\mathbf{n} \in \mathbb{Z}^3$, in case of a cubic simulation box with box length L_Box), have the functional form:

$$\phi_{i,\sigma}(\mathbf{x}) = \mathrm{e}^{i\mathbf{k}\cdot\mathbf{x}}\,u_{i,\sigma;\mathbf{k}}(\mathbf{x}), \quad \text{with} \quad u_{i,\sigma;\mathbf{k}}(\mathbf{x}) = u_{i,\sigma;\mathbf{k}}(\mathbf{x}+\mathbf{R}). \tag{3.79}$$

Here, $\mathbf{k}$ is a wave-vector of the reciprocal space of the first Brillouin zone, according to the periodicity of $u_{j,\sigma;\mathbf{k}}(\mathbf{x})$.

In practice, the terms $u_{i,\sigma;\mathbf{k}}$ in equation (3.79) are expanded in terms of an orthonormal basis set. It is convenient to expand $u_{i,\sigma;\mathbf{k}}$ in terms of plane waves as in this approach the boundary conditions are automatically satisfied. This results in:

$$u_{i,\sigma;\mathbf{k}}(\mathbf{x}) = \frac{1}{\sqrt{V}} \sum_{\mathbf{G}\in\frac{2\pi\,\mathbf{n}}{L_{\mathrm{Box}}}} C_{i,\sigma;\mathbf{G},\mathbf{k}}\, \mathrm{e}^{i\mathbf{G}\cdot\mathbf{x}} \quad \text{and} \quad \phi_{i,\sigma} = \frac{1}{\sqrt{V}} \sum_{\mathbf{G}\in\frac{2\pi\,\mathbf{n}}{L_{\mathrm{Box}}}} C_{i,\sigma;\mathbf{G},\mathbf{k}}\, \mathrm{e}^{i(\mathbf{G}+\mathbf{k})\cdot\mathbf{x}}. \tag{3.80}$$

The summation over vectors $\mathbf{G}$ is restricted to reciprocal lattice vectors, meaning $\mathbf{G} \in \frac{2\pi\,\mathbf{n}}{L_{\mathrm{Box}}}$, $\mathbf{n} \in \mathbb{Z}^3$, to fulfill equation (3.79). In this work, all DFT calculations are carried out with the Vienna Ab initio Simulation Package (VASP) [77–79], which is a plane wave code. In practice, only distinct $\mathbf{k}$-values of the Brillouin zone are chosen and the expansion over $\mathbf{G}$-vectors has to be cut off at a certain value $\mathbf{G}_{\mathrm{cut}}$ such that only plane waves are included with

$$\frac{1}{2}\left|\mathbf{G}+\mathbf{k}\right|^2 < E_{\mathrm{cut}}. \tag{3.81}$$

The number of $\mathbf{k}$-points included and the cutoff energy E_{cut} influence the accuracy of the calculation.

3.2.4 Exchange-correlation functionals

As explained in subsection 3.2.3, the solution of the complex quantum mechanical many-body problem of n electrons in an external potential V_{ext} in terms of the KS approach depends on the a-priori unknown choice of the exchange-correlation functional $\mathrm{E_{xc}}\left[n_\sigma(\mathbf{x})\right]$.

The simplest approximation of an exchange-correlation functional is the local (spin) density approximation (LDA):

$$\mathrm{E}_{\mathrm{xc}}^{\mathrm{LDA}} = \int \mathbf{dx}\, e_{\mathrm{xc}}^{\mathrm{hom}}\left(n_\uparrow(\mathbf{x}), n_\downarrow(\mathbf{x})\right). \tag{3.82}$$

Here, $e_{\mathrm{xc}}^{\mathrm{hom}}\left(n_\uparrow(\mathbf{x}), n_\downarrow(\mathbf{x})\right)$ is the energy density of a homogeneous electron gas with the density $n_\sigma(\mathbf{x})$. This means that the corresponding eigenstates are plane waves. The exchange part of equation (3.77) can be calculated by inserting the latter in equation (3.78). The correlation part can be parametrized [80]. The justification for this approach is that, in solids with slowly varying electron density, the density is often close to the one of a homogeneous electron gas [74].

The exchange-correlation functional $\mathrm{E}_{\mathrm{xc}}^{\mathrm{LDA}}$ is uniquely defined. It tends to lead to systematically too large binding energies by about 1 eV per bond [70] and too short bond lengths by about 1% [81].

The next step in improving the exchange-correlation functional is taking into account the gradient of the electron density, leading to the generalized gradient approximation (GGA):

$$\mathrm{E}_{\mathrm{xc}}^{\mathrm{GGA}} = \int \mathbf{dx}\, e_{\mathrm{xc}}^{\mathrm{GGA}} \left(n_{\uparrow}\left(\mathbf{x}\right), n_{\downarrow}\left(\mathbf{x}\right), \left|\nabla_{\mathbf{x}} n_{\uparrow}\left(\mathbf{x}\right)\right|, \left|\nabla_{\mathbf{x}} n_{\downarrow}\left(\mathbf{x}\right)\right| \right). \tag{3.83}$$

Another approach is the use of so-called hybrid functionals [70]:

$$\mathrm{E}_{\mathrm{xc}}^{\mathrm{Hybrid}} = c\, \left(\mathrm{E}_{\mathrm{x}} - \mathrm{E}_{\mathrm{x}}^{\mathrm{GGA}}\right) + \mathrm{E}_{\mathrm{xc}}^{\mathrm{GGA}}. \tag{3.84}$$

Here, $\mathrm{E}_{\mathrm{x}}^{\mathrm{GGA}}$ is the exchange part of equation (3.83) and E_{x} is the "exact" exchange energy, obtained by putting the KS eigenstates into equation (3.78) and $c \in [0, 1]$ is some parameter.

In contrast to the local (spin) density approximation (LDA), the functionals of the generalized gradient approximation (GGA) and hybrid functionals are not uniquely defined. On the one hand, they can be parametrized empirically by parameter fits to reference data of atoms and molecules. On the other hand, they can be parametrized without the empirical data by known exact conditions of the functional. The standard GGA potential, parametrized in the second way, is the Perdew-Burke-Ernzerhof (PBE) type [82, 83]. The GGA exchange-correlation functional of the PBE type reduces the overbinding of the LDA potential to about 0.3 eV [70]. However, it tends to lead to overestimate the bond lengths systematically by about 1%[81]. In this work, the GGA potential of type PBE, revised for solids, is used [84]. This leads to a slightly better fitting of the bond lengths [81].

3.2.5 Pseudopotentials

In subsections 3.2.1 to 3.2.4, the basic ideas of calculating quantum mechanical properties on the basis of density functional theory are explained. However, the chemical properties of a system are largely determined by the outer or valence electrons of the atoms, in contrast to the core electrons which are localized close to the nuclei. The strong Coulomb potentials of the nuclei $\hat{\mathrm{V}}_{\mathrm{Ne}}$ (see equation (3.57)) lead to strongly varying electronic wave functions in their vicinity, increasing the computational effort, as more plane waves have to be included (see equations (3.80) and (3.81)). Also, in principle, relativistic effects play a role, due to the rather high (kinetic) energy ($E = \mathbf{k}^2/2$) of the electrons close to the nuclei. A way to overcome this, is the employment of pseudopotentials. Here, the potential terms of the nuclei V_{Ne} (see equation (3.57)) are replaced by effective potentials that include the effects of core electrons within a core

radius r_{core} around the nuclei. This means that the external potential $\hat{\text{V}}_{\text{ext}} = \hat{\text{V}}_{\text{Ne}}$ in equations (3.68) and (3.69) is replaced by an effective potential $\hat{\text{V}}_{\text{eff}}$ and only the valence electrons are treated explicitly in the way described in the subsections 3.2.1 to 3.2.4. The KS eigenstates $\phi_{i,\sigma}(\mathbf{x})$ and the respective gradients $\nabla_{\mathbf{x}}\phi_{i,\sigma}(\mathbf{x})$ of the valence electrons, according to $\hat{\text{V}}_{\text{eff}}$, must agree with the ones, resulting from calculations with the original $\hat{\text{V}}_{\text{ext}} = \hat{\text{V}}_{\text{Ne}}$ with all electrons, outside the core radius r_{core}.

There are different types of pseudopotentials. In general, it is desired that the pseudopotentials are a smooth function of $\mathbf{x} - \mathbf{r}_i$, with $\mathbf{r}_i$ being the positions of the i^{th} nuclei. This allows a lower cutoff energy E_{cut}, according to equation (3.81). For the norm-conserving pseudopotentials, the integrated charge density, due to equation (3.67), is the same for the eigenstates of the effective potential $\hat{\text{V}}_{\text{eff}}$, as well, as for the ones of the original potential $\hat{\text{V}}_{\text{ext}} = \hat{\text{V}}_{\text{Ne}}$. For the ultrasoft pseudopotentials (USPP) [85], this restriction is given up, leading to an increased smoothness of the pseudopotentials and a lower E_{cut}.

In this work, the projector augmented-wave method [86, 87] is applied. Here, the contributions of all electrons are treated explicitly. The all-electron wave function $|\Psi\rangle$ is replaced by a pseudo wave function $\left|\tilde{\Psi}\right\rangle$ inside the core radius r_{core} (or augmentation sphere). Here, $|\Psi\rangle = \sum_{i,\sigma}(|\phi_{i,\sigma}\rangle$ is the all-electron wave function of the KS system, not of the real system. Outside the augmentation sphere, the two are constructed to be the same. This can be achieved by means of a projection operator $\hat{\text{T}}$:

$$|\Psi\rangle = \hat{\text{T}}\left|\tilde{\Psi}\right\rangle. \tag{3.85}$$

3.3 Static and dynamic correlation functions

During a simulation run, several structural and dynamical quantities are measured. As explained in section 3.1, classical molecular dynamics simulations allow the calculation of ensemble averages in terms of time averages over the respective trajectories. In the following, $\langle\cdot\rangle$ represents such a time average. In practice, every N_{dis} time steps the atom configurations are stored to calculate the structural properties. This is done N_{rep} times. A typical value of N_{rep} is $N_{\text{rep}} = 1000$, meaning the quantities are averaged over 1000 (independent) configurations. This requires to select the value of N_{dis} in a way that the configurations are uncorrelated. In the following, the indices α, β and γ stand for the different occurring atom types, namely $\alpha, \beta, \gamma \in \{B, Si, O\}$, in this work.

Pair correlation function

One important structural quantity is the partial pair correlation function or pair distribution function $g_{\alpha\beta}(r)$. The pair correlation function $g_{\alpha\beta}(r)$ describes the probability density of finding

two particles, one of type α and the other of type β, at a distance r, divided by the probability density of the same event in a noninteracting system, namely an ideal gas. It is defined as:

$$g_{\alpha\beta}(r) := \mathcal{N}_{\alpha\beta} \left\langle \sum_{i=1}^{N_\alpha} \sum_{j=1}^{N_\beta} \frac{1}{4\pi\, r^2}\, \delta\left(r - |\mathbf{r}_i - \mathbf{r}_j|\right) \right\rangle, \tag{3.86}$$

with $i \neq j$ for $\alpha \neq \beta$ and the normalization constant

$$\mathcal{N}_{\alpha\beta} = \begin{cases} \frac{N}{\rho\, N_\alpha (N_\alpha - 1)} = \frac{V}{N_\alpha (N_\alpha - 1)} & , \alpha = \beta \\ \frac{N}{\rho\, N_\alpha N_\beta} = \frac{V}{N_\alpha N_\beta} & , \alpha \neq \beta \end{cases}. \tag{3.87}$$

Here, N is the total number of atoms in the system, $\rho = {}^{N}/_{V}$ is the total particle number density, N_α and N_β are the total numbers of atoms of type α, β in the configuration and V is the volume of the simulation box. This means that $\lim_{r\to\infty} g_{\alpha\beta}(r) = 1$ as then no correlations between the particles due to inter-atomic interactions are visible.

In practice, the pair correlation function can be calculated, applying the following formula [40]:

$$g_{\alpha\beta}(r) = \langle N_{\alpha\beta}(r) \rangle\, \mathcal{N}_{\alpha\beta} \left(\frac{4\pi}{3} \left[(r + dr)^3 - r^3 \right] \right)^{-1}. \tag{3.88}$$

In equation (3.88), the distance r refers to the minimal image distance between the atoms of types α and β, according to the considerations in subsection 3.1.1. $N_{\alpha\beta}(r)$ is the number of particles, one of type α and the other of type β, within a minimal image distance between r and $r+dr$ and $\frac{4\pi}{3}\left[(r+dr)^3 - r^3\right]$ is the volume of a 2-dimensional shell of width dr. This means that the computation is done with respect to bins of width dr. In case of a cubic simulation box with box length L_{Box}, the formulation of equation (3.88) holds for all minimal image distances smaller than ${}^{L_{\text{Box}}}/_{2}$, restricting the distances r, $g_{\alpha\beta}(r)$ can be calculated for. In case of a simulation box with a different shape, the same holds for distances smaller than half of the smallest dimension of the box.

Static structure factor

Scattering experiments give access to information in reciprocal space, in contrast to real space. A structural quantity in reciprocal space corresponding to the partial pair correlation function is the partial static structure factor. It is defined by:

$$S_{\alpha\beta}(k) := \frac{f_{\alpha\beta}}{N} \left\langle \sum_{i=1}^{N_\alpha} \sum_{j=1}^{N_\beta} \exp\left[i\,\mathbf{k}\cdot(\mathbf{r}_i - \mathbf{r}_j)\right] \right\rangle, \tag{3.89}$$

with N being the total atom number, N_α and N_β being the atom numbers of types α and β and $f_{\alpha\beta} = 0.5$ for $\alpha \neq \beta$ and $f_{\alpha\beta} = 1$ for $\alpha = \beta$ being normalization constants, correcting for the double counting in case of $\alpha \neq \beta$. For an isotropic system, $S_{\alpha\beta}(k)$ only depends on the magnitude of the wave-vector $k = |\mathbf{k}|$. The connection between $S_{\alpha\beta}(k)$ and $g_{\alpha\beta}(r)$ is as follows [40]:

$$S_{\alpha\beta}(k) = 1 + \frac{N}{V} \int \mathbf{dr} \exp\left[i\,\mathbf{k}\cdot\mathbf{r}\right]\, g_{\alpha\beta}(r)\,. \tag{3.90}$$

Regarding this expression, it can be seen that $S_{\alpha\beta}(k)$ diverges at $k = 0$ ($S_{\alpha\beta}(k = 0) \propto \delta(k)$ as $\lim_{r\to\infty} g_{\alpha\beta}(r) = 1$). This contribution, of course, is inaccessible experimentally and is ignored in the following.

For simulations in a finite box, only specific $\mathbf{k}$-values are allowed in the calculation of $S_{\alpha\beta}(k)$. In this work $S_{\alpha\beta}(k)$ is calculated only in the case of a cubic simulation box. This leads to $\mathbf{k} \in \frac{2\pi\,\mathbf{n}}{L_{\text{Box}}}$, $\mathbf{n} \in \mathbb{Z}^3$, as in equations (3.24) and (3.25) for the calculation of the long-range part of the Ewald summation. In practice, first all possible $\mathbf{k}$-vectors are determined with $0 \leq k_1 \leq n_{\max}\frac{2\pi}{L_{\text{Box}}}$, $-n_{\max}\frac{2\pi}{L_{\text{Box}}} \leq k_2 \leq n_{\max}\frac{2\pi}{L_{\text{Box}}}$ and $-n_{\max}\frac{2\pi}{L_{\text{Box}}} \leq k_3 \leq n_{\max}\frac{2\pi}{L_{\text{Box}}}$ for some maximum $n_{\max} \in \mathbb{N}$. If $k_1 = 0$, the minimum value of k_2 considered is 0 and if $k_1 = 0$ and $k_2 = 0$, the minimum value of k_3 considered is 0. Then, the degeneracy $d(k)$ of possible $\mathbf{k}$-vectors with the same absolute value k is determined. In this way, all vectors $\mathbf{k}$, together with all vectors $-\mathbf{k}$, represent all allowed $\mathbf{k}$-vectors with $|k_\alpha| \leq n_{\max}\frac{2\pi}{L_{\text{Box}}}$, $\alpha \in \{1,2,3\}$. For $k \leq k_{\text{all}}$, all possible $\mathbf{k}$-vectors are included in the calculation of the partial static structure factors. Whereas, for $k > k_{\text{all}}$, the k-range up to a maximum value of k is divided into a certain number of intervals and for each interval a fixed number of $\mathbf{k}$-vectors is chosen randomly. Regarding this, the partial static structure factors are calculated by implementing the following formulas:

$$S_{\alpha\beta}(k) = \frac{1}{N d(k)} \sum_{\mathbf{k},|\mathbf{k}|=k} \left\langle \left(\sum_{i=1}^{N_\alpha} e^{i\,\mathbf{k}\cdot\mathbf{r}_i}\right)\left(\sum_{i=1}^{N_\alpha} e^{-i\,\mathbf{k}\cdot\mathbf{r}_i}\right)\right\rangle \tag{3.91}$$

$$= \frac{1}{N d(k)} \sum_{\mathbf{k},|\mathbf{k}|=k} \left\langle \left(\sum_{i=1}^{N_\alpha} \cos\mathbf{k}\cdot\mathbf{r}_i\right)^2 + \left(\sum_{i=1}^{N_\alpha} \sin\mathbf{k}\cdot\mathbf{r}_i\right)^2 \right\rangle \tag{3.92}$$

and

$$S_{\alpha\beta}(k) = \frac{1}{2Nd(k)} \sum_{\mathbf{k},|\mathbf{k}|=k} \left\langle \left(\sum_{i=1}^{N_\alpha} e^{i\,\mathbf{k}\cdot\mathbf{r}_i} \right) \left(\sum_{i=1}^{N_\beta} e^{-i\,\mathbf{k}\cdot\mathbf{r}_i} \right) + \left(\sum_{i=1}^{N_\beta} e^{i\,\mathbf{k}\cdot\mathbf{r}_i} \right) \left(\sum_{i=1}^{N_\alpha} e^{-i\,\mathbf{k}\cdot\mathbf{r}_i} \right) \right\rangle \tag{3.93}$$

$$= \frac{1}{2Nd(k)} \sum_{\mathbf{k},|\mathbf{k}|=k} \left\langle \left(\sum_{i=1}^{N_\alpha} \cos\mathbf{k}\cdot\mathbf{r}_i \right) \left(\sum_{i=1}^{N_\beta} \cos\mathbf{k}\cdot\mathbf{r}_i \right) + \left(\sum_{i=1}^{N_\alpha} \sin\mathbf{k}\cdot\mathbf{r}_i \right) \left(\sum_{i=1}^{N_\beta} \sin\mathbf{k}\cdot\mathbf{r}_i \right) \right\rangle . \tag{3.94}$$

In sections 4.2 and 6.5, the simulation results are compared to neutron diffraction experiments. According to [88], the neutron structure factors $S_{\text{neutr.}}(k)$ can be extracted from the partial static structure factors $S_{\alpha\beta}(k)$:

$$S_{\text{neutr.}}(k) = \frac{N}{\sum_\alpha (N_\alpha\, b_\alpha^2)} \sum_{\alpha,\beta} b_\alpha b_\beta S_{\alpha\beta}(k)\,. \tag{3.95}$$

In fact, in [88], the factor N is not present. However, without N, wrong results are obtained. Here, b_α and b_β are the neutron scattering lengths of the respective elements [89].

Angular distributions

In addition to the partial pair correlation functions and partial static structure factors it is also interesting to get information about the distribution of angles in the system. This can be obtained by the angular distribution. Following the description of [51], the latter is defined as:

$$p_{\alpha\beta\gamma}(\Phi) := \frac{1}{C} \left\langle \sum_{i=1}^{N_\alpha} \sum_{j=1}^{N_\beta} \sum_{k=1}^{N_\gamma} \delta(\Phi_{ijk} - \Phi)\; \theta(r_{\min,\alpha\beta} - r_{ij})\; \theta(r_{\min,\gamma\beta} - r_{kj}) \right\rangle . \tag{3.96}$$

Here, C is a normalization constant. In this work it is chosen in a way that the integrated distribution is equal to $\int_{0^\circ}^{180^\circ} d\Phi\, p_{\alpha\beta\gamma}(\Phi) = 1$. Here, $r_{ij} = |\mathbf{r}_{ij}| = |\mathbf{r}_i - \mathbf{r}_j|$ and $r_{kj} = |\mathbf{r}_{kj}| = |\mathbf{r}_k - \mathbf{r}_j|$ are the actual minimal image distances between the triplet of atoms i, j and k, forming an angle, and $\Phi_{ijk} = \arccos\left[\frac{\mathbf{r}_{ij}}{r_{ij}} \cdot \frac{\mathbf{r}_{kj}}{r_{kj}}\right]$ are the respective angles. The function $\theta(x)$ is the Heaviside step function which, in equation (3.96), is equal to zero for distances greater than $r_{\min,\alpha\beta}$ and $r_{\min,\gamma\beta}$. These distances are chosen as the positions of the first minima in the corresponding partial pair correlation functions (see equation (3.86)). This is a common way to define the maximum bond length of an atom correlation.

Distribution of coordination numbers

Other structural quantities of interest are the partial coordination numbers of all correlations

of atom types. In principle, the average partial coordination numbers $\bar{n}_{\alpha\beta}$ are equal to the integrated areas of the first peaks in the corresponding partial pair correlation functions:

$$\bar{n}_{\alpha\beta} = \int_0^{r_{\min,\alpha\beta}} dr\, g_{\alpha\beta}(r)\,. \tag{3.97}$$

In practice, the number of atomic neighbors of the specific type with a minimal image distance $r < r_{\min,\alpha\beta}$ is counted in each case. Again, $r_{\min,\alpha\beta}$ is the distance corresponding to the first minimum in $g_{\alpha\beta}(r)$. In this way, the average coordination number $\bar{n}_{\alpha\beta}$ and the distribution of coordination numbers $p_{\alpha\beta}(n)$ can be determined for each atom correlation.

Probability of an atom to be a member of a ring of size n

Additional interesting quantities are the probability that an atom of type α is member of a ring of size n, $p_\alpha(n)$, or the probability to find a ring of size n. According to [20], these are two different quantities. In this work, the first one is computed. For that, starting with an atom of type α, all neighboring atoms of type β are explored and, subsequently, all atom neighbors of type α of the latter. This procedure is repeated until the starting atom α is reached again. The number n of atoms of type α defines the ring size n. Again, neighboring atoms are all atoms with a minimal image distance $r < r_{\min,\alpha\beta}$. Rings of size $n = 1$ are defined as follows: Either an atom of type α with only one atom neighbor of type β or vice versa. In this work, only rings are examined with $\alpha \in \{Si, O\}$ and $\beta \in \{O\}$.

Computation of time correlation functions on a logarithmic time scale

In addition to these structural quantities, also dynamical properties are of interest. For this purpose, atom configurations are stored on a logarithmic time scale, to calculate the time correlation functions for time differences that differ in many orders of magnitude. This is done by first choosing a fixed number N_s of time steps for each considered order of magnitude n_m. Subsequently, for each order of magnitude $n_\mathrm{m} = 1, \ldots, n_\mathrm{max}$, the relevant time steps are computed by truncation of $10^{n_\mathrm{m}-1} \cdot 10^{1/N_\mathrm{s}}\, ts, 10^{n_\mathrm{m}-1} \cdot 10^{2/N_\mathrm{s}}\, ts, \ldots, 10^{n_\mathrm{m}-1} \cdot 10^{1}\, ts$ to integer values. The time step 0 is always included. So, for instance, for $n_\mathrm{max} = 4$ and $N_\mathrm{s} = 4$, the appropriate time steps are: 0, 1, 3, 5, 10, 17, 31, 56, 100, 177, 316, 562, 1000, 1778, 3162, 5623, 10000. Next, N_rep repetitions of these lists are constructed with starting points shifted on a linear timescale by $0 \cdot N_\mathrm{dis}, \ldots, (N_\mathrm{rep-1}) \cdot N_\mathrm{dis}$. Therefore, the total list contains $N_\mathrm{rep} \cdot n_\mathrm{max} \cdot N_\mathrm{s}$ time steps. This list is sorted and double counted time steps are rejected. Typical values of the parameters are, for example, $n_\mathrm{max} = 7$, $N_\mathrm{s} = 5$, $N_\mathrm{rep} = 1000$ and $N_\mathrm{dis} = 100000$. After sorting and rejecting the double counted time steps, the final list for these values of the parameters, for example, contains 33100 time steps. In the course of a simulation run, the atom configurations are saved at the distinct time steps, contained in the final list.

Mean square displacement

One important time correlation function is the mean square displacement $\left\langle r_\alpha^2(t)\right\rangle$. It is defined as:

$$\left\langle r_\alpha^2(t)\right\rangle := \frac{1}{N_\alpha}\sum_{i=1}^{N_\alpha}\left\langle\left(\mathbf{r}_{i,\mathrm{u.}}(t)-\mathbf{r}_{i,\mathrm{u.}}(0)\right)^2\right\rangle. \tag{3.98}$$

In fact, $\sqrt{\left\langle r_\alpha^2(t)\right\rangle}$ is the mean absolute distance, an atom of type α moved away from its starting position in the simulation time t. In equation (3.98), $\mathbf{r}_{i,\mathrm{u.}}(t)$ are the unwrapped atom coordinates, as explained in subsection 3.1.1. In case of normal diffusion, the mean square displacement is proportional to t in the limit of $t\to\infty$ and the self-diffusion constant D_α can be determined as follows [7]:

$$D_\alpha = \lim_{t\to\infty}\frac{\left\langle r_\alpha^2(t)\right\rangle}{6t}. \tag{3.99}$$

Incoherent intermediate scattering function

Another important time correlation function is the incoherent intermediate scattering function $F_{\mathrm{S},\alpha}(k,t)$. It characterizes how a density fluctuation of a tagged particle of type α decays. It is formally defined as:

$$F_{\mathrm{S},\alpha}(k,t) := \frac{1}{N}\left\langle\sum_{i=1}^{N_\alpha}\exp\left[i\,\mathbf{k}\cdot\left(\mathbf{r}_i(t)-\mathbf{r}_i(0)\right)\right]\right\rangle. \tag{3.100}$$

Here, $\mathbf{r}_i$ are the atom coordinates within the original simulation box, in contrast to the unwrapped coordinates in case of the mean square displacement $\left\langle r_\alpha^2(t)\right\rangle$. In practice, the incoherent intermediate scattering functions are calculated in the following way:

$$F_{\mathrm{S},\alpha}(k,t) := \frac{1}{2Nd(k)} \sum_{\mathbf{k},|\mathbf{k}|=k} \left\langle \sum_{i=1}^{N_\alpha} e^{i\,\mathbf{k}\cdot(\mathbf{r}_i(t)-\mathbf{r}_i(0))} + \sum_{i=1}^{N_\alpha} e^{-i\,\mathbf{k}\cdot(\mathbf{r}_i(t)-\mathbf{r}_i(0))} \right\rangle \tag{3.101}$$

$$= \frac{1}{2Nd(k)} \sum_{\mathbf{k},|\mathbf{k}|=k} \left\langle \sum_{i=1}^{N_\alpha} \left(e^{i\,\mathbf{k}\cdot\mathbf{r}_i(t)}\, e^{-i\,\mathbf{k}\cdot\mathbf{r}_i(0)} \right) + \sum_{i=1}^{N_\alpha} \left(e^{-i\,\mathbf{k}\cdot\mathbf{r}_i(t)}\, e^{i\,\mathbf{k}\cdot\mathbf{r}_i(0)} \right) \right\rangle \tag{3.102}$$

$$= \frac{1}{Nd(k)} \sum_{\mathbf{k},|\mathbf{k}|=k} \left\langle \sum_{i=1}^{N_\alpha} \left(\cos(\mathbf{k}\cdot\mathbf{r}_i(t)) \cos(\mathbf{k}\cdot\mathbf{r}_i(0)) + \sin(\mathbf{k}\cdot\mathbf{r}_i(t)) \sin(\mathbf{k}\cdot\mathbf{r}_i(0)) \right) \right\rangle . \tag{3.103}$$

$F_{\mathrm{S},\alpha}(k,t)$ is computed for one absolute value $k = |\mathbf{k}|$ and all possible $\mathbf{k}$-vectors with this absolute value are considered. As in case of the partial static structure factors, using the formulas above, a summation over $\mathbf{k}$ and over $-\mathbf{k}$ is performed.

3.4 Vibrational properties

In this section, the basic concepts of the theory of lattice vibrations are given. As explained in subsection 3.2.3, the set of atoms is located in a simulation box with periodic boundary conditions and surrounding replicas of the latter can be viewed as a crystalline structure with the unit cell being the simulation box. Therefore, the theory of lattice vibrations can be applied to the amorphous structures as well. Here, the so-called "frozen-phonon" method is explained, meaning the vibrational properties are calculated at a temperature of $T = 0\mathrm{K}$. This method is based on the assumption that for small displacements of the atoms from their equilibrium position at 0 K, the potential energy V of the system increases proportionally to the displacement of the respective atom. Therefore, it is named harmonic approximation. Following the description in the manual of the open source package Phonopy [90, 91], this allows to calculate the force constants

$$F_{i,\alpha} := -\frac{\partial V(\{\mathbf{r}_i\})}{\partial r_{i,\alpha}}, \quad i \in \{1,\ldots,N\}, \quad \alpha \in \{1,2,3\}. \tag{3.104}$$

Here, $V(\{\mathbf{r}_i\})$ is the total potential energy of the system for the equilibrium atom positions $\mathbf{r}_i$. In this description, only the case of the restriction of the calculation to the original unit cell is presented. In principle, the calculation can be extended to larger supercells in a straightforward way by introducing another index, labeling the unit cells. Calculating the force constants $F_{i,\alpha}$ for all N atoms of the unit cell and all Cartesian directions $\{1,2,3\}$ leads to the force constant matrix:

$$\Phi_{\alpha\beta;i,j} := \frac{\partial^2 V\left(\{\mathbf{r}_i\}\right)}{\partial r_{i,\alpha} \partial r_{j,\beta}} = -\frac{\partial F_{j,\beta}}{\partial r_{i,\alpha}}. \tag{3.105}$$

In practice, the derivatives with respect to the particle positions $r_{i,\alpha}$ are calculated numerically with respect to finite displacements $\Delta r_{i,\alpha}$. Therefore, all atoms of the equilibrium configuration are displaced by $\Delta r_{i,\alpha}$ in each Cartesian direction and the resulting forces on all atoms are computed: $F_{j,\beta}\left(\Delta r_{i,\alpha}\right)$ with $i, j \in \{1, N\}$ and $\alpha, \beta \in \{1, 2, 3\}$. This results in the approximation:

$$\Phi_{\alpha\beta;i,j} := -\frac{F_{j,\beta}\left(\Delta r_{i,\alpha}\right) - F_{j,\beta}}{\Delta r_{i,\alpha}}. \tag{3.106}$$

Based on the force constant matrix, the dynamical matrix can be calculated [92]:

$$D_{\alpha\beta;i,j}\left(\mathbf{k}\right) := \frac{1}{\sqrt{M_i\, M_j}}\, \Phi_{\alpha\beta;i,j}\, \exp\left[i\, \mathbf{k} \cdot \left(\mathbf{r}_i - \mathbf{r}_j\right)\right] \tag{3.107}$$

Here, M_i and M_j are the masses of the atoms. The $\mathbf{k}$ vector can take all possible values in the first Brillouin zone, as described in subsection 3.2.3.

The dynamical matrix can be diagonalized:

$$\sum_{j=1}^{N} \sum_{j=1}^{N} D_{\alpha\beta;i,j}\left(\mathbf{k}\right)\, \hat{\mathbf{e}}_{j;n} := \left[2\pi\, \nu_n\left(\mathbf{k}\right)\right]^2\, \hat{\mathbf{e}}_{i;n}. \tag{3.108}$$

Here, $\nu_n\left(\mathbf{k}\right)$, $n \in \{1, \ldots, 3N\}$ is the n^{th} eigenfrequency, according to the n^{th} eigenvalue of the $3N \times 3N$ dimensional dynamical matrix and $\hat{\mathbf{e}}_{i;n}$ is the contribution of the i^{th} atom to the eigenvector of the corresponding vibrational mode. The product $D_{\alpha\beta;i,j}\left(\mathbf{k}\right)\, \hat{\mathbf{e}}_{j;n}$ in equation has to be understood as a product of the 3×3-dimensional matrix $D_{\alpha\beta;i,j}\left(\mathbf{k}\right)$ with the 3-dimensional vector $\hat{\mathbf{e}}_{j;n}$. In case of an amorphous system, no degeneracy of the eigenfrequencies is observed due to lattice symmetries and all $3N$ eigenfrequencies $\nu\left(\mathbf{k}\right)_n$ are different.

Based on $\nu_n\left(\mathbf{k}\right)$ the phonon density of states can be calculated [93]. In case of discrete $\mathbf{k}$-values, it is defined as:

$$g\left(\nu\right) := \frac{1}{3\, N\, N_{\mathbf{k}}} \sum_{\mathbf{k}} \sum_{n=1}^{3N} \delta\left(\nu - \nu_n\left(\mathbf{k}\right)\right). \tag{3.109}$$

Following the description in [93], the vibrations can be treated as $3\,N$ independent quantum mechanical oscillators. This leads to a description of the internal energy of the system in terms of the $3N$ eigenfrequencies $\nu_n\left(\mathbf{k}\right)$:

$$U_{\mathrm{Vib}}\left(T\right) = \frac{1}{N_{\mathbf{k}}} \sum_{\mathbf{k}} \sum_{n=1}^{3N} h\nu_n\left(\mathbf{k}\right) \left[n\left(\nu_n\left(\mathbf{k}\right)\right) + \frac{1}{2} \right] \tag{3.110}$$

$$\Leftrightarrow U_{\mathrm{Vib}}\left(T\right) = \frac{1}{N_{\mathbf{k}}} \sum_{\mathbf{k}} \sum_{n=1}^{3N} h\nu_n\left(\mathbf{k}\right) \left[\frac{1}{\exp\left[\frac{h\nu_n(\mathbf{k})}{k_{\mathrm{B}}T}\right] - 1} + \frac{1}{2} \right] \tag{3.111}$$

$$\Leftrightarrow U_{\mathrm{Vib}}\left(T\right) = \frac{1}{2\,N_{\mathbf{k}}} \sum_{\mathbf{k}} \sum_{n=1}^{3N} h\nu_n \coth\left[\frac{h\nu_n\left(\mathbf{k}\right)}{2\,k_{\mathrm{B}}T} \right]. \tag{3.112}$$

The quantum mechanical treatment of the vibrations in lattices as a phonon gas is reflected in the occupation number due to a Bose-Einstein statistics $n\left(\nu_n\left(\mathbf{k}\right)\right)$ [63]. According to statistical mechanics, the internal energy can be written as derivative of the canonical partition function Z_{Vib}

$$U_{\mathrm{Vib}}\left(T\right) = k_{\mathrm{B}}T^2 \frac{\partial}{\partial T} \ln\left[Z_{\mathrm{Vib}}\right], \quad Z_{\mathrm{Vib}} = \sum_i \mathrm{e}^{-\frac{U_{\mathrm{Vib},i}}{k_{\mathrm{B}}T}}, \tag{3.113}$$

for a system with discrete energy levels $U_{\mathrm{Vib},i}$:

$$U_{\mathrm{Vib},i} = \frac{1}{N_{\mathbf{k}}} \sum_{\mathbf{k},n} U_{\mathrm{Vib},i;n}\left(\mathbf{k}\right) = \frac{1}{N_{\mathbf{k}}} \sum_{\mathbf{k},n} h\nu_n\left(\mathbf{k}\right) \left[n_{i;n}\left(\mathbf{k}\right) + \frac{1}{2} \right]. \tag{3.114}$$

Here, $U_{\mathrm{Vib},i}$ is expressed as a sum over individual modes $n_{i;n}\left(\mathbf{k}\right)$, with $n_{i;n}\left(\mathbf{k}\right)$ being an integer value $n_{i;n} \in \mathbb{N}_0$. This leads to the following expression for the canonical partition function Z_{Vib}:

$$Z_{\mathrm{Vib}}\left(T\right) = \prod_{\mathbf{k},n} \left[\sum_i \mathrm{e}^{-\frac{U_{\mathrm{Vib},i;n}(\mathbf{k})}{k_{\mathrm{B}}T}} \right]^{\frac{1}{N_{\mathbf{k}}}} \tag{3.115}$$

$$\Leftrightarrow Z_{\mathrm{Vib}}\left(T\right) = \prod_{\mathbf{k},n} \left[\left(\mathrm{e}^{-\frac{h\nu_n(\mathbf{k})}{2\,k_{\mathrm{B}}T}} + \mathrm{e}^{\frac{-3\,h\nu_n(\mathbf{k})}{2\,k_{\mathrm{B}}T}} + \mathrm{e}^{\frac{-5\,h\nu_n(\mathbf{k})}{2\,k_{\mathrm{B}}T}} + \ldots \right) \right]^{\frac{1}{N_{\mathbf{k}}}} \tag{3.116}$$

$$\Leftrightarrow Z_{\mathrm{Vib}}\left(T\right) = \prod_{\mathbf{k},n} \left[\frac{\mathrm{e}^{-\frac{h\nu_n(\mathbf{k})}{2\,k_{\mathrm{B}}T}}}{1 - \mathrm{e}^{-\frac{h\nu_n(\mathbf{k})}{k_{\mathrm{B}}T}}} \right]^{\frac{1}{N_{\mathbf{k}}}}. \tag{3.117}$$

From this, the vibrational part of the Helmholtz free energy $F_{\mathrm{Vib}}(T)$ follows as

$$F_{\mathrm{Vib}}(T) = -k_{\mathrm{B}}T \ln\left[Z_{\mathrm{Vib}}(T)\right] = k_{\mathrm{B}}T \frac{1}{N_{\mathbf{k}}} \sum_{\mathbf{k}} \sum_{n=1}^{3N} \ln\left[2 \sinh\left(\frac{h\nu_n(\mathbf{k})}{2k_{\mathrm{B}}T}\right)\right] \tag{3.118}$$

and the vibrational entropy follows as:

$$S_{\mathrm{Vib}}(T) = -\frac{\partial F_{\mathrm{Vib}}(T)}{\partial T} = \frac{U_{\mathrm{Vib}}(T)}{T} + k_{\mathrm{B}} \ln\left[Z_{\mathrm{Vib}}(T)\right] \tag{3.119}$$

$$\Leftrightarrow S_{\mathrm{Vib}}(T) = \frac{1}{2\,T\,N_{\mathbf{k}}} \sum_{\mathbf{k}} \sum_{n=1}^{3N} h\nu_n \coth\left[\frac{h\nu_n(\mathbf{k})}{2\,k_{\mathrm{B}}T}\right] - \frac{k_{\mathrm{B}}}{N_{\mathbf{k}}} \sum_{\mathbf{k}} \sum_{n=1}^{3N} \ln\left[2 \sinh\left(\frac{h\nu_n(\mathbf{k})}{2k_{\mathrm{B}}T}\right)\right]. \tag{3.120}$$

The specific heat at constant volume can be calculated using the following thermodynamic relation:

$$C_{\mathrm{V}}(T) = \left(\frac{\partial U_{\mathrm{Vib}}(T)}{\partial T}\right)_{\mathrm{V}} = \frac{k_{\mathrm{B}}}{N_{\mathbf{k}}} \sum_{\mathbf{k}} \sum_{n=1}^{3N} \left(\frac{h\nu_n(\mathbf{k})}{k_{\mathrm{B}}T}\right)^2 \frac{\exp\left[\frac{h\nu_n(\mathbf{k})}{k_{\mathrm{B}}T}\right]}{\left(\exp\left[\frac{h\nu_n(\mathbf{k})}{k_{\mathrm{B}}T}\right] - 1\right)^2}. \tag{3.121}$$

3.5 Determination of classical potentials

As explained in subsection 3.1.1, the classical interaction potential $V(\{\mathbf{r}_i(t)\})$, in principle, includes up to N-body interactions for a system of N particles (see equation (3.2)). For many systems, 2-body terms $V_{ij}(r_{ij})$ are sufficient to get appropriate estimates for the structural and dynamical properties of the system. Here, $r_{ij} = |\mathbf{r}_i - \mathbf{r}_j|$ is the minimal image distance between a pair of atoms i and j. As explained in chapter 4, in the case of the model glass former SiO_2, the description with only 2-body potentials leads to reasonable results. In this case, the system can be described quite well in terms of a Buckingham potential [94] with Coulomb interactions:

$$V^{\mathrm{Buck+Coul}}(r) = V^{\mathrm{Buck}}(r) + V^{\mathrm{Coul}}(r) = A_{\alpha\beta} \exp\left[-b_{\alpha\beta}\, r\right] - \frac{C_{\alpha\beta}}{r^6} + C_{\mathrm{Coul}} \frac{q_\alpha\, q_\beta}{r}. \tag{3.122}$$

As in section 3.3, the indices α and β stand for the different atom types, namely $\alpha, \beta \in \{B, Si, O\}$. The different terms of the short-range Buckingham potential describe the Pauli repulsion energy $A_{\alpha\beta} \exp\left[-b_{\alpha\beta}\, r\right]$ and the attractive van der Waals energy $-\frac{C_{\alpha\beta}}{r^6}$ for non-bonded atoms. Other common functional forms of short-range 2-body potentials are the Lennard-Jones potential [95]:

$$V^{\mathrm{LJ}}(r) = 4\epsilon_{\alpha\beta}\left[\left(\frac{\sigma_{\alpha\beta}}{r}\right)^{12} - \left(\frac{\sigma_{\alpha\beta}}{r}\right)^{6}\right] \tag{3.123}$$

and the Morse potential [96]:

$$V^{\mathrm{Morse}}(r) = A_{\alpha\beta}\left(1 - \exp\left[-b_{\alpha\beta}\left(r - r_{0,\alpha\beta}\right)\right]\right)^2. \tag{3.124}$$

The two terms in the Lennard-Jones potential describe the Pauli repulsion energy $\left(\frac{\sigma_{\alpha\beta}}{r}\right)^{12}$ and the attractive van der Waals energy $-\left(\frac{\sigma_{\alpha\beta}}{r}\right)^{6}$, as in the case of the Buckingham potential. On the other hand, the Morse potential describes the potential energy of a 2-atomic molecule with equilibrium distance $r_{0,\alpha\beta}$.

However, any classical potential is an approximation of the real interactions with some empirical force field parameters. This means that a priori, no functional form is preferred. In fact, the depth and gradient around the local minimum is most important. For all functional forms, the latter strongly depend on the parameter set. As the description of the model glass former SiO_2 in terms of the Buckingham potential with Coulomb interactions is quite successful, in this work only this functional form is considered.

Regarding 3-body potentials, typically angular potentials $V_{ijk}(\Phi_{ijk})$, $i, j, k \in \{1, \ldots, N\}$, are studied. Here, $\Phi_{ijk} = \arccos\left[\frac{\mathbf{r}_{ij}}{r_{ij}} \cdot \frac{\mathbf{r}_{kj}}{r_{kj}}\right]$ is the angle between the triplet of atoms with positions $\mathbf{r}_i$, $\mathbf{r}_j$ and $\mathbf{r}_k$. Usually, angular potentials are only included for certain triplets of atom types, for example the O-B-O or the B-O-B angle in case of the model glass former B_2O_3, with minimal image distances r_{ij} and r_{kj} closer than the maximum bond lengths. In section 6.3, a way to smoothly switch on and off the 3-body angular potentials, depending on the distances between the corresponding atoms, is presented.

Common functional forms of 3-body angular potentials are a harmonic potential

$$V^{\mathrm{Harm}}(\Phi) = \frac{1}{2} K_{\alpha\beta\gamma}\left(\Phi - \Phi_{0,\alpha\beta\gamma}\right)^2, \tag{3.125}$$

or a cosine potential

$$V^{\mathrm{Cos}}(\Phi) = K_{\alpha\beta\gamma}\left[1 + \cos\left(\Phi - \Phi_{0,\alpha\beta\gamma}\right)\right]. \tag{3.126}$$

Another possible functional form, used in [97], is the one of a Gaussian type with negative sign

$$V^{\text{Gauss}}(\Phi) = -K_{\alpha\beta\gamma} \exp\left[-\sigma_{\alpha\beta\gamma}\left(\Phi - \Phi_{0,\alpha\beta\gamma}\right)^2\right]. \tag{3.127}$$

In all cases, an equilibrium angle $\Phi_{0,\alpha\beta\gamma}$ is defined and the potential increases steadily for $\Phi < \Phi_{0,\alpha\beta\gamma}$ and $\Phi > \Phi_{0,\alpha\beta\gamma}$. Again, $\alpha\beta\gamma \in \{B, Si, O\}$ stand for the different considered atom types.

There are different ways to determine the potential parameters of force fields. Typically, force fields are parametrized with respect to ab initio data from crystals or small molecules in conjunction with experimental data. In contrast to this, in the work of Carré [43], the force field parameters of the BKS potential [22] for SiO_2 are improved, according to an ab initio MD simulation of liquid SiO_2 at high temperature of 3600 K. In this case, the parameter fitting, according to the structural properties of the liquid leads to better results than a force matching scheme [51]. In the work of Carré [43], the structure matching is done by means of a minimization of the differences in $r\, g_{\alpha\beta}(r)$ between the classical MD simulation and the ab initio MD run at the same temperature. In this work, this scheme is adapted and extended to include the angular distributions $p_{\alpha\beta\gamma}(\Phi)$ as well.

Following the description of [51], one can define a Chi-Square χ^2 as:

$$\begin{aligned}\chi^2(\{a_i\}) := &\sum_{\alpha,\beta}\sum_{i=1}^{N_\text{d}}\left[\frac{g_{\alpha\beta}^{\text{ab initio}}\left(\triangle_\text{d}\left(i-\frac{1}{2}\right)\right) - g_{\alpha\beta}^{\text{classical}}\left(\triangle_\text{d}\left(i-\frac{1}{2}\right);\{a_i\}\right)}{\sigma_{\alpha\beta}\left(\triangle_\text{d}\left(i-\frac{1}{2}\right)\right)}\right]^2 \\ &+ \sum_{\alpha,\beta,\gamma}\sum_{i=1}^{N_\text{a}}\left[\frac{p_{\alpha\beta\gamma}^{\text{ab initio}}\left(\triangle_\text{a}\left(i-\frac{1}{2}\right)\right) - p_{\alpha\beta\gamma}^{\text{classical}}\left(\triangle_\text{a}\left(i-\frac{1}{2}\right);\{a_i\}\right)}{\sigma_{\alpha\beta\gamma}\left(\triangle_\text{a}\left(i-\frac{1}{2}\right)\right)}\right]^2.\end{aligned} \tag{3.128}$$

Here, $g_{\alpha\beta}^{\text{ab initio}}$ and $p_{\alpha\beta\gamma}^{\text{ab initio}}$ are the pair correlation functions and the angular distributions of the liquid ab initio MD simulation, the structural fit is based on. The label classical in $g_{\alpha\beta}^{\text{classical}}$ and $p_{\alpha\beta\gamma}^{\text{classical}}$ stands for the corresponding structural quantities of the classical MD simulation at the same temperature with some interaction potential with a parameter set of M potential parameters: $\{a_i\}$, $i \in \{1, \ldots, M\}$. The values of N_d and N_a refer to the number of discretization points or bins of the pair correlation functions and angular distributions. As the pair correlation functions are calculated only for distances smaller than $L_\text{Box}/2$ (see section 3.3), the corresponding bin width is $\triangle_\text{d} = L_\text{Box}/2N_\text{d}$. The bin width of the angular distributions is $\triangle_\text{a} = 180°/2N_\text{d}$. In equation (3.128), different data points can be given different statistical weight, according to their statistical error or standard deviation, namely $\sigma_{\alpha\beta}\left(\triangle_\text{d}\left(i-\frac{1}{2}\right)\right)$ and $\sigma_{\alpha\beta\gamma}\left(\triangle_\text{a}\left(i-\frac{1}{2}\right)\right)$. In case of $\sigma_{\alpha\beta} = \sigma_{\alpha\beta\gamma}$ all data points are equally weighted. In fact, $\chi^2(\{a_i\})$ is a measure of the quality of the actual parameter set $\{a_i\}$, $i \in \{1, \ldots, M\}$, implying that, the lower χ^2, the lower are the mean-squared differences between the structural quantities of the ab initio and the classical MD simulation.

In the procedure of parameter fitting, starting with an initial guess of $\{a_i\}$, the next (local) minimum of $\chi^2(\{a_i\})$ is searched employing a Levenberg-Marquardt procedure. This is a combination of searching the next minimum via the gradient of $\chi^2(\{a_i\})$ and a second order method, using the Hessian of $\chi^2(\{a_i\})$ with respect to the fit parameters $\{a_i\}$. Following the description in [51], the following notations are introduced:

$$\beta_i := -\frac{1}{2}\frac{\partial\chi^2(\{a_i\})}{\partial a_i} \tag{3.129}$$

$$\begin{aligned} &= \sum_{\alpha,\beta}\sum_{i=1}^{N_\mathrm{d}} \frac{g_{\alpha\beta}^{\text{ab initio}} - g_{\alpha\beta}^{\text{classical}}}{\sigma_{\alpha\beta}^2} \frac{\partial g_{\alpha\beta}^{\text{classical}}\left(\triangle_\mathrm{d}\left(i-\frac{1}{2}\right);\{a_i\}\right)}{\partial a_i} \\ &+ \sum_{\alpha,\beta\gamma}\sum_{i=1}^{N_\mathrm{a}} \frac{p_{\alpha\beta\gamma}^{\text{ab initio}} - p_{\alpha\beta\gamma}^{\text{classical}}}{\sigma_{\alpha\beta\gamma}^2} \frac{\partial p_{\alpha\beta\gamma}^{\text{classical}}\left(\triangle_\mathrm{a}\left(i-\frac{1}{2}\right);\{a_i\}\right)}{\partial a_i} \end{aligned} \tag{3.130}$$

and

$$\alpha_{ij} := \frac{1}{2}\frac{\partial^2\chi^2(\{a_i\})}{\partial a_i \partial a_j} \tag{3.131}$$

$$\begin{aligned} &= \sum_{\alpha,\beta}\sum_{i=1}^{N_\mathrm{d}} \frac{1}{\sigma_{\alpha\beta}^2}\left[\frac{\partial g_{\alpha\beta}^{\text{classical}}}{\partial a_i}\frac{\partial g_{\alpha\beta}^{\text{classical}}}{\partial a_j} - \left[g_{\alpha\beta}^{\text{ab initio}} - g_{\alpha\beta}^{\text{classical}}\right]\frac{\partial^2 g_{\alpha\beta}^{\text{classical}}}{\partial a_i \partial a_j}\right] \\ &+ \sum_{\alpha,\beta\gamma}\sum_{i=1}^{N_\mathrm{a}} \frac{1}{\sigma_{\alpha\beta\gamma}^2}\left[\frac{\partial p_{\alpha\beta\gamma}^{\text{classical}}}{\partial a_i}\frac{\partial p_{\alpha\beta\gamma}^{\text{classical}}}{\partial a_j} - \left[p_{\alpha\beta\gamma}^{\text{ab initio}} - p_{\alpha\beta\gamma}^{\text{classical}}\right]\frac{\partial^2 p_{\alpha\beta\gamma}^{\text{classical}}}{\partial a_i \partial a_j}\right]. \end{aligned} \tag{3.132}$$

Regarding these definitions, the Levenberg-Marquardt procedure can be written as follows:

$$\sum_{j=1}^{M} \alpha_{ij}\left(1+\lambda\,\delta_{ij}\right)\left(a_i^{(n+1)} - a_i^{(n)}\right) =: \sum_{j=1}^{M} \alpha'_{ij}\left(a_i^{(n+1)} - a_i^{(n)}\right) = \beta_i. \tag{3.133}$$

Here, $a_i^{(n)}$ stands for the actual value of the parameter a_i at the n^{th} iteration step of the iterative procedure. Equation (3.133) has to be understood in the sense that, starting with a parameter set $\{a_i\}^{(n)}$, the next set of parameters $\{a_i\}^{(n+1)}$ is found by inverting the matrix α'_{ij}, leading to

$$a_i^{(n+1)} = \sum_{j=1}^{M} \left(\alpha'\right)_{ij}^{-1} \beta_j + a_i^{(n)}. \tag{3.134}$$

Close to the (local) minimum, the following assumption holds

$$\left[g_{\alpha\beta}^{\text{ab initio}}\left(\triangle_{\text{d}}\left(i-\frac{1}{2}\right)\right)-g_{\alpha\beta}^{\text{classical}}\left(\triangle_{\text{d}}\left(i-\frac{1}{2}\right);\{a_i\}\right)\right]\simeq 0 \tag{3.135}$$

and the matrix α_{ij} can be approximated as:

$$\alpha_{ij}\simeq\sum_{\alpha,\beta}\sum_{i=1}^{N_{\text{d}}}\frac{1}{\sigma_{\alpha\beta}^2}\left[\frac{\partial g_{\alpha\beta}^{\text{classical}}}{\partial a_i}\frac{\partial g_{\alpha\beta}^{\text{classical}}}{\partial a_j}\right]. \tag{3.136}$$

The parameter λ in equation (3.133) controls the balance between the first-order and second-order terms. For $\lambda \ll 1$, the redefined α'_{ij} is basically equal to the original Hessian matrix α_{ij} and for $\lambda \gg 1$, the diagonal terms in α'_{ij} dominate. During the iterative solving process λ is divided by the factor 1.5 if the new parameter set leads to a decrease of $\chi^2\left(a_1,\ldots,a_M\right)$ and λ is multiplied by the factor 1.5 if the new parameters give a higher $\chi^2\left(a_1,\ldots,a_M\right)$ (see equation (3.128)).

To apply this algorithm, the numerical derivatives

$$\frac{\partial g_{\alpha\beta}^{\text{classical}}}{\partial a_i}=\lim_{\epsilon_i\to 0}\frac{g_{\alpha\beta}^{\text{classical}}\left(a_i,\ldots,a_i+\epsilon_i,\ldots,a_M\right)-g_{\alpha\beta}^{\text{classical}}\left(a_i,\ldots,a_i-\epsilon_i,\ldots,a_M\right)}{2\epsilon_i} \tag{3.137}$$

and

$$\frac{\partial p_{\alpha\beta\gamma}^{\text{classical}}}{\partial a_i}=\lim_{\epsilon_i\to 0}\frac{p_{\alpha\beta\gamma}^{\text{classical}}\left(a_i,\ldots,a_i+\epsilon_i,\ldots,a_M\right)-p_{\alpha\beta\gamma}^{\text{classical}}\left(a_i,\ldots,a_i-\epsilon_i,\ldots,a_M\right)}{2\epsilon_i} \tag{3.138}$$

have to be calculated. This is done by calculating $g_{\alpha\beta}^{\text{classical}}\left(r\right)$ for a small perturbation of the specific parameter a_i, while keeping the other parameters constant and evaluating the numeric derivative for each of the N_{d} and N_{a} discretization points. This implies that for each iteration step $2\cdot M+1$ different classical MD simulations have to be carried out.

Chapter 4

Model glass former SiO_2

In this chapter, the simulation results of the model glass former SiO_2 are summarized. In section 4.1, the structural and dynamical properties of liquid SiO_2 are described in a temperature range between 4300 K and 2700 K. After conducting several test runs, simulations at different system sizes are carried out at a constant system density of $\rho = 2.37\,\mathrm{g/cm^3}$, employing the BKS [22] potential. The BKS potential has the unphysical property that the mean density is slightly higher than $\rho = 2.2\,\mathrm{g/cm^3}$ in a temperature range from about 6000 K down to 0 K [20], meaning the mean pressure of a system at $\rho = 2.2\,\mathrm{g/cm^3}$ is negative in this temperature range. This motivates to study also a slightly higher mass density. The main finite size effects are the slowing down of the dynamics and a decrease of the number of rings containing more than 6 Si atoms with decreasing system size. Next, the properties, according to the BKS [22], are compared to the ones, according to the CHIK [43] potential, at a constant system density of $\rho = 2.2\,\mathrm{g/cm^3}$, which is the experimental density of vitreous SiO_2 [98]. These simulation results are in agreement with the ones, presented in [43], taking into account finite size effects. In section 4.2, glass structures are generated by means of a quench from the melt with classical MD simulations, using the BKS and the CHIK potential. The corresponding glass structures before and after a structural relaxation with quantum mechanical forces are compared to one glass structure generated by means of a full ab initio quench. The glass structures after the quantum mechanical relaxation are in good agreement with experimental results, in all cases. In section 4.3, the vibrational spectra are calculated, using classical and quantum mechanical forces. The vibrational spectra, according to the quantum mechanical forces, show a significantly improved agreement with results from inelastic neutron scattering [99, 100], compared to the ones, according to the classical forces of the BKS, as well as the CHIK potential.

In principle, the liquid properties of the BKS and the CHIK potential are well studied. Also, the structural differences of glass structures before and after a structural relaxation with quantum mechanical forces have been examined before [10, 11] for glass samples, generated initially by a quench from the melt with classical MD simulations. However, it has not been investigated if there are differences in the glass structures, generated with the BKS and the CHIK potential, both, before and after a structural relaxation with DFT forces.

4.1 Liquid properties by means of classical MD simulation

As already described in section 3.5, the BKS as well as the CHIK potential only consists of pair interactions of the functional form of a Buckingham potential with Coulomb interactions (see equation (3.122)). In the case of the BKS potential, the Si-Si interaction is purely electrostatic. The parameters are listed in Table 4.2.

parameters	units	BKS	CHIK
q_{Si}	[e]	2.4	1.910418
A_{SiSi}	[eV]		3150.462646
b_{SiSi}	$[\text{Å}^{-1}]$		2.851451
C_{SiSi}	$[\text{eV Å}^{6}]$		626.751953
A_{SiO}	[eV]	18003.7572	27029.419922
b_{SiO}	$[\text{Å}^{-1}]$	4.87318	5.158606
C_{SiO}	$[\text{eV Å}^{6}]$	133.5381	148.099091
A_{OO}	[eV]	1388.7730	659.595398
b_{OO}	$[\text{Å}^{-1}]$	2.760	2.590066
C_{OO}	$[\text{eV Å}^{6}]$	175.0	26.836679

TABLE 4.2: Parameters of the BKS [22] and the CHIK [43] potential.

In subsection 3.1.1, the necessity of a cutoff radius for the short-range interactions, the introduction of a smoothing function (3.13) and the technique of splitting the long-range Coulomb interaction into a short-range $V^{\text{CS}}(r)$ (3.20), evaluated in real space, and a long-range part, evaluated in Fourier space, have been explained. In all simulations of this work, the long-range part of the Coulomb interaction is computed by means of a standard Ewald summation over k-vectors. The simulation box for the smallest system size has only a box length $L_{\text{Box}} = 13.22944\,\text{Å}$. Therefore, in all cases, a cutoff radius of $r_{\text{c}} = 5.5\,\text{Å}$ is chosen for the short-range Buckingham part of the potential, $V^{\text{Buck}}(r)$. The cutoff radius of $V^{\text{CS}}(r)$, r_{c}^{ew}, depends on the system size to ensure a good balance of the computational effort for the computation of the real space and the Fourier space parts. To guarantee an overall smooth potential, both, $V^{\text{Buck}}(r)$ and $V^{\text{CS}}(r)$ are shifted to zero at the respective cutoff distances, $r_{\text{c}} = 5.5$ and r_{c}^{ew}, and, subsequently, are multiplied by a smoothing function, namely $G(r)$ and $G^{\text{ew}}(r)$, with the functional form of equation (3.13). In all cases, a value of $d = d^{\text{ew}} = 0.05\,\text{Å}^2$ is chosen.

The Buckingham potential has the unphysical property that it diverges to minus infinity for $r \to 0$. In order that particle distances become close to zero, an energy barrier has to be crossed. This is very unlikely, but not impossible. To prevent such problems, the shifted and smoothed Buckingham potential with Coulomb interactions

$$V^{\mathrm{ModBuck+Coul}}(r) = \left(V^{\mathrm{Buck}}(r) - V^{\mathrm{Buck}}(r_{\mathrm{c}})\right) G(r) + V^{\mathrm{Coul}}(r) \tag{4.1}$$

is substituted by a harmonic potential of the form

$$V^{\mathrm{Harm}}(r) = a_{1,\alpha\beta} + a_{2,\alpha\beta}\left(r - a_{3,\alpha\beta}\right)^2 \tag{4.2}$$

for particle distances smaller than the positions of the local maxima $r < r_{\mathrm{in},\alpha\beta}$, again, with $\alpha, \beta \in \{Si, O\}$. For a smooth crossover from the potential, according to equation (4.1), to the harmonic potential $V^{\mathrm{Harm}}(r)$ at $r_{\mathrm{in},\alpha\beta}$, the parameters in (4.2) have to be chosen as follows: $a_{3,\alpha\beta}$ is the position of the local maximum for the specific atom pair, according to equation (4.1), $a_{1,\alpha\beta}$ is the value of the potential at $r = a_{3,\alpha\beta}$, according to equation (4.1) and $a_{2,\alpha\beta}$ is still unfixed. The positions of the local maxima are determined by means of Newton's method [101]. In case of the BKS potential, the values of $a_{2,\alpha\beta}$ are chosen, according to [57]. In case of the CHIK potential, the values of $a_{2,\alpha\beta} = 100\,\mathrm{eV\,\AA^{-2}}$ are chosen in all cases. This results in the following parameters, listed in Table 4.4.

Finally, this leads to the following functional form of total the short-range pair potential used in the simulations:

$$V^{\mathrm{S}}(r) = \begin{cases} V^{\mathrm{Harm}}(r) - V^{\mathrm{Coul}}(r) + \left(V^{\mathrm{CS}}(r) - V^{\mathrm{CS}}(r_{\mathrm{c}}^{\mathrm{ew}})\right) G^{\mathrm{ew}}(r) & , r \leq r_{\mathrm{in}} \\ \left(V^{\mathrm{Buck}}(r) - V^{\mathrm{Buck}}(r_{\mathrm{c}})\right) G(r) + \left(V^{\mathrm{CS}}(r) - V^{\mathrm{CS}}(r_{\mathrm{c}}^{\mathrm{ew}})\right) G^{\mathrm{ew}}(r) & , r_{\mathrm{in}} \leq r \leq r_{\mathrm{c}} \\ 0 & , r > r_{\mathrm{c}} \end{cases} . \tag{4.3}$$

Using this short-range potential $V^{\mathrm{S}}(r)$ together with the long-range part of the Coulomb interaction, the total pair potential $V(r)$ for $r \leq r_{\mathrm{in}}$ then resembles the harmonic $V^{\mathrm{Harm}}(r)$ potential (4.2), within the accuracy of the Ewald summation.

In Fig. 4.1, the original BKS potential is compared to the modified one, according to equation (4.1), with the short-range harmonic correction (see equation (4.2)). This illustrates the divergence of the Buckingham potential for $r \to 0$. In Fig. 4.2, the total short-range potential is shown, given by equation (4.3), for the BKS parameter set [22].

4.1.1 Tests

In this work, all classical MD simulations are conducted with the open source software package LAMMPS [60, 61]. The package LAMMPS has several built in potential forms for pair potentials,

parameters	units	BKS	CHIK
$a_{1,SiSi}$	[eV]		29.728739
$a_{2,SiSi}$	[eV Å^{-2}]		100
$a_{3,SiSi}$	[Å]		1.7201447
$a_{1,SiO}$	[eV]	-27.330929	-14.725522
$a_{2,SiO}$	[eV Å^{-2}]	12.5	100
$a_{3,SiO}$	[Å]	1.1941241	1.0982165
$a_{1,OO}$	[eV]	20.854644	35.961774
$a_{2,OO}$	[eV Å^{-2}]	13.5	100
$a_{3,OO}$	[Å]	1.4384771	1.0299079

TABLE 4.4: Parameters of short-range the repulsive substitution $V^{\mathrm{Harm}}(r)$ (see equation (4.2)) of the BKS [22] and the CHIK [43] potential at distances $r \leq r_{\mathrm{in}}$.

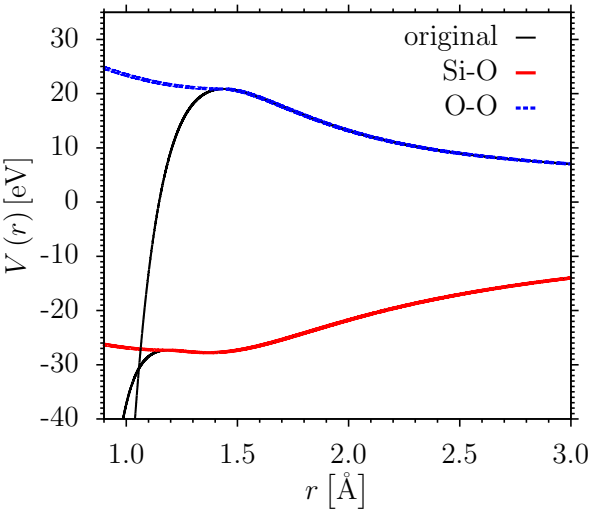

FIGURE 4.1: Comparison between the original BKS potential (3.122) and the modified potential (4.1) with harmonic correction for small r.

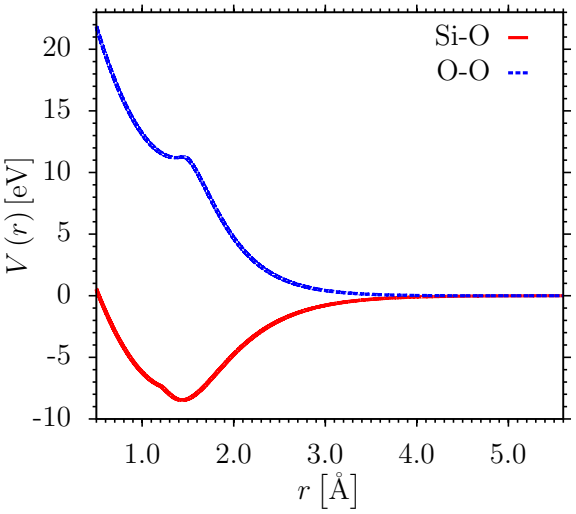

FIGURE 4.2: Total short-range potential $V^{S}(r)$ (4.3) used in simulation in case of BKS parameters.

many-body interactions, et cetera. However, the functional form of the total short-range potential, used in this work (see equation (4.3)), is not included. It is decided to use tabulated potentials. The numerical values of the total short-range pair potentials $V^{\mathrm{S}}(r)$ (see equation (4.3)) and the total short-range pair forces $-\frac{\partial}{\partial r}V^{\mathrm{S}}(r)$ are pre-computed for certain values of r_{ij} in a tabulated form, for pair distances $r \geq 0.25$ Å. For the Si-Si interactions of the BKS potential, only the smoothed and shifted short-range part of the Coulomb potential $\left(V^{\mathrm{CS}}(r) - V^{\mathrm{CS}}(r_{\mathrm{c}}^{\mathrm{ew}})\right) G^{\mathrm{ew}}(r)$ has to be taken into account. A table style of the so-called bitmap style is chosen, according to [102]. The table has 2^N table entries. Numerical values of the pair potential and the pair force are stored equally spaced in r^2 between all relevant powers of two in the range of $2^z \leq r^2 < 2^{z+1}$. An inner cutoff of the pair distances of 0.25 Å and an outer cutoff smaller than 64 Å lead to the relevant exponents: $z = -4, -3, -2, -1, 0, 1, 2, 3, 4, 5, 6, 7, 8, 9, 10, 11$. The dependence of the pair distance r on the position in the bitmap table with 2^{16} table entries, as used in the

simulation, is displayed in Fig. 4.3. For particle distances between adjacent table entries a linear interpolation is performed within the LAMMPS package. The k-space parts of the Coulomb interactions, in all cases, are computed with the standard routine for Ewald summations of the LAMMPS package. In all cases, a skin distance of $r_{\text{skin}} = 2\,\text{Å}$ is used and the Verlet neighbor lists are rebuilt when the first atom has moved more than half the skin distance.

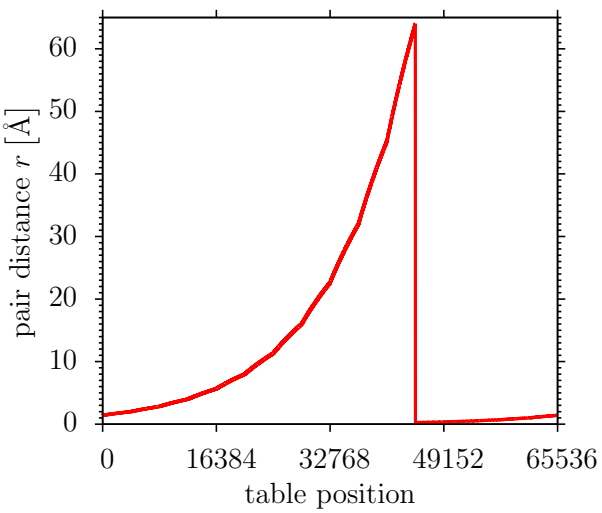

FIGURE 4.3: Dependence of the pair distance r on the position in a table of bitmap style with 2^{16} table entries.

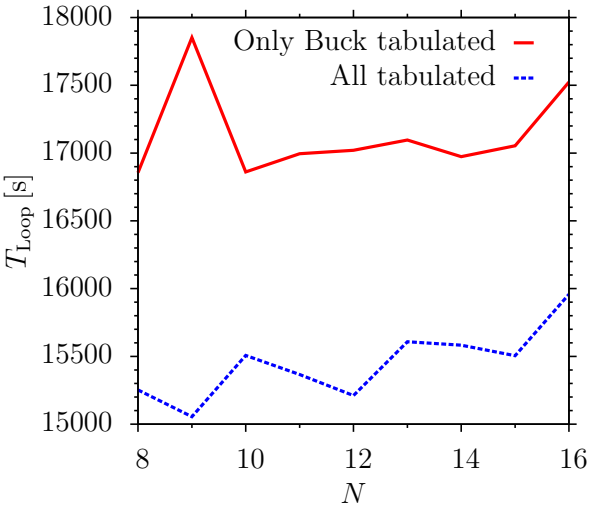

FIGURE 4.4: Dependence of the total simulation time (Loop time) for $2 \cdot 10^7$ time steps on the precision 2^N of the bitmap table.

To test the tabulated potentials, several different cases are studied. These first tests are carried out for a system size of 165 atoms at a constant system density of $\rho = 2.37\,\text{g/cm}^3$ with the BKS parameters. The atoms are randomly initialized in a cubic simulation box with a box length of $L_{\text{Box}} = 13.22944$ Å. Next, Lennard-Jones potentials are switched on. The parameters are tuned in a way that for each atom pair the minima are roughly at the positions of the first peaks in the corresponding pair correlation functions. Then, the system is relaxed to those minima by a short NVE run with a maximum limit each atom can move in a simulation step of 0.1 Å. Afterwards, the Lennard-Jones potentials are switched off and the real potentials are switched on. In all cases, the system is equilibrated for $5 \cdot 10^5$ ts at 4300 K, followed by a test run of $2 \cdot 10^7$ ts, where the mean total energy, the mean potential energy and the mean pressure are measured. In all cases, a time step of $\delta t = 0.6\,\text{fs}$ and a chain of 3 Nosé-Hoover thermostats (see subsection 3.1.2) is chosen, integrating the equations of motions according to [68]. A damping parameter of 60 fs is used, meaning the temperature is relaxed to the target temperature in a timespan of 100 time steps.

First it is tested, if the tabulated potentials are generated in a correct way. In one approach, only the shifted and smoothed Buckingham part of the BKS potential is tabulated and not the short-range part of the Coulomb interactions, according to equation (4.3) without the parts containing V^{CS}. The Coulomb interaction is calculated by means of the coul/long routine of the LAMMPS software package, which means that the total pair potential has a small discontinuity at $r_{\text{c}}^{\text{ew}} = 6.5\,\text{Å}$, as the short-range part of the Coulomb interactions is just cut off at r_{c}^{ew} and

not shifted to zero and/or smoothed. In the second approach, exactly the same form of the short-range potential is used and the total short-range potential is tabulated. Different numbers of table entries are tested in the range from 2^8 to 2^{16}. Simulations are carried out with an $g_{\text{ew}} = 0.473375$ which corresponds to an Ewald accuracy of about 10^{-5}, as explained in subsection 3.1.1. In Fig. 4.4, the total simulation time (Loop time) for $2 \cdot 10^7$ ts on 8 CPUs is compared for the different forms of the potential. It can be seen in general that the simulation time is smaller for the fully tabulated potentials and there is only a slight increase with increasing number of table entries. As shown in Table 4.6, there is no significant difference in the mean total energy per atom and mean pressure between the fully tabulated potential and the one with a tabulation of just the Buckingham part. This justifies the use of fully tabulated potentials with 2^{16} table entries. The quite weak dependence of the simulation time on the number of table entries comes from the fact that for this very small system about $60 - 70\%$ of the simulation time is used for the k-space summation. In Fig. 4.8, the speed up of the simulation with respect to the number of parallel processors N_{proc} is displayed, again for runs of $2 \cdot 10^7$ ts with a fully tabulated short-range potential. It can be seen that the speed up is sublinear and the slope of the curve decreases with increasing N_{proc}. As explained in subsection 3.1.1, this is connected to communication times and an unequal load balancing on each processor. These effects get more pronounced for smaller system sizes, as in case of the 165 atom system. For simulations of these small system sizes, a parallelization on $N_{\text{proc}} = 8$ CPUs seems reasonable. Only in some cases of very long simulation runs at low temperatures, $N_{\text{proc}} = 32$ or $N_{\text{proc}} = 64$ is chosen.

Run	E_{tot}/N [eV]	p [GPa]
$N = 165$, V^{CS} only cut off, only Buckingham part tabulated, $P_{\text{ew}} = 10^{-5}$	-17.820	0.633
$N = 165$, V^{CS} only cut off, fully tabulated potential, $P_{\text{ew}} = 10^{-4}$	-17.821	0.664
$N = 165$, V^{CS} only cut off, fully tabulated potential, $P_{\text{ew}} = 10^{-5}$	-17.821	0.662
$N = 165$, V^{CS} only cut off, fully tabulated potential, $P_{\text{ew}} = 10^{-6}$	-17.820	0.627
$N = 165$, V^{CS} only cut off, fully tabulated potential, $P_{\text{ew}} = 10^{-7}$	-17.820	0.651
$N = 165$, V^{CS} only cut off, fully tabulated potential, $P_{\text{ew}} = 10^{-8}$	-17.822	0.656
$N = 165$, V^{CS} shifted and smoothed, all tab., $P_{\text{ew}} = 10^{-5}$	-17.806	0.645

TABLE 4.6: Comparison of mean total energies per atom and mean pressures for partly and fully tabulated, partly and fully smoothed short-range potentials and different Ewald precisions. NVT runs at 4300 K of 165 atom system at a system density of $\rho = 2.37\,\text{g/cm}^3$.

Next, the effect of the accuracy of the Ewald summation is tested for the same functional form of the potential with V^{CS} only cut off at $r_c^{\text{ew}} = 6.5\,\text{Å}$. For this, additional simulations with an Ewald precision of $P_{\text{ew}} = 10^{-4}$, $P_{\text{ew}} = 10^{-6}$, $P_{\text{ew}} = 10^{-7}$ and $P_{\text{ew}} = 10^{-8}$ are carried out, which corresponds to $g_{\text{ew}} = 0.453903$, $g_{\text{ew}} = 0.561272$, $g_{\text{ew}} = 0.607886$ and $g_{\text{ew}} = 0.651171$, according to subsection 3.1.1. The effect of the Ewald accuracy on the mean total energy per atom and mean pressure is negligible (see Table 4.6), whereas the total simulation time (Loop time) for $2 \cdot 10^7$ ts on 8 CPUs increases from 12751.2 s to 51690.2 s for $P_{\text{ew}} = 10^{-4}$ to $P_{\text{ew}} = 10^{-8}$. Therefore, in the following, an Ewald accuracy of 10^{-5} is chosen.

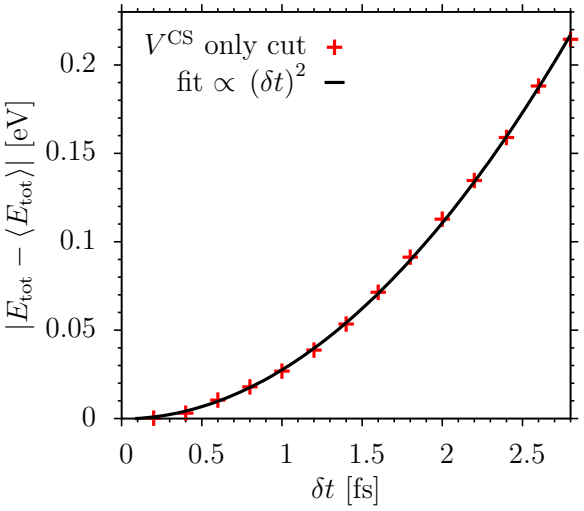

FIGURE 4.5: Test of relation $|E_{\text{tot}} - \langle E_{\text{tot}}\rangle| \propto (\delta t)^2$ for different time steps δt with short-range Coulomb part V^{CS} only cut off at r_{c}^{ew}.

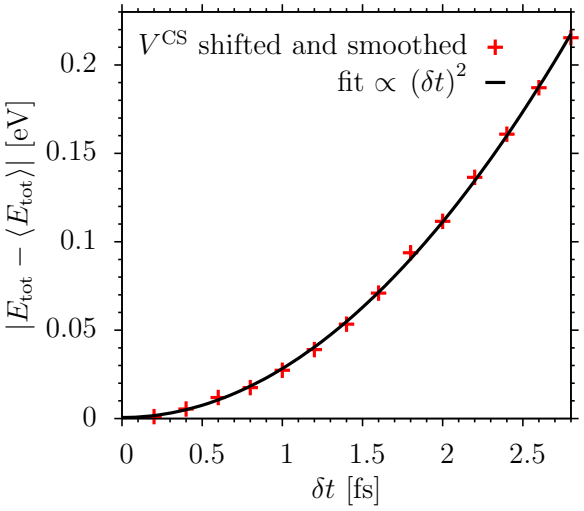

FIGURE 4.6: Test of relation $|E_{\text{tot}} - \langle E_{\text{tot}}\rangle| \propto (\delta t)^2$ for different time steps δt with short-range Coulomb part V^{CS} cut off at r_{c}^{ew}, shifted to zero and smoothed.

Dynamical quantities like time correlation functions have to be measured in the microcanonical ensemble as a thermostat always has an influence on the dynamics of the system (see subsection 3.1.1). This means that after the equilibration of the system at a given temperature, the thermostat has to be switched off for the microcanonical production run. For the small system sizes considered in this work, the thermodynamical quantities show large fluctuations. This leads to the problem that the mean temperature, total energy, et cetera, in the microcanonical run depend strongly on the exact state of the system at the time step when the thermostat is switched off. To overcome that problem 10000 configurations are stored at the end of each equilibration run. As a starting point of the microcanonical run the configuration is chosen with a total energy $E_{\text{tot}} = E_{\text{kin}} + E_{\text{pot}}$ closest to the mean total energy of the equilibration run at the given temperature.

As explained in subsection 3.1.1, the absolute value of the fluctuations of the total energy $|E_{\text{tot}} - \langle E_{\text{tot}}\rangle|$ of the system should be proportional to the times step squared (δt^2) (see equation (3.11)). To test this, short microcanonical runs of $1 \cdot 10^5$ ts with different time steps from $\delta t = 0.2$ fs to $\delta t = 2.8$ fs are carried out, after the equilibration of the 165 atom system at 4300 K. This test is performed for two different cases. First, only the Buckingham part of the potential is cut off at $r_{\text{c}} = 5.5$ Å, shifted and smoothed and the short-range part of the Coulomb interactions is just cut off at $r_{\text{c}}^{\text{ew}} = 6.5$ Å. Therefore, the total pair potential has a small discontinuity at r_{c}^{ew}, as explained above. Second, the Buckingham part is cut off, shifted and smoothed and the short-range Coulomb part is cut off at r_{c}^{ew}, shifted to zero and smoothed, as well. Thus, the total short-range part of the potential has the functional form of equation (4.3) and is continuous and smooth over the whole range. The amplitude of fluctuations is determined by computing half of the mean difference between neighboring maxima and minima of E_{tot} in the microcanonical run. The neighboring maxima and minima are only taken into account if there is a time difference

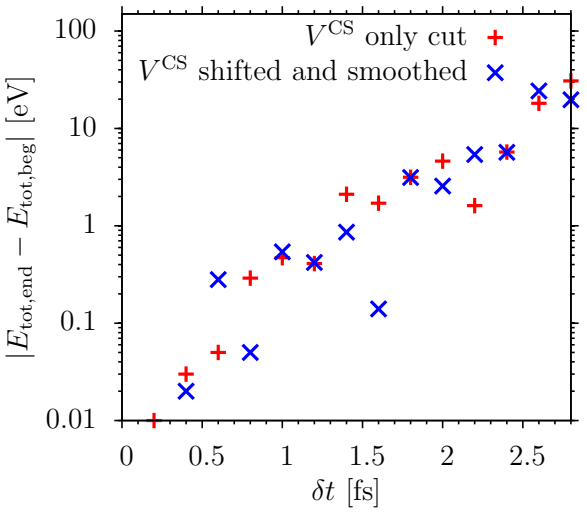

FIGURE 4.7: $|E_{tot,end} - E_{tot,beg}|$ in microcanonical production runs with respect to time step δt for different potentials (4.3).

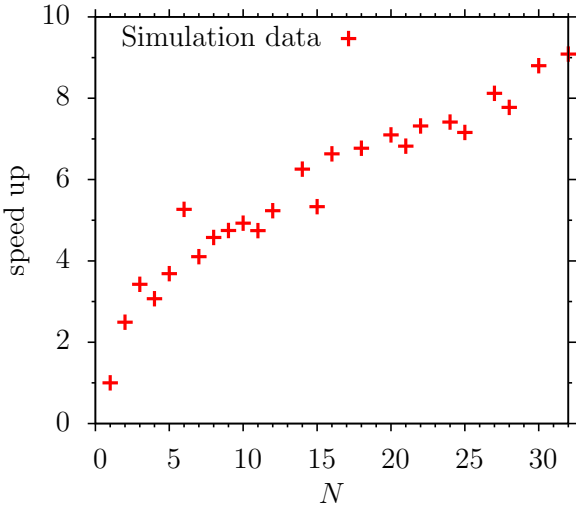

FIGURE 4.8: Scaling of Loop times with respect to the number of processors for fully tabulated short-range potential.

of 10 time steps in between. In Figs. 4.5 and 4.6, it can be seen that the prediction holds quite good for the whole range of examined time steps δt, in both cases. Despite the relation $\delta E_{\text{tot}} \propto (\delta t)^2$ being fulfilled quite well also in case of V^{CS}, only cut off at r_{c}^{ew}, the potential form with V^{CS} cut off at r_{c}^{ew}, shifted to zero and smoothed is chosen in all simulations of this work, due to the preference of an overall continuous potential. In addition to the fulfillment of $|E_{\text{tot}} - \langle E_{\text{tot}} \rangle| \propto (\delta t)^2$, the system also should show no significant drift of the total energy in the microcanonical production runs. In Fig. 4.7, the absolute difference of the total energy between the end and the beginning of a microcanonical production run of 10 ns is shown for both potential forms for time steps in the range of $\delta t = 0.2$ fs to $\delta t = 2.8$ fs at 4300 K on a logarithmic scale. It can be seen that in both cases, the energy difference $|E_{tot,end} - E_{tot,beg}|$ increases by orders of magnitude with increasing time step δt. It seems to be a good compromise between computational efficiency and accuracy to chose a time step of $\delta t = 0.6$ fs at this temperature. At lower temperatures the time step can be increased up to $\delta t = 1.6$ fs without a noticeable energy drift.

4.1.2 Comparison of different system sizes

As explained above, the relaxation of glass structures by means of a quantum mechanical DFT calculation and the subsequent calculation of the phonon density of states $g(\nu)$ requires rather small system sizes of about 100-200 atoms. The purpose of this subsection is to justify the simulation of systems with only a few hundred atoms. In [103] it has been shown that simulations of liquid SiO_2 with the BKS potential with only 99 atoms show all characteristic features of glassy dynamics. However, the dynamics of this small system is significantly slower compared to a system size of 1002 atoms. In [104], simulations of SiO_2 are presented for system sizes of 336, 1002, 3006 and 8016 atoms. Also in this case, finite size effects are visible in the dynamical

properties in the system. However, no dependence of the structural quantities on the system size is found. In this subsection, system sizes of 114, 165, 216 and 1152 are studied at a system density of $\rho = 2.37\,\mathrm{g/cm^3}$, using the modified BKS potential, according to equation (4.3). In all cases the Ewald accuracy is chosen as 10^{-5}. This leads to the following parameters: $r_c^{ew} = 5.5\,\text{Å}$, $g_{ew} = 0.559443$, $|\mathbf{k}| \leq 7 \cdot 2\pi/L_{Box}$ and $L_{Box} = 11.6954\,\text{Å}$ (114 atoms), $r_c^{ew} = 6.5\,\text{Å}$, $g_{ew} = 0.473375$, $|\mathbf{k}| \leq 6 \cdot 2\pi/L_{Box}$ and $L_{Box} = 13.22944\,\text{Å}$ (165 atoms), $r_c^{ew} = 7\,\text{Å}$, $g_{ew} = 0.439563$, $|\mathbf{k}| \leq 6 \cdot 2\pi/L_{Box}$ and $L_{Box} = 14.4721\,\text{Å}$ (216 atoms) and $r_c^{ew} = 10\,\text{Å}$, $g_{ew} = 0.307694$, $|\mathbf{k}| \leq 8 \cdot 2\pi/L_{Box}$ and $L_{Box} = 25.2851\,\text{Å}$ (1152 atoms). In the case of 114 and 216 atoms, five independent cooling runs are carried out. In the case of 165 atoms, 10 independent runs are conducted and for the 1152 atoms one cooling run is carried out. The cutoff of the short-range part of the Coulomb interaction can be increased within the minimum-image convention as the box length increases with increasing number of atoms which results in a better balancing of the pair time and k-space time.

temperature	# time steps	simulation time	δt
4300 K	$5 \cdot 10^6$ ts	3 ns	0.6 fs
4000 K	$2 \cdot 10^6$ ts	1.2 ns	0.6 fs
3800 K	$2 \cdot 10^6$ ts	1.6 ns	0.8 fs
3600 K	$4 \cdot 10^6$ ts	4 ns	1.0 fs
3400 K	$8 \cdot 10^6$ ts	9.6 ns	1.2 fs
3200 K	$1.5 \cdot 10^7$ ts	24 ns	1.6 fs
3100 K	$2 \cdot 10^7$ ts	32 ns	1.6 fs
3000 K	$3 \cdot 10^7$ ts	48 ns	1.6 fs
2900 K	$6 \cdot 10^7$ ts	96 ns	1.6 fs
2800 K	$1 \cdot 10^8$ ts	160 ns	1.6 fs
2700 K	$1.5 \cdot 10^8$ ts	240 ns	1.6 fs

TABLE 4.8: Cooling procedure of liquid SiO_2 with number of time steps and equilibration times at each temperature.

All systems are first randomly initialized and then pre-relaxed with Lennard-Jones potentials, as explained in subsection 4.1.1. Subsequently, the systems are equilibrated in NVT runs at 4300 K and then cooled down in different steps to 2700 K. In each case, a chain of 3 Nosé-Hoover thermostats (see subsection 3.1.2) is chosen with a damping parameter of 100 ts. The equilibration times are tabulated in Table 4.8. At each temperature, microcanonical production runs are carried out at the mean total energy of the preceding equilibration run, following the procedure described in subsection 4.1.1.

The comparison of the structural and dynamic properties of the different system sizes is demonstrated at a temperature of 3200 K. At this temperature the systems already show a pronounced two-step relaxation with α- and β-relaxation times separated by about four orders of magnitude. In all cases, the depicted curves represent the averaged data over all independent runs.

In Figs. 4.9 and 4.10, the partial static structure factors (see equation (3.89)) and the partial pair correlation functions (see equation (3.86)) are shown for the Si-Si correlation. The curves of the

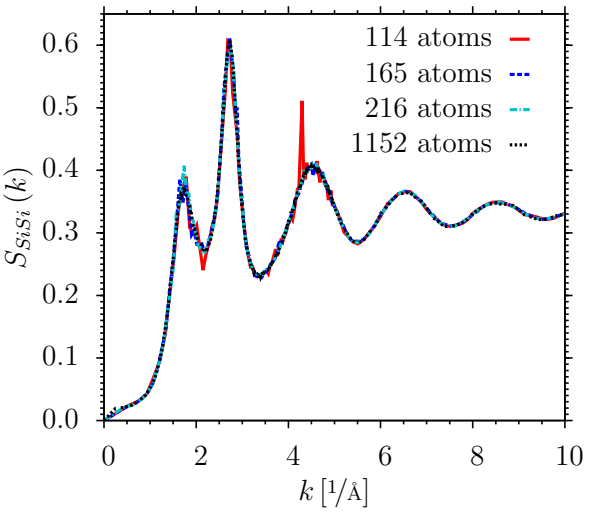

FIGURE 4.9: Partial static structure factors $S_{SiSi}(k)$ for different system sizes at 3200 K

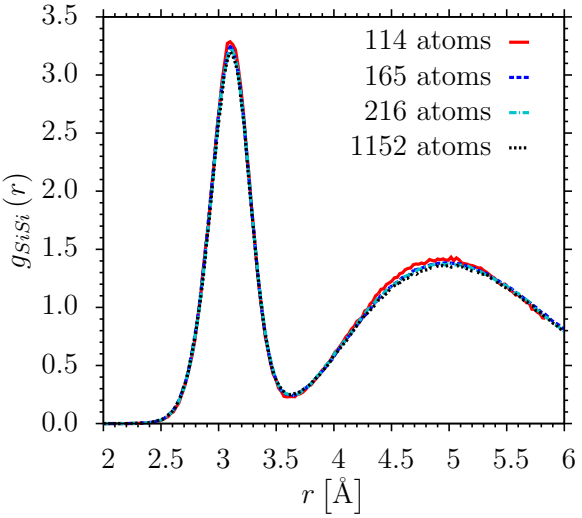

FIGURE 4.10: Partial pair correlation functions $g_{SiSi}(k)$ for different system sizes at 3200 K

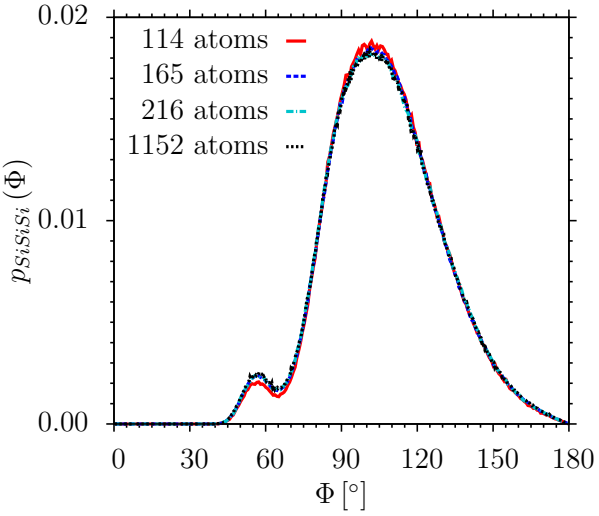

FIGURE 4.11: Angular distributions $p_{SiSiSi}(\Phi)$ for different system sizes at 3200 K

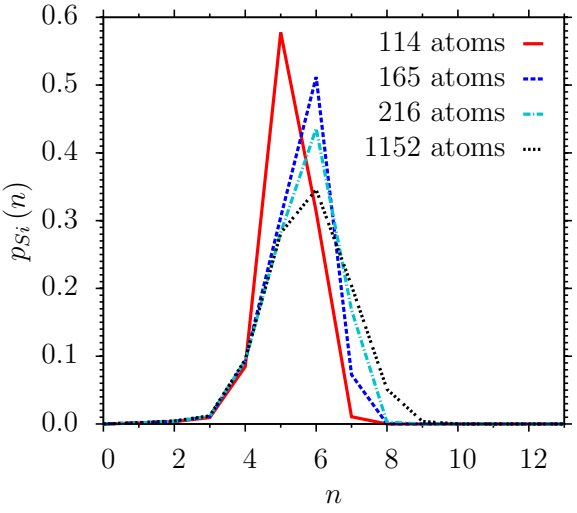

FIGURE 4.12: Probability of an Si atom being member of a ring of size n, $p_{Si}(n)$, for different system sizes at 3200 K

different system sizes are in quite good agreement with each other. However, little discrepancies between the different system sizes can be observed, which are most pronounced for the Si-Si correlation. The accordance of the different curves of the Si-O and O-O correlation is better. In general, the discrepancies between the different system sizes are most pronounced for the second peaks of the corresponding pair correlation functions, representing the next-nearest neighbors. In all cases, the deviations are largest for the smallest system size of 114 atoms. Regarding the partial static structure factors, $S_{SiSi}(k)$ and to some extend $S_{OO}(k)$ show an additional extra-peak at about $k = 4.298\,\text{Å}^{-1} = 8 \cdot 2\pi/L_{\text{Box}}$ for the 114 atom system. This is clearly a finite size effect, as the extra-peak vanishes for larger system sizes. It is connected to the intermittency of the periodic images of the simulation box. In Figs. 4.11 and 4.12, the angular distributions $p_{SiSiSi}(\Phi)$ (see equation (3.96)) between three neighboring Si atoms and the probability of

an Si atom being member of a ring of size n, $p_{Si}(n)$, is shown (see section 3.3). Regarding $p_{SiSiSi}(\Phi)$, slight discrepancies between the different system sizes are visible. All other angular distributions show nearly negligible differences, which are in all cases most pronounced for the 114 atom system. The distribution of ring sizes displays the largest variation of static properties between systems of different size. In particular, the probability of an Si atom to be in a ring of size $n > 6$ decreases with decreasing system size. This truncation of $p_{Si}(n)$ for large n is clearly a finite size effect. In addition, the 114 atom system shows the peculiarity that the maximum of $p_{Si}(n)$ is shifted from $n = 6$ to $n = 5$ and the probability of a Si atom being in a ring of size $n = 4$ is significantly decreased with respect to the other system sizes.

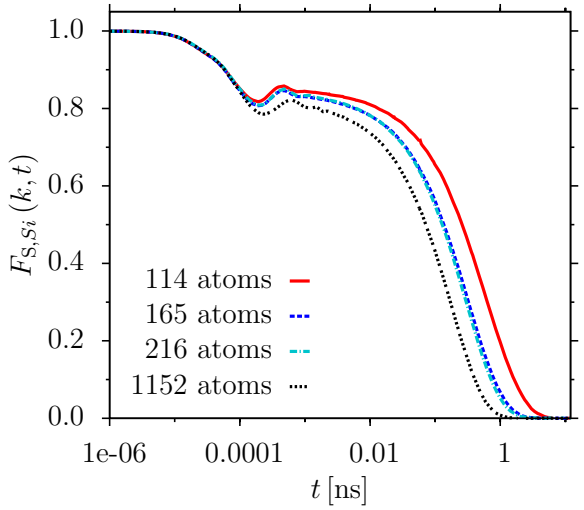

FIGURE 4.13: Incoherent intermediate scattering functions $F_{S,Si}(k,t)$ for different system sizes at 3200 K, $k = 1.74\,\text{Å}^{-1}$ to $k = 1.78\text{Å}^{-1}$.

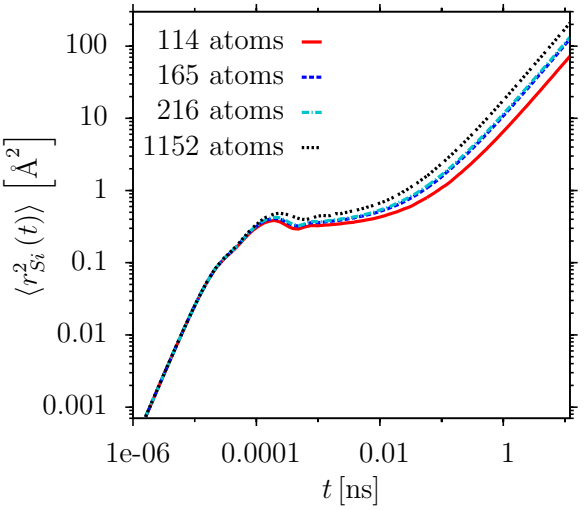

FIGURE 4.14: Mean square displacements $\langle r_{Si}^2(t)\rangle$ for different system sizes at 3200 K.

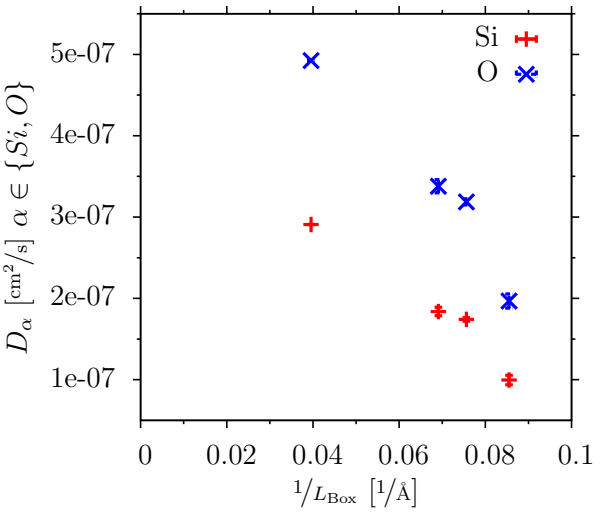

FIGURE 4.15: Dependence of Diffusion constant for Si and O on system size at 3200 K.

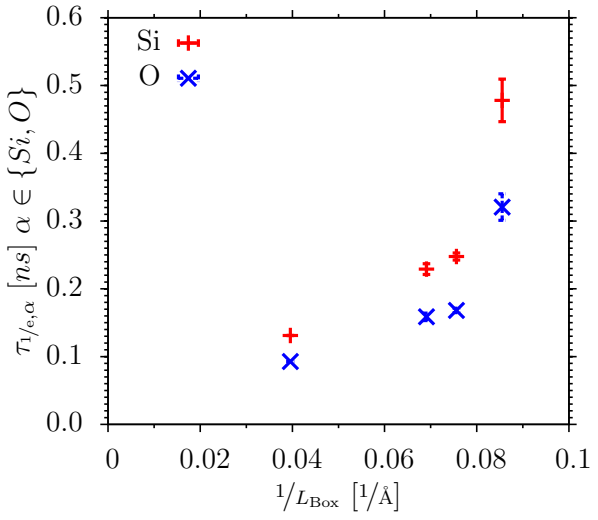

FIGURE 4.16: Dependence of $1/e$ relaxation time $\tau_{1/e,\alpha}$ of $F_{S,\alpha}(k,t)$ on system size at 3200 K.

Next, the dynamical properties are compared. In Figs. 4.13 and 4.14, the incoherent intermediate scattering functions $F_{\mathrm{S},Si}(k,t)$ (see equation (3.100)) and the mean square displacements $\left\langle r_{Si}^2(t)\right\rangle$ (see equation (3.98)) are shown. The incoherent intermediate scattering functions are evaluated at $k = 1.78\,\text{Å}^{-1}$ (114 and 165 atoms) and $k = 1.74\,\text{Å}^{-1}$ (216 and 1152 atoms). This is about the k-value of the so-called first sharp diffraction peak (FSDP) visible in all partial static structure factors. It can be seen that the curves of the different system sizes show the same qualitative characteristics of a two-step decay with an intermediate plateau. However, the α-relaxation times and the plateau heights of the normalized incoherent intermediate scattering functions decrease with increasing system size. The same feature is visible in the mean square displacements, whereas the plateau heights increase with increasing system size. In Fig. 4.15, the self-diffusion constants D_α, $\alpha \in \{Si, O\}$, are displayed with respect to the inverse box length $1/L_{\mathrm{Box}}$, to further illustrate the dependence of the dynamical properties on the system size. They are determined by means of the slope of a linear fit to the corresponding mean square displacements at large simulation times, where the Einstein relation $D_\alpha = \lim_{t\to\infty} \frac{\left\langle r_\alpha^2(t)\right\rangle}{6t}$ [15] holds (see equation (3.99)). In Fig. 4.16, the $1/e$ relaxation times are displayed, meaning the times $\tau_{1/e,\alpha}$ at which the incoherent intermediate scattering functions $F_{\mathrm{S},\alpha}(k,t)$ have decayed to the numerical value of $1/e$. The shown statistical errors are computed as the standard deviation of the mean, with respect to the independent runs, $\overline{\sigma} = \frac{\sigma}{\sqrt{N}}$. It can be seen that the diffusion constants of the 114 atom system are about 2.5 times (O) and 3 times (Si) as large as the ones of the 1152 atom system. This is in agreement with the $1/e$ relaxation times being about 3.5 (O) to 4 (Si) times as large in case of the 114 atom system compared to the 1152 atom system. In all cases, the differences between the 165 and the 216 atom system are the smallest. The slowing down of the dynamics with decreasing system size is clearly a finite size effect [103, 104].

Summarizing, the structural properties show only a small dependence on the system size. The most pronounced differences between the different system sizes are visible in the distribution of ring sizes, which show a decrease of the number of rings containing more than 6 Si atoms with decreasing system size. In contrast to all other considered system sizes, the maximum of $p_{Si}(n)$ is shifted from $n = 5$ to $n = 6$ for the 114 atom system. This feature is reflected in the other structural quantities, where the 114 atom system also shows the largest finite-size effects. The dynamical properties show a greater dependence on the system size. However, all system sizes show the generic features of glassy dynamics like the two-step decay process with the separation of time scales. Having this in mind, this subsection motivates and justifies the choice of a 165 atom system for further considerations.

4.1.3 Liquid properties at different temperatures

This subsection provides an overview over the structural and dynamical properties of liquid SiO_2 at different temperatures, comparing the BKS [22] with the CHIK [43] potential. Here, simulations are carried out for 165 atom systems at the experimental glass density of $\rho = 2.2\,\mathrm{g/cm^3}$ [98]. For all simulations the modified form of the Buckingham potential (4.3) is used, as explained in subsection 4.1.1. This leads to the following parameters: $r_{\mathrm{c}}^{\mathrm{ew}} = 5.5\,\text{Å}$, $g_{\mathrm{ew}} = 0.473375$,

$|\mathbf{k}| \leq 7 \cdot {}^{2\pi}/_{L_{\text{Box}}}$ and $L_{\text{Box}} = 13.5618\,\text{Å}$. As mentioned in the beginning of this chapter, the BKS potential has the property that the mean density is slightly larger than $2.2\,{}^{\text{g}}/_{\text{cm}^3}$ for temperatures lower than 6000 K [20]. However, the simulations of the 165 atom systems at $\rho = 2.2\,{}^{\text{g}}/_{\text{cm}^3}$ show only a small mean negative pressure of about $-0.5\,GPa$ at the maximum with no noticeable negative effects. The simulations with the CHIK potential show a positive pressure over the whole temperature range.

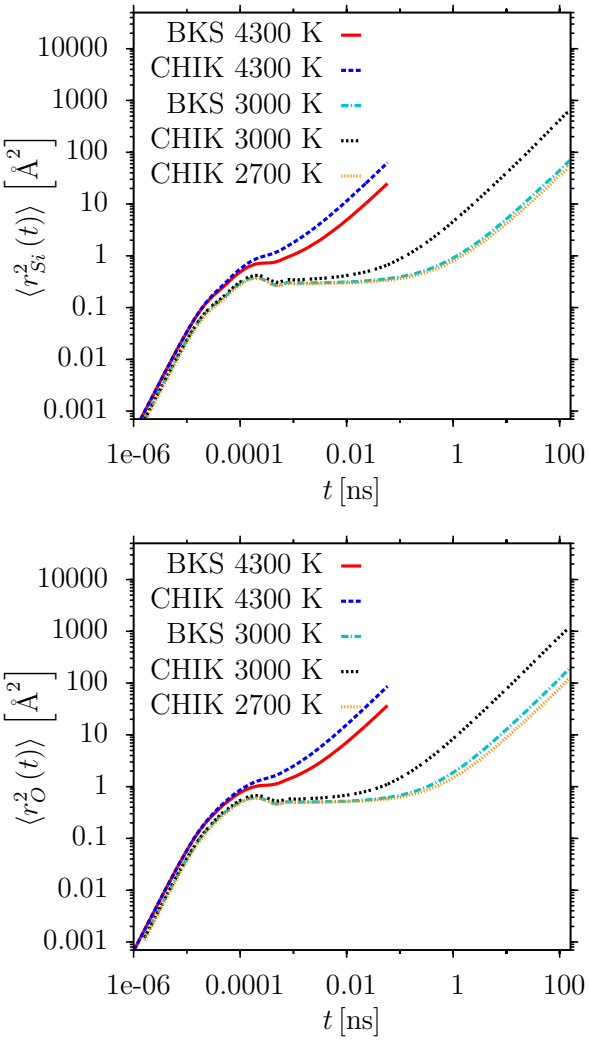

FIGURE 4.17: Mean square displacements $\langle r^2_\alpha(t)\rangle$, $\alpha \in \{Si, O\}$, comparison of BKS and CHIK potential

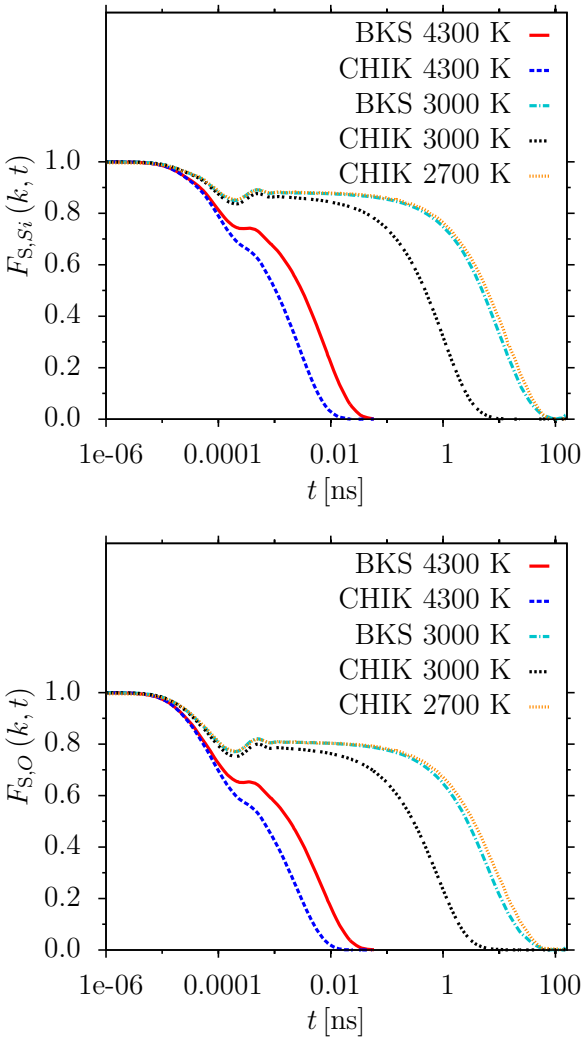

FIGURE 4.18: Incoherent intermediate scattering functions $F_{S,\alpha}(k,t)$, $\alpha \in \{Si, O\}$, comparison of BKS and CHIK potential

The systems are initialized as explained in section 4.1 and then subsequently cooled from 4300 K to 2700 K, as given in Table 4.8. Again, the properties are analyzed in a microcanonical production run at the mean total energy of the preceding equilibration run at the same temperature.

In Figs. 4.17 and 4.18, the mean square displacements $\langle r^2_\alpha(t)\rangle$ and the incoherent intermediate scattering functions $F_{S,\alpha}(k,t)$ are compared for both potentials at different temperatures. The incoherent intermediate scattering functions are evaluated at $k = 1.60\,\text{Å}^{-1}$. Again, this is about the k-value of the first sharp diffraction peak (FSDP) visible in all partial static structure

factors. As already described before, the curves show the characteristic two-step process with an intermediate plateau. The longest time scales considered in the production run are 160 ns. It can be seen that the α-relaxation times of the BKS potential are longer by about the factor $3-10$ at the same temperature. So, for example the α-relaxation time at 2700 K for the CHIK potential is of the order of the relaxation time at 3000 K for the BKS potential. Actually, the lowest temperature at which the system still can be relaxed within the simulation time of 160 ns is 3000 K in case of the BKS potential. Therefore, in the following, only temperatures down to 3000 K are considered.

In Fig. 4.19. the partial pair correlation functions are compared at 4300 K and 3000 K. As expected, the peak heights increase with decreasing temperature. This indicates a higher degree of structuring in the liquid. In all cases, the peak heights of the CHIK potential are slightly reduced compared to the corresponding peaks of the BKS potential, as already explained in [43]. Also, the average first neighbor distances in all cases are slightly larger by about 0.02 Å to 0.03 Å for the CHIK parameters.

In Fig. 4.20, the partial static structure factors are compared at 4300 K and 3000 K. Again, the height of the peaks increases with decreasing temperature and peaks are slightly less pronounced in case of the CHIK potential. As before, the peak positions are nearly identical for the two different potentials. The most dominant peaks of $S_{\alpha\beta}(k)$ are located at about $k = 2.7\,\text{Å}^{-1}$, corresponding to a length scale of $2\pi/2.7\text{Å} \simeq 2.3\,\text{Å}$ for the Si-Si and the Si-O correlation and at approximately $k = 2.8\,\text{Å}^{-1}$, corresponding to a length scale of $2\pi/2.8\text{Å} \simeq 2.2\,\text{Å}$ for the O-O correlation. These length scales are of the order of the first minimum of $g_{SiO}(r)$, in agreement with [42]. The reason for the occurrence of the first sharp diffraction peak (FSDP) at approximately $1.6\,\text{Å}^{-1}$, corresponding to a length scale of $2\pi/1.6\text{Å} \simeq 3.9\,\text{Å}$, in all correlations, is the ordering of the ions in a tetrahedral-like structure [42] with a distance of about 3.9 Å between neighboring tetrahedra.

In Fig. 4.21, the angular distributions are shown for the Si-Si-Si and the Si-O-Si correlation at 4300 K and 3000 K. In general, the angular distributions get narrower with decreasing temperature, as expected. They are also slightly more pronounced for the CHIK potential, which corresponds to the slightly higher peaks of the partial pair correlation functions at the same temperature. Regarding $p_{SiSiSi}(\Phi)$, for both potentials the average angle increases from about 105° at 4300 K to 108° at 3000 K. Also, in both cases, there is an additional peak visible at about 56° that nearly vanishes at 3000 K. The main peak is connected to rings of size $n = 6$, which in all cases is the dominant ring size and the extra peak is connected to defect structures, like 3- and 4-membered rings. The mean Si-O-Si angle increases from about 139° (4300 K) to about 146° (3000 K) for the CHIK potential and from about 142° (4300 K) to about 148° (3000 K) for the BKS potential. In addition to the main peak, a shoulder at about 90° is visible for both potentials which vanishes for lower temperatures. It is connected to the emergence of edge-sharing tetrahedra [43]. The mean O-Si-O angle in all cases is about 109°, which is in nearly perfect agreement with the theoretical value of 109.5° for a tetrahedral structure.

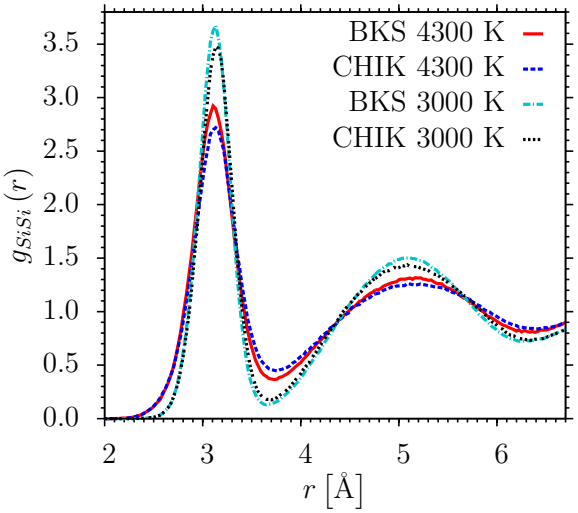

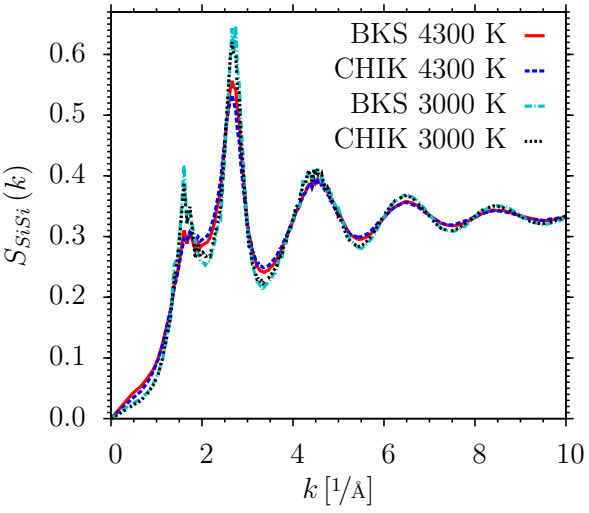

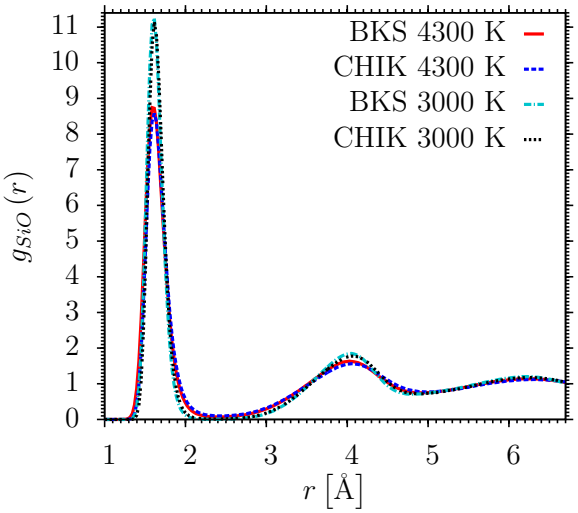

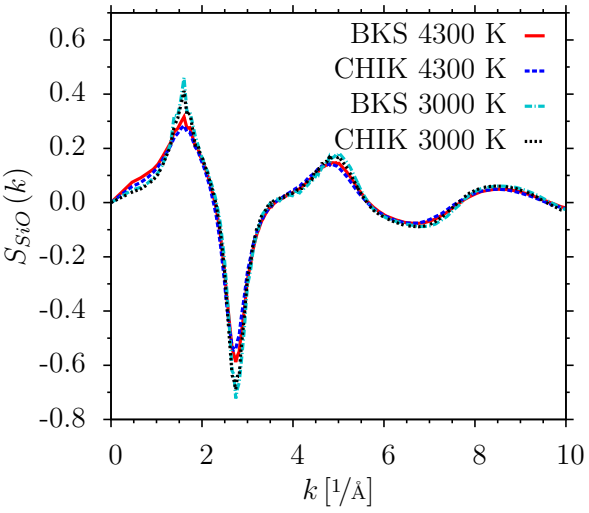

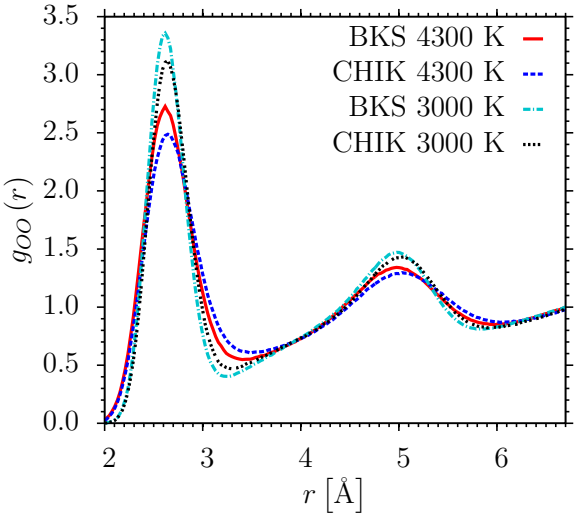

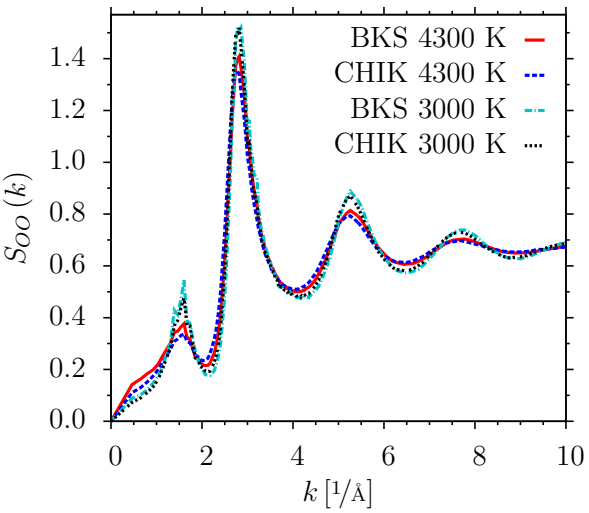

FIGURE 4.19: $g_{\alpha\beta}(r)$, $\alpha, \beta \in \{Si, O\}$, comparison of BKS and CHIK potential

FIGURE 4.20: $S_{\alpha\beta}(k)$, $\alpha, \beta \in \{Si, O\}$, comparison of BKS and CHIK potential

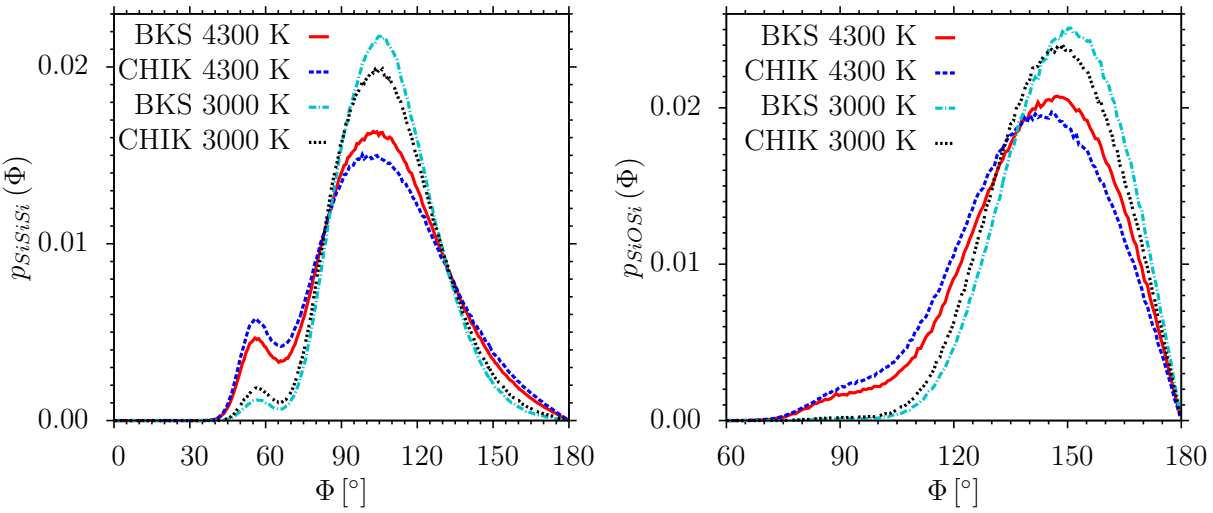

FIGURE 4.21: Angular distributions $p_{\alpha\beta\gamma}(\Phi)$, $\alpha, \beta, \gamma \in \{Si, O\}$, comparison of BKS and CHIK potential.

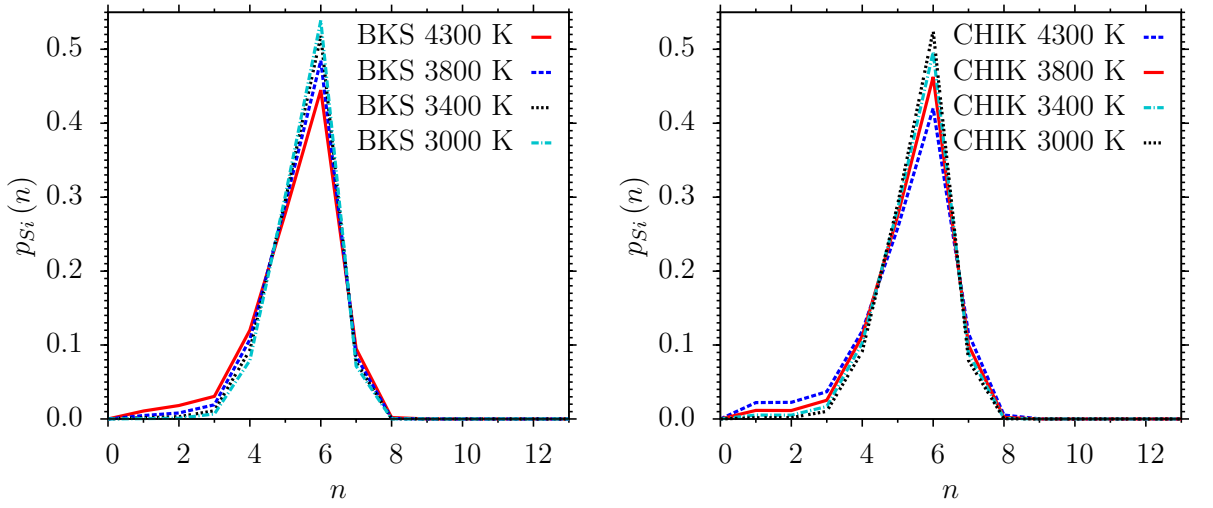

FIGURE 4.22: Probability that a Si atom is member of a ring of size n, $p_{Si}(n)$, at different temperatures, comparison of BKS and CHIK potential

In Fig. 4.22, the probability of a Si atom being member of a ring of size n, $p_{Si}(n)$, is shown for both potentials in the temperature range from 4300 K to 3000 K. Both potentials show a similar behavior. The most dominant ring size in all cases is $n = 6$. This can be understood by the fact that the equilibrium crystalline phase at zero pressure is β-cristobalite, which consists of 6-membered rings [38], as already mentioned in section 2.2. With decreasing temperature, the probability $p_{Si}(n = 6)$ to find 6-membered rings increases and the probabilities $p_{Si}(n)$ decrease for $n \neq 6$, both, for the BKS and the CHIK potential. As mentioned above, the decrease of the number of small rings corresponds to the vanishing of the small extra peak in $p_{SiSiSi}(\Phi)$. The ring statistics of the BKS and the CHIK potential are pretty similar. At each temperature, the number of Si atoms located in 6-membered rings of the BKS potential is slightly higher.

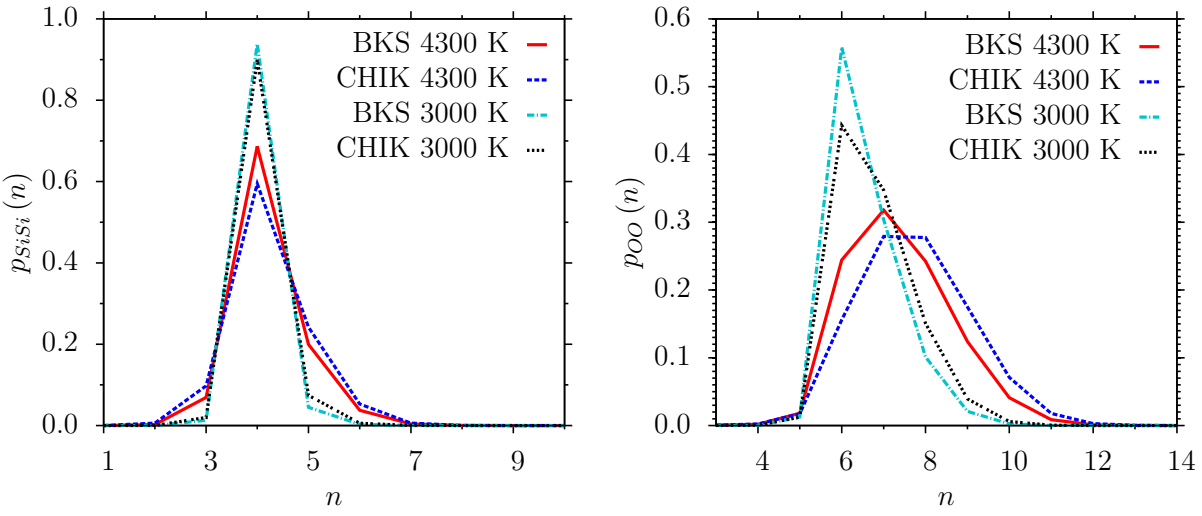

FIGURE 4.23: Distribution of coordination numbers $p_{\alpha\beta}(n)$, $\alpha, \beta \in \{Si, O\}$ at different temperatures, comparison of BKS and CHIK potential

In Fig. 4.23, the distribution of coordination numbers are shown for the Si-Si and the O-O correlation at 4300 K and 3000 K for both potentials. In all cases, the probability of the Si atoms $p_{\alpha\beta}(n)$, $\alpha, \beta \in \{Si, O\}$, to have a partial coordination of $n = 4$ with respect to neighboring oxygen, as well as silicon atoms, increases with decreasing temperature. At 3000 K, about 94% of the Si atoms are coordinated fourfold with respect to the next nearest Si atoms, in case of the BKS potential. This holds for approximately 90% of the Si atoms, in case of the CHIK potential. At the same temperature, nearly 100% of the Si atoms are coordinated fourfold with respect to neighboring O atoms for both potentials. Correspondingly, nearly 100% of the oxygen atoms are coordinated twofold with respect to neighboring silicon atoms for both potentials. Regarding the coordination of the oxygen atoms, at 4300 K the predominant coordination number with respect to neighboring oxygen atoms is 7 in case of the BKS potential, whereas the probability for 7- and 8-fold coordinated oxygen atoms is nearly identical in case of the CHIK potential. At 3000 K about 56% of the oxygen atoms have 6 oxygen neighbors in case of the BKS potential, whereas the probability is only about 44% in case of the CHIK potential.

In Fig. 4.24, the self-diffusion constants D_α, $\alpha \in \{Si, O\}$ are plotted on a logarithmic scale against the inverse temperatures $1/T$. As in subsection 4.1.3, they are determined by means of the slope of a linear fit to the corresponding mean square displacements, shown in Fig. 4.17 at large simulation times, where the Einstein relation $D_\alpha = \lim_{t\to\infty} \frac{\langle r_\alpha^2(t)\rangle}{6t}$ [15] holds (see equation (3.99)). Here, the whole examined temperature range from 4300 K to 2700 K is shown. The shown statistical errors are computed as the standard deviation of the mean with respect to the 10 independent runs, $\overline{\sigma} = \frac{\sigma}{\sqrt{N}}$. As expected, D_α decreases by about four orders of magnitude from the highest to the lowest temperature for the CHIK, as well as for the BKS potential. At a given temperature, the self-diffusion constants of the CHIK potential are about $3 - 10$ times larger than the appropriate values of the BKS potential, in agreement with the behavior of the α-relaxation times.

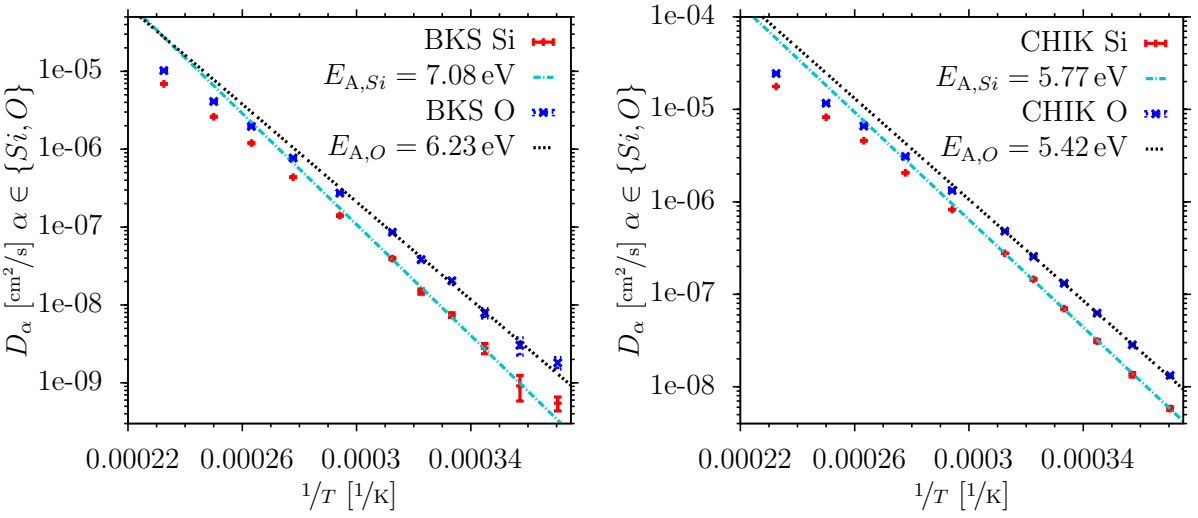

FIGURE 4.24: Arrhenius plot of self diffusion constants for Si and O at different temperatures, comparison of BKS and CHIK potential

The activation energies are extracted by means of an Arrhenius fit [105]

$$D_\alpha = A_\alpha \exp\left[-E_{A,\alpha}/k_B T\right] \; \alpha \in \{Si, O\} \tag{4.4}$$

at temperatures $\leq 3200\,K$. In this temperature range, the self-diffusion constants can be well described by an Arrhenius law (4.4). In case of the BKS potential, the lowest temperature of 2700 K is not included into the fit, as D_α, $\alpha \in \{Si, O\}$ is significantly larger than expected, according to equation (4.4). This can be explained by the fact that, at 2700 K the equilibration time of 240 ns (Table 4.8) is too short for the equilibration of the system. In all cases, the given errors are the asymptotic standard errors of the least-squares fit with gnuplot [101, 106].

The extracted activation energies for the BKS potential are: $E_{A,Si} \simeq 7.08 \pm 0.30\,eV$ and $E_{A,O} \simeq 6.23 \pm 0.24\,eV$. They show significant differences to values reported in previous simulations, namely $E_{A,Si} = 5.18\,eV$ and $E_{A,O} = 4.66\,eV$ for simulations of 8016 atoms at a system density of $\rho = 2.37\,g/cm^3$ [42] and $E_{A,O} = 4.84\,eV$ for simulations of 99 atoms at $\rho = 2.30\,g/cm^3$ [107, 108]. These differences can be understood in terms of effects of the system size and the system density, as the activation energies increase with decreasing system size and decreasing system density. To illustrate these effects, the respective low-temperature activation energies of the 114, 165, 216 and 1152 atom simulations at $\rho = 2.37\,g/cm^3$ (see subsection 4.1.2) are extracted in exactly the same way, leading to: $E_{A,Si} \simeq 6.29 \pm 0.44\,eV$ and $E_{A,O} \simeq 5.82 \pm 0.28\,eV$ (114 atoms), $E_{A,Si} \simeq 5.81 \pm 0.13\,eV$ and $E_{A,O} \simeq 5.21 \pm 0.09\,eV$ (165 atoms), $E_{A,Si} \simeq 5.99 \pm 0.14\,eV$ and $E_{A,O} \simeq 5.36 \pm 0.11\,eV$ (216 atoms) and $E_{A,Si} \simeq 5.34 \pm 0.09\,eV$ and $E_{A,O} \simeq 4.77 \pm 0.11\,eV$ (1152 atoms). In particular, the activation energies of the 1152 atom simulations are in reasonable agreement with the values reported for the 8016 atom system at the same density [42].

In case of the CHIK potential, the extracted activation energies are $E_{A,Si} \simeq 5.77 \pm 0.03\,eV$ and $E_{A,O} \simeq 5.42 \pm 0.03\,eV$ for the 165 atom system at $\rho = 2.2\,g/cm^3$. Again, they show differences to values reported in previous simulations, namely $E_{A,Si} = 4.9712\,eV$ and $E_{A,O} = 4.5109\,eV$ [43].

In this case, the differences can be explained in terms of system size effects as the simulations, reported in [43], have been carried out at the same system density. Experimental values are $E_{A,Si} = 6.0\,\text{eV}$ for the diffusion of ^{30}Si in amorphous silicon [109] and $E_{A,O} = 4.7\,\text{eV}$ for diffusion of ^{16}O and ^{18}O in a thin-film structure of vitreous SiO_2 [110].

In this subsection, structural and dynamical properties of liquid SiO_2 have been compared at different temperatures for the BKS and the CHIK potential at a small system size of 165 atoms. Here, finite size effects are apparent, especially in the dynamics of the systems. To compare the properties of the BKS and the CHIK potential without the strong influence of finite size effects, simulations at larger system sizes are necessary. This has already been done in [43]. However, the purpose of this section is to demonstrate that the structural differences, according to the different potentials, are in rather good agreement with results obtained by simulations of larger system sizes. Again, this justifies the employment of small system sizes.

4.2 Glass Structure

In the previous section, the model glass former SiO_2 has been examined in the liquid state. Here, the structural properties in the glassy state are described. In this section, only system sizes of 165 atoms at the experimental glass density of $\rho = 2.2\,\text{g/cm}^3$ [98] are considered. As explained in subsection 4.1.2, this is a reasonable system size in terms of balancing between the influence of finite size effects and computational feasibility for quantum mechanical DFT calculations. As already mentioned in section 2.4, the glass structures are generated in the following way: After a random initialization (see section 4.1), the systems are equilibrated at 4300 K for 1.6 ns with a time step of 1.6 fs and then linearly cooled down to 300 K at a cooling rate of $\Gamma = 1 \cdot 10^{11}\,\text{K/s}$. After annealing at 300 K for 1.6 ns, the configurations are quenched down to 0 K. Following this cooling scheme, 10 independent runs with the BKS potential and 10 independent runs with the CHIK potential are carried out. During the cooling procedure, the systems fall out of equilibrium at the temperature, where the relaxation time is of the order of the time scale of the cooling process, which is at about 3000 K, in case of the BKS potential, and at approximately 2700 K, in case of the CHIK potential. After the quench to 0 K, in each case, the configurations are structurally relaxed by means of a quantum mechanical DFT calculation. In the last part of this section, the structural properties of these configurations are compared to one the glass structure generated by a full ab initio quench from the melt and to experimental results.

As already mentioned in subsection 3.2.3, in this work, all DFT calculations are carried out using the Vienna Ab initio Simulation Package (VASP) [77–79]. In the following, all references to electronic states or energies are with respect to the "fictive" electrons in the Kohn-Sham system, as explained in subsection 3.2.3. The different types of exchange-correlation functionals and the use of pseudopotentials have been explained in detail in subsections 3.2.4 and 3.2.5. For all DFT calculations of this work, a Perdew-Burke-Ernzerhof (PBE) type exchange-correlation functional of the generalized gradient approximation (GGA), revised for solids (PBEsol) [84], is chosen. Computations are conducted using a plane wave basis set and the projector augmented-wave

method (PAW) [86, 87]. A Gaussian smearing method is applied for the partial occupancies of the energy levels of the electronic states around the Fermi-level with a smearing width of $\sigma = 0.02\,\text{eV}$. Due to the large simulation box, only Gamma-point calculations are conducted with one k-point at the zone center of the Brillouin zone ($\mathbf{k} = (0,0,0)^T$). Also, the projection operators of the PAW wave functions are evaluated in real space (see subsection 3.2.5).

A set of single point calculations at 0 K is performed, based on the structural configuration of one cooling run with the BKS potential. In this test calculations, the convergence of the total energy at zero temperature E_0 and the diagonal elements of the external stress tensor $S_{\alpha\alpha} = -S_{\text{int},\alpha\alpha}$, $\alpha \in \{1,2,3\}$ (see equation (3.34)), are examined with respect to the number of k-points, the cutoff energy E_{cut} for the plane wave basis set and the accuracy of the relaxation of the electronic degrees of freedom. The external stress tensor describes the stress imposed on the system, meaning negative values of $S_{\alpha\alpha}$ would cause an expansion of the system. The energy E_0 consists of all electronic contributions, the Coulomb energy of the interactions between the nuclei and the contributions of the atomic energies according to the PAW potentials (see subsection 3.2.5). It is the ground state energy of the system in the limit of zero smearing width $E_0 = \lim_{\sigma\to 0} E_\sigma$. Tests are done with accurate and normal VASP precision. Accurate precision means that Fourier components up to $2\,G_{\text{cut}}$ instead of $1.5\,G_{\text{cut}}$ are taken into account in the evaluation of charge densities and the action of the Hamiltonian on a wave function, to overcome so-called wrap around errors. Here, G_{cut} is the cutoff wave vector corresponding to E_{cut} of the plane wave basis set (see equation (3.81)). Also, a finer grid spacing is chosen for the evaluation of the real space projection operators.

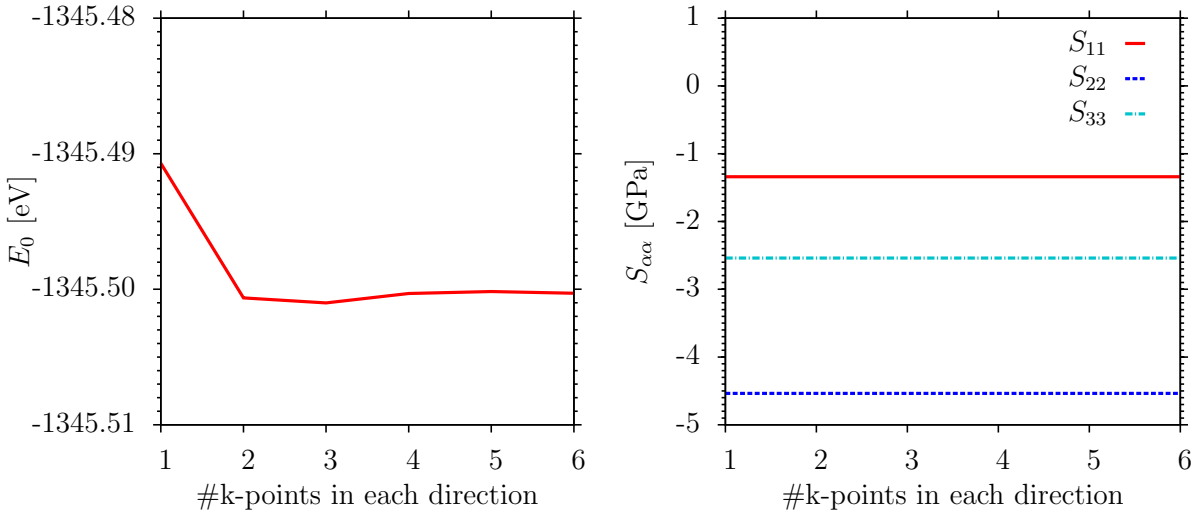

FIGURE 4.25: Dependence of E_0 and $S_{\alpha\alpha}$ on the number of k-points for 165 atom system of SiO_2

First, the influence of k-mesh is examined. Calculations are done with a cutoff energy $E_{\text{cut}} = 500\,\text{eV}$ and the electronic relaxation is stopped when the relative change in total energy between two adjacent steps of the self-consistent field loop is less than 10^{-6}. In Fig. 4.25, the dependence of the ground state energy E_0 and the diagonal elements of the external stress tensor $S_{\alpha\alpha}$ on the number of k-points in each direction of the simulation cell is shown for accurate precision. It

can be seen that the values show nearly no dependence on the number of k-points. This justifies the utilization of Gamma point ($\mathbf{k} = (0,0,0)^T$) calculation for this large system sizes.

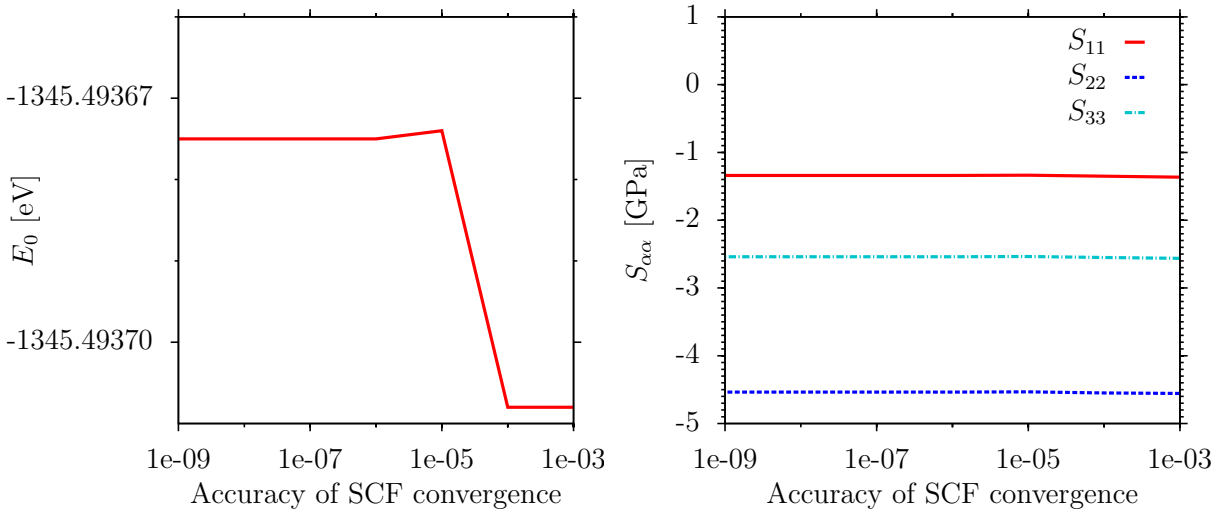

FIGURE 4.26: Dependence of E_0 and $S_{\alpha\alpha}$ on the accuracy of the electronic relaxation for 165 atom system of SiO_2

In Fig. 4.26, the dependence of E_0 and $S_{\alpha\alpha}$, $\alpha \in \{1,2,3\}$, on the accuracy of the electronic relaxation is examined in terms of Gamma point calculations ($\mathbf{k} = (0,0,0)^T$) with fixed $E_{\text{cut}} = 500\,\text{eV}$, again with accurate precision. Both, E_0 and $S_{\alpha\alpha}$ show a slight increase with increasing accuracy of the electronic relaxation with a transition into a plateau at about the value of 10^{-6}. However, the overall dependence of E_0 and $S_{\alpha\alpha}$ on the accuracy is quite small.

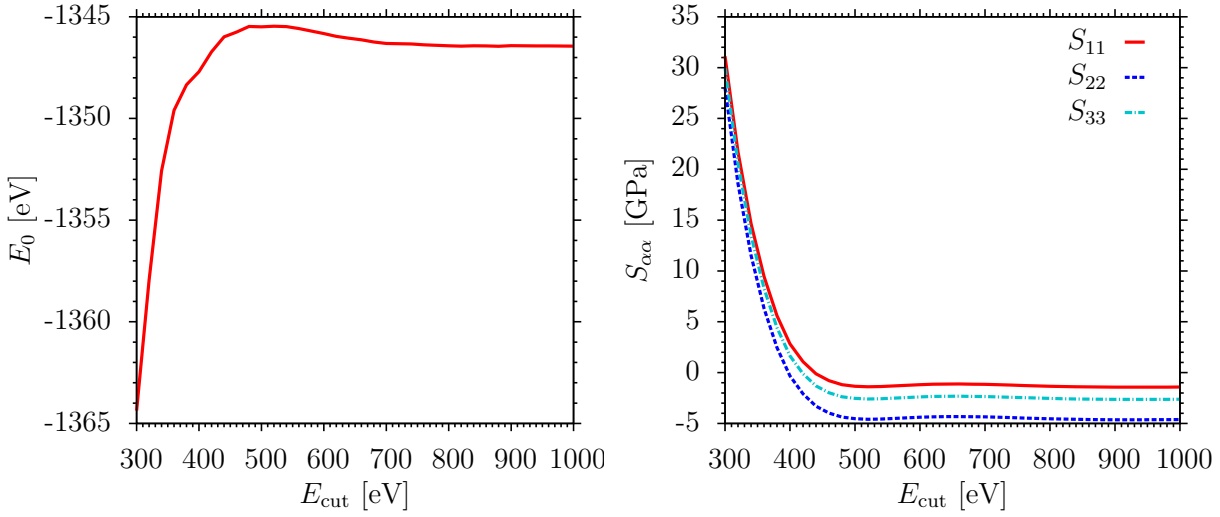

FIGURE 4.27: Dependence of E_0 and $S_{\alpha\alpha}$ on the plane wave cutoff E_{cut} for 165 atom system of SiO_2

In Fig. 4.27, the dependence of E_0 and $S_{\alpha\alpha}$, $\alpha \in \{1,2,3\}$, on the plane-wave cutoff E_{cut} is shown. Again, Gamma point calculations ($\mathbf{k} = (0,0,0)^T$) are conducted with accurate precision and fixed accuracy of 10^{-6} for the electronic relaxation. The total energy E_0 shows an initial increase with increasing E_{cut} with a maximum at about $E_{\text{cut}} = 500\,\text{eV}$, followed by a slight

decrease and the transition into a plateau at about $E_{\text{cut}} = 800\,\text{eV}$. This would motivate the choice of the latter value of E_{cut}. However, such a high cutoff energy leads to significantly longer computation times, as the number of plane waves increases with E_{cut}^2. In contrast to this, the diagonal elements of the external stress tensor $S_{\alpha\alpha}$ show a strong decrease with increasing E_{cut} and a transition into a plateau at about $E_{\text{cut}} = 500\,\text{eV}$. Regarding this behavior, a value of $E_{\text{cut}} = 500\,\text{eV}$ can be justified and this numerical value is used in all DFT calculations of SiO_2. In fact, the absolute value of the total energy of a DFT calculation is rather meaningless. It is important to use the same numerical value in all calculations. The recommended minimal values for the employed PAW potentials [86, 87] are $E_{\text{cut}} = 400\,\text{eV}$ in the case of oxygen and $E_{\text{cut}} = 245\,\text{eV}$ in the case of silicon.

In Figs. 4.25, 4.26 and 4.27, only the curves for accurate VASP precision are shown. However, the curves for normal VASP precision show the same behavior.

As described in the first paragraph of this section, the atomic configurations are structurally relaxed after the classical quench employing a conjugate gradient algorithm [111]. The system volume is fixed and the relaxation is stopped when all forces on the atoms are smaller than $5 \cdot 10^{-4}\,\text{eV/Å}$. Here, accurate VASP precision is applied and the break condition for the electronic relaxation is a relative energy difference of 10^{-8}. The DFT forces are calculated, according to the Hellman-Feynman theorem [112]. In the following, the main structural changes before and after the relaxation are compared for configurations generated with the BKS and the CHIK potential. In each case, the displayed results are averaged over 10 independent runs.

In Fig. 4.28, the pair correlation functions are shown before and after the structural relaxation. In contrast to the observations in the liquid state, no significant differences can be observed between the curves of the BKS and the CHIK potential, both before and after the structural relaxation for all different correlations. In both cases, the main effect of the structural relaxation is the slight decrease of the mean first neighbor Si-Si distance and the slight increase of the mean first neighbor Si-O and O-O distance. In addition, the first neighbor peaks of $g_{SiSi}(r)$ and $g_{SiO}(r)$ are slightly broadened and the first neighbor peak of $g_{OO}(r)$ is slightly narrowed. In comparison to the liquid state, the corresponding peaks are much higher and more pronounced, as expected. However, the peak positions of the first and second-neighbor peaks are rather similar to the positions at 3000 K.

To further illustrate the structural changes, in Fig. 4.29, the angular distributions are shown before and after the relaxation for the Si-Si-Si, the Si-O-Si and the O-Si-O correlations. Regarding the Si-Si-Si correlation, no significant differences can be observed, both, between the BKS and the CHIK potential and before and after the structural relaxation. This indicates that the medium-range structure of the network is not altered in the process of the structural relaxation. Similar to the behavior at 3000 K, $p_{SiSiSi}(\Phi)$ shows a broad peak with a mean angle of about 109° and an additional small extra peak at about 60°. As explained in subsection 4.1.3, this small peak is connected to the amount of small rings. In contrast to $p_{SiSiSi}(\Phi)$, $p_{SiOSi}(\Phi)$ and $p_{OSiO}(\Phi)$ are altered during the structural relaxation. The main effects are the slight decrease of the mean Si-O-Si angle from about 153° to about 147° (BKS potential) and from about 152°

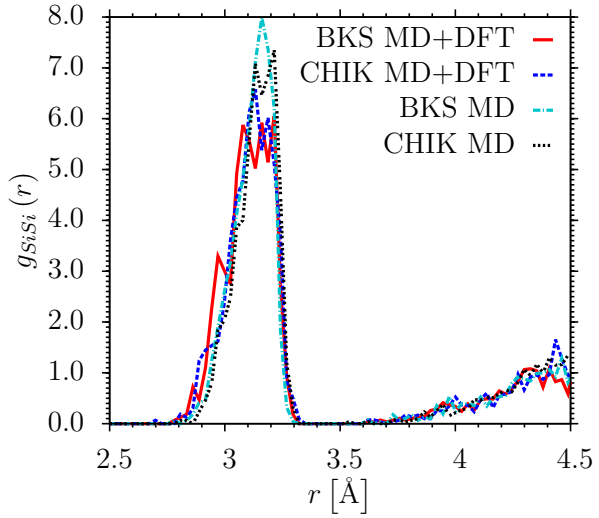

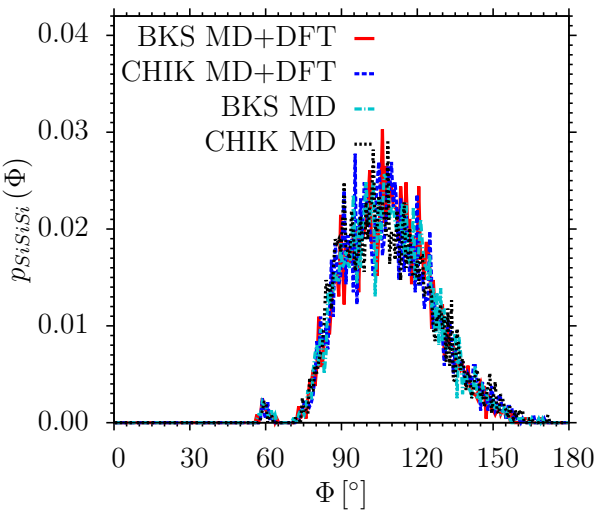

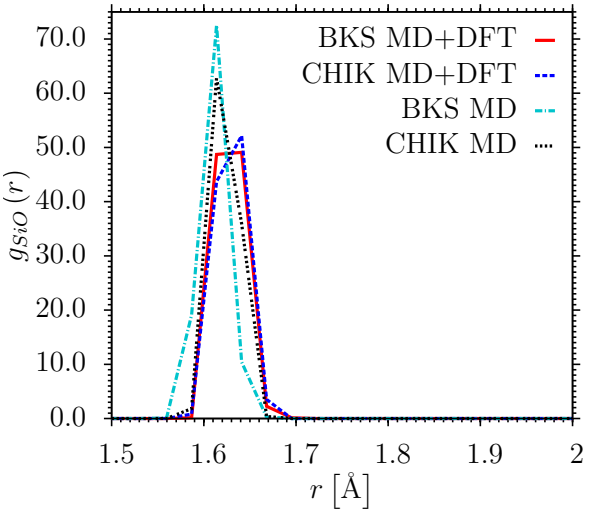

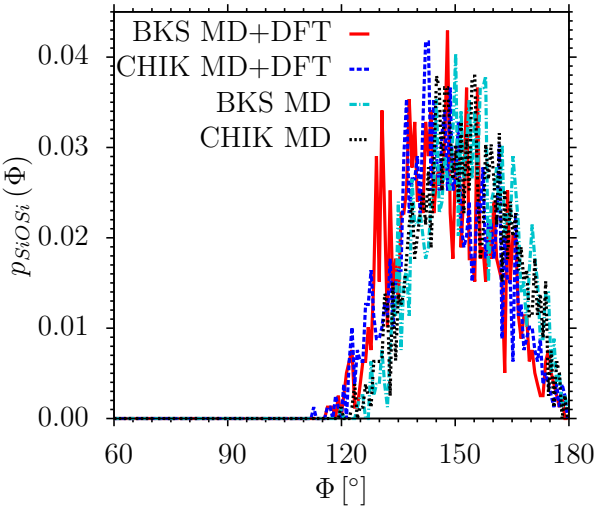

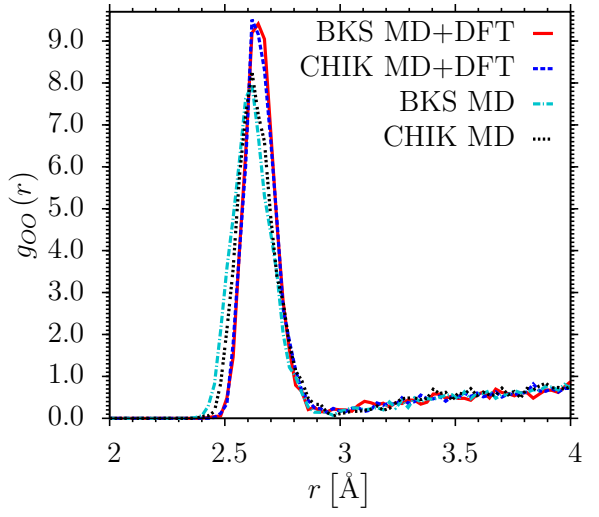

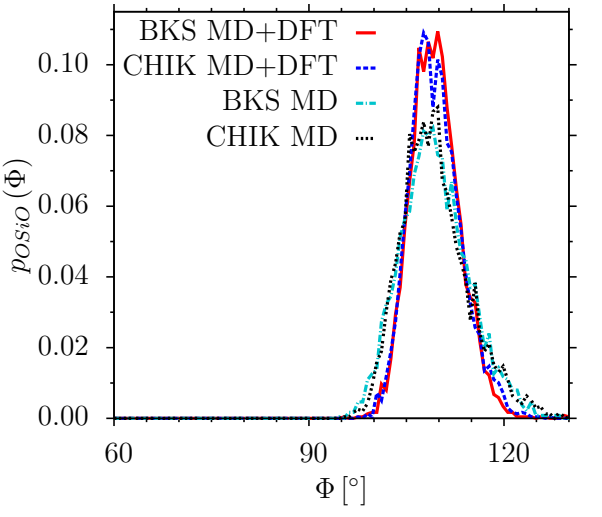

FIGURE 4.28: $g_{\alpha\beta}(r)$, $\alpha, \beta \in \{Si, O\}$ at 0 K, before and after structural relaxation. Comparison of BKS and CHIK potential

FIGURE 4.29: $p_{\alpha\beta\gamma}(\Phi)$, $\alpha, \beta, \gamma \in \{Si, O\}$ at 0 K, before and after structural relaxation. Comparison of BKS and CHIK potential

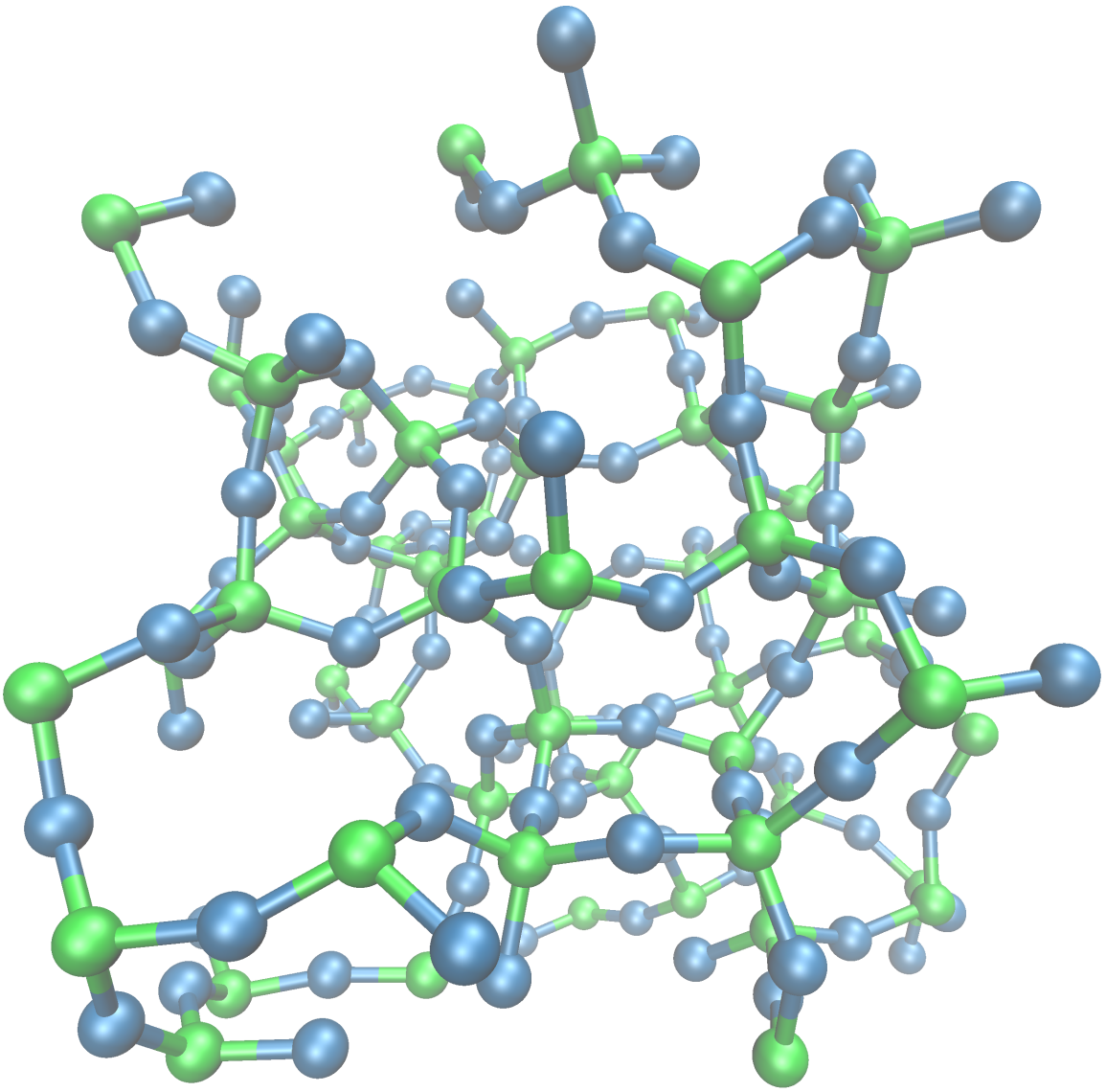

FIGURE 4.30: Snapshot of the glass structure of a 165 atom system SiO_2 after the full ab initio quench and the structural relaxation. Si atoms are displayed green and O atoms are displayed blue.

to about 148° (CHIK potential) and the sharpening of the O-Si-O angular distribution. This is in agreement with [10]. The mean O-Si-O angle, in all cases, perfectly agrees to the theoretical value of 109.5° for a tetrahedral structure. Again, no significant differences are observed in the shape of the distributions between the BKS and the CHIK potential.

In Fig. 4.30, a snapshot of a 165 atom glass structure of SiO_2 is shown after the structural relaxation. Here, the structure of interconnected SiO_4 tetrahedra is clearly visible.

Next, the effect of the structural relaxation on the probability of a Si atom being member of a ring of size n, $p_{Si}(n)$, and the distribution of coordination numbers $p_{\alpha\beta}(n)$, $\alpha, \beta \in \{Si, O\}$ are examined. Regarding $p_{Si}(n)$, the structural relaxation has no effect at all. The probability

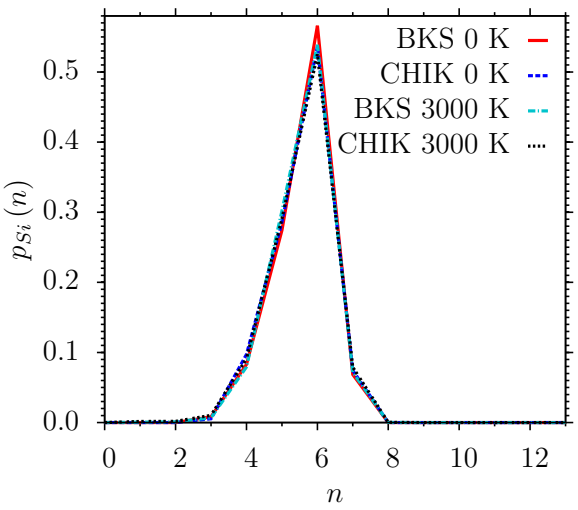

FIGURE 4.31: Probability that a Si atom is member of a ring of size n, $p_{Si}(n)$, at 0 K. Comparison of BKS and CHIK potential and to 3000 K.

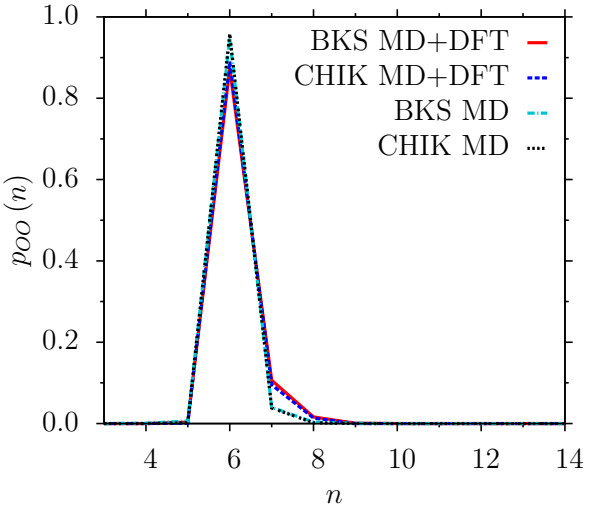

FIGURE 4.32: Distribution of coordination numbers $p_{OO}(n)$ at 0 K before and after structural relaxation. Comparison of BKS and CHIK potential

that a Si atom is member of a ring of size n is exactly the same before and after the structural relaxation for the BKS, as well as for the CHIK potential. In Fig. 4.31, the corresponding curves of the BKS and the CHIK potential are compared to the ones at 3000 K. As already described in subsection 4.1.3, $p_{Si}(n)$ has a maximum at ring sizes of $n = 6$ and the probability $p_{Si}(n)$ is slightly higher for $n = 6$ and lower for $n = 4$ in case of the BKS potential, compared to the CHIK potential. In general, $p_{Si}(n)$ at 0 K shows no significant differences to the distribution at 3000 K. For both potentials, the probability of a Si atom to be in a ring of size $n = 6$ has slightly increased at 0 K, whereas the probability is about the same in the case of $n = 4$. Rings of size $n = 3$ are still apparent in the glass configurations for both potentials with a probability of about $p_{Si}(n = 3) \simeq 0.5\% - 1\%$.

Regarding the distribution of coordination numbers $p_{\alpha\beta}(n)$, $\alpha\beta \in \{Si, O\}$, all Si atoms are 4-fold coordinated with respect to Si atoms and O atoms, in contrast to the liquid state at 3000 K, where the value is only about 90% (CHIK) to 94% (BKS) in case of the Si-Si coordination. All O atoms are 2-fold coordinated with respect to Si atoms and the most prominent coordination number for the O-O coordination is still $n = 6$, before, as well as after the structural relaxation. In Fig. 4.32, the distribution of $p_{OO}(n)$ is compared before and after the structural relaxation for both potentials. It can be seen that the curves of the BKS and the CHIK potential are nearly identical. In both cases, $p_{OO}(n = 6)$ slightly decreases and $p_{OO}(n = 7)$ slightly increases during the structural relaxation by about 6 to 8 percentage points.

Summarizing, the main effect of the structural relaxation is the reduction of the mean O-Si-O angle of about 6° (BKS potential) and 4° (CHIK potential). This is reflected in the slight decrease of the mean first neighbor Si-Si distance in both cases and a slight change of the distribution of coordination numbers $p_{OO}(n)$. The medium range structure, in terms of the distribution of ring sizes and the Si-Si-Si angular distribution of the glass systems, is not altered

significantly during the structural relaxation. Furthermore, the structure of the configurations generated with the BKS potential are nearly identical to the structure of the ones generated with the CHIK potential.

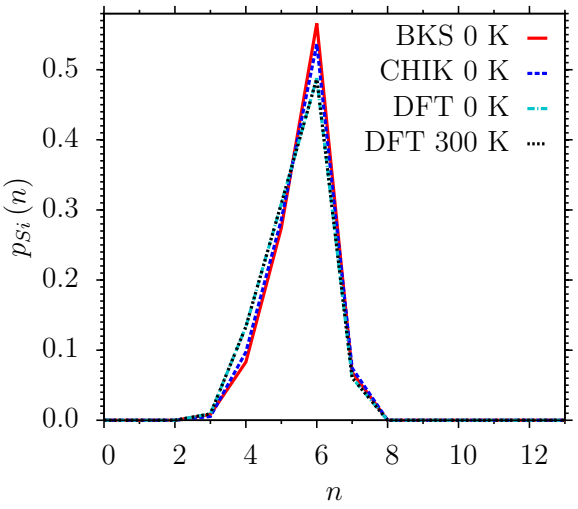

FIGURE 4.33: Probability that a Si atom is member of a ring of size n, $p_{Si}(n)$, at 0 K. Comparison of BKS and CHIK potential after structural relaxation with full ab initio quench at 0 K and 300 K.

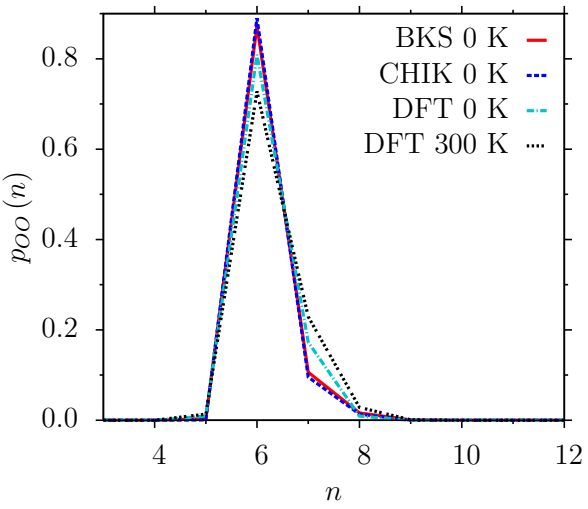

FIGURE 4.34: Distribution of coordination numbers $p_{OO}(n)$ at 0 K. Comparison of BKS and CHIK potential after structural relaxation with full ab initio quench at 0 K and 300 K.

In addition, one glass structure is generated by a quench from the melt with a Born-Oppenheimer ab initio MD simulation. Again, the VASP software package [77–79] is used and the simulation is conducted at the experimental glass density of $\rho = 2.2\text{g/cm}^3$ [98]. The DFT parameters are the same as in case of the structural relaxation, besides using normal instead of accurate VASP precision and a relative energy difference of 10^{-6} instead of 10^{-8} as break condition for the electronic relaxation. In a Born-Oppenheimer ab initio MD simulation, at each time step, the forces on the ions are calculated, according to the Hellman-Feynman theorem [112]. Based on this forces, the ion positions are updated in the same manner as in a classical MD simulation. As mentioned in section 3.2, the DFT calculations are with respect to the electronic ground state, implying this MD scheme is applicable in a temperature range where electronic excitations are negligible. The Born Oppenheimer MD run is carried out in a NVT ensemble, where the ionic motion is coupled to a Nosé thermostat (see subsection 3.1.2) with a Nosé-mass corresponding to a period of 40 time steps. First, the configuration is equilibrated at 3600 K for 31797 ts (38.1564 ps) with a time step of 1.2 fs. Next, the system is linearly quenched to 300 K and afterwards to 0 K with a cooling rate of $\Gamma = 1.\overline{6} \cdot 10^{14}\,\text{K/s}$. Subsequently, the system is structurally relaxed in the same way as described above. In addition, a Born-Oppenheimer MD run at 300 K is carried out for 5000 ts (6 ps), again, with a time step of 1.2 fs. In the following, the structural quantities at 300 K refer to the last 3 ps of this Born-Oppenheimer run.

In general, the structure of this configuration does not differ significantly from the structure of the systems generated by classical MD simulations with a subsequent quantum mechanical relaxation. However, it has to be kept in mind that in case of the ab initio quench, only a

single atomic configuration is regarded. Again, all Si-atoms are 4-fold coordinated with respect to Si and O atoms and all O atoms are 2-fold coordinated with respect to Si atoms. The main differences with respect to samples generated employing the BKS and the CHIK potential are the probabilities that a Si atom is member of a ring of size n, $p_{Si}(n)$, and the distribution of coordination numbers $p_{OO}(n)$. In Fig. 4.33, it can be seen that $p_{Si}(n)$ at 0 K is identical to the distribution at 300 K, in case of the single ab initio quench. This implies there is no difference in the medium range structure between 300 K and 0 K. Regarding the differences to the classical quenches, the values of $p_{Si}(n=4)$ and $p_{Si}(n=5)$ are slightly higher and the value of $p_{Si}(n=6)$ is slightly lower compared to the corresponding values of the CHIK and BKS potential after the structural relaxation. However, 6-membered rings are still the dominant rings size of the full ab initio quench and also 3-membered rings are still apparent in the glass structure with a probability of $p_{Si}(n=3) \simeq 0.9\%$. Regarding the coordination distribution $p_{OO}(n)$, the probability of an O atom to have 6 neighboring O atoms is slightly lower in case of the ab initio quench at 0 K, compared to the classical quenches after the structural relaxation (see Fig. 4.34). This trend is enhanced, regarding the coordination distribution $p_{OO}(n)$ at 300 K.

	BKS [22] 0 K	CHIK [43] 0 K	ab initio 0 K	ab initio 300 K	experiment [113, 114]
$\overline{r}_{SiSi}$ [Å]	3.106 ± 0.004	3.114 ± 0.004	3.082	3.085	3.08 ± 0.10
$\overline{r}_{SiO}$ [Å]	1.6288 ± 0.0007	1.6303 ± 0.0005	1.6276	1.6317	1.61 ± 0.05
$\overline{r}_{OO}$ [Å]	2.663 ± 0.001	2.665 ± 0.001	2.661	2.669	2.63 ± 0.09
$p_{SiOSi}(\Phi)$ [°]	147.2 ± 0.3	147.8 ± 0.5	145.0	144.5	148.3 ± 7.5
$p_{OSiO}(\Phi)$ [°]	109.468 ± 0.002	109.467 ± 0.002	109.468	109.426	109.47 ± 4.2

TABLE 4.10: Mean first neighbor distances and average angles of classical quenches and one full ab initio quench at 0 K after the structural relaxation. Comparison with single ab initio run at 300 K and experimental results [113, 114].

In addition to the structural quantities, it is interesting to compare the total energies E_0 and the total energies per atom E_0/N of the respective structures. In case of the classical quenches, the corresponding values after the quantum mechanical relaxation are $E_0 = -1349.8878 \pm 0.2608$ eV and $E_0/N = -8.1811 \pm 0.\,0.0016$ eV (BKS quench) and $E_0 = -1349.3441 \pm 0.1687$ eV and $E_0/N = -8.1778 \pm 0.\,0.0010$ eV (CHIK quench). The statistical errors, in both cases, are the standard deviations of the mean with respect to the 10 independent cooling runs, $\overline{\sigma} = \frac{\sigma}{\sqrt{N}}$. The corresponding values of the one ab initio quench are $E_0 = -1347.4409$ eV and $E_0/N = -8.1663$ eV. The value of the full ab initio quench is shown without the specification of an error, because only one independent run is carried out. Overall, these values are in good agreement with each other. However, the mean energy per atom of the full ab initio quench is about $0.012 - 0.015$ eV higher compared to the other cases. This could suggest that in this case the method of the MD quenches with the subsequent quantum mechanical relaxation lead to slightly better glass structures.

In the first three columns of Table 4.10, the average first neighbor distances and average inter- and intra-tetrahedral angles are shown for the glass structures of the classical MD simulations

and the glass structure of the full ab initio quench. In each case, the results refer to the atomic configurations after the structural relaxation at 0 K. The values of the fourth column refer to the single Born-Oppenheimer run at 300 K. Again, the depicted errors of the BKS and the CHIK potential are the standard deviations of the mean of the 10 independent cooling runs and the values of the full ab initio quench are shown without the specification of an error. The mean first neighbor distances are compared to experimental results from neutron scattering [113] at room temperature. The experimental data is extracted from the real space correlation function $T(r)$, which basically is the Fourier transform of the interference function. The displayed experimental errors are the root mean square of the Gaussian fits of the peaks in $T(r)$. The mean Si-O-Si and O-Si-O angles are compared to experimental results, which are re-determined combining previous neutron diffraction and high energy X-ray diffraction experiments [114]. Here, the experimental value of the mean O-Si-O angle, in fact, is the theoretical value from an ideal tetrahedron. The experimental errors represent the peak width of the angular distributions. In all cases the agreement with experimental data is very good. On the one hand, nearly no differences between the different schemes of generating the glass structures are visible. On the other hand, the structural properties at 0 K are nearly identical to the structural properties at 300 K in case of the single ab initio quench. This justifies the comparison of glass properties after the structural relaxation at 0 K with experimental results at room temperature.

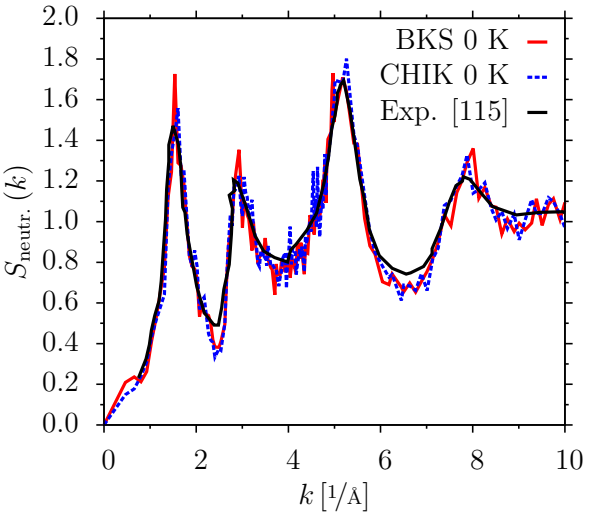

FIGURE 4.35: $S_{\text{neutr.}}(k)$. Comparison of BKS and CHIK potential after structural relaxation with experimental results [115].

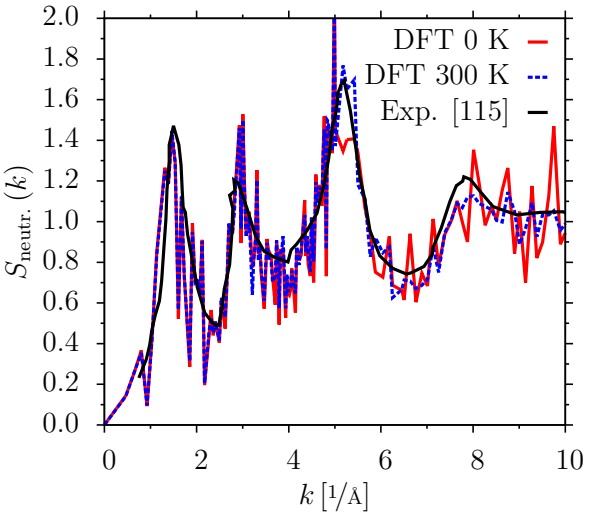

FIGURE 4.36: $S_{\text{neutr.}}(k)$. Comparison of full ab initio quench at 0 K and 300 K with experimental results [115].

Next, the total neutron structure factor $S_{\text{neutr.}}(k)$ is examined. As explained in section 3.3, it is obtained by weighting the partial static structure factors $S_{\alpha\beta}(k)$, $\alpha, \beta \in \{Si, O\}$, with the Si and O neutron scattering lengths (see equation (3.95)). The neutron scattering lengths are $b_{Si} = 4.1491$ fm and $b_O = 5.803$ fm [89]. In Fig. 4.35, $S_{\text{neutr.}}(k)$ of the BKS and CHIK potential after structural relaxation at 0 K are compared to experimental results [115]. In Fig. 4.36, the corresponding curves of the single ab initio quench at 0 K and 300 K are compared to the same experimental curve. The experimental data shown in this case is generated by means of time-of-flight measurements at room temperature. Again, the overall agreement is quite good,

in all cases. Nearly no difference is visible between the ab initio results at 0 K and 300 K. The greatest differences between the experimental data and the simulation results are visible in the position of first sharp diffraction peak (FSDP) (see 4.1.2). The experimental peak is located at about $k = 1.45\,\text{Å}^{-1}$. In case of the single ab initio quench the peak position is about the same, whereas the position of the BKS and the CHIK potential after the structural relaxation is shifted to slightly larger k-values by approximately $k = 0.1\,\text{Å}^{-1}$. However, the curve of the single ab initio quench is much more noisy.

4.3 Vibrational Properties

In this section, different vibrational properties of the model glass former SiO_2 are examined and compared with experimental results. As explained in section 3.4, the thermal occupation of the phonon density of states $g(\nu)$ (see equation (3.109)) or the respective eigenmodes with eigenfrequencies ν_n, gives access to the thermodynamic properties at low temperatures. In principle, the vibrational density of states includes harmonic and anharmonic terms. However, the importance of anharmonic terms decreases with decreasing temperature and at low temperatures, $g(\nu)$ can be well described in terms of the harmonic approximation. Therefore, in this section all vibrational properties are calculated employing the so-called "frozen phonon" method. For a detailed description, see section 3.4. In this approach, the vibrational properties are described in terms of the dynamical matrix $D_{\alpha\beta;i,j}(\mathbf{k})$, $\alpha, \beta, \in \{1,2,3\}$ and $i, j, \in \{1, N\}$ (see equation (3.107)). The latter is based on the force constant matrix $\Phi_{\alpha\beta;i,j}$ (see equation (3.105)). In this approach, the glass structures are treated as crystalline structures with a large unit cell containing all 165 atoms.

In principle, it is favorable to consider larger supercells of the original system to increase the accuracy of the calculation. However, the 165 atom system is already quite large regarding quantum mechanical calculations. As a consequence, the calculations of the vibrational properties of vitreous SiO_2 are restricted to the original system size. In this section, the vibrational properties, due to quantum mechanical forces are compared to the vibrational properties, due to the BKS [22] and the CHIK [43] potential. The basis for calculating the vibrational properties are the corresponding glass configurations at 0 K after structural relaxation, as explained in section 4.2. Ideally, in these structures the forces on all atoms are equal to zero. To calculate the vibrational spectra for the BKS and the CHIK potential, also a structural relaxation of the configurations at 0 K is performed with respect to the classical forces. Again, this is done by means of a conjugate gradient algorithm [111]. After the structural relaxation, in each case, all atoms $i \in \{1, N\}$ are displaced by $\Delta r_{\alpha;i} = \pm 0.02\,\text{Å}$, $\alpha\,\{1,2,3\}$ and the forces on all atoms $F_{\alpha;i}(\Delta r_{\beta;j})$ are computed. Again, all quantum mechanical calculations are conducted with the VASP package, using the same DFT parameters as in section 4.2 for the structural relaxation and the DFT forces are calculated, according to the Hellman-Feynman theorem [112]. The classical forces are computed with the LAMMPS package [60, 61].

In the DFT case, two different software packages are used to calculate the vibrational properties, namely the Phonon routine, originally developed by Krzysztof Parlinski [116], contained in the MedeA® software package [117] and the open source package Phonopy [90, 91]. In case of the classical forces, only the Phonopy package is employed. The input parameters, in both cases, are the forces with respect to all atomic displacements $F_{\alpha;i}(\Delta r_{\beta;j})$. The computation of the force constants $\Phi_{\alpha\beta;i,j}$, the dynamical matrix $D_{\alpha\beta;i,j}(\mathbf{k})$ and the derived properties is done by the respective software package.

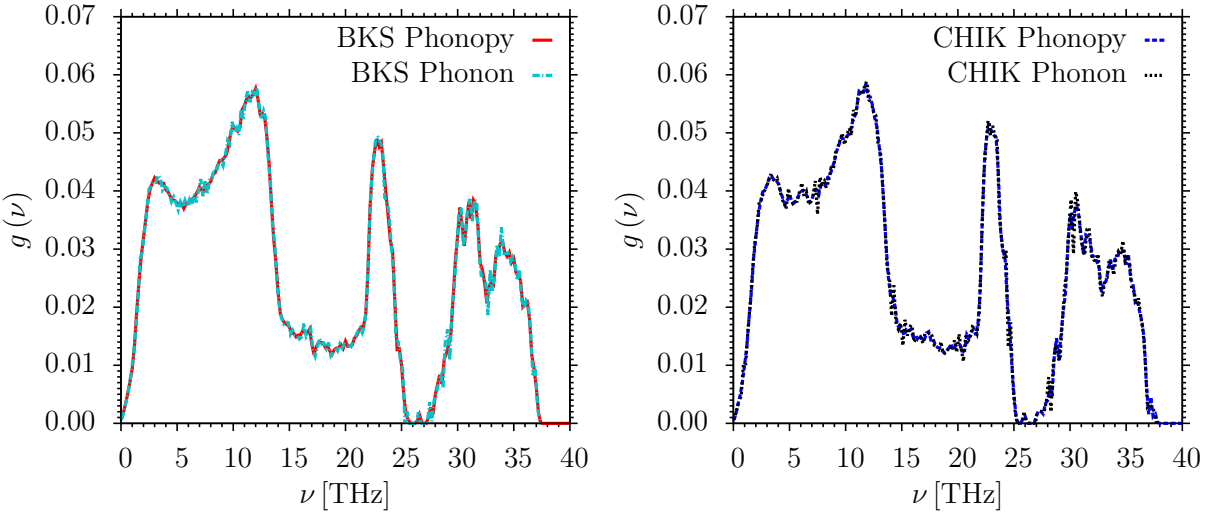

FIGURE 4.37: $g(\nu)$ of SiO_2 after structural relaxation with DFT calculation. Comparison of different software packages

In Fig. 4.37, the phonon densities of states are are compared to each other, calculated with the different software packages. The calculations are based on the atomic configurations after the classical quench with the BKS and the CHIK potential and the structural relaxation with quantum mechanical forces. All curves are averaged over 5 independent configurations. In case of the Phonon routine, the force constants $\Phi_{\alpha\beta;i,j}$ are computed employing the so-called original Parlinski-Li-Kawazoe method [116] and the dynamical matrix $D_{\alpha\beta;i,j}(\mathbf{k})$ is calculated, according to a statistical sampling over k-points in the Brillouin-zone. In case of the Phonopy package, the force constants $\Phi_{\alpha\beta;i,j}$ are computed using a slightly modified form of the original Parlinski-Li-Kawazoe method [118] and $D_{\alpha\beta;i,j}(\mathbf{k})$ is evaluated on a fixed mesh of k-points within the Brillouin-zone with a mesh-grid of 5 points along each of the $\mathbf{k}$-axes. In each case, the phonon density of states $g(\nu)$ (see equation (3.109)) is evaluated according to the eigenfrequencies of $D_{\alpha\beta;i,j}(\mathbf{k})$ at the specific k-points $\nu_n(\mathbf{k})$, $n \in \{1, \ldots, 3N\}$ (see equation (3.108)). In the Phonopy routine, a Gaussian smearing is applied with a smearing width of 0.1 THz. It can be seen that both curves are nearly identical. As in case of the classical forces, only the Phonopy software package could be employed, the following results are according to this package.

In Fig. 4.38, the phonon densities of states $g(\nu)$, according to the quantum mechanical forces after the structural relaxation, are compared to the ones, according to the classical forces, both, for the BKS and the CHIK potential. The DFT curves after the structural relaxation are identical to the ones in Fig. 4.37. Here, also the phonon density of states $g(\nu)$ of the one full

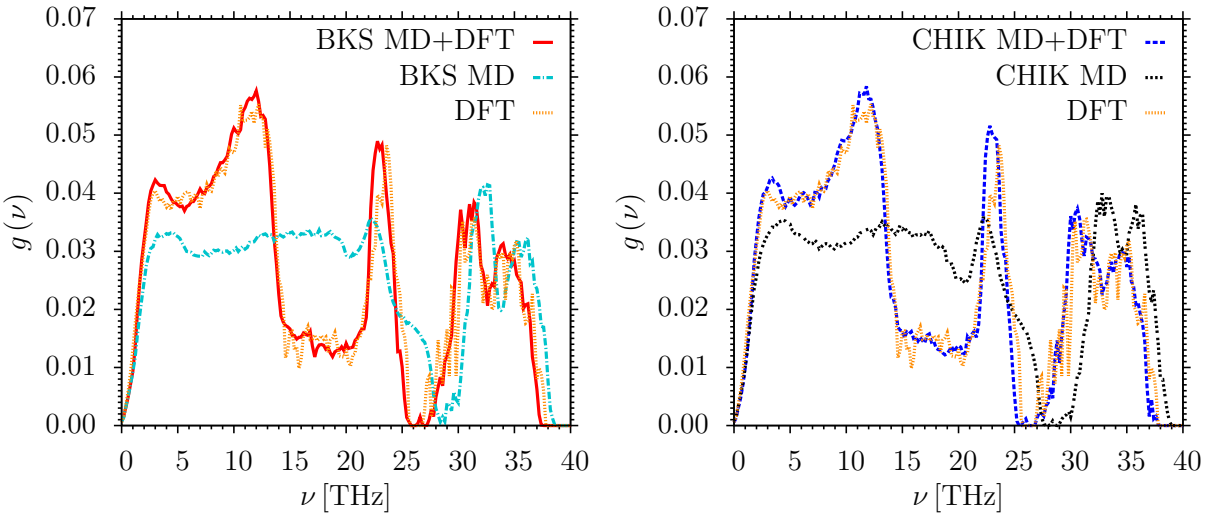

FIGURE 4.38: $g(\nu)$ of SiO_2. Comparison of classical with quantum mechanical forces

ab initio quench is shown. The curves according to the classical potentials are averaged over 10 different configurations. In all cases, there are significant differences between the DFT and the classical phonon densities of states. The main difference is the reduced number of low frequency modes between 0 THz and about 14 THz and the excess of modes between about 14 THz and 22 THz in the classical spectra. The peak at approximately 12 THz, in both cases, is completely missing in the classical spectra. According to [11], the vibrational modes below about 22 THz are delocalized and have a collective nature in the sense that many atoms in the whole simulation box take part in the vibrational motion of these modes. Exceptions are the so-called D1 and D2 lines at approximately 14.8 THz and 18.2 THz, which are connected to the breathing motion of four-membered ($n = 4$) and three-membered ($n = 3$) rings [27, 28]. However, these modes are not visible in the vibrational spectra, both for the classical as well as the quantum mechanical forces. In contrast to this, the high frequency modes with frequencies greater than about 22 THz are more localized. According to [119], the modes in this frequency range can be predominantly assigned to vibrational motions within the SiO_4 tetrahedra. In this frequency range, the peak at approximately $22 - 23$ THz is much less pronounced in the classical spectra and slightly shifted to lower frequencies, in both cases. The high-frequency doublet at about $30 - 38$ THz is present in the DFT, as well as in the classical spectra. However the position is shifted by approximately 1.5 to 2 THz to lower frequencies in the quantum mechanical spectra. The low frequency part of this doublet and the peak at approximately $22 - 23$ THz are predominantly assigned to asymmetric stretching motions of the oxygen atoms with respect to the central Si atom and bond-bending motions of the Si-O-Si bonds [119] and the position of the $22 - 23$ THz peak mainly depends on the mean Si-O-Si angle [120]. The peak positions of the DFT curves (approximately 23 THz) and the mean Si-O-Si angle of about $145° - 148°$ (see Table 4.10) are comparable to the ones of model I (about 24 THz and 148°) in [120]. The high frequency part of the double peak at about $30 - 38$ THz is ascribed to an in-phase stretching motion of the oxygen atoms with respect to the central Si atom in a tetrahedron [119].

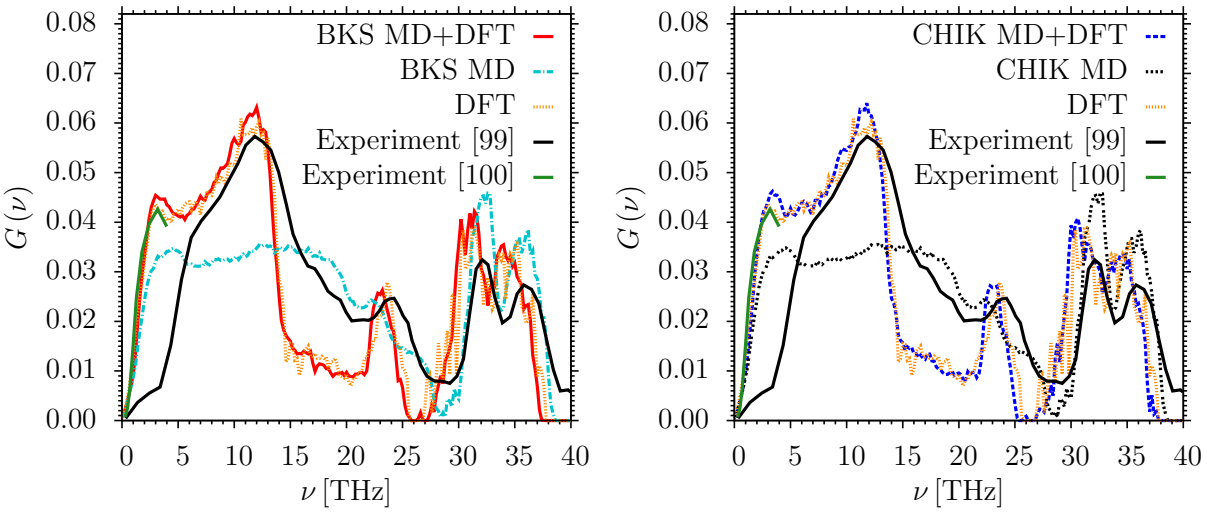

FIGURE 4.39: $G(\nu)$ of SiO_2. Comparison of classical and DFT spectra with inelastic neutron scattering [99, 100].

In Fig. 4.39, the so-called effective neutron scattering cross section $G(\nu) = C(\nu)\, g(\nu)$ is compared to experimental results from inelastic neutron scattering [99, 100]. The correction function $C(\nu)$ is calculated using the incoherent approximation, according to [121]. In this case, the correction function can be approximated by

$$C(\nu) = 1 + \frac{\langle m \rangle}{\langle b^2 \rangle} \left(\frac{g_{Si}(\nu)}{g(\nu)} - \frac{N_{Si}\, m_{Si}}{N \langle m \rangle} \right) \left(\frac{b_{Si}^2}{m_{Si}} - \frac{b_O^2}{m_O} \right). \tag{4.5}$$

Here, $b_{Si} = 4.1491\,\text{fm}$ and $b_O = 5.803\,\text{fm}$ [89] are the neutron scattering lengths, $\langle m \rangle = 20.028100333\,\text{amu}$ is the mean atomic mass of the system, $\langle b^2 \rangle = N^{-1} \sum_i b_i^2 = 28.18821627\,\text{fm}^2$ is the mean squared neutron scattering length, $g(\nu)$ is the full phonon density of states and $g_\alpha(\nu), \alpha \in \{Si, O\}$, are the partial phonon densities of states. In fact, Si and O in equation (4.5) can be exchanged, as $\frac{g_O(\nu)}{g(\nu)} - \frac{N_O\, m_O}{N \langle m \rangle} = -\frac{g_{Si}(\nu)}{g(\nu)} + \frac{N_{Si}\, m_{Si}}{N \langle m \rangle}$. In this formulation, a Debye-Waller factor of $\exp\left[-k^2 \langle u_\alpha^2 \rangle / 3\right] \simeq 1$, $\alpha \in \{Si, O\}$, [92] is assumed, which is a good assumption at low temperature. Here, $\langle u_\alpha^2 \rangle$ are the mean square atomic displacements of atoms of type α. Comparing the curves in Fig. 4.39 with the ones in Fig. 4.38, it can be seen that the main effect of $C(\nu)$ is the reduction of the height of the $22 - 23\,\text{THz}$ peak and the peak positions are not altered. The experimental curves show data measured at 33 K [99] and a combination of different measurements at three different spectrometers in a temperature range from 50 K to room temperature [100]. The experimental resolution is about 3.6 THz [99] and 0.15 THz [100]. The lack of vibrational modes for $\nu < 5\,\text{THz}$ in [99] is due to the substraction of resolution-broadened elastic scattering in this region. In Fig. 4.39, the experimental curve [99], as well as the calculated ones, are normalized to $\int G(\nu) = 1$. In case of the quantum mechanical spectra after the structural relaxation, the calculated $G(\nu)$ are in good agreement with the experimental results. This agreement is in accordance with previous studies [11, 28, 119, 120]. Nearly

no difference is visible between the curves of the BKS and the CHIK potential and the full ab initio quench and all relevant peaks are resolved. The main difference is a shift of $22-23\,\mathrm{THz}$ peak and the high-frequency doublet to lower frequencies. One reason for this can be the tendency to overestimate bond-length and to underestimate vibrational frequencies in case of the applied exchange-correlation functional (PBEsol) [81]. The classical spectra, in both cases, show an inferior agreement with the experimental $G(\nu)$, mainly due to the reduced number of low frequency modes and the missing 12 THz peak. However, in both cases, the high-frequency doublet is in good agreement with the experimental $G(\nu)$. Regarding $G(\nu)$ of the CHIK potential, the $22-23\,\mathrm{THz}$ peak is slightly more pronounced and the $30-38\,\mathrm{THz}$ double peak is shifted to slightly higher frequencies compared to the curve, according to the BKS forces. A similar behavior has been already observed at 300 K [43].

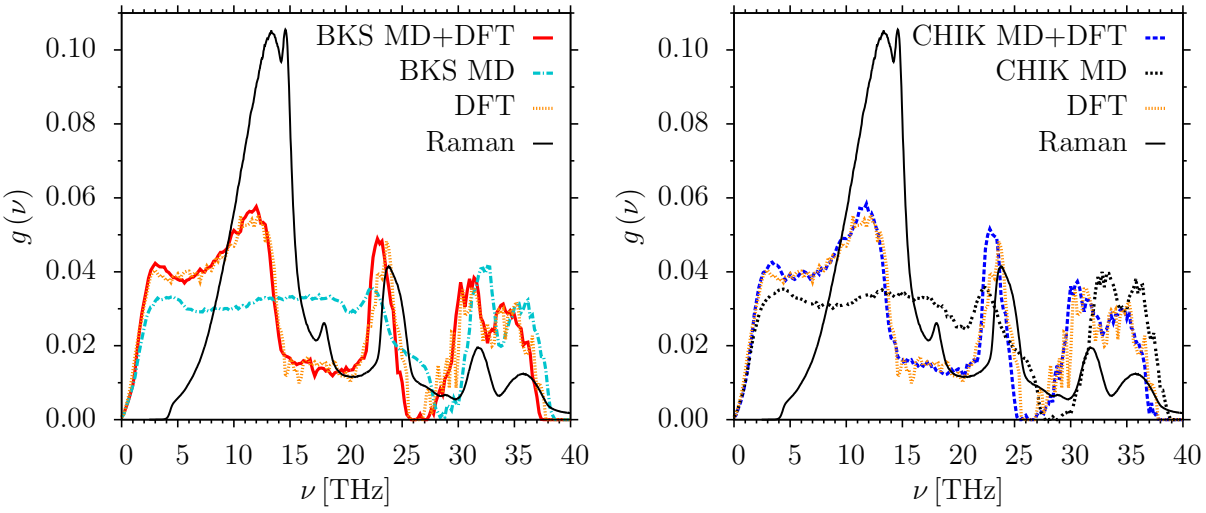

FIGURE 4.40: $g(\nu)$ of SiO_2. Comparison with Raman scattering of fused silica. Measured at Otto Schott Research Centre in Mainz.

In Fig. 4.40, the vibrational spectra are compared to results from Raman scattering. The Raman measurements have been conducted at the Otto Schott Research Centre in Mainz. The experimental curve is recorded based on a sample of fused silica (Schott Lithosil®, [122]) with a focal point about $150\,\mu\mathrm{m}$ below the surface of the sample to measure the bulk properties. It is recorded with a diffraction grating with 600 lines per mm. A frequency-doubled Nd:YAG-Laser is used with an incident laser power of 1 W and wavelength of 532 nm. All polarization directions are included. The curve is averaged over 60 measurements, each of a duration of 10 s. The experimental Raman scattering cross section is proportional to

$$I_s \propto |\hat{\mathbf{e}}_s \cdot \mathbf{R} \cdot \hat{\mathbf{e}}_i| \, \frac{1}{\nu} \left(n_\mathrm{B}(\nu) + 1\right) g(\nu), \quad n_\mathrm{B}(\nu) = \frac{1}{\exp\left[\frac{h\nu}{k_\mathrm{B} T}\right] - 1}, \tag{4.6}$$

where $g(\nu)$ is the phonon density of states, $\hat{\mathbf{e}}_s$ and $\hat{\mathbf{e}}_i$ are the polarizations of the scattered and incident light beams and $\mathbf{R}$ is the second-rank Raman tensor [120]. The shown curve is the

experimental data divided by $\frac{1}{\nu}\left(n_{\mathrm{B}}\left(\nu\right)+1\right)$ with $T = 300\,\mathrm{K}$ and then normalized to $\int g\left(\nu\right) = 1$. The general shape of the spectrum is similar to the shape of the effective neutron scattering cross section. Differences in the peak heights are due to the different Raman susceptibilities of the respective modes. In the Raman measurement, the D1 and D2 lines at about 14.8 THz and 18.2 THz [27, 28] are clearly visible. Regarding the comparison with the simulated spectra, the same arguments hold as in case of the comparison with the effective neutron scattering cross section $G\left(\nu\right)$.

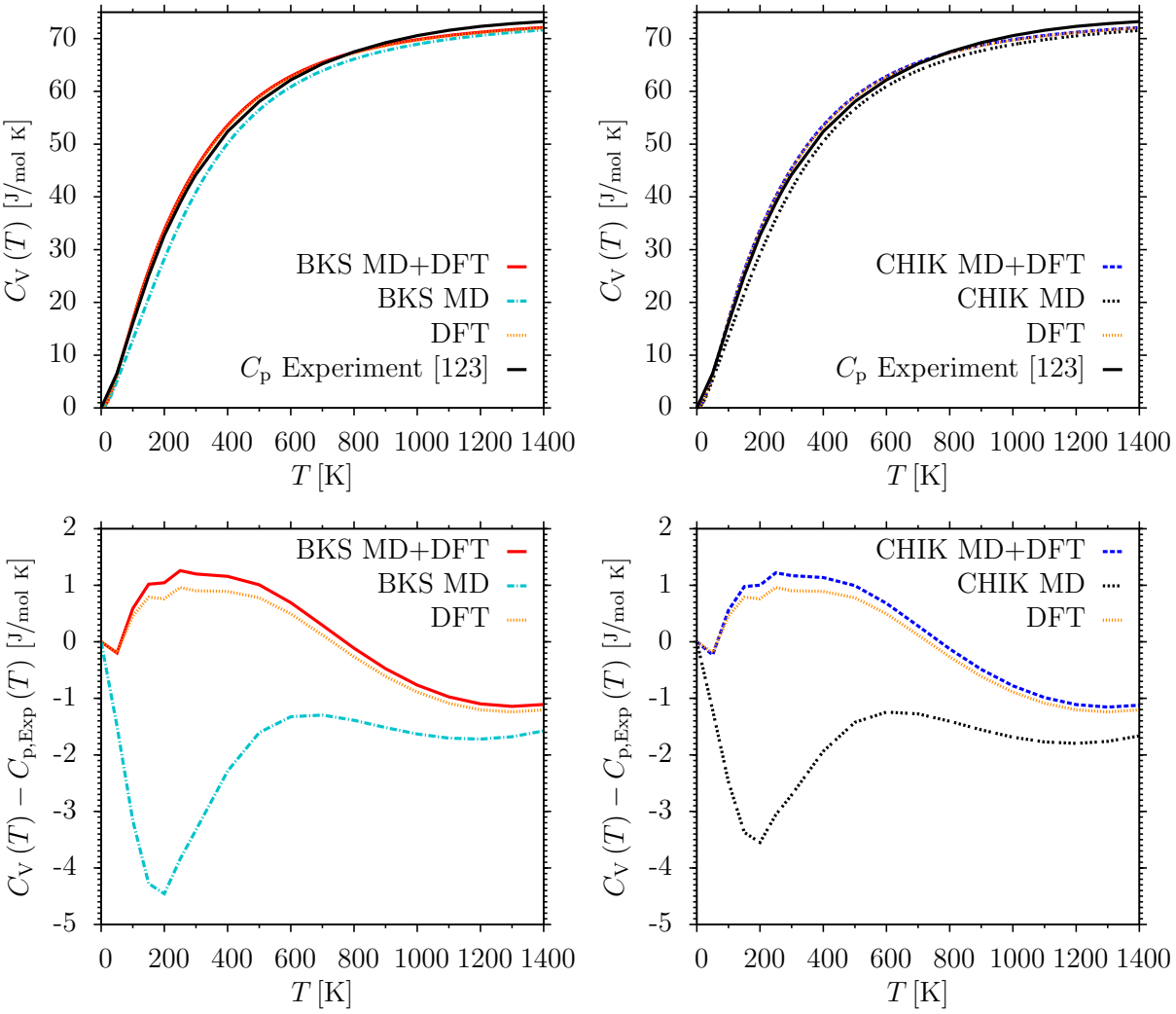

FIGURE 4.41: $C_{\mathrm{V}}\left(T\right)$ of SiO_2. Comparison with experimental results of $C_{\mathrm{p}}\left(T\right)$ [123]

Next, the specific heat at constant volume $C_{\mathrm{V}}\left(T\right)$ is calculated, according to equation (3.121), multiplied by the factor $\frac{N_{\mathrm{A}}}{N_{\mathrm{units}}}$ to obtain the numerical values in units of [J/mol]. Here, N_{A} is the Avogadro constant and N_{units} is the number of structural units in the configuration, which is 55 SiO_2 units in the case of a 165 atom system of SiO_2. The calculation is based on the eigenfrequencies $\nu_n\left(\mathbf{k}\right)$, $n \in \{1,\ldots,3N\}$, on a k-mesh with 15 points along each of the $\mathbf{k}$-axes. In Fig. 4.41, $C_{\mathrm{V}}\left(T\right)$ based on $\nu_n\left(\mathbf{k}\right)$, $n \in \{1,\ldots,3N\}$, according to the quantum mechanical and the classical forces, are compared to $C_{\mathrm{p}}\left(T\right)$ from calorimetric measurements [123] for all

considered cases. The difference between C_V and C_p per mol is expressed by the thermodynamic relation [124]

$$C_\mathrm{p} - C_\mathrm{V} = T\,\frac{M}{\rho}\,\alpha_\mathrm{V}^2\,K, \quad \alpha_\mathrm{V} = \frac{1}{V}\left(\frac{\partial V}{\partial T}\right)_\mathrm{p}, \quad K = -V\left(\frac{\partial p}{\partial V}\right)_T \tag{4.7}$$

where M is the molar mass, ρ the density, α_V the volumetric coefficient of thermal expansion at constant pressure and K the bulk modulus at constant temperature. In case of SiO_2, the values at room temperature are $M = 60.08430\,\mathrm{g/mol}$ (molar mass of one SiO_2 unit), $\rho \simeq 2.2\,\mathrm{g/cm^3}$ [98], $\alpha_\mathrm{V} \simeq 3 \times \alpha_L \simeq 3 \times 5.5 \cdot 10^{-7} K^{-1}$ [122] and $K \simeq 37\,\mathrm{GPa}$ (derived from the values of the Young's modulus, Shear modulus and Poisson's ratio, given in [122]). Due to the low thermal expansion of SiO_2, the difference between C_p and C_V is only about $C_\mathrm{p} - C_\mathrm{V} = 2.75 \cdot 10^{-6}\,\frac{\mathrm{J}}{\mathrm{K^2\,mol}}\,T\,[K]$ and can be neglected. The agreement between the theoretical curves and the experimental curve is rather good, in all cases. However, in the temperature range between 50 K and 900 K the agreement with the experimental curve is significantly better for the data based on the quantum mechanical forces, both for the BKS and the CHIK potential, as well as for the full ab initio quench. In this temperature range, $C_\mathrm{V}(T)$ based on the classical forces is visibly below the experimental curve, which can be explained due to the reduced number of low frequency modes in the vibrational spectrum. Comparing the BKS and the CHIK potential, the corresponding curves are virtually on top of each other.

In this chapter, the simulation results of the model glass former SiO_2 are summarized. First, simulations of the liquid state are presented in a temperature range between 4300 K and 2700 K. On the one hand, the effects of different system sizes are studied, carrying out simulations of 114, 165, 216 and 1152 systems with the BKS potential [22] at a constant system density of $\rho = 2.37\,\mathrm{g/cm^3}$. The main finite size effects are the slowing down of the dynamics and a decrease of the number of rings, containing more than 6 Si atoms, with decreasing system size. The 114 atom system shows some additional artifacts in the curves of the static structure factors. This motivates the choice of a 165 atom system for further considerations. On the other hand, the structural and dynamical properties of the BKS [22] and the CHIK [43] potential are compared. The main differences are slightly larger peak heights and about $3-10$ times larger α-relaxation times, in case of the BKS potential. In addition, the temperature dependence of of the self-diffusion constants D_α, $\alpha \in \{Si, O\}$, is studied. At temperatures below about 3200 K, the curves of D_α with respect to $1/T$ show an Arrhenius behavior (see equation (4.4)). Regarding the BKS potential, the extracted activation energies $E_{A,\alpha}$, $\alpha \in \{Si, O\}$, are significantly larger than the ones reported in [42] and [107, 108]. The differences can be explained in terms of finite size effects and effects due to different system densities. Regarding the CHIK potential, the values of $E_{A,\alpha}$, $\alpha \in \{Si, O\}$, are also larger than the ones reported in [43], which can be explained in terms of finite size effects. Next, glass structures are generated by quenches from the melt with classical MD simulations, employing the BKS and the CHIK potential. Afterwards, a structural relaxation is carried out with respect to quantum mechanical forces, mainly reducing

the mean Si-O-Si angle by about $4° - 6°$, in agreement with [10]. After the quantum mechanical relaxation, no significant differences are visible in the glass structures generated by the BKS and the CHIK potential and the agreement, both, with one glass structure generated by a full ab initio quench from the melt and with experimental results is good. Finally, the vibrational properties are studied. Here, the vibrational spectra, according to the quantum mechanical forces, show a good agreement with results from inelastic neutron scattering [99, 100]. The agreement is significantly better compared to the spectra, according to the classical forces of the BKS, as well as the CHIK potential. The latter show a reduced number of vibrational modes in the low frequency range. This leads to a significantly better agreement of the specific heat at constant volume $C_{\mathrm{V}}(T)$ with experimental results as well. The results of this chapter suggest that, both, a classical quench with a subsequent quantum mechanical relaxation and a full ab initio quench can lead to comparable glass structures, given a reliable classical potential.

Chapter 5

Calculating thermal expansion

In this chapter, the temperature dependence of the system volume, $V(T)$, is examined for the model glass former SiO_2. The calculations are based on the glass structures, generated in section 4.2, and the concept of the so-called quasi-harmonic approximation is applied. In section 5.1, the theoretical background is summarized. In section 5.2, the numerical results of the model glass former SiO_2 are presented for quantum mechanical and classical forces. Here, a change of sign of the linear coefficient of thermal expansion $\alpha_L(T)$ is observed with a range of negative thermal expansion at temperatures below approximately 130 K to 160 K (quantum mechanical forces) and 290 K to 325 K (classical forces). This behavior is in accordance with experimental results. To my knowledge, the calculation of the thermal expansion of vitreous silica by means of ab initio calculations has not been done before.

5.1 Theoretical considerations

In section 3.4, the theory of lattice vibrations within the harmonic approximation has been summarized. As already explained in section 4.3, the simulated glass structures are theoretically treated as crystalline structures with a large unit cell containing 165 atoms. In this context, harmonic approximation means that the forces on each of the N atoms of a solid are considered to be proportional to the atomic displacements and the individual atoms can be treated as 3-dimensional harmonic oscillators. Therefore, the vibrational properties of the whole configuration can be mathematically treated as an ensemble of $3N$ independent quantum mechanical harmonic oscillators. According to equations (3.113), (3.120) and (3.118), the relevant thermodynamical properties, as the internal energy, the entropy and the free energy of the lattice vibrations can be described in terms of the respective eigenfrequencies $\nu_n(\mathbf{k})$, $n \in \{1, \ldots 3N\}$. This model is not capable to describe the thermal expansion of the solid as the eigenfrequencies $\nu_n(\mathbf{k})$ are independent of the temperature.

The quasi-harmonic approximation [125] is a way to introduce the temperature dependence of the eigenmodes $\nu_n(\mathbf{k})$ and provides a way to describe thermal expansion. In this model, the

lattice vibrations are still described within the harmonic approximation, however the assumption is that the eigenfrequencies depend on the volume of the system: $\nu_n(\mathbf{k}; V)$. As a consequence, the phonon density of states and the thermodynamical properties have a volume dependence, as well. The exact relation between the Helmholtz free energy $F(T, V)$ and the internal energy $U(T, V)$ of a system is [63]:

$$F(T, V) = U(T, V) - T\,S(T, V)\,. \tag{5.1}$$

Neglecting effects due to electronic excitations and configurational degrees of freedom, the relation can be written in the following form:

$$F(T, V) = E_0(V) + U_{\text{Vib}}(T, V) - T\,S_{\text{Vib}}(T, V)\,, \tag{5.2}$$

$$\Leftrightarrow F(T, V) = E_0(V) + F_{\text{Vib}}(T, V)\,. \tag{5.3}$$

Here, $U_{\text{Vib}}(T, V)$ is the internal energy, $S_{\text{Vib}}(T, V)$ the entropy and $F_{\text{Vib}}(T, V)$ the free energy of the lattice vibrations. They have the same functional forms as in equations (3.113), (3.120) and (3.118), introducing the volume dependence by means of the volume dependence of the eigenfrequencies $\nu_n(\mathbf{k}; V)$. This leads to the functional form of the vibrational free energy of

$$F_{\text{Vib}}(T, V) = \frac{RT}{N_{\text{units}}\,N_{\mathbf{k}}} \sum_{\mathbf{k}} \sum_{n=1}^{3N} \ln\left[2\,\sinh\left(\frac{h\nu_n(\mathbf{k}; V)}{2k_{\text{B}}T}\right)\right] \tag{5.4}$$

in units of [J/mol] (equation (3.118) multiplied by $\frac{N_{\text{A}}}{N_{\text{units}}}$). Here, N_{units} is the number of structural units in the configuration, which is 55 SiO_2 units in the case of a 165 atom system of SiO_2. The energy $E_0(V)$ in equations (5.2) and (5.3) is the total energy of the structural configuration at 0 K at a given volume V. It consists of all electronic contributions, the Coulomb energy of the interactions between the nuclei and the contributions of the atomic energies, according to the PAW potentials, as already explained in section 4.2. Given the Helmholtz free energy $F(T, V)$, the Gibbs free energy $G(T, p)$ can be written as

$$G(T, p) = \min_{\text{V}}\left[F(T, V) + p\,V\right] = \min_{\text{V}}\left[E_0(V) + F_{\text{Vib}}(T, V) + p\,V\right]. \tag{5.5}$$

Equation (5.5) has to be understood in a sense that for each temperature T and external pressure p, the minimization of $[F(T, V) + p\,V]$ with respect to V yields the Gibbs free energy of the system. Following the volume with minimal $[F(T, V) + p\,V]$, the volume dependence on temperature $V(T)$ can be obtained.

This means that in this approximation, the overall volume dependence of the Helmholtz free energy $F(T,V)$ and the Gibbs free energy $G(T,p)$ comes from the volume dependence of the total energy $E_0(V)$ of the atomic configuration at 0 K and the volume dependence of the eigenfrequencies $\nu_n(\mathbf{k};V)$.

In this chapter, only properties at normal conditions are studied, meaning an external pressure of $p = 1\,\text{atm} \simeq 0.1\,\text{MPa}$. The magnitude of relevant pressures in solids is of the order of GPa, meaning an external pressure of $p \simeq 0$ is a reasonable assumption. In practice, the unit cell of the given structure has to be slightly compressed and enlarged, without altering the relative coordinates of the atoms in the system. This leads to a series of configurations at slightly different volumes V. For each of the configurations, a structural relaxation has to be conducted to obtain the total energy for the specific system volume $E_0(V)$, followed by a calculation of the vibrational properties with the "frozen phonon" method to compute $F_{\text{Vib}}(T,V)$. Given the set of $F(T,V)$ at discrete cell volumes V, at each temperature T, the volume with minimal $F(T,V)$ ($p \simeq 0$) is found by means of a fit to a given functional form of $E(V)$.

To describe the volume-dependence of the eigenfrequencies $\nu_n(\mathbf{k})$, the so-called dimensionless microscopic mode Grüneisen parameters can be defined [93]:

$$\gamma_n(\mathbf{k}) = -\frac{V}{\nu_n(\mathbf{k})}\frac{\partial \nu_n(\mathbf{k})}{\partial V}. \tag{5.6}$$

Based on equation (5.6), the macroscopic Grüneisen parameter $\gamma(T)$ can be defined in terms of a weighted average of the microscopic $\gamma_n(\mathbf{k})$:

$$\gamma(T) = \frac{\sum_{\mathbf{k}}\sum_{n=1}^{3N}\gamma_n(\mathbf{k})\, c_{\text{V},n}(\mathbf{k};T)}{\sum_{\mathbf{k}}\sum_{n=1}^{3N} c_{\text{V},n}(\mathbf{k};T)}, \tag{5.7}$$

$$c_{\text{V},n}(\mathbf{k};T) = \left(\frac{h\nu_n(\mathbf{k})}{k_{\text{B}}T}\right)^2 \frac{\exp\left[\frac{h\nu_n(\mathbf{k})}{k_{\text{B}}T}\right]}{\left[\exp\left[\frac{h\nu_n(\mathbf{k})}{k_{\text{B}}T}\right]-1\right]^2}. \tag{5.8}$$

Here, $c_{\text{V},n}(\mathbf{k};T)$ is the contribution of each individual vibrational mode n to the specific heat at constant volume $C_{\text{V}}(T)$, according to equation (3.121). It can be shown that the macroscopic Grüneisen parameter $\gamma(T)$ correlates $C_{\text{V}}(T)$ with the volumetric thermal expansion coefficient $\alpha_{\text{V}}(T)$ and the isothermal bulk modulus $K(T)$ (see equation (4.7)) by the following relation:

$$\gamma(T) = \frac{\alpha_{\text{V}}(T)\, K(T)\, M}{C_{\text{V}}(T)\, \rho}. \tag{5.9}$$

Here, M is the molar mass, ρ is the density of the system and $C_V(T)$ is given in units of $[\mathrm{J/mol}]$. As a result of equation (5.9), a temperature regime with negative thermal expansion coefficient $\alpha_V(T)$ relates to a negative macroscopic Grüneisen parameter $\gamma(T)$ in the respective temperature range and, due to equation (5.7), a negative $\gamma(T)$ relates to negative microscopic Grüneisen parameters $\gamma_n(\mathbf{k})$. As a consequence of equation (5.6), the vibrational modes contributing to a temperature regime with negative thermal expansion show a positive frequency dependence with respect to the system volume V, namely $\partial\nu_n(\mathbf{k})/\partial V > 0$. This means that the corresponding force constants increase with V.

5.2 Application to model glass former SiO_2

In this section, the method to calculate thermal expansion is applied to the model glass former SiO_2. The basis for the calculations are the 165 atom glass structures after the classical quench and the subsequent quantum mechanical relaxation, as explained in section 4.2. Following the considerations of section 4.3, the analysis is done for 5 independent glass structures generated with the BKS potential and 5 configurations generated with the CHIK potential. Additionally, the thermal expansion is calculated for 10 independent configurations generated by the BKS and the CHIK potential, where all calculations are done with respect to the classical force fields (see section 4.3). As explained in section 5.1, it is necessary to calculate the vibrational properties of the same structural configuration at different system volumes. Therefore, the densities of the configurations are manually changed to $\rho = 2.1\,\mathrm{g/cm^3}$, $\rho = 2.3\,\mathrm{g/cm^3}$ and $\rho = 2.4\,\mathrm{g/cm^3}$, corresponding to box lengths of $L_{\mathrm{Box}} = 13.7737\,\text{Å}$, $L_{\mathrm{Box}} = 13.3623\,\text{Å}$ and $L_{\mathrm{Box}} = 13.17407\,\text{Å}$. In case of the classical force fields, the system density of $\rho = 2.0\,\mathrm{g/cm^3}$ is included, as well, in all calculations. The latter corresponds to a box length of $L_{\mathrm{Box}} = 13.99954\,\text{Å}$. In case of the DFT forces, the additional system densities of $\rho = 2.0\,\mathrm{g/cm^3}$, $\rho = 2.15\,\mathrm{g/cm^3}$, $\rho = 2.22\,\mathrm{g/cm^3}$, $\rho = 2.23\,\mathrm{g/cm^3}$, $\rho = 2.25\,\mathrm{g/cm^3}$ and $\rho = 2.275\,\mathrm{g/cm^3}$ are examined for one glass configuration, generated with the BKS potential. These densities correspond to box lengths of $L_{\mathrm{Box}} = 13.99954\,\text{Å}$, $L_{\mathrm{Box}} = 13.6661\,\text{Å}$, $L_{\mathrm{Box}} = 13.52173767\,\text{Å}$, $L_{\mathrm{Box}} = 13.501\,\text{Å}$, $L_{\mathrm{Box}} = 13.4606\,\text{Å}$ and $L_{\mathrm{Box}} = 13.411\,\text{Å}$. In each case, a structural relaxation at constant box size is performed by means of a conjugate gradient algorithm [111]. Again, the VASP software package [77–79] is used in case of DFT forces and the LAMMPS package [60, 61] is employed in case of the classical force fields. The computational details and DFT parameters are the same as in section 4.2 for the structural relaxation. The vibrational properties are calculated with the "frozen phonon" method, using the Phonopy package [90, 91]. The respective parameters are the same as in section 4.3. Again, the atomic displacements are $d = 0.02\,\text{Å}$ and the thermodynamic properties are evaluated according to the eigenfrequencies $\nu_n(\mathbf{k})$, $n \in \{1, \ldots, 3N\}$, on a k-mesh with a grid of 15 points along each of the $\mathbf{k}$-axes.

In Fig. 5.1, the Helmholtz free energy $F(T, V)$ is shown at 0 K and 500 K, according to equation (5.3). Calculations are done with respect to quantum mechanical forces for one glass configuration of the BKS potential after the structural relaxation. Here, the configuration is chosen

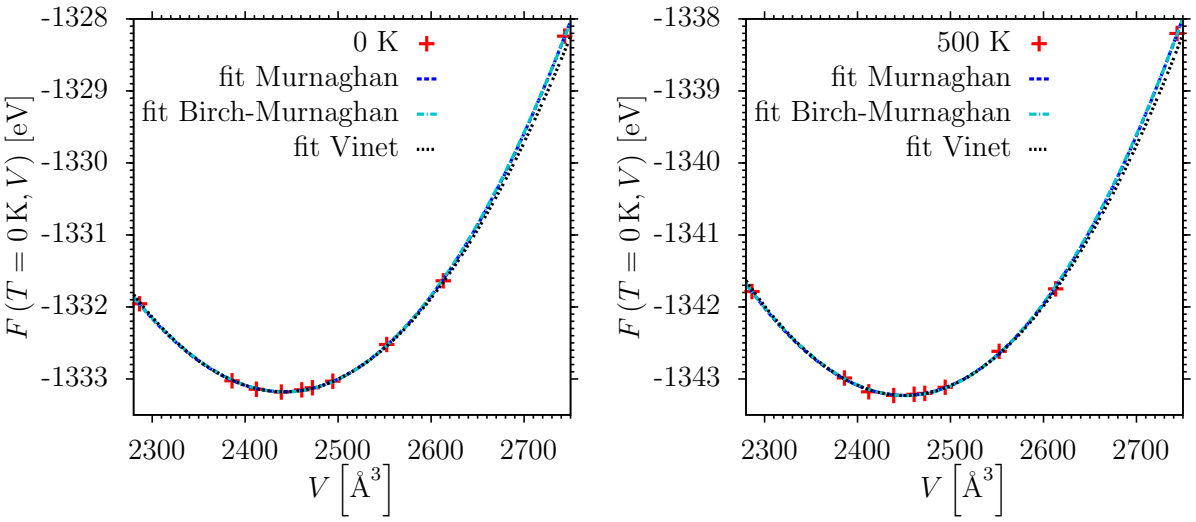

FIGURE 5.1: Helmholtz free energy $F\,(T,V)$ of one glass configuration SiO_2 at different temperatures, DFT forces.

where the 10 different system densities are studied. To determine $\min_{\mathrm{V}}\left[F\,(T,V)\right]$ at a given temperature, parameter fits to theoretical curves are conducted. Three different theoretical equations of states $E\,(V)$ are considered that describe the dependence of the volume of a solid on external pressure. The simplest theoretical form is the so-called Murnaghan equation of state [126], based on the assumption that the bulk modulus at constant temperature (see equation (4.7)) is a linear function of the pressure ($K = K_0 + p\,K_0'$). Here, K_0 is the bulk modulus at zero external pressure $p = 0$ and K_0' is the first derivative of the bulk modulus evaluated at zero external pressure $\frac{\partial K}{\partial p}|_{\mathrm{p=0}}$. A generalization of the latter, including the effects of finite strain in crystals, is the so-called Birch-Murnaghan equation of state [127]. The third functional form is the so-called Vinet equation of state [128]. It is based on a study of universal features in the energetics of metals and theoretical arguments are given that it holds for all classes of solids also at temperatures $T > 0$ in the absence of phase transitions. The functional forms of the three equations of state are the following:

$$E\,(V) = E_0 + \frac{K_0\,V}{K_0'}\left[\left(\frac{V_0}{V}\right)^{K_0'}\frac{1}{K_0'-1}+1\right] - \frac{K_0\,V_0}{K_0'-1}, \tag{5.10}$$

$$E\,(V) = E_0 + \frac{9\,K_0\,V_0}{16}\left\{\left[\left(\frac{V_0}{V}\right)^{\frac{2}{3}}-1\right]^3 K_0' + \left[\left(\frac{V_0}{V}\right)^{\frac{2}{3}}-1\right]^2\left[6-4\left(\frac{V_0}{V}\right)^{\frac{2}{3}}\right]\right\}, \tag{5.11}$$

$$E\,(V) = E_0 + \frac{9\,K_0\,V_0}{\left(\left(\frac{3}{2}\right)\,(K_0'-1)\right)^2}\left\{1+\left[\left(\frac{3}{2}\right)\,(K_0'-1)\left(1-\left(\frac{V}{V_0}\right)^{\frac{1}{3}}\right)-1\right]\exp\left[A\right]\right\}, \tag{5.12}$$

$$A = \frac{3}{2}\,(K_0'-1)\left[1-\left(\frac{V}{V_0}\right)^{\frac{1}{3}}\right]. \tag{5.13}$$

In Fig. 5.1, it can be seen that at both temperatures all three different equations of state show

a good agreement with the discrete set data points of $F(T,V)$ at the 10 considered system densities. The differences between the shape of the fitted curves is rather small, especially around the minimum value V_0. As a second check, the parameter fit is repeated based only on 4 discrete points of $F(T,V)$ at the system densities $\rho = 2.1\,\mathrm{g/cm^3}$, $\rho = 2.2\,\mathrm{g/cm^3}$, $\rho = 2.3\,\mathrm{g/cm^3}$ and $\rho = 2.4\,\mathrm{g/cm^3}$ of the same configuration, again at $T = 0\,\mathrm{K}$ and $T = 500\,\mathrm{K}$.

10 data points, 0 K	V_0 [Å^3]	E_0 [eV]	K_0 [GPa]	K_0' [ ]
Murnaghan [126]	2441.68	-1333.18	40.49	-2.10
Birch-Murnaghan [127]	2442.88	-1333.18	41.29	-2.86
Vinet [128]	2441.65	-1333.18	40.48	-2.09
4 data points, 0 K	V_0 [Å^3]	E_0 [eV]	K_0 [GPa]	K_0' []
Murnaghan [126]	2440.56	-1333.18	40.45	-1.16
Birch-Murnaghan [127]	2440.56	-1333.18	40.87	-1.13
Vinet [128]	2440.56	-1333.18	40.44	-1.16
10 data points, 500 K	V_0 [Å^3]	E_0 [eV]	K_0 [GPa]	K_0' []
Murnaghan [126]	2450.49	-1343.23	43.38	-2.42
Birch-Murnaghan [127]	2451.64	-1343.23	44.45	-3.08
Vinet [128]	2450.48	-1343.23	43.38	-2.41
4 data points, 500 K	V_0 [Å^3]	E_0 [eV]	K_0 [GPa]	K_0' []
Murnaghan [126]	2451.33	-1343.22	42.70	-2.44
Birch-Murnaghan [127]	2451.15	-1343.22	43.36	-2.22
Vinet [128]	2451.33	-1343.22	42.70	-2.44

TABLE 5.2: Fit parameters V_0, E_0, K_0 and K_0' for fits of different equations of state $E(V)$ to the numerical values of $F(T,V)$, based on DFT forces. One glass configuration, generated with the BKS potential, after the structural relaxation. Fits to all 10 and 4 data points at $T = 0\,\mathrm{K}$ and $T = 500\,\mathrm{K}$.

In Table 5.2, the values of the parameters V_0, E_0, K_0 and K_0' are exemplarily shown for this configuration at $T = 0\,\mathrm{K}$ and $T = 500\,\mathrm{K}$ for the fits to 4 and to 10 data points. In all cases, the differences of the fit parameters for the different equations of state $E(V)$ are small. Regarding the different parameters, the biggest deviation is visible in the value of K_0', which is the parameter with the largest asymptotic standard error of about $10 - 20\,\%$. In general, the parameters, according to the Murnaghan equation of state [126] are nearly identical to the ones, according to the Vinet equation of state [128], in all cases.

Regarding the thermal expansion, the dependence of the fit parameter V_0 on the temperature T is of the greatest interest. In Fig. 5.2, the $V(T)$ curve is shown for the parameter fits to the 4 and 10 different system densities of this specific glass configuration, according to the Vinet equation of state (equation (5.12)). In Fig. 5.3, $V(T)$ is shown for parameter fits to the 10 different system densities, according to the three different equations of state (equations (5.10) to (5.12)). Regarding the different equations of state, nearly no differences are visible between the three curves. The differences are largest for small temperatures. Here, the curves according to the Vinet [128] and the Murnaghan [126] equation of state are virtually on top of each other and

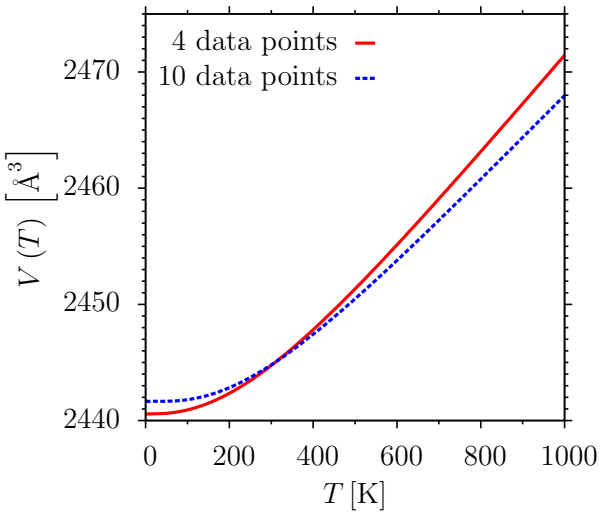

FIGURE 5.2: $V(T)$ of one glass configuration SiO_2. Evaluation according to 4 and 10 different system densities, DFT forces, Vinet equation of state (equation (5.12)).

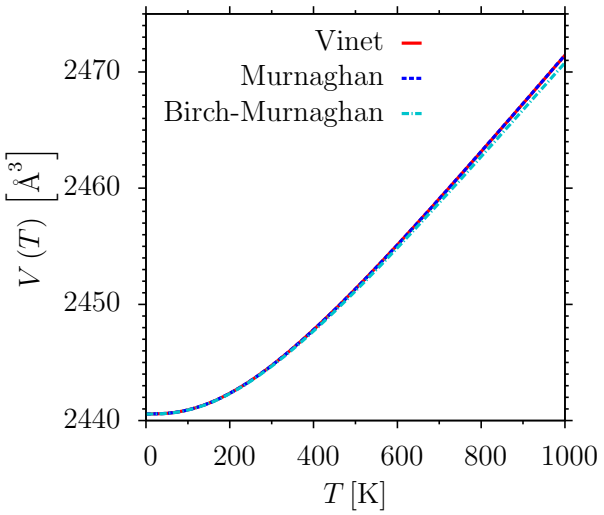

FIGURE 5.3: $V(T)$ of one glass configuration SiO_2. Evaluation according to different equations of state (equations (5.10) to (5.12)), DFT forces, 4 data points.

the curve, according to the Birch-Murnaghan equation of state [127] shows slight differences. Regarding the different number of system densities, the deviations between the two curves are larger. The curve fitted to 4 system densities is slightly steeper than the curve according to the 10 different densities.

In the following, all calculations are based on a fit with respect to the Vinet equation of state (equation (5.12)). This is clearly justified by the previous considerations as the differences, according to the different equations of state, are small. Regarding the number of system densities, a higher number of data points for each configuration would be desirable. So far, only calculations, according to 4 different system densities, have been conducted for all considered configurations. However, the previous considerations suggest that the error due to the limited number of data points is controllable.

In Fig. 5.4, the $V(T)$ curves are displayed for the 5 independent glass configurations generated with the BKS and the CHIK potential, using DFT forces. The parameter fits are conducted in the way described above, employing the Vinet [128] equation of state and the free energies $F(T,V)$ of the 4 different system densities $\rho = 2.1\,\mathrm{g/cm^3}$, $\rho = 2.2\,\mathrm{g/cm^3}$, $\rho = 2.3\,\mathrm{g/cm^3}$ and $\rho = 2.4\,\mathrm{g/cm^3}$. In Fig. 5.5, the curves of the BKS and the CHIK potential are shown, according to the classical force fields. Again, the Vinet [128] equation of state is employed and, in this case, 5 different system densities are studied, namely $\rho = 2.0\,\mathrm{g/cm^3}$, $\rho = 2.1\,\mathrm{g/cm^3}$, $\rho = 2.2\,\mathrm{g/cm^3}$, $\rho = 2.3\,\mathrm{g/cm^3}$ and $\rho = 2.4\,\mathrm{g/cm^3}$. For either classical potential, the dependence of the volume on the temperature exhibits differences between the different glass samples, both, with respect to the equilibrium volume at a given temperature, as well as the gradient of the curves. The volume, according to $\min_V [F(T,V)]$ at 0 K, corresponds to system densities from $2.25\,\mathrm{g/cm^3}$ to $2.30\,\mathrm{g/cm^3}$ for the BKS potential and to system densities from to $2.25\,\mathrm{g/cm^3}$ for $2.29\,\mathrm{g/cm^3}$ the CHIK potential, in case of the DFT forces. In case of the classical force fields, the corresponding system densities

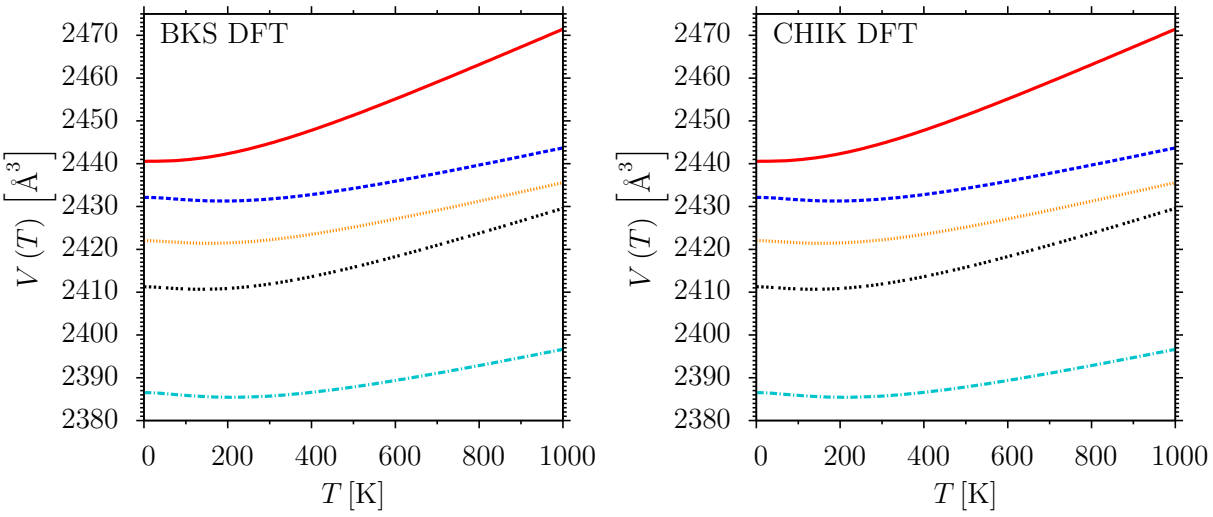

FIGURE 5.4: $V(T)$ of 5 different glass configurations SiO_2. BKS and CHIK potential, DFT forces.

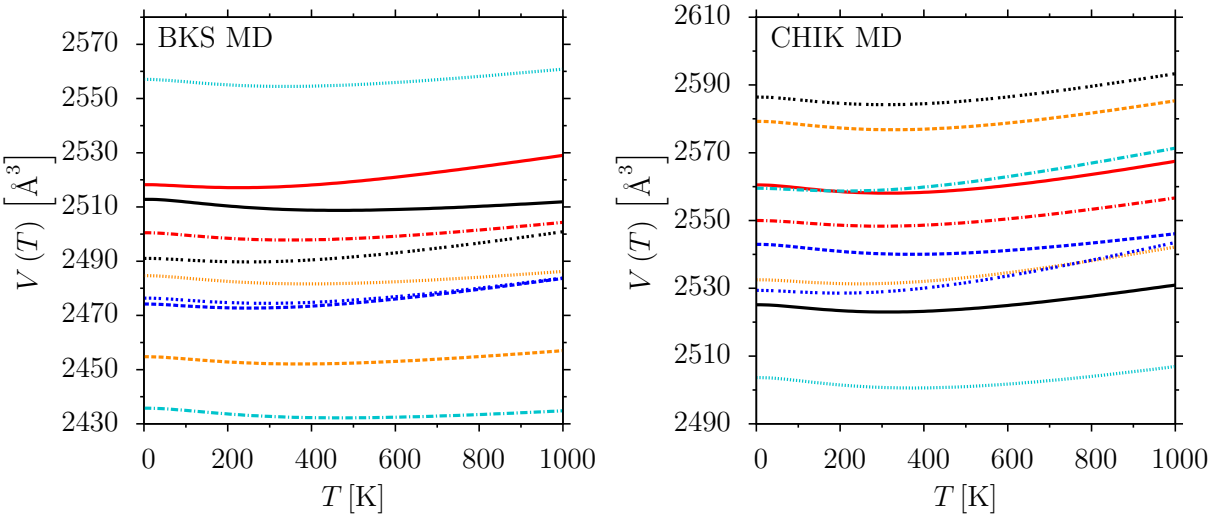

FIGURE 5.5: $V(T)$ of 10 different glass configurations SiO_2. BKS and CHIK potential, classical forces.

are located between 2.15 g/cm³ and 2.25 g/cm³ for the BKS potential and between 2.12 g/cm³ and 2.17 g/cm³ for the CHIK potential.

In Figs. 5.6 and 5.7, the linear expansion coefficients $\alpha_L(T) = \frac{1}{L}\left(\frac{\partial L}{\partial T}\right)_p$ of the latter glass configurations are shown. For isotropic systems, the linear expansion coefficient is about one third of the volumetric expansion coefficient (see equation (4.7)) $\alpha_L(T) = 1/3\,\alpha_V(T)$ within the order of $\mathcal{O}(\Delta T)$. The volumetric expansion coefficients are obtained by means of numerical derivatives of the $V(T)$ curves. Again, there are distinct differences visible between the curves of the different independent samples, in all cases. For example, at room temperature, the numerical values of $\alpha_L(T)$ lie in a range between $0.8 \cdot 10^{-6}$ 1/K and $3.8 \cdot 10^{-6}$ 1/K for the BKS potential and between $0.8 \cdot 10^{-6}$ 1/K and $2.8 \cdot 10^{-6}$ 1/K for the CHIK potential, in case of the DFT forces. In case of the classical forces, the respective values lie in a range between $-1.0 \cdot 10^{-6}$ 1/K and $0.7 \cdot 10^{-6}$ 1/K for the BKS potential and between $-0.6 \cdot 10^{-6}$ 1/K and $1.0 \cdot 10^{-6}$ 1/K for the CHIK potential.

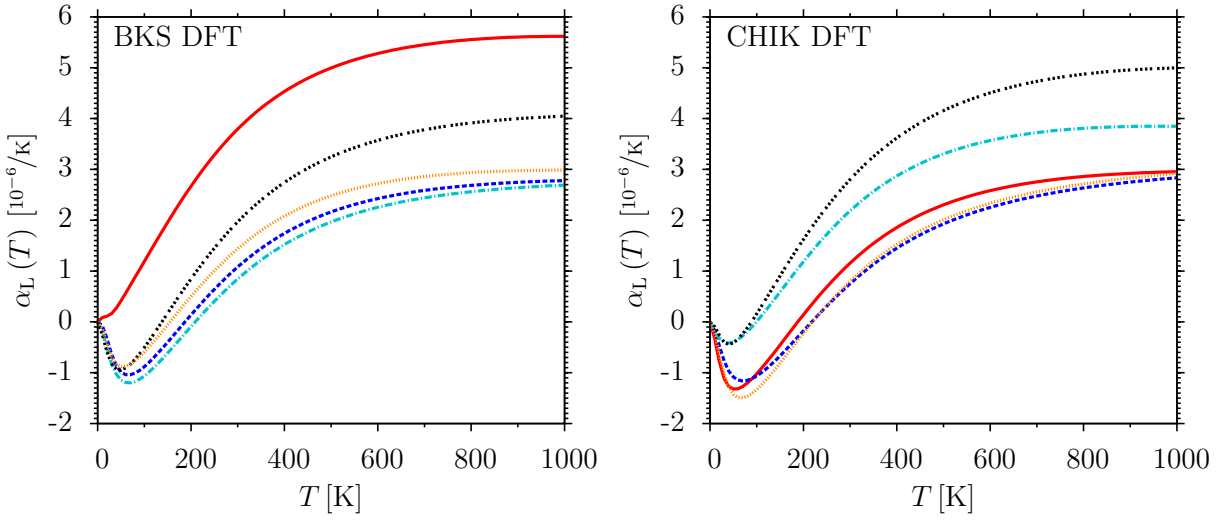

FIGURE 5.6: Linear expansion coefficient $\alpha_L(T)$ of 5 different glass configurations SiO_2. BKS and CHIK potential, DFT forces.

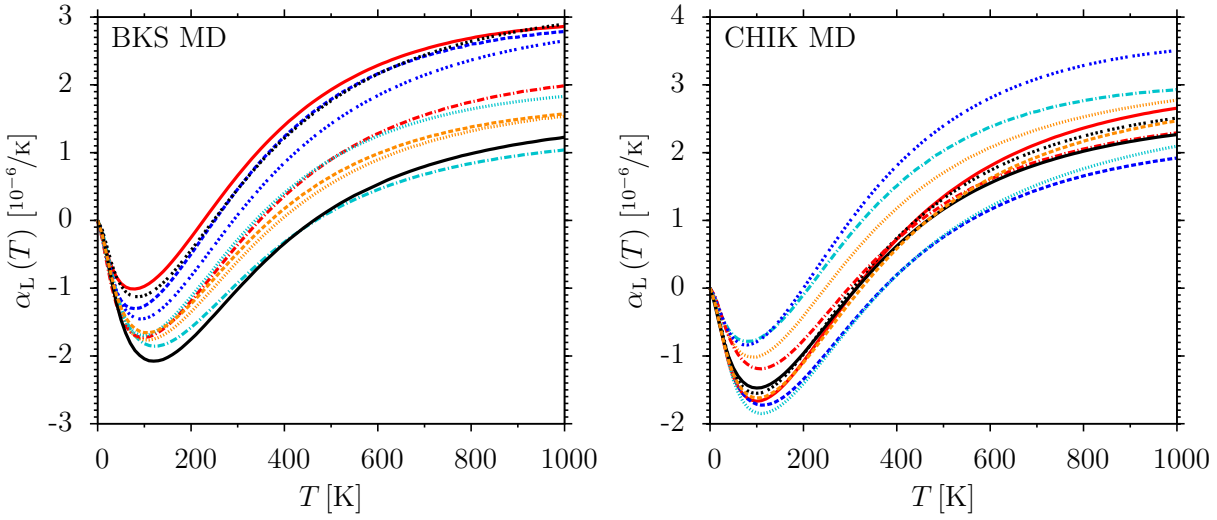

FIGURE 5.7: Linear expansion coefficient $\alpha_L(T)$ of 10 different glass configurations SiO_2. BKS and CHIK potential, classical forces.

Regarding the shapes of the DFT curves, in case of the BKS potential, all configurations but one show a change of sign of α_L and a regime of negative thermal expansion in the low temperature regime below about $140-200\,\mathrm{K}$. In case of the CHIK potential, this behavior is apparent for all configurations at temperatures below about $100-200\,\mathrm{K}$. It is remarkable that this temperature regime of negative thermal expansion is apparent in all curves of the classical force fields, both, in case of the BKS potential (below about $225-470\,\mathrm{K}$) and in case of the CHIK potential (below about $200-370\,\mathrm{K}$). At higher temperatures, the linear expansion coefficients in all cases show a steady increase until reaching a plateau value at about $1000\,\mathrm{K}$. The range of the plateau values is less pronounced and lies in a range between about $2.7\cdot10^{-6}\,1/\mathrm{K}$ and $5.6\cdot10^{-6}\,1/\mathrm{K}$ for the BKS and about $2.8\cdot10^{-6}\,1/\mathrm{K}$ and $5.0\cdot10^{-6}\,1/\mathrm{K}$ for the CHIK potential, in case of the DFT forces. In case of the classical forces, the plateau values lie in a range between $1.0\cdot10^{-6}\,1/\mathrm{K}$ and $2.9\cdot10^{-6}\,1/\mathrm{K}$ for the BKS potential and between $1.9\cdot10^{-6}\,1/\mathrm{K}$ and $3.5\cdot10^{-6}\,1/\mathrm{K}$ for the CHIK

potential.

As described in the previous section, the temperature range of negative thermal expansion is connected to a negative sign of the macroscopic Grüneisen parameters and mode Grüneisen parameters. The macroscopic Grüneisen parameters, according to equation (5.9), in each case have a negative sign in the temperature range where the linear expansion coefficients $\alpha_{\mathrm{L}}(T)$ get negative (see Figs. 5.6 and 5.7). As already mentioned before, this is the case in all independent configurations except for one glass configuration generated with the BKS potential and employing quantum mechanical forces. To get a better understanding of the underlying mechanism, the mode Grüneisen parameters γ_n are calculated, according to equation (5.6). This is done in the following way. For each vibrational mode $n \in \{1, \ldots, 3N\}$, a quadratic fit of ν_n with respect to the system volume V is conducted

$$f_n(V) = a_n + b_n \, (V - x_{0,n})^2 \,, \tag{5.14}$$

taking into account the system volumes corresponding to the system densities used for the determination of $V(T)$. After the parameter fit, according to equation (5.14), in each case, the numerical value of γ_n is approximated in the following way:

$$\gamma_n \simeq -\frac{V_0}{f_n(V_0)} \left.\frac{\partial f_n(V)}{\partial V}\right|_{V=V_0} = -\frac{V_0}{a_n + b_n \, (V_0 - x_{0,n})^2} \, 2\, b_n \, (V_0 - x_{0,n}) \,. \tag{5.15}$$

Here, V_0 is the equilibrium volume of the system at 0 K, determined by means of the Vinet equation of state [128]. Of course this is an approximation. However, regarding the discrete set of system volumes at which the eigenfrequencies ν_n are calculated, this method gives more reliable results than using a standard scheme of numerical differentiation, like $\frac{\partial \nu_n(V)}{\partial V} \simeq \frac{\nu_n(V+\Delta V) - \nu_n(V)}{\Delta V}$ or $\frac{\partial \nu_n(V)}{\partial V} \simeq \frac{\nu_n(V+\Delta V) \nu_n(V-\Delta V)}{2\,\Delta V}$. Here, only the numerical values at 2 discrete system volumes are taken into account. In the following, the analysis of the mode Grüneisen parameters γ_n is presented, with the restriction to the numerical values at the Gamma-point ($\mathbf{k} = (0,0,0)^T$).

In Fig. 5.8, the dependence of the eigenfrequencies on the volume is exemplarily shown for the eigenmodes $n = 4$ and $n = 5$ for two different glass configurations generated with the BKS potential, using DFT forces. Additionally, the quadratic fits $f_n(V)$, according to equation (5.14), are shown. The equilibrium volumes at 0 K are (1: $V_0 = 2440.56\,\text{Å}^3$, 2: $V_0 = 2432.12\,\text{Å}^3$). The lowest 3 eigenfrequencies are not displayed as the first 3 eigenmodes are so-called soft modes or Goldstone bosons and are related to the lattice translations in 3 dimensions [93]. At the Gamma-point ($\mathbf{k} = (0,0,0)^T$), the corresponding eigenfrequencies should be equal to zero [93]. In practice, they show slight imaginary values due to numerical inaccuracies. The glass configuration 1 is the one configuration that does not show a change of sign of α_{L} and a range of negative thermal expansion. In Fig. 5.8, it can be seen that it makes sense to include the

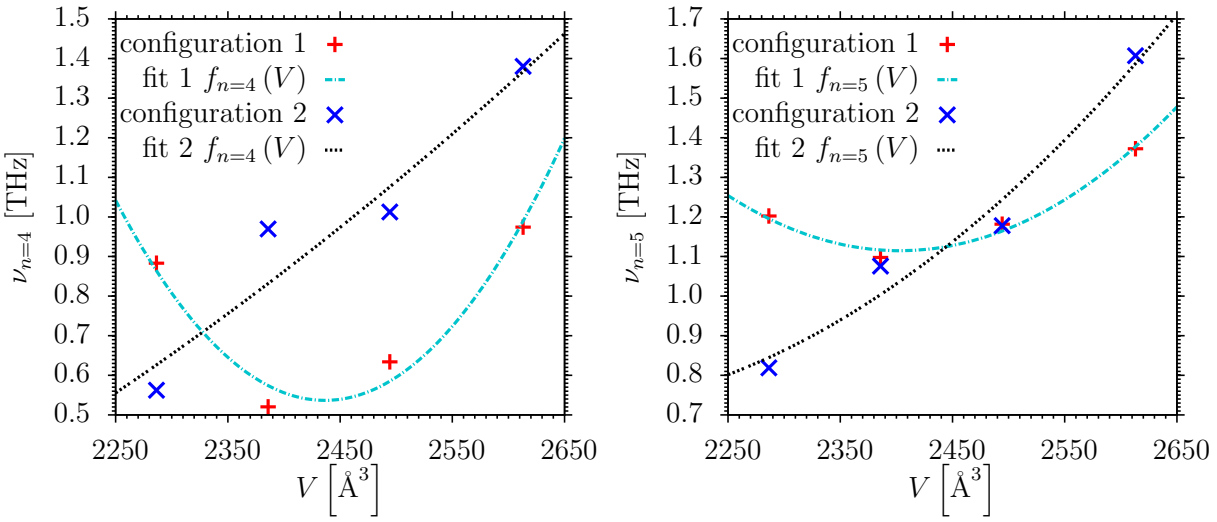

FIGURE 5.8: eigenfrequencies ν_n with respect to V. Mode $n = 4$ and $n = 5$. Two configurations of SiO_2 according to BKS potential, DFT forces.

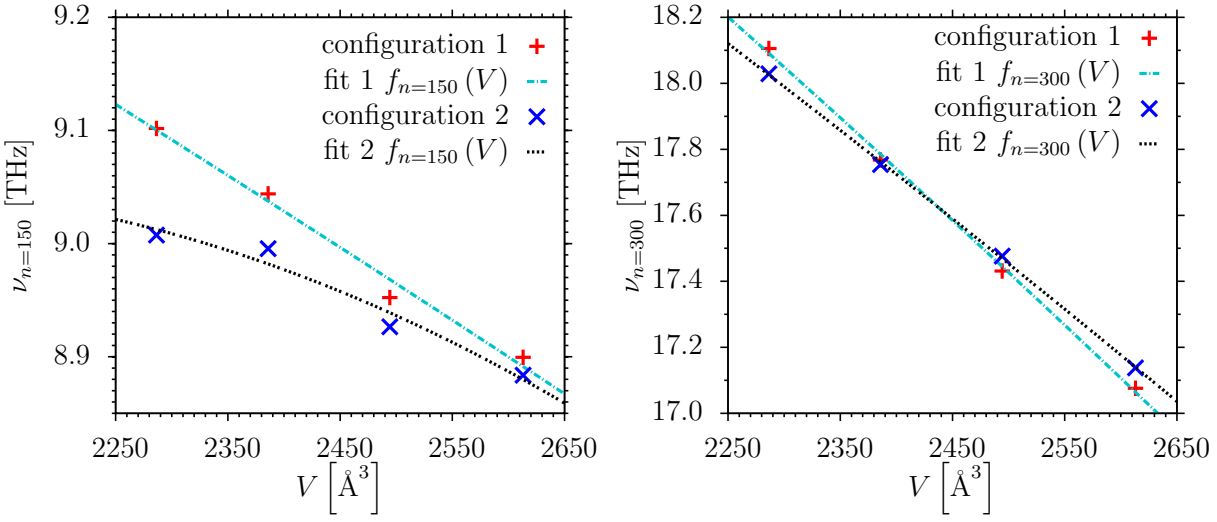

FIGURE 5.9: eigenfrequencies ν_n with respect to V. Mode $n = 150$ and $n = 300$. Two configurations of SiO_2 according to BKS potential, DFT forces.

numerical value of ν_n at all system volumes into the determination of γ_n and that a quadratic fit is an acceptable method. Due to the definition of the mode Grüneisen parameters γ_n (equation (5.6)), a positive slope of $f_n(V_0)$ at the equilibrium volume V_0 leads to a negative value of the respective γ_n and vice versa. In the case of glass configuration 1, the slope of $f_n(V)$ changes, in contrast to a monotonous increasing behavior in the case of glass configuration 2 in the range of the examined system volumes V. This is the case also for the other low frequency eigenmodes ν_n and the other 3 glass configurations of the BKS potential with DFT forces, not displayed here, show a similar behavior as glass configuration 2. This difference in the volume dependence of $\nu_n(V)$ could explain the deviating behavior of glass configuration 1 with respect to the missing change of sign of α_L and temperature range of negative thermal expansion. However, this explanation is speculative. In Fig. 5.9, the same investigation is carried out for two eigenmodes

($n = 150$ and $n = 300$) in a frequency range where all 5 different glass configurations show a similar behavior and the corresponding mode Grüneisen parameters γ_n are positive, in all cases. Here, the quadratic fits $f_n(V)$ show a monotonous increasing behavior in both cases (glass configurations 1 and 2), leading to a positive γ_n. Again, the other 3 glass configurations, not displayed here, show a similar behavior.

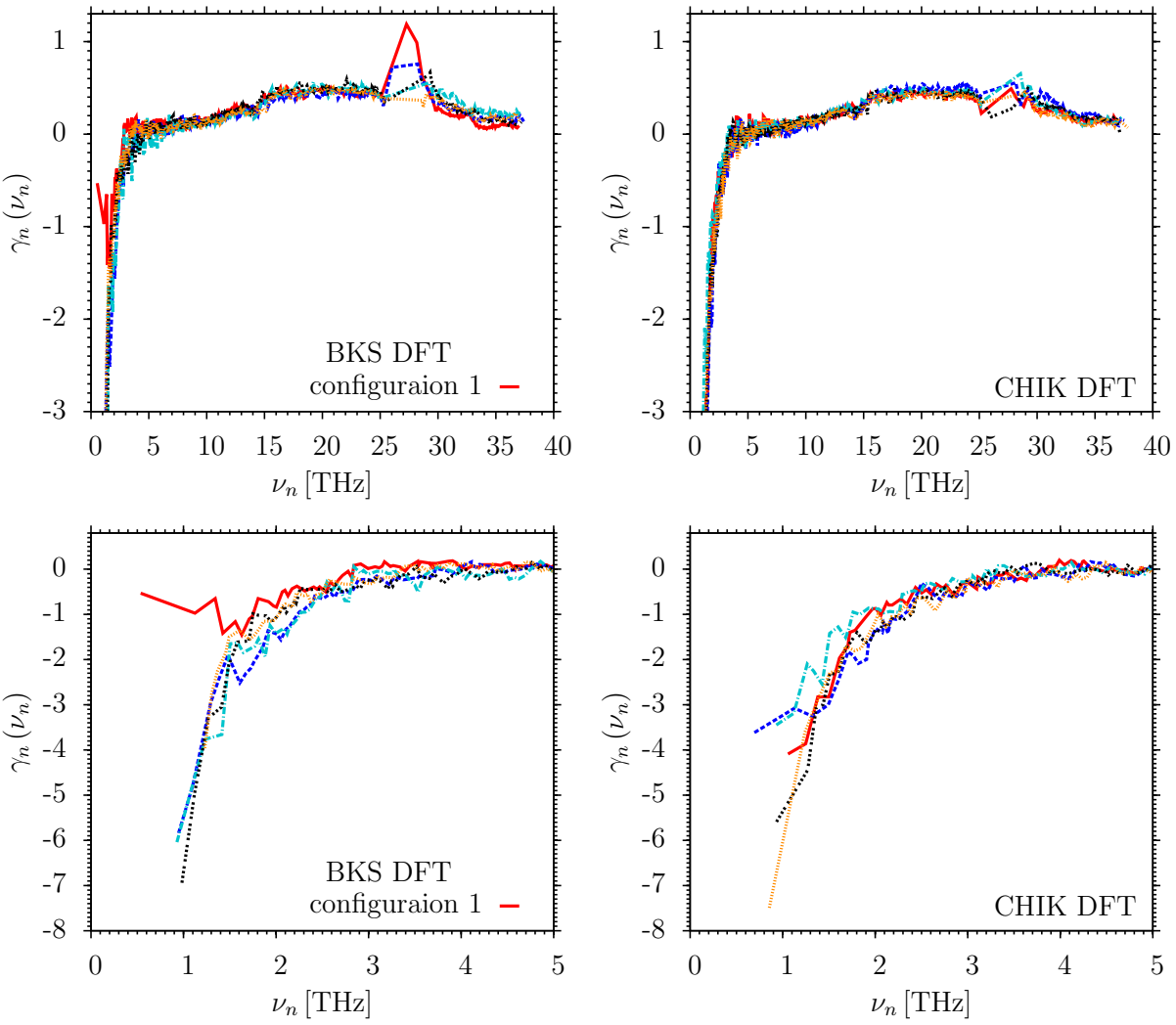

FIGURE 5.10: Mode Grüneisen parameters γ_n of 5 different glass configurations SiO_2. BKS and CHIK potential, DFT forces.

In Figs. 5.10 and 5.11, the mode Grüneisen parameters $\gamma_n(\mathbf{k})$ at $\mathbf{k} = (0,0,0)^T$ are plotted against the eigenfrequencies ν_n for all examined glass configurations, using DFT and classical forces. The numerical values of γ_n are calculated, according to equation (5.15) and the numerical values of ν_n are calculated, according to the quadratic fits (equation (5.14)) evaluated at the equilibrium volumes, namely $f_n(V_0)$. Again, the lowest 3 eigenfrequencies are not displayed. It can be seen that the microscopic Grüneisen parameters γ_n of the eigenmodes with low eigenfrequencies have a negative sign for all examined glass configurations. In case of the one glass structure (configuration 1, BKS potential, DFT forces) that does not show a temperature range with

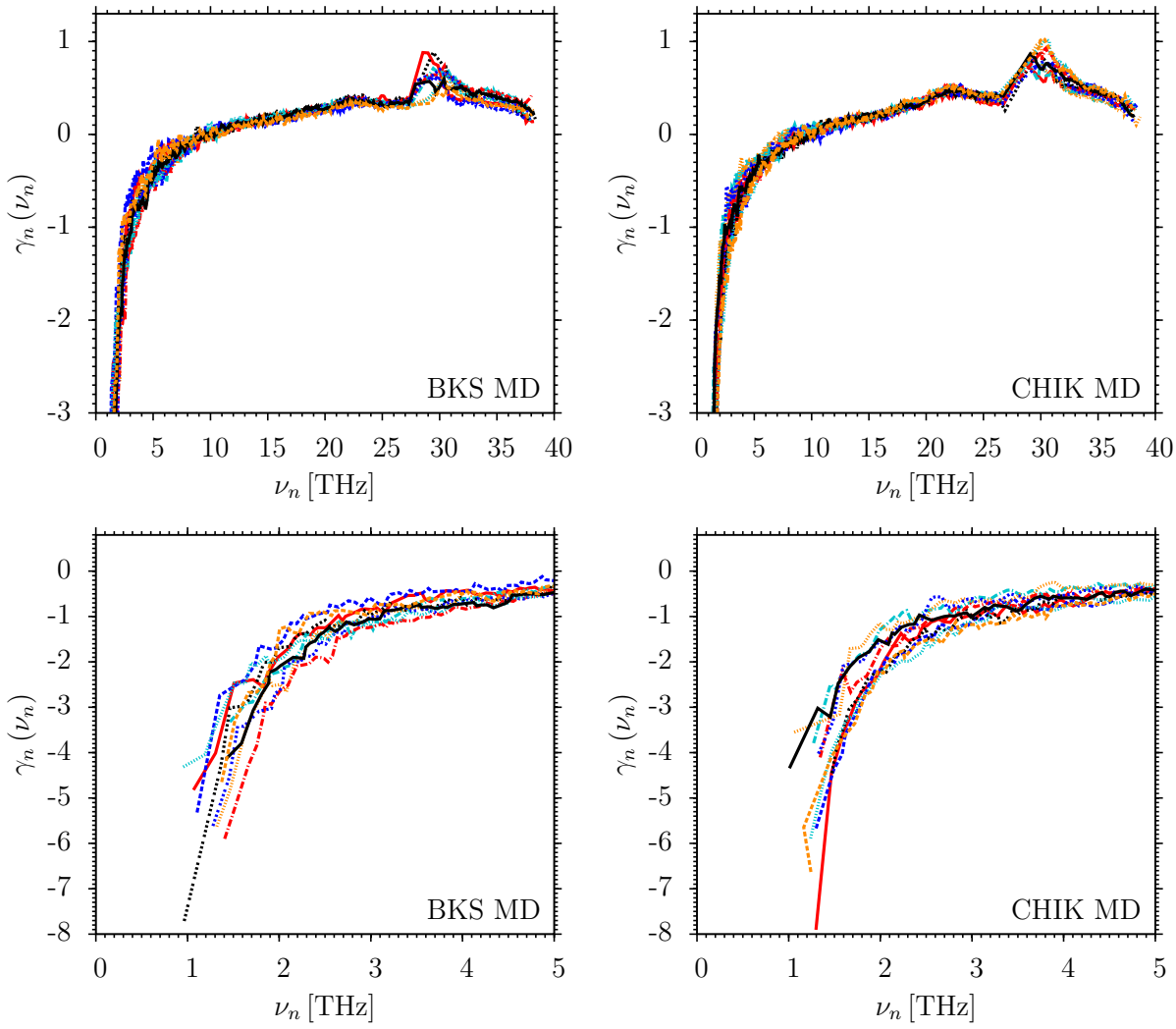

FIGURE 5.11: Mode Grüneisen parameters γ_n of 10 different glass configurations SiO_2. BKS and CHIK potential, classical forces.

negative thermal expansion, the magnitude of the negative value of γ_n for the lowest eigenmodes is significantly smaller as in case of the other glass configurations (see Fig. 5.10).

In Figs. 5.12 and 5.13, the average linear expansion coefficients $\alpha_{\mathrm{L}}(T)$ are shown. The error bars displayed are the the standard deviation of the mean with respect to the N independent configurations: $\overline{\sigma} = \frac{\sigma}{\sqrt{N}}$. First, they are compared to measurements of the NIST standard reference material 739 [32] down to 80 K with an experimental error of about $\pm 0.03 \cdot 10^{-6}\,\mathrm{K}^{-1}$. This material is synthetically fused silica, annealed at 1373 K and then cooled to 1173 K at 12 K per hour. Second, the calculated $\alpha_{\mathrm{L}}(T)$ are compared to low-temperature measurements down to 10 K of Spectrosil which is synthetically fused silica and Vitreosil, which is electrically fused from quartz powder, both, annealed at 1400 C° [33]. Here, the experimental error is about $\pm 0.01 \cdot 10^{-6}\,\mathrm{K}^{-1}$ below 30 K and about $\pm 0.1 \cdot 10^{-6}\,\mathrm{K}^{-1}$ for higher temperatures. In the low-temperature regime, in fact, the curves of these different materials are identical. All measurements show a range of negative thermal expansion below about 200 K with a minimum of approximately $-0.8 \cdot 10^{-6}\,\mathrm{K}^{-1}$ at about 50 K. Afterwards, $\alpha_{\mathrm{L}}(T)$ increases until it reaches a

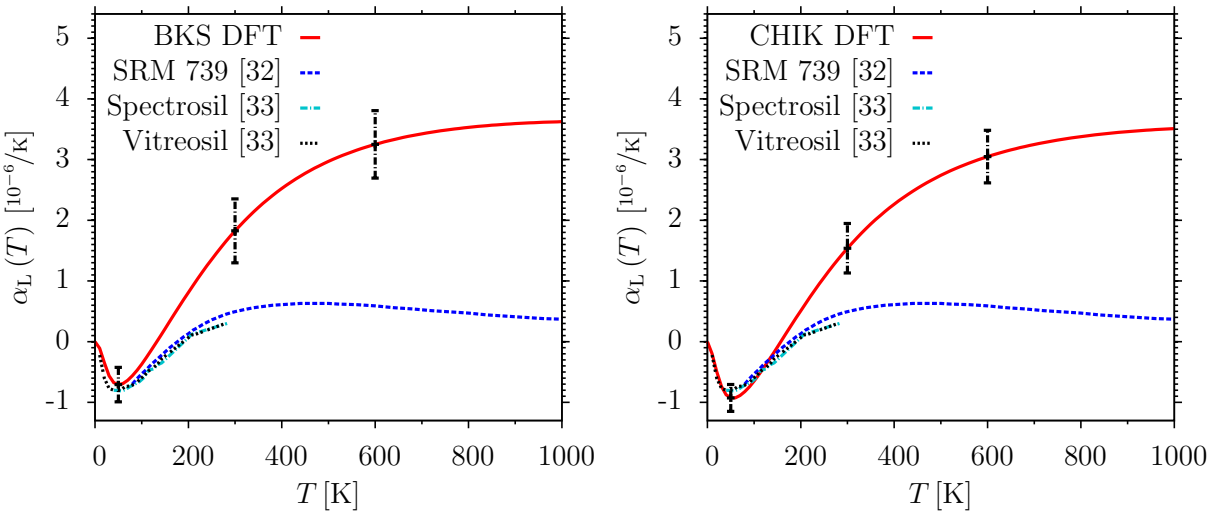

FIGURE 5.12: Average linear expansion coefficient $\alpha_L(T)$, SiO_2. BKS and CHIK potential, DFT forces. Comparison with experimental measurements of NIST Standard Reference Material 739, Spectrosil and Vitreosil [32, 33].

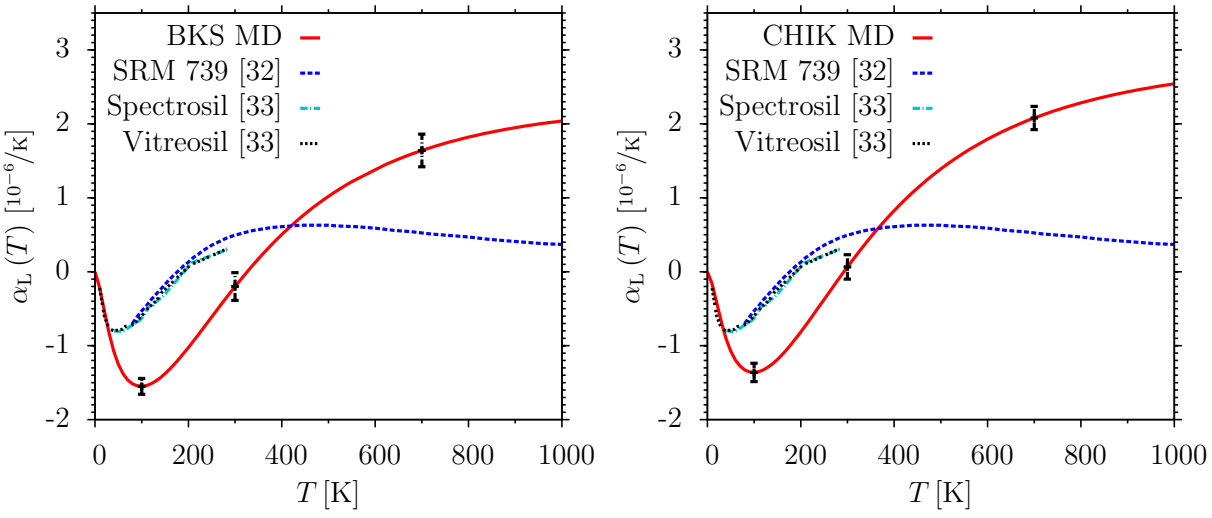

FIGURE 5.13: Average linear expansion coefficient $\alpha_L(T)$, SiO_2. BKS and CHIK potential, classical forces. Comparison with experimental measurements of NIST Standard Reference Material 739, Spectrosil and Vitreosil [32, 33].

maximum of about $0.63 \cdot 10^{-6}\,\mathrm{K}^{-1}$ at approximately 450 K with a subsequent steady decrease. In Fig. 5.12, it can be seen that the agreement of the calculated $\alpha_L(T)$ with the experimental values is quite good in the low-temperature regime below 200 K in both cases for the DFT forces. At higher temperatures, the increase of $\alpha_L(T)$ of the calculated curves is significantly steeper, compared to the experimental results, leading to a value of $\alpha_L(T)$ at 1000 K that is about one order of magnitude higher than the corresponding experimental value. In case of the classical forces, the behavior is similar in both cases (see 5.13). However, the agreement at low temperatures is significantly inferior compared to the DFT curves, as the range of negative thermal expansion is more extended in both cases. This behavior is slightly more apparent in the $\alpha_L(T)$ curve, according to the BKS forces.

As already explained in section 4.3, calculating the vibrational properties employing the harmonic approximation is only valid at low temperatures as at higher temperatures anharmonic effects become more important. The calculation of the thermal expansion is based on these harmonic vibrational properties. Therefore, it is understandable that the agreement with experimental results gets inferior at higher temperatures. The observed range of negative thermal expansion is connected to the network structure of vitreous silica, as it is for example not observed in crystalline α-quartz [129]. One explanation is that it comes from the low frequency vibrational modes of the oxygen atoms vibrating normal to the Si-O-Si interconnection between two neighboring tetrahedra [130]. This explanation is consistent with the observation of the negative mode Grüneisen parameters γ_n at low eigenfrequencies. It is striking that the range of negative thermal expansion is apparent, as well, for the calculations based on the classical forces. However, one should be aware of the fact that the theoretical considerations underlying the calculation of $\alpha_\mathrm{L}(T)$ are based on the theoretical description of $3N$ independent quantum mechanical harmonic oscillators (see section 5.1). This means that somehow, a quantum mechanical description is combined with inter-atomic forces from classical force fields.

Summarizing, in this chapter the temperature dependence of the system volume $V(T)$ is examined for the model glass former SiO_2, based on the quasi-harmonic approximation. Following the volume with minimal $F(T,V)$ (assumption of $p \simeq 0$), allows to obtain $V(T)$ and, subsequently, the linear thermal expansion coefficient $\alpha_\mathrm{L}(T)$. The striking observation is a change of sign of $\alpha_L(T)$, both, using quantum mechanical (DFT) forces and classical forces for all but one examined glass configuration. To my knowledge, this has not been reported before. The temperature range of negative thermal expansion is about 130 K to 160 K (quantum mechanical forces) and 290 K to 325 K (classical forces). In particular, in the low-temperature regime below about 200 K, the curves of $\alpha_L(T)$ due to the DFT forces show a very good agreement with experimental results [32, 33]. The change of sign in the thermal expansion can be explained by negative microscopic mode Grüneisen parameters γ_n at low eigenfrequencies.

Chapter 6

Model glass former B_2O_3

In this chapter, the simulation results of the model glass former B_2O_3 are summarized. As already emphasized in sections 2.2 and 2.4, the glass structure of pure B_2O_3 has the special feature that about $60\% - 80\%$ of the boron atoms are localized within planar rings, consisting of 3 boron and 3 oxygen atoms. These are called boroxol rings when the participating boron atoms are all 3-fold coordinated with respect to the oxygen atoms and the oxygen atoms are all 2-fold coordinated with respect to the boron atoms [31]. In section 6.1, different experiments are summarized, supporting the high fraction of boroxol rings in vitreous B_2O_3. Additionally, an overview over several previous classical molecular dynamics studies of boron oxide is given with classical potentials, as simple as pair potentials, up to complicated many-body potentials. In section 6.2, the results of Born-Oppenheimer molecular dynamics (MD) simulations based on quantum mechanical DFT forces are presented. Here, the structural and dynamical properties of liquid B_2O_3 in a temperature range between 3600 K and 2300 K are discussed. The latter is the lowest temperature at which the system still can be equilibrated by means of an ab initio MD simulation. The liquid structure at 2300 K shows an increased amount of rings containing 3 boron and 3 oxygen atoms, compared to the liquid structures at 2500 K and 2700 K. In section 6.3, the fitting of new force field parameters for classical MD simulations is discussed, using a modified form of the structural fitting procedure, described in [43]. Basis for the parameter fits is the ab initio MD trajectory at 2300 K. The inclusion of 3-body terms leads to improved results, regarding the accordance of the liquid properties of the classical MD and ab initio MD simulations. In section 6.4, the structural and dynamical properties of liquid B_2O_3 are examined, in detail, at different temperatures for the two most promising parameter sets after the structural fit in the previous section. Special focus is on the temperature dependence of certain structural quantities and the self-diffusion constants D_α, $\alpha \in \{B, O\}$. The latter show an unusual temperature dependence, not observed in case of the model glass former SiO_2. In section 6.5, a set of glass samples is analyzed, generated in different ways, namely by classical quenches from the melt with a subsequent quantum mechanical relaxation and by full ab initio quenches from different starting temperatures. The classical MD simulations are conducted with the two different parameter sets employed in section 6.4 and the original parameter set before

the structural fit. The structural properties of this set of glass structures are in reasonable agreement with experimental results from neutron scattering [29]. However, the boroxol ring fraction is significantly lower than the experimental prediction and varies from about $f = 2.5\%$ (one classical potential with 3-body terms) to $f = 15\%$ (full ab initio quench from 2300 K). In addition, a comparison to a structural model is presented, generated in an alternative way [131–133], where $f = 75\%$ of the boron atoms are located in boroxol rings. In section 6.6, the vibrational properties of the glass configurations are studied. The calculated vibrational spectra show an acceptable agreement with experimental results from inelastic neutron scattering [30, 134]. The significantly too low boroxol ring fraction is reflected in the significantly reduced intensity of the corresponding peak.

6.1 Experimental evidence for the existence of boroxol rings and overview over previous classical molecular dynamics simulations

First, a summary of different experiments is given, supporting the hypothesis of a boroxol ring fraction of about $60\% - 80\%$ in B_2O_3 glass. Second, an overview over several previous studies of boron oxide by means of classical MD simulations is given, including pair interactions and many-body potentials.

Regarding the experimental evidence of the existence of boroxol rings in vitreous B_2O_3, the first summary is given in [135]. Here, it is concluded that the best structural model is the one of a random three-dimensional network of BO_3 triangles with a high fraction of boroxol rings. One experimental evidence for the existence of boroxol rings comes from Raman measurements, showing a very sharp and pronounced peak in the horizontal-horizontal (HH) Raman spectrum at $808\,\mathrm{cm}^{-1} \hat{=} 24.2\,\mathrm{THz}$, where the polarization of the incident and the scattered laser beam are parallel [26]. This peak is assigned to the breathing mode of a symmetric boroxol ring. Regarding Raman measurements, in [36], the Raman spectrum of vitreous and liquid B_2O_3 is measured in a temperature range from room temperature to 1273 K. Here, a decrease of the boroxol ring fraction from about $f \simeq 0.62$ to $f \simeq 0.22$ at 1273 K is derived with an experimental error of $\triangle f \simeq 0.15$.

Another independent evidence comes from nuclear magnetic resonance (NMR) measurements. In [136], ^{10}B, ^{11}B and ^{17}O NMR is used to study the respective chemical environment in B_2O_3 glass. From the ^{17}O spectra the presence of two distinct oxygen sites is predicted of oxygen atoms within and outside of boroxol rings. From this, a boroxol ring fraction of $f \simeq 0.82 \pm 0.08$ is deduced. In [137], a boroxol ring fraction of $f \simeq 0.7$ is derived from ^{11}B dynamic angle spinning (DAS) NMR results. This value is in agreement to ^{17}O high-resolution magic angle spinning (MAS) NMR measurements, reported [138]. Here, a value of 0.5 ± 0.1 is reported for the fraction of oxygen atoms in boroxol rings, corresponding to $f = 0.75 \pm 0.15$.

In addition, X-ray and neutron diffraction experiments are in good agreement with model structures, containing a high amount of boroxol rings. In [139], the real space correlation function $T(r)$ derived from X-ray diffraction is found to be in good agreement with a structural model containing a high fraction of B atoms localized within boroxol rings. In [140] it is stated that a model structure with $f \simeq 0.6 \pm 0.2$ shows the best agreement with the $T(r)$, according to [139], and to the one derived from neutron scattering in their work. A fit to the neutron diffraction results in [29], yields a value of $f \simeq 0.8 \pm 0.05$. In the same work, results from inelastic neutron scattering are reported. The neutron-weighted vibrational density of states has a signature at the energy of the boroxol ring breathing mode at about 100.2 meV $\hat{=}$ 24.2 THz with a similar area to the one predicted for a structural model with $f = 0.75$. In [30], inelastic neutron scattering experiments also show a sharp peak at 100.2 meV $\hat{=}$ 24.2 THz. In addition, another small peak at 151.1 meV $\hat{=}$ 36.5 THz is visible, which is also assigned to boroxol rings. Here, no estimate of the boroxol ring fraction is given.

A boroxol ring fraction of $f \simeq 0.75$ is also supported by two DFT studies. In [141], a 160 atom glass sample is generated by an ab initio MD quench from the melt, using the Car-Parrinello method [142]. The resulting model glass structure contains 2 boroxol rings, corresponding to $f = 0.094$. By comparing the intensity of the boroxol ring peak in the HH Raman spectrum of the simulated structure to the experimental one [26] and by comparing the simulated ^{11}B NMR chemical shift to the experimental one [137], a value of $f \simeq 0.75$ is derived. In [133], DFT calculations of an alternative model structure with $f = 0.75$ are presented. This model structure is obtained, starting from the crystal structure of caesium enneaborate $Cs_2O.9B_2O_3$ [143] and extracting the Cs_2O units and several BO_3 units from the original structure [131, 132]. The calculated ^{11}B DAS and ^{17}O MAS NMR spectra show a good agreement with the experimental ones [137, 138]. In addition, the simulated HH Raman spectrum matches the experimental one [26], within an estimated error, associated to the comparison, of 15%. This supports a boroxol ring fraction of $f \simeq 0.75$ in pure B_2O_3 glass.

Regarding the computer modeling of B_2O_3, in [144], [145] and [146, 147], classical molecular dynamics simulations are presented with pure pair interactions. In all cases, an interaction potential of the so-called Born-Mayer-Huggins type is employed. This corresponds to the functional form of the Buckingham potential with Coulomb interactions (see equation (3.122)), without the attractive van der Waals term $-C/r^6$. In [144], the potential parameters are determined empirically, according to the size of the respective ions. The same set of parameters for the B and O atoms is used in [146, 147]. The potential parameters in [145] are determined in a way that the MD simulations reproduce the experimental crystal structures. In all cases, the full atomic charges ($q_B = 3\,e$, $q_O = -2\,e$) are used and the glass structures resemble a network of BO_3 triangles, containing no boroxol rings at all. Also, the first neighbor B-B distances (2.71 Å [144], 2.72 Å [145], 2.68 Å [146] and 2.71 Å [147]) are significantly larger as derived from neutron diffraction [29]. This reflects in the distribution of B-O-B angles, having a maximum at significantly too large values of 155° to 156°, compared to the experimental value of about 130° for boron atoms outside of boroxol rings [139, 140], in all cases. These values correspond to simulations at the experimental glass density [144, 146, 147] or an external pressure of 1 GPa to

obtain a reasonable glass density [145]. Simulations at external pressure of about $p = 0$ which is a reasonable assumption for normal conditions ($p = 1\,\text{atm} \simeq 0.1\,\text{MPa}$) lead to a glass density of about $\rho = 1.21\,\text{g/cm}^3$ in [146].

In the following, classical molecular dynamics simulations are discussed, including 2-body and 3-body interactions. In [148], the pair potentials are of the Born-Mayer-Huggins type, as described above. Here, the 3-body terms are introduced by assuming an additional ion at the center of mass of the BO_3 triangles and additional pair potentials between this artificial ion and the B and O atoms are introduced. Here, the full atomic charges ($q_B = 3\,\text{e}$, $q_O = -2\,\text{e}$) are used. The resulting glass structure for simulations at the experimental glass density shows a rather sharp B-O-B angular distribution with a maximum at about 120° and a boroxol ring fraction of $f \simeq 0.225$ (3 boroxol rings and 40 B atoms).

In [149], angular potentials for the O-B-O and the B-O-B angle of the harmonic form (3.125) are introduced with equilibrium angles of $\Phi_{0,OBO} = 120°$ and $\Phi_{0,BOB} = 130°$ in potential 4. The constant K_{OBO} is chosen in a way, to obtain the correct energy for the high frequency mode in the simulated infrared spectra and the constant K_{BOB} is chosen empirically. Here, partial charges are employed ($q_B = 2\,\text{e}$, $q_O = -1.\bar{3}\,\text{e}$). Simulations at constant experimental density lead to a glass structure with a maximum of the B-O-B angular distribution at approximately 140.5°, which is significantly lower than in case of the pure 2-body potentials [146, 147]. However, no boroxol rings are found in the glass structure.

In [44, 45], the most promising potential sets $C1$ and $C2$ are derived by means of a simultaneous fit to ab initio calculations of the energy surfaces of both known crystalline polymorphs $B_2O_3 - I$ and $B_2O_3 - II$ with additional constraints. The potential form is of the Buckingham type with Coulomb interactions (see equation (3.122)) for the O-O and the B-B interactions and the Morse type with Coulomb interactions (see equation (3.124)) for the B-O interactions. Additional harmonic 3-body terms (see equation (3.125)) for the O-B-O and the B-O-B interactions with equilibrium angles of $\Phi_{0,BOB} = 120°$, $\Phi_{0,OBO} = 120°$ for 3-fold coordinated B atoms and $\Phi_{0,OBO} = 109.47°$ for 4-fold coordinated B atoms are used. Here, the atomic charges are $q_B = 1.2\,\text{e}$, $q_O = -0.8\,\text{e}$ (C1) and $q_B = 0.9\,\text{e}$, $q_O = -0.6\,\text{e}$ (C2). The parameters of the B-O and the O-O interactions depend on the coordination number around the oxygen atoms. To study liquids and glasses, a continuous interpolation between the parameter sets of the different coordination states is introduced, depending on the local coordination numbers. Also, a bonding state function is introduced, which allows bonds to break. The resulting glass structures for simulations at the experimental glass density show B-O-B bond angle distributions with Φ_{BOB} between about 120° and 130° and boroxol ring fractions of about $f \simeq 0.25$ (C1) to $f \simeq 0.42$ (C2). However, in the latter case about 6% of the B atoms are fourfold coordinated with respect to O atoms. Simulations at $p = 0$ external pressure lead to configurations with about $f \simeq 0.36$ (C1) to $f \simeq 0.53$ (C2) and glass densities of $1.43\,\text{g/cm}^3$ (C1) and $1.15\,\text{g/cm}^3$ (C2). In [150], a coupled MD/MC simulation is presented. Starting with a model crystal structure with $f = 0.5$ [131], BO_3 units and B_3O_6 are exchanged randomly and the resulting structures are quenched to 0 K without allowing bond breakage. After each sampling, the structure with the lower energy

is chosen. Also the box volume is varied to keep the system at the experimental glass density. Calculations are performed based on the before mentioned classical potential, according to [44, 45]. For the final structure, corresponding to a (local) energy minimum, a boroxol ring fraction of $f = 0.74$ is reported and two corresponding maxima in $p_{BOB}(\Phi)$ are reported at 120° and 130°. In [151], the dependence of the total energy on the boroxol ring concentration is studied, based on the same classical potential [44, 45] without the coordination dependence. Here, glass configurations are generated by MD quenches from the melt. Samples with boroxol ring contents from 0% to 100% are generated by preparing initial configurations with a mixture of randomly distributed boroxol rings and additional B and O atoms and constraining the boroxol rings during the simulation. Here, system sizes of 90 atoms at fixed experimental density are studied. After the quench, a structural relaxation is carried out with a quantum mechanical DFT calculation, using GGA and LDA exchange-correlation functionals (see subsection 3.2.4). Here, mean first neighbor B-O distances of 1.36 Å, O-O distances of 2.33 Å and B-B distances of 2.44 Å to 2.55 Å are reported, depending on the number of boroxol rings. Minima of the total energy with respect to f at about $f = 0.15$ and $f = 0.7$ are reported.

In [152], exactly the same functional forms of the 2- and 3-body potentials is applied. In addition, the angular potential is multiplied by a term, decaying exponentially with respect to the inter-atomic distances. Following [45], the strength of the interaction depends on the local coordination of the oxygen atoms. The atomic charges of the atoms and exact parameters are not given. Simulations at constant glass density lead to glass structures with a boroxol ring fraction of about $f \simeq 0.15$ and a good agreement of the real space correlation function $T(r)$ with the experimental one from neutron scattering [29].

Another study of B_2O_3 with a potential including 3-body terms is presented in [37]. Here, a potential of the Born-Mayer-Huggins type (as explained above) is combined with 3-body terms of the Gaussian type with negative sign (see equation (3.127)), multiplied with a term decaying exponentially with respect to the inter-atomic distances. The parameters are determined empirically, based on a potential for SiO_2 [153]. The atomic charges, first neighbor B-B distances and B-O-B angles are not stated. However, a boroxol ring fraction of $f \simeq 0.2$ is reported.

In [154], the 3-body potential with O-B-O and B-O-B angular interactions, according to [149] is refined to yield a better agreement with the experimental total neutron structure factor $S_{\text{neutr.}}(k)$ [140], leading, for example to $\Phi_{0,BOB} = 110°$. In addition, a O-B-O-B 4-body dihedral term is introduced, parametrized according to Hartree-Fock calculations [71] on model $B_3O_3(OH)_3$ structures [46]. The partial charges are the same as in potential 4 of [149]. However, simulations at the experimental glass density lead to a boroxol ring fraction of only $f \simeq 0.036$ (2 boroxol rings in a 420 atom sample). The first neighbor B-B distances and B-O-B angles are not stated.

In [47], the functional form of the 2-body and 3-body terms correspond to the ones in [45, 152]. Here, only a 3-body term is chosen for the O-B-O interaction with $\Phi_{0,OBO} = 120°$. In addition, a B-O-B-O 4-body term is introduced with a minimum at the torsion angle of $\Phi_0 = 0°$. Parameters are obtained by DFT calculations of BO_3, B_2O_5, BO_3H_3, B_3O_6, $B_3O_6H_3$, B_4O_8 and $B_4O_8H_4$ aggregates. The atomic charges of the atoms and exact parameters are not stated. The glass

structures are generated in NVT runs at the experimental glass density, with a subsequent NpT run at room temperature at atmospheric external pressure, leading to system densities of about $\rho = 1.67 \mathrm{g/cm^3}$ to $\rho = 1.77 \mathrm{g/cm^3}$ in the slow cooling case and boroxol ring fractions of $f \simeq 0.1$ to $f \simeq 0.32$, depending on the system size. The first neighbor B-B distances are 2.367 Å, showing a good agreement to the one of B atoms in boroxol rings in [29]. However, the system density and boroxol ring fraction decreases with increasing system size.

In [48], a coordination dependent charge-transfer potential is presented, based on a previous one for the study of SiO_2 [155]. The potential consists of 2-body terms of the Born-Mayer-Huggins type (Buckingham potential with Coulomb interactions (see equation (3.122)), without the van der Waals term $-C/r^6$) and 3-body terms of the Gaussian type with negative sign (see equation (3.127)), multiplied with a term decaying exponentially with respect to the inter-atomic distances. The equilibrium angles are $\Phi_{0,BOB} = 120°$ and $\Phi_{0,OBO} = 120°$ or $\Phi_{0,OBO} = 109.47°$, depending on the local coordination environment of the B atom (3-fold or 4-fold with respect to O atoms). In addition to this local coordination dependence, the atomic charge is determined dynamically depending on the coordination number ($q_B = 1.7\,\mathrm{e}$ for 3-fold and $q_B = 1.48\,\mathrm{e}$ for 4-fold coordinated B atoms). The potential is parametrized, according to the crystal structure of $B_2O_3 - I$ in combination with the adjustment to available experimental data of the structure and vibrational properties of vitreous B_2O_3. Here, glass structures are generated in NpT runs, with the starting configuration of the alternative model structure with $f = 0.75$ [131, 132]. Depending on the equilibration time at 2500 K, glass structures with different values of $f \simeq 0.1$ to $f \simeq 0.75$ are generated with corresponding system densities of $\rho = 1.75\,\mathrm{g/cm^3}$ to $\rho = 1.81\,\mathrm{g/cm^3}$ [35, 48, 156]. However, no additional rings are generated in the cooling process. The first neighbor B-B distances and B-O-B angles are not stated. The calculated $S_{\mathrm{neutr.}}(k)$ shows good agreement with experimental results.

In [49], a many-body polarizable force field is introduced. This force field includes a non-additive interaction, describing the dipole moments induced by local electric fields and is rather complicated. The parameters are confirmed by a comparison of the minimum energy structures, according to the classical force field, with experimental and ab initio structures of B_2O_3, HBO_2, H_3BO_3, $H_3B_3O_6$ and $H_4B_2O_5$. Also, the system is confined by external forces as an alternative to periodic boundary conditions. For a system of 81 boron and 124 oxygen atoms, equilibrated at 1800 K, 4 boroxol rings are reported, corresponding to $f \simeq 0.15$. The first neighbor peak of $g_{BB}(r)$ is located at approximately 2.4 Å and the density differs less than 1% from the experimental glass density. In [157], boroxol ring fractions of about $f \simeq 0.22$ are reported in a temperature range between 1761 K and 2163 K in the liquid state at experimental glass density.

Another complicated interaction potential is reported in [50], including polarization terms and changes in the shape of the ions due to dipolar and quadrupolar shape distortions. The repulsive and polarization terms of the aspherical ion model (AIM) are parametrized, according to forces and dipoles from ab initio calculations on glass structures of 100 atoms, with boroxol ring fractions from $f = 0.0$ to $f = 0.22$, according to [133]. In [50], the focus is on structural transformations in B_2O_3 glass under pressure. The simulations are performed with a starting

configuration of the alternative model structure with $f = 0.75$, according to [131, 132]. In [50], it is not reported if the AIM is capable of yielding glass structures with a high number of boroxol rings f when starting with a random initial configuration. However, the AIM is capable to reproduce the experimental dependence of the system density ρ with respect to external pressure p, measured for the cold compression of glass in in situ experiments [158], which is very promising.

6.2 Liquid properties by means of ab initio calculations

In this section, the properties of liquid B_2O_3 are examined, based on ab initio MD simulations at a fixed system density of $\rho = 1.83\,\mathrm{g/cm^3}$. This corresponds to the experimental glass density, measured at about 300 K [159]. Following the considerations of chapter 4, a system size of 150 atoms is chosen, leading to a box length of $L_{\mathrm{Box}} = 12.375\,\text{Å}$. (Due to numerical inaccuracies, at some temperatures the initial simulation box has been set up with a very small deviation from the cubic shape, leading to a triclinic simulation box. Here, the angles between the faces of the simulation box are 89.999998935° instead of 90°.) Some of the results are compared to previous ab initio molecular dynamics studies of a 120 atom system at different system densities [160–162].

Again, all quantum mechanical DFT calculations are carried out with the VASP package [78, 79], using a Perdew-Burke-Ernzerhof (PBE) type exchange-correlation functional of the generalized gradient approximation (GGA), revised for solids (PBEsol) [84]. As explained in section 4.2, all computations are done, using a plane wave basis set, the PAW method [86, 87], Gaussian smearing with a smearing width of $\sigma = 0.02\,\mathrm{eV}$ and all projection operators of the PAW wave functions are evaluated in real space.

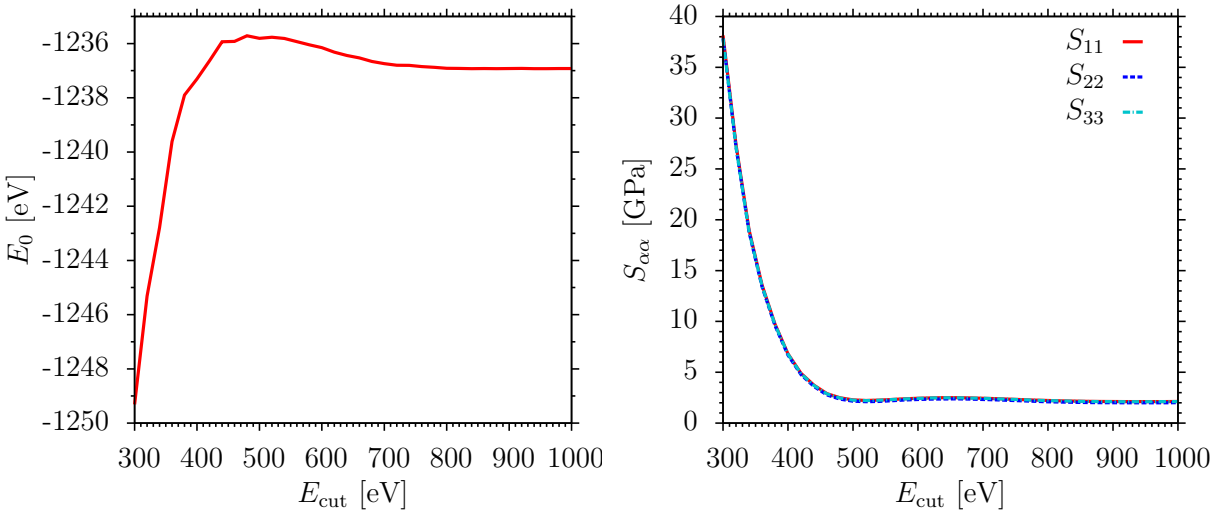

FIGURE 6.1: Dependence of E_0 and $S_{\alpha\alpha}$ on the plane wave cutoff E_{cut} for 150 atom system of B_2O_3

Next, the convergence of the total energy is studied with respect to the number of k-points for accurate, as well as normal VASP precision. Again, different k-meshes with 1 (Gamma

point calculation) to 6 points along each of the **k**-axes are chosen and the electronic relaxation is stopped when the relative change of the total energy E_0 of two adjacent steps of the self-consistent field loop is less than 10^{-6}. Same as in case of the 165 atom system SiO_2 (see section 4.2), the dependence of the number of k-points is rather weak. This justifies the restriction to Gamma point calculations ($\mathbf{k} = (0,0,0)^T$), which is a reasonable choice for this rather large system (150 atoms) in terms of DFT calculations.

To fix the cutoff energy E_{cut} for the plane wave basis set, the dependence of the total energy E_0 and the diagonal elements of the external stress tensor $S_{\alpha\alpha} = -S_{\text{int},\alpha\alpha}$, $\alpha \in \{1,2,3\}$ (see equation (3.34)) are examined. In Fig. 6.1, the dependence of E_0 and $S_{\alpha\alpha}$ on the plane-wave cutoff E_{cut} is shown for Gamma point calculations ($\mathbf{k} = (0,0,0)^T$) with accurate VASP precision and fixed accuracy of 10^{-6} for the electronic relaxation. However, the plots show the same behavior for normal VASP precision as well. Similar to the 165 atom system SiO_2, the total energy E_0 shows an increase with increasing E_{cut} with a maximum at about $E_{\text{cut}} = 500\,\text{eV}$, followed by a slight decrease and a transition into a plateau at approximately $E_{\text{cut}} = 800\,\text{eV}$. Again, this would motivate the choice of the latter value of E_{cut}. However, as explained in section 4.2, the number of plane waves increases with E_{cut}^2, making large values of E_{cut} unfavorable due to a significant increase of the computational effort. Again, the diagonal elements of the external stress tensor $S_{\alpha\alpha}$ show a strong decrease with increasing E_{cut} and a transition into a plateau at about $E_{\text{cut}} = 500\,\text{eV}$, which justifies a value of $E_{\text{cut}} = 500\,\text{eV}$ for the subsequent simulations of B_2O_3. The recommended minimal values for the used PAW potentials [86, 87] are $E_{\text{cut}} = 400\,\text{eV}$, in the case of oxygen and $E_{\text{cut}} = 319\,\text{eV}$, in the case of boron.

temperature	# time steps	simulation time	δt
3600 K	30000 ts	36 ps	1.2 fs
3300 K	30000 ts	36 ps	1.2 fs
3000 K	31508 ts	63.018 ps	2.0 fs
2700 K	45900 ts	55.08 ps	1.2 fs
2500 K	70352 ts	84.4224 ps	1.2 fs
2300 K	103500 ts	124.2 ps	1.2 fs

TABLE 6.2: Number of time steps and simulation time at each temperature for ab initio MD simulations of liquid B_2O_3 (150 atom system at constant density of $\rho = 1.83\,\text{g/cm}^3$).

All ab initio MD simulations presented in this section are of the the Born-Oppenheimer type. As described in section 4.2, at each time step a single point DFT calculation is conducted, taking into account only the electronic ground state, and the forces on the ions are the Hellman-Feynman forces [112]. Simulations are carried out in a NVT ensemble where the ionic motion is coupled to a Nosé thermostat (see subsection 3.1.2) with a Nosé-mass corresponding to a period of 40 time steps, using normal VASP precision and a fixed accuracy of 10^{-6} for the electronic relaxation. In table 6.2, the considered temperatures and simulation times are displayed.

In Figs. 6.2 and 6.3, the mean square displacements $\left\langle r_\alpha^2(t)\right\rangle$ (see equation (3.98)) and the incoherent intermediate scattering functions $F_{\text{S},\alpha}(k,t)$ (see equation (3.100)) are shown at the

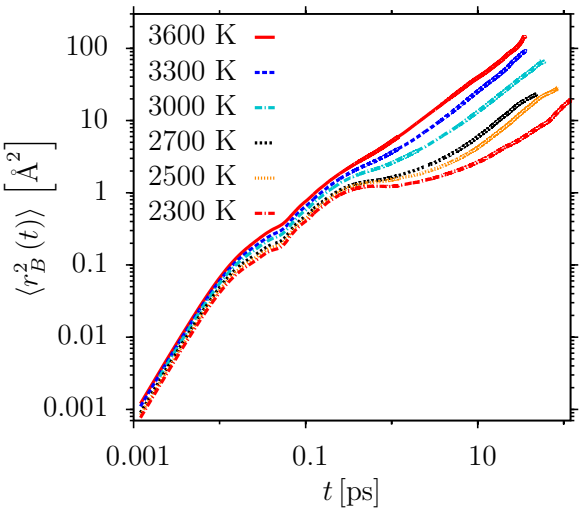

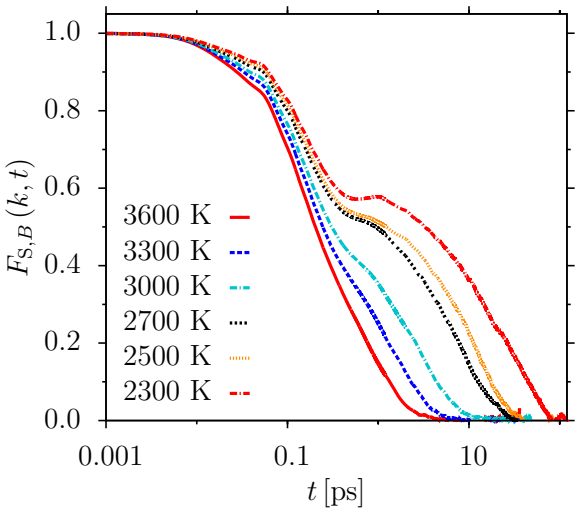

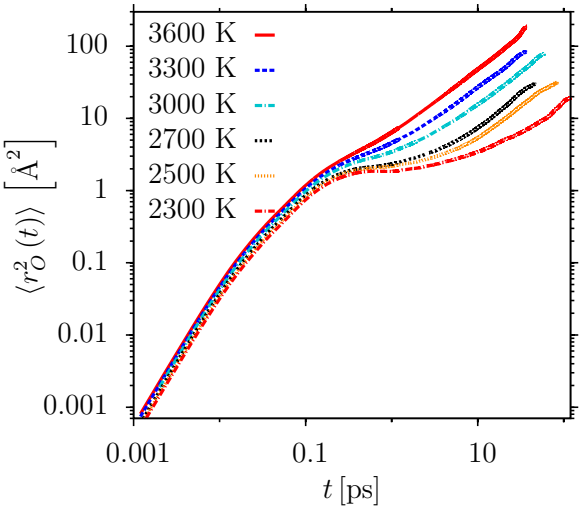

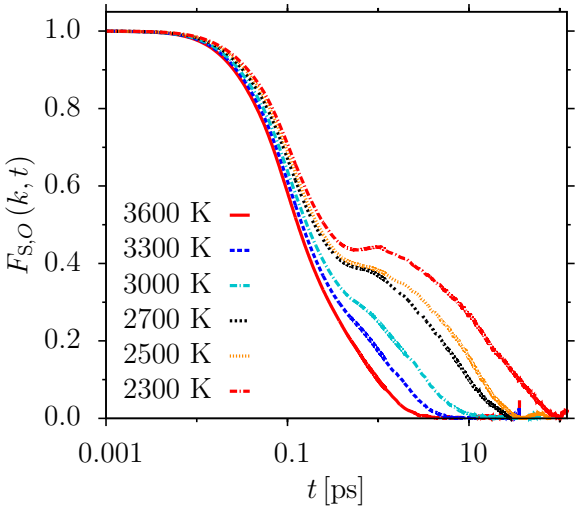

FIGURE 6.2: Mean square displacements $\langle r_\alpha^2(t)\rangle$, $\alpha \in \{B, O\}$, B_2O_3. Ab initio MD at different temperatures.

FIGURE 6.3: Incoherent intermediate scattering functions $F_{S,\alpha}(k,t)$, $\alpha, \beta \in \{B, O\}$, B_2O_3. Ab initio MD at different temperatures.

examined temperatures. The incoherent intermediate scattering functions are evaluated at $k = 1.68\,\text{Å}^{-1}$. Again, this is about the k-value of the first sharp diffraction peak (FSDP), visible in all partial static structure factors. In contrast to the classical MD simulations, the analysis is done according to the ab initio MD runs in the NVT ensemble and not, according to microcanonical runs. Also, the underlying data is from a single simulation run only due to the huge computational effort. As a consequence, one has to be careful when interpreting the displayed curves. However, the shape of the curves give an indication about the relaxation times at the examined temperatures. It can be seen that also in case of the Born-Oppenheimer MD runs, the curves show the characteristic two-step process with an intermediate plateau. They indicate that at all regarded temperatures the configurations could be equilibrated within the simulation run. The α-relaxation times increase by a factor of 30 from 3600 K to 2300 K.

Next, the behavior of different structural quantities in the observed temperature range is studied. These quantities are averaged over the last 20000 time steps (24 ps) of the simulation runs, except

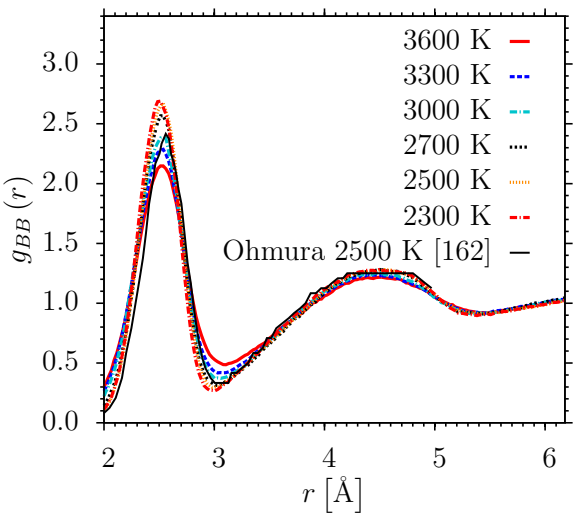

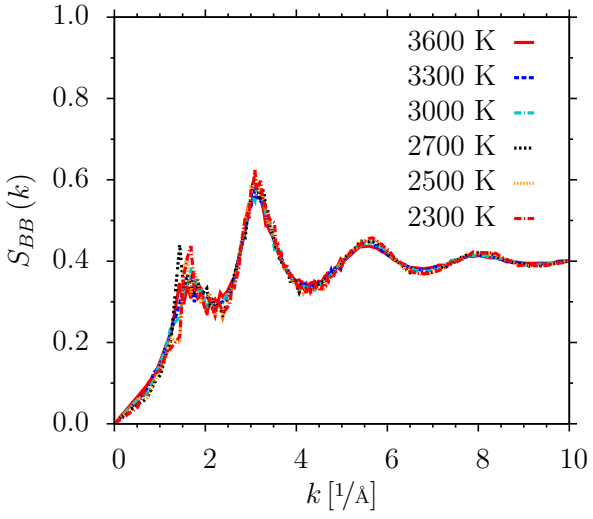

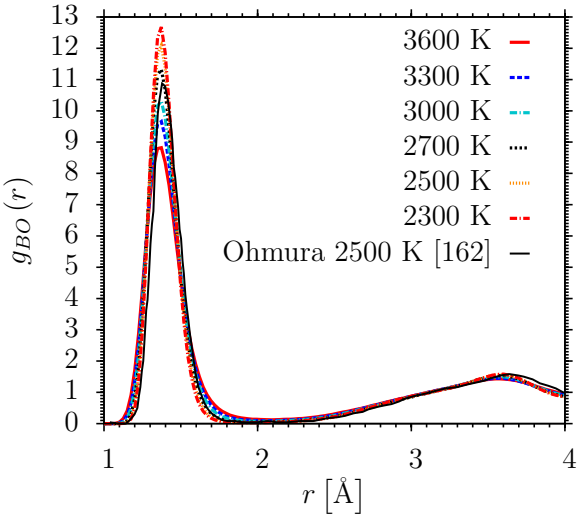

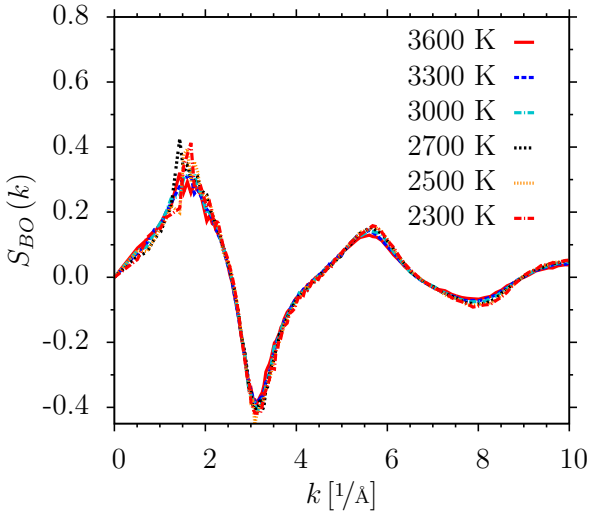

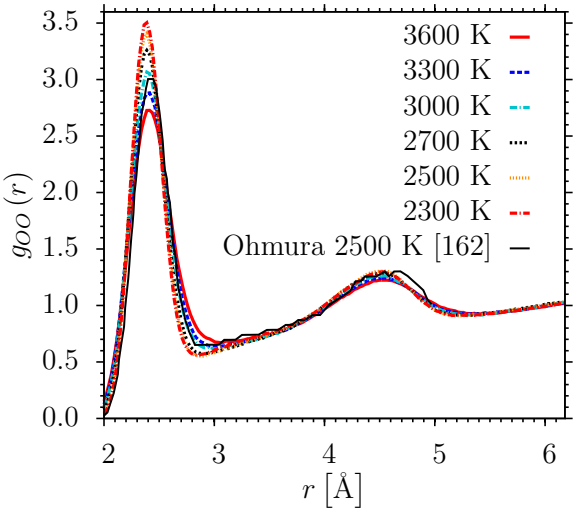

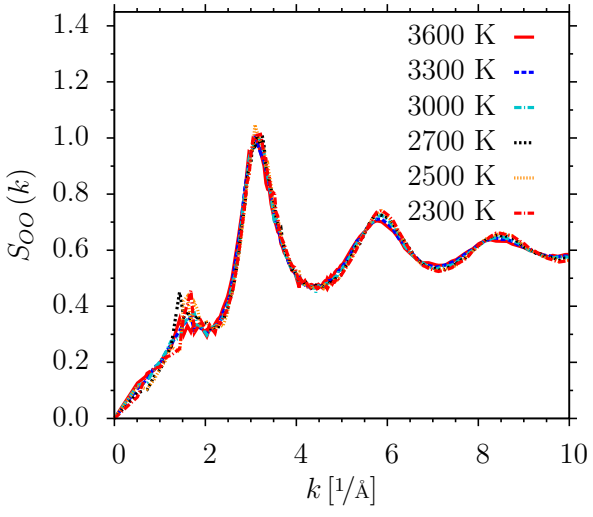

FIGURE 6.4: Partial pair correlation functions $g_{\alpha\beta}(r)$, $\alpha, \beta \in \{B, O\}$, B_2O_3. Ab initio MD at different temperatures. Comparison with ab initio MD simulation at 2500 K and 1.92 g/cm³ [162].

FIGURE 6.5: Partial static structure factors $S_{\alpha\beta}(k)$, $\alpha, \beta \in \{B, O\}$, B_2O_3. Ab initio MD at different temperatures.

the displayed data at 3000 K. Here, the data is averaged over the last 10000 ts (20 ps), due to a larger time step of 2.0 fs. In Figs. 6.4, the partial pair correlation functions are shown. As expected, the peak heights increase with decreasing temperature. The curves at 2500 K are compared to simulation data of a 120 atom system at 2500 K at a system density of 1.92 g/cm^3 [162]. In this work, the properties of liquid B_2O_3 are studied at 2500 K and 3500 K for systems under external pressure. The latter system density is the one closest to the system density of this work (1.83 g/cm^3) and corresponds to an external pressure of 3.2 GPa, according to [161]. Basis of the displayed curves is an ab initio MD run of 21.6 ps with a time step of 1.2 fs, using the PAW-method [86, 87] and a Perdew-Burke-Ernzerhof (PBE) type exchange-correlation functional of the generalized gradient approximation (GGA) [163], instead of the one revised for solids (GGA-PBEsol), used in this work [84]. In [162], the mean square displacements after 8 ps are given to be about $\left\langle r_B^2\left(t = 8\,\text{ps}\right)\right\rangle \simeq 6.6\,\text{Å}^2$ and $\left\langle r_B^2\left(t = 8\,\text{ps}\right)\right\rangle \simeq 8.0\,\text{Å}^2$ for a slightly lower system density of 1.69 g/cm^3. Having this in mind, one has to be careful about the equilibration of the system at 2500 K. Regarding this, the agreement is acceptable.

In Fig. 6.5, the partial static structure factors are shown in the examined temperature range. Again, the height of the peaks increases with decreasing temperature. However, the difference is less apparent as in case of the partial pair correlation functions. The most dominant peaks of $S_{\alpha\beta}\left(k\right)$ are located at about $k = 3.1\,\text{Å}^{-1}$, corresponding to a length scale of $2\pi/3.1\,\text{Å} \simeq 2.0\,\text{Å}$ for the all correlations. Similar to the structural properties of SiO_2 (see section 4.1), this length scale is of the order of the first minimum of $g_{BO}\left(r\right)$. There is an additional peak for all correlations at approximately $k = 1.7\,\text{Å}^{-1}$, corresponding to a length scale of about $2\pi/1.7\,\text{Å} \simeq 3.7\,\text{Å}$. As in case of SiO_2, this first sharp diffraction peak (FSDP) is a signature of a medium range structure. At the temperature of 2700 K, the quite sharp maximum of the FSDP is shifted to about $1.44\,\text{Å}^{-1}$, corresponding to a length scale of about 4.4 Å, which is not clearly understood. In [160], the partial static structure factors are displayed for a simulation of liquid B_2O_3 at 2500 K and 1.50 g/cm^3, corresponding to an external pressure of 0.0 GPa. The DFT parameters are the same as described in the previous paragraph and the simulation time is 10.8 ps. The displayed results are in agreement with this work. The FSDP and the most dominant peak are located at about $1.6\,\text{Å}^{-1}$ and $3.0\,\text{Å}^{-1}$. The slight shift to lower k-values, compared to this work, can be explained by the slightly lower system density.

Regarding the distribution of coordination numbers, the probability of the B atoms $p_{\alpha\beta}\left(n\right), \alpha, \beta \in \{B, O\}$, to have a partial coordination of $n = 3$ with respect to neighboring oxygen, as well as boron atoms increases with decreasing temperature. At 2300 K, about 81% of the B atoms are threefold coordinated with respect to the neighboring B atoms and about 98% are threefold coordinated with respect to the neighboring oxygen atoms. About 99% of the oxygen atoms are twofold coordinated with respect to neighboring boron atoms. Regarding the coordination of the oxygen atoms, at 3600 K the predominant coordination number with respect to neighboring oxygen atoms is 5. At 2300 K, the predominant coordination number is 4 and about 51% of the oxygen atoms have 4 oxygen neighbors.

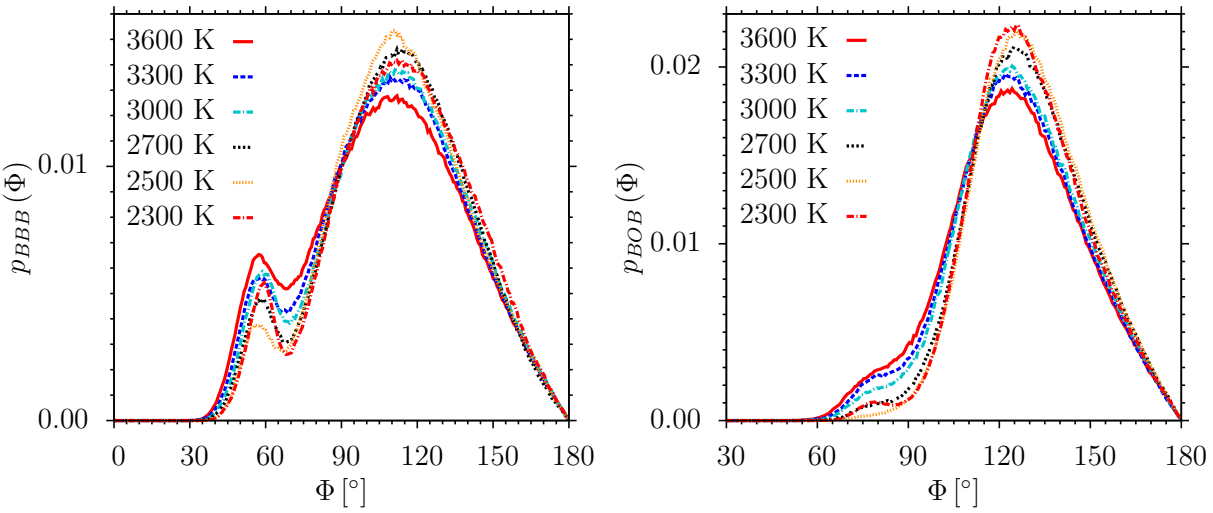

FIGURE 6.6: Angular distributions $p_{\alpha\beta\gamma}(\Phi)$, $\alpha, \beta, \gamma \in \{B, O\}$, B_2O_3. Ab initio MD at different temperatures.

In Fig. 6.6, the angular distributions are exemplarily shown for the B-B-B and the B-O-B correlation at the examined temperatures. In general, the angular distributions get narrower with decreasing temperature, as expected. Regarding $p_{BBB}(\Phi)$, the average angle increases from about 107° at 3600 K to about 113° at 2300 K. In all cases there is an additional peak visible at about 58°. The main peak is connected to rings of size $n = 6$ to $n = 8$, which are the dominant ring sizes in all cases. The extra peak is mainly connected to smaller ring sizes $n \leq 4$. Regarding the latter, the 3-membered rings are of specific interest, due to the high number of boroxol rings observed in vitreous B_2O_3. It can be seen that the peak height of this additional peak decreases with temperature for all temperatures $T \geq 2500$K. An exception is the temperature of 3000 K, where the peak height is about the same as at 3300 K. This reflects the decreases of defect structures in the liquid with decreasing temperature. However, at the lowest temperature of 2300 K, the peak height is significantly higher than at $T = 2500$ K and $T = 2700$ K. This is connected to the increased formation of 3-membered rings at lower temperatures. Regarding $p_{BOB}(\Phi)$, the average angle increases from about 125° at 3600 K to about 129° at 2300 K. In addition to the main peak, there is a shoulder visible at approximately 80°, connected to defect structures of edge-sharing BO_3 triangles.

In Fig. 6.7, the probability that a B atom is member of a ring of size n, $p_B(n)$, is shown in the examined temperature range. The most dominant ring size is $n = 7$ for temperatures in the range of 3000 K − 3600 K and $n = 8$ for the temperatures 2300 K and 2700 K. In the case of 2500 K, the probability $p_B(n = 6)$ is a about the same than for the most dominant ring size $p_B(n = 7)$. In all cases, $p_B(n = 2)$, reflecting the before-mentioned edge-sharing BO_3 triangles, decreases with decreasing temperature. In the case of $p_B(n = 4)$ the same behavior is observed, with the exception of $T = 2500$ K. Here, $p_B(n = 4)$ is slightly higher than at the temperatures 2300 K and 2700 K. Also, this is the only temperature where $p_B(n = 4) > p_B(n = 3)$. Reflecting the behavior of $p_{BBB}(\Phi)$, the probability $p_B(n = 3)$ decreases with decreasing temperature, except

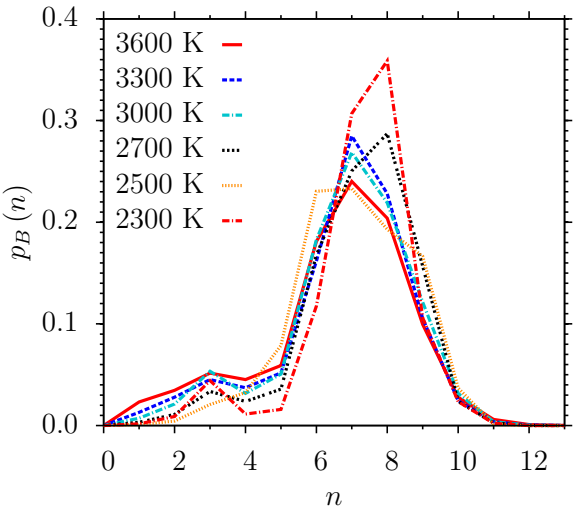

FIGURE 6.7: Probability that a B atom is member of a ring of size n, $p_B(n)$, at different temperatures, B_2O_3. Ab initio MD.

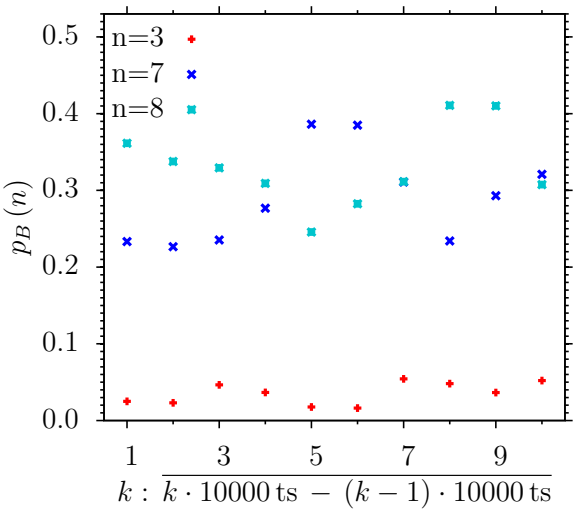

FIGURE 6.8: Probability that a B atom is member of a ring of size n, $p_B(n)$. Temporal development at 2300 K, B_2O_3. Ab initio MD.

at the temperature of 3000 K. However, at the lowest temperature of 2300 K, $p_B(n=3)$ is greater again than the corresponding values at 2700 K and 2500 K.

In Fig. 6.8, the evolution of $p_B(n)$ is followed during the last 100000 ts of the 124.2 ps simulation run at 2300 K, in the cases of $n=3$, $n=7$ and $n=8$. Each data point represents the averaged data over 10000 time steps. It can be seen that all displayed probabilities $p_B(n)$ show an unsteady behavior with minima and maxima during the examined last 100000 ts (120 ps) of the simulation run at 2300 K. This reflects the rather long equilibration time at this temperature of about 80 ps to 100 ps (see Fig. 6.3). As explained above, the value of $n=3$, corresponds to the formation of boroxol rings. Regarding the development of the latter, an increase of $p_B(n=3) \simeq 0.025$ to $p_B(n=3) \simeq 0.052$ can be observed during the simulation run with an intermediate minimum of about $p_B(n=3) \simeq 0.016$. As explained above, this can be interpreted as the onset of the formation of 3-membered rings at 2300 K, also seen in Fig. 6.7.

6.3 Determination of classical potential parameters

As already mentioned in section 2.4, one theme of this work is to develop a rather simple interaction potential based on the structural properties of liquid B_2O_3 with ab initio MD simulations, as presented in the previous section.

Regarding the overview over previous studies in section 6.1, to my knowledge, so far no interaction potential has been parametrized according to the structure of an ab initio MD trajectory of liquid B_2O_3. In case of the model glass former SiO_2, the force field parameters of the BKS potential [22] could be improved by means of a structural fit to $r \cdot g_{\alpha\beta}(r)$, $\alpha, \beta \in \{Si, O\}$ of an ab initio MD run at 3600 K [43]. Here, the structure matching scheme proved to be superior

to a force matching method [51]. This motivates the application of this method also to the model glass former B_2O_3. In this section it is tested, whether this structure matching scheme in combination with a rather simple interaction potential leads to an acceptable classical force field for the model glass former B_2O_3. The basis for the development of an improved interaction potential is the classical force field, due to the dissertation of C. R. Trott [97]. In the second part of this thesis, a classical force field has been developed for a general composition of $wLi_2O - xSiO_2 - yB_2O_3 - zP_2O_5$. The basis of this force field is the existing interaction potential of J. Habasaki [164] for alkali silicates which has been developed by quantum mechanical calculations of potential energy surfaces of small clusters. The interaction potential has the functional form of a Buckingham potential with Coulomb interactions $V^{\text{Buck+Coul}}(r)$ (see equation (3.122)), in all cases. In addition, angular 3-body terms are introduced for the O-B-O angle and the O-P-O angle.

The parameters of the B-B, B-O and O-O interaction are tabulated in Table 6.5. It is found that the simulation results are practically the same if the B-B interaction is chosen to be purely electrostatic, meaning $A_{BB} = 0\,\text{eV}$. This can be understood by the very large value of $b_{BB} = 15.2207\,\text{Å}^{-1}$ and the value of $C_{BB} = 0\,\text{eV}\,\text{Å}^6$. Therefore, the short-range Buckingham part of the potential $V^{\text{Buck}}(r)$ (see equation (3.122)) only consists of a fast decaying exponential term, which is virtually equal to zero at relevant inter-particle distances. Therefore, in the following considerations, only the Coulomb part of the potential is considered for the B-B interaction.

As in case of the model glass former SiO_2, all classical MD simulations are carried out with the LAMMPS software package [60, 61] and a slightly modified form of the Buckingham potential is used. Following the considerations of section 4.1, the Coulomb interaction is split up into a short-range part $V^{\text{CS}}(r)$ (see equation (3.20)), evaluated in real space, and a long-range part, evaluated in Fourier space employing a standard Ewald summation over k-vectors. Again, a skin distance of $r_{\text{skin}} = 2\,\text{Å}$ is used and the Verlet neighbor lists are rebuilt when the first atom has moved more than half the skin distance. In all cases, $r_c = 5.5\,\text{Å}$ is chosen as cutoff radius for the short-range Buckingham part of the potential $V^{\text{Buck}}(r)$. In this section, the cutoff distance of $V^{\text{CS}}(r)$ is equal to $r_c^{\text{ew}} = 5.5$, as well, as the system size of the classical MD simulations is chosen to be equivalent to the one of the ab initio MD simulations in section 6.2, namely 150 atoms. This means that the box length is $L_{\text{Box}} = 12.375\,\text{Å}$, when simulating at the experimental glass density of $\rho = 1.83\,\text{g/cm}^3$ [159]. Computations are carried out with an $g_{\text{ew}} = 0.599052$, which corresponds to an Ewald accuracy of about 10^{-5}, as explained in subsection 3.1.1. Again, $V^{\text{Buck}}(r)$ and $V^{\text{CS}}(r)$ are shifted to zero at $r_c = 5.5$ and r_c^{ew} and subsequently multiplied by a smoothing function, namely $G(r)$ and $G^{\text{ew}}(r)$, with the functional form of equation (3.13). In all cases, a value of $d = d^{\text{ew}} = 0.05\,\text{Å}^2$ is chosen. As explained in section 4.1, the shifted and smoothed Buckingham potentials with Coulomb interactions are substituted by harmonic potentials $V^{\text{Harm}}(r)$ (see equation (4.2)) for particle distances smaller than the positions of the local maxima $r < r_{\text{in},\alpha\beta}, \quad \alpha, \beta \in \{B, O\}$. In cases where $V^{\text{Buck+Coul}}(r)$ shows no local maximum, the shifted and smoothed $V^{\text{Buck+Coul}}(r)$ is substituted by a harmonic potential $V^{\text{Harm}}(r)$ for pair distances smaller than $r = 1\,\text{Å}$. As explained in section 4.1, $a_{3,\alpha\beta}$ is the position of local maximum for the specific atom pair, according to equation (4.1), and

$a_{1,\alpha\beta}$ is the value of the potential at $r = a_{3,\alpha\beta}$, according to equation (4.1). In cases, where no local maximum is found, the latter are substituted by the respective values at $r = 1\,\text{Å}$. Regarding the third parameter, the value of $a_{2,\alpha\beta} = 100\,eV\,\text{Å}^{-2}$ is chosen in all cases. Again, these considerations lead to the functional form of the short-range pair potential used in the simulations, according to equation (4.3). As in the case of SiO_2 (see subsection 4.1.1), the numerical values of the total short-range pair potentials $V^{\text{S}}(r)$ (see equation (4.3)) and the total short-range pair forces $-\frac{\partial}{\partial r}V^{\text{S}}(r)$ are pre-computed for certain values of r_{ij} in a tabulated form for pair distances $r \geq 0.25\,\text{Å}$ and $r < 64\,\text{Å}$. Again, a table style of the so-called bitmap style is chosen, according to [102] with 2^{16} table entries.

parameters	units	start parameter set [97]	3600 K fit
q_B	[e]	2.01	1.401065
A_{BB}	[eV]	873077800	-
b_{BB}	$[\text{Å}^{-1}]$	15.2207	-
C_{BB}	$[\text{eV Å}^6]$	0.0	-
A_{BO}	[eV]	108500	85950.148438
b_{BO}	$[\text{Å}^{-1}]$	7.9365	8.176078
C_{BO}	$[\text{eV Å}^6]$	13.02	9.752701
A_{OO}	[eV]	1758.3076	1978.926025
b_{OO}	$[\text{Å}^{-1}]$	2.8464	2.938332
C_{OO}	$[\text{eV Å}^6]$	214.9168	267.403687

Parameters	Units	2300 K fit 1	2300 K fit 2
q_B	[e]	0.967746	1.018960
A_{BB}	[eV]	-	-
b_{BB}	$[\text{Å}^{-1}]$	-	-
C_{BB}	$[\text{eV Å}^6]$	-	-
A_{BO}	[eV]	199523.734375	202543.21875
b_{BO}	$[\text{Å}^{-1}]$	8.607712	8.642187
C_{BO}	$[\text{eV Å}^6]$	20.803251	20.122923
A_{OO}	[eV]	8276.772461	6406.353516
b_{OO}	$[\text{Å}^{-1}]$	4.089084	3.757303
C_{OO}	$[\text{eV Å}^6]$	-	78.624069

TABLE 6.5: Different parametrizations of the pair potential (see equation (3.122)) for B_2O_3. Comparison of original parameter set [97] to 3 different parametrizations after structural fits at 3600 K and 2300 K.

Starting with the parameter set of Table 6.5, according to [97], with the B-B interaction being purely electrostatic ($A_{BB} = 0\,\text{eV}$), parameter fits are carried out with respect to the liquid trajectories of the ab initio MD simulations of B_2O_3 at the temperatures of 3600 K and 2300 K.

These are the highest and the lowest temperatures at which ab initio MD simulations are carried out, described in detail in section 6.2. Therefore, it is interesting to examine if the fitting procedures at these two temperatures lead to significantly different parameter sets. At the temperature of 2300 K, two different fits are carried out. In the second one, the O-O interaction is chosen to be purely repulsive, meaning a fixed value of $C_{OO} = 0\,\mathrm{eV\,\AA^6}$ is chosen. This means that, in each case, a set of $M = 7$ ($M = 6$ in the case of $C_{OO} = 0\,\mathrm{eV\,\AA^6}$) parameters $a_1, \ldots, a_M$ is optimized, including the charge of the boron atoms, namely q_B, A_{BO}, b_{BO}, C_{BO}, A_{OO}, b_{OO} and C_{OO}. The charge of the oxygen atoms follows from the requirement of charge neutrality ($q_O = -2/3\, q_B$). The basis for the structural fits are the last 20000 time steps of the liquid trajectories at 3600 K and 2300 K. The parameter optimization is performed by a Levenberg-Marquardt algorithm, which is an iterative scheme to find the (local) minimum of the sum of squares χ^2 of the deviations between a set of data points and a model curve depending on a set of parameters. The method of structure matching and the Levenberg-Marquardt procedure are described in detail in section 3.5. The optimization of the force field parameters is carried out with respect to the partial pair correlation functions of all correlations $g_{BB}(r)$, $g_{BO}(r)$ and $g_{OO}(r)$ and all 6 relevant angular distributions $p_{\alpha\beta\gamma}(\Phi)$, $\alpha, \beta, \gamma \in \{B, O\}$, meaning $p_{BBB}(\Phi)$, $p_{BBO}(\Phi)$, $p_{BOB}(\Phi)$, $p_{BOO}(\Phi)$, $p_{OBO}(\Phi)$ and $p_{OOO}(\Phi)$. ($p_{OBB}(\Phi)$ is identical to $p_{BBO}(\Phi)$ and $p_{OOB}(\Phi)$ is identical to $p_{BOO}(\Phi)$.) The values of the relevant $p_{\alpha\beta\gamma}(\Phi)$, $\alpha, \beta, \gamma \in \{B, O\}$, are multiplied by the factor 100. This ensures that the numerical values of $p_{\alpha\beta\gamma}(\Phi)$ are of the same order of magnitude as the ones of $g_{\alpha\beta}(r)$. The determination of new parameters is based on the original fitting routine of A. Carré [51], which is extended to include the relevant angular distributions into the fitting procedure. Regarding these considerations, the numerical value of Chi-Square $\chi^2(a_1, \ldots, a_M)$ at each iteration step is calculated, according to equation (3.128) with $\sigma_{\alpha\beta} = 1$, $\alpha, \beta, \gamma \in \{B, O\}$, in case of the pair correlation functions and $\sigma_{\alpha\beta\gamma} = 0.01$, $\alpha, \beta, \gamma \in \{B, O\}$, in case of the angular distributions. (The multiplication of the angular distributions by a factor 100 is equivalent to the choice of $\sigma_{\alpha\beta\gamma} = 0.01$.) $g_{\alpha\beta}^{\text{classical MD}}(r)$ and $P_{\alpha\beta\gamma}^{\text{classical MD}}(\Phi)$ in equation (3.128) are computed with respect to a classical molecular dynamics run of the same system size (150 atoms, $L_{\text{Box}} = 12.375\,\text{Å}$) and at the same temperature as in case of the ab initio molecular dynamics run. In each case, a numerical discretization of 250 data points is chosen, meaning that the corresponding parameters in equation (3.128) are $\triangle_d = \frac{L_{\text{Box}}}{2 \cdot 250} = \frac{12.375\,\text{Å}}{2 \cdot 250} = 0.02475\,\text{Å}$, in case of the pair correlation functions and $\triangle_a = \frac{180°}{2 \cdot 250} = 0.36°$, in case of the angular distributions. Except for the reweighting of $p_{\alpha\beta\gamma}(\Phi)$ with respect to $g_{\alpha\beta}(r)$, all data points are considered to have the same weight.

At each iteration step of the Levenberg-Marquardt procedure (see section 3.5), the numerical derivatives with respect to the independent fit parameters $a_1, \ldots, a_M$ ($M = 7$ or $M = 6$) have to be calculated (see equations (3.129) to (3.132) and (3.137) to (3.138)). This requires two additional classical MD runs per parameter for each iteration step with the parameter sets $a_1, \ldots, a_i \pm \epsilon_{a_i}, \ldots, a_M, \quad i \in \{1, \ldots, M\}$, meaning a total of $2\,M + 1$ classical MD runs per iteration step. In each case, the parameters ϵ_{a_i} are chosen in the following way: $\epsilon_{q_B} = 0.02 \cdot q_B = 0.0402\,\text{e}$, $\epsilon_{A_{BO}} = 0.1 \cdot A_{BO} = 10850\,\text{eV}$, $\epsilon_{b_{BO}} = 0.03 \cdot b_{BO} = 0.238095\,\text{Å}^{-1}$, $\epsilon_{C_{BO}} = 0.05 \cdot C_{BO} = 0.651\,\mathrm{eV\,\AA^6}$, $\epsilon_{A_{OO}} = 0.1 \cdot A_{OO} = 175.83076\,\text{eV}$, $\epsilon_{b_{OO}} = 0.03 \cdot b_{OO} = 0.085392\,\text{Å}^{-1}$

and $\epsilon_{C_{OO}} = 0.1 \cdot C_{OO} = 21.49168\,\text{eV}\,\text{Å}^6$. Here, the value of a_i refers to the original parameter set [97], as listed in Table 6.5. The numerical value of ϵ_{a_i} remains unchanged during the structural fitting procedure. As explained in section 3.5, in case of a small $\lambda \ll 1$, the second order terms (Hessian of $\chi^2(a_1, \ldots, a_M)$) dominate and in case of a large $\lambda \gg 1$, the first order terms (gradient of $\chi^2(a_1, \ldots, a_M)$) dominate when computing a new trial parameter set. As explained in section 3.5, a larger value of λ should be more favorable at a larger value of $\chi^2(a_1, \ldots, a_M)$ and a smaller value of λ should be more favorable at a smaller value of $\chi^2(a_1, \ldots, a_M)$ close to the (local) minimum, with respect to the parameter set $a_1, \ldots, a_M$. Therefore, in all cases, λ is multiplied by 1.5 if the new parameter set leads to an increase of χ^2 and λ is divided by 1.5 if the new parameter set leads to a decrease of χ^2 during the iterative solving process. In each case, the Levenberg-Marquardt procedure is run for $n = 40$ iteration steps starting with a parameter of $\lambda = 0.01$. Next, the optimization scheme is conducted again with $n = 30$ iteration steps and a start value of $\lambda = 0.001$ as the numerical value of $\chi^2(a_1, \ldots, a_M)$ now already is closer to the (local) minimum. The latter is repeated until the parameter set does not change any more significantly during the 30 optimization steps.

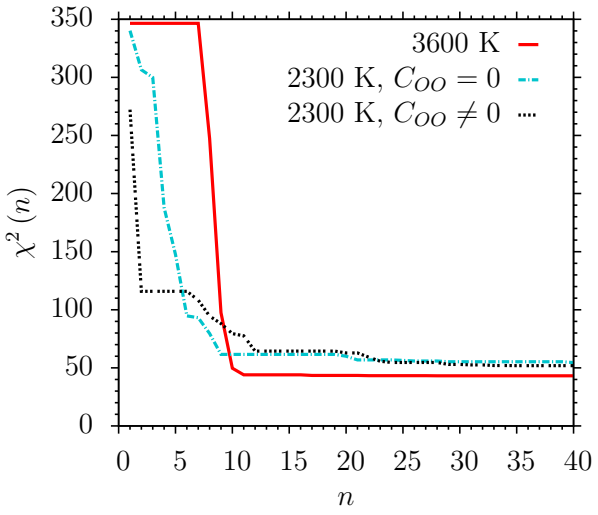

FIGURE 6.9: χ^2 with respect to iteration step. Parameter fitting of pair potentials for B_2O_3 at 3600 K and 2300 K.

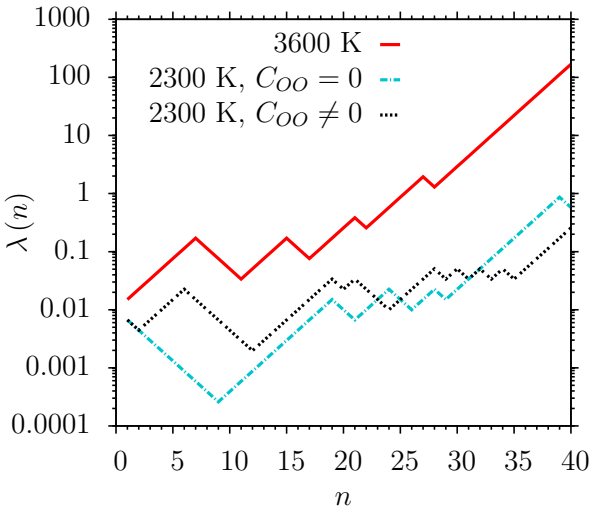

FIGURE 6.10: λ with respect to iteration step. Parameter fitting of pair potentials for B_2O_3 at 3600 K and 2300 K.

In all cases, the classical molecular dynamics simulations are carried out with a time step of 1.2 fs. As described subsection 4.1.1, a chain of 3 Nosé-Hoover thermostats (see subsection 3.1.2) is employed with a damping parameter of 120 fs, integrating the equations of motions according to [68]. This means that the temperature is relaxed to the target temperature in a timespan of 100 time steps. In all cases, the systems are equilibrated for 100000 ts, followed by a production run of 100000 ts, where configurations are stored every 10 ts to calculate the pair correlation functions and angular distributions.

In Fig. 6.9, the evolution of χ^2 (see equation (3.128)) is displayed with respect to the iteration steps n for the first $n = 40$ steps of the structural fits at 3600 K and 2300 K. It can be seen that, in all cases, χ^2 decreases quite rapidly during the first iteration steps. This is an indication that

the structural fitting procedure according to the Levenberg-Marquardt scheme works reasonably well and the start parameter of $\lambda = 0.01$ is a sensible choice. In Fig. 6.10, the evolution of λ is displayed with respect to the iteration steps n, again for the first $n = 40$ steps of the structural fits at 3600 K and 2300 K. The decrease of λ at a specific iteration step implies that at this step a parameter optimization could be achieved and vice versa. It can be seen that, in all cases, after several iteration steps at which λ decreases, an increase can be observed at the end of this set of iteration steps. In general, the parameter λ stays larger for the optimization at 3600 K, meaning there are less iteration steps, where the fit parameters could be optimized. It should be noted that the optimization procedures at 2300 K, displayed in Figs. 6.9 and 6.10, are conducted with respect to the liquid structure between time steps 62000 and 72000 of the 124.2 ps ab initio run at 2300 K. At the point in time where these structural fits have been performed, the simulation of the liquid trajectory at 2300 K has not yet been completed. However, no significant change of the fit parameters is observed when the optimization scheme is rerun with respect to the last 20000 ts of the 124.2 ps run, starting with the already optimized parameter set after 72000 time steps and a start parameter of $\lambda = 0.001$. The final values of χ^2 after all iterations of the parameter optimizations are: $\chi^2 = 43.1828$ at 3600 K and $\chi^2 = 50.267151$ ($C_{OO} = 0\,\mathrm{eV\,\AA^6}$) and $\chi^2 = 50.831890$ ($C_{OO} \neq 0\,\mathrm{eV\,\AA^6}$) at 2300 K.

The optimized parameter sets are displayed in table 6.5 together with the start parameters, according to [97]. It can be seen that at $T = 3600$ K, as well as $T = 2300$ K, a main effect of the structure matching scheme is to reduce the charge of the boron atoms q_B (and as a consequence also the charge of the oxygen atoms q_O). The decrease of the atomic charges is more pronounced at the temperature of 2300 K. Of course, in this considerations, q_B only is a force field parameter and the numerical value of q_B (and q_O) should not be taken literally. However, it is known that the bonding of B_2O_3 is partly covalent [165]. In this work, the Mulliken charges of crystalline B_2O_3 are calculated and it is found that both investigated crystalline phases show a degree of covalency in the bonding, which is more pronounced for the low-pressure phase $B_2O_3 - I$. Also, the most-promising classical force fields, according to [44], show a partial charge of $q_B = 1.2\,\mathrm{e}$ (C1) and $q_B = 0.9\,\mathrm{e}$ (C2). These values of the parameter q_B agree quite well with the results of this work.

In Figs. 6.11 and 6.12, the partial pair correlation functions $g_{BB}(r)$ and $g_{OO}(r)$ and the angular distributions $p_{BOB}(\Phi)$ and $p_{OBO}(\Phi)$, according to the structural fit at $T = 3600$ K, are compared to the curves, based on the last 20000ts of the ab initio MD trajectory at the same temperature, and to the curves of the original parameter set [97]. These are the correlations that show the most pronounced differences between the classical and the ab initio MD run. The main difference between the classical MD simulation with the new parameter set and the ab initio MD run is that the peak position of the first neighbor peak in $g_{BB}(r)$ is shifted to a larger distance r of about 0.1 Å in the classical MD run. This reflects in the peak position of the main peak in $p_{BOB}(\Phi)$ being shifted to larger angles by about 10°, as well. The classical $g_{OO}(r)$ curve shows some irregularities for small r-values. In general, the peak heights of the classical curves after the structural fit are slightly lower than in the ab initio MD run. However, these curves show a significantly improved agreement to the ab initio curves, compared to the original parameter

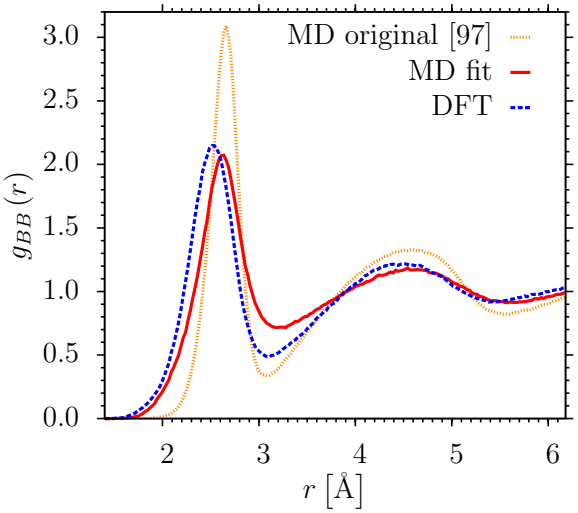

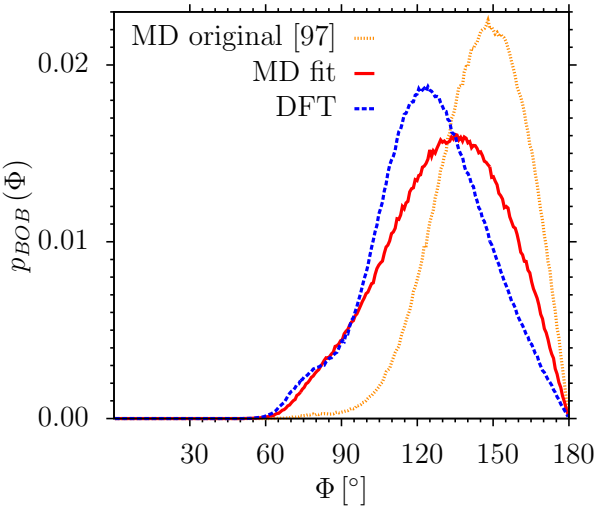

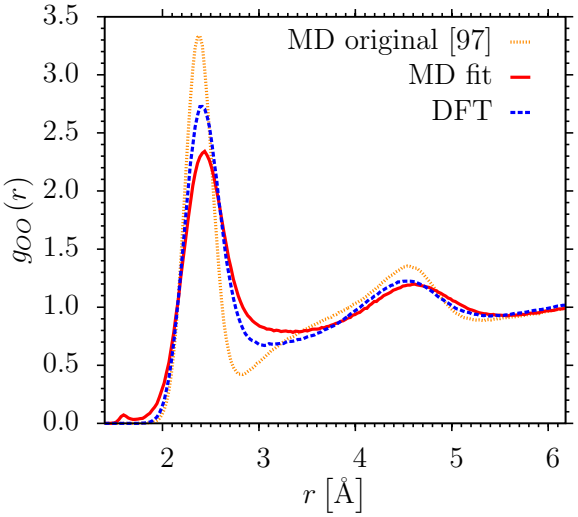

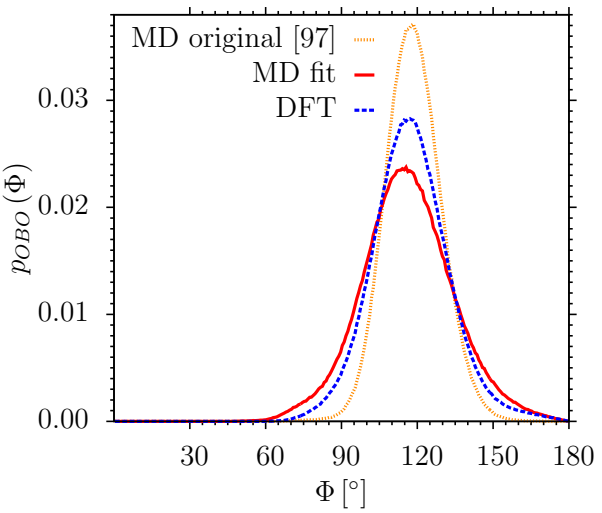

FIGURE 6.11: $g_{BB}(r)$ and $g_{OO}(r)$. Result of parameter fitting of pair potentials for B_2O_3 at 3600 K and comparison with original parameter set [97].

FIGURE 6.12: $p_{BOB}(\Phi)$ and $p_{OBO}(\Phi)$. Result of parameter fitting of pair potentials for B_2O_3 at 3600 K and comparison with original parameter set [97].

set. Here, the corresponding peak heights are substantially increased, compared to the curves after the structural fit. Also, the mean first neighbor B-B distance and the mean B-O-B angle are significantly larger.

In Figs. 6.13 and 6.14, the partial pair correlation functions $g_{BB}(r)$ and $g_{OO}(r)$ and the angular distributions $p_{BOB}(\Phi)$and $p_{OBO}(\Phi)$, according to the structural fits at $T = 2300\,\mathrm{K}$, are compared to the curves based on the last 20000ts of the ab initio MD trajectory at the same temperature and, once again, to the curves of the original parameter set [97]. It can be seen that the curves of the two different fits ($C_{OO} = 0\,\mathrm{eV\,\AA^6}$ and $C_{OO} \neq 0\,\mathrm{eV\,\AA^6}$) have a pretty similar shape. Again, the peak positions of the main peaks in $g_{BB}(r)$ and $p_{BOB}(\Phi)$ are shifted to larger values of about 0.1 Å and 10° for both classical force fields. Also, the peak heights of the classical MD runs with both new parameter sets are significantly lower, compared to the ab initio MD simulation. This feature is even more pronounced than at $T = 3600\,\mathrm{K}$. Again, the

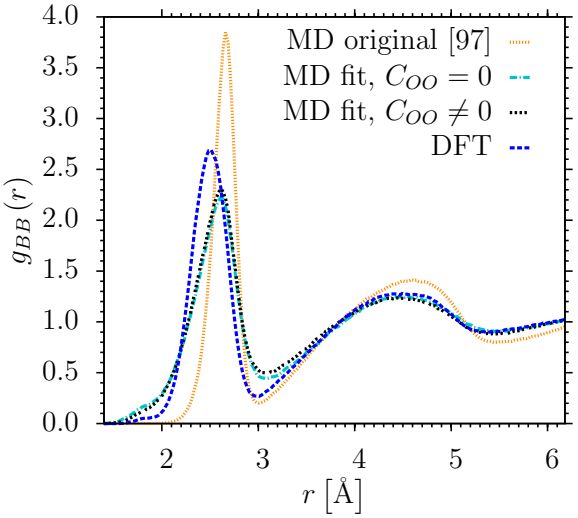

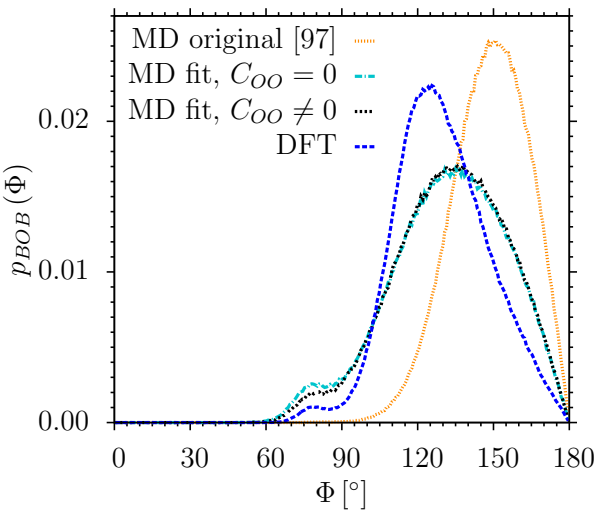

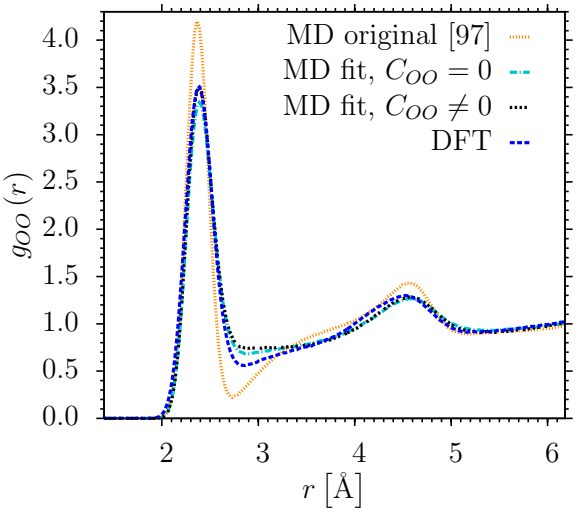

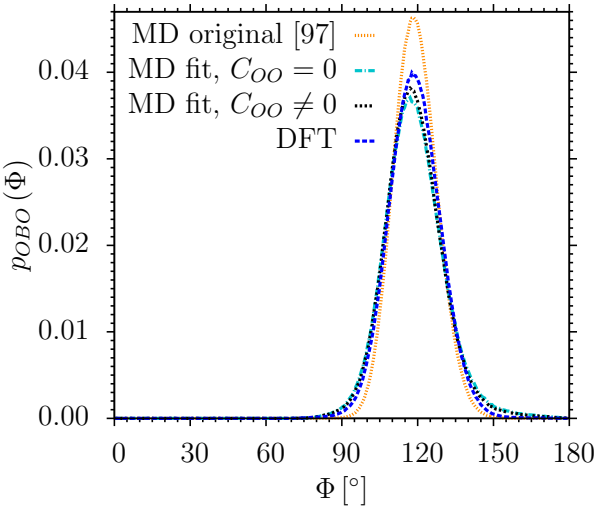

FIGURE 6.13: $g_{BB}(r)$ and $g_{OO}(r)$. Result of parameter fitting of pair potentials for B_2O_3 at 2300 K and comparison with original parameter set [97].

FIGURE 6.14: $p_{BOB}(\Phi)$ and $p_{OBO}(\Phi)$. Result of parameter fitting of pair potentials for B_2O_3 at 2300 K and comparison with original parameter set [97].

curves of the original parameter set show a significantly inferior agreement with the ab initio curves, with substantially increased peak heights and a larger first neighbor B-B distance and mean B-O-B angle.

Following these results, the next step is to include 3-body terms into the description of the system. As already mentioned above, the B-O bonding shows a rather high degree of covalency. To model the directional properties of covalent bonding, it seems sensible to include angular potential terms $V(\Phi)$ into the classical force field. In the beginning of this section, it is already mentioned that all force-fields leading to a significant amount of 3-membered boroxol rings include at least 3-body terms. Also in the work of C.R. Trott [97], used as a starting point for the parameter optimization in this section, angular terms for the O-B-O and the P-O-P interactions are introduced. When simulating in the liquid state, angular terms have to be introduced in a way that angles can form and dissolve dynamically during the simulation run.

In [97], this is accomplished in terms of an additional fix of the LAMMPS software package (LAMMPS fix dynamic/angles). Here, every n time steps, the list of angles is re-written based on the inter-particle distances. This list includes all triplets of atoms that form an angle and for this triplets, forces according to the derivative of $V_{ijk}(\Phi)$, $i,j,k \in \{1,\ldots,N\}$, have to be included into the calculation of the total force on each atom. The angular terms $V_{ijk}(\Phi)$ are only included if the three atoms with indices i, j and k are of a specific type, for example O, B and O. However, in this approach, either three atoms of the specific types form an angle (for example an O-B-O angle if the two O atoms both have a distance r to the central B atom smaller than a specific cutoff radius r_c^{ang}) or they do not form an angle. This means that the additional potential terms $V_{ijk}(\Phi)$ are instantaneously switched on and off, meaning the total energy of the system $V(\{\mathbf{r}_i(t)\})$ is a discontinuous function of the atomic coordinates $\{\mathbf{r}_i(t)\}$.

Therefore, a slightly different approach is chosen to introduce the angular interactions in this work. The functional form of the angular potential, in all cases, is chosen to be of the Gaussian type with negative sign (see equation (3.127))

$$V_{ijk}^{\text{Gauss}}(\Phi) = V_{ijk}^{\text{Gauss}}(\Phi(\mathbf{r}_i,\mathbf{r}_j,\mathbf{r}_k)) = -K_{ijk}\exp\left[-\sigma_{ijk}\left(\Phi(\mathbf{r}_i,\mathbf{r}_j,\mathbf{r}_k)-\Phi_{0,ijk}\right)^2\right], \tag{6.1}$$

$i,j,k \in \{1,\ldots,N\}$, following the work of [97]. Again, the angular potential is only included, if the atoms with indices i, j and k are of specific types. In the following, only angular interactions between two oxygen and one boron atom, forming a O-B-O angle, and interactions between two boron and one oxygen atom, forming a B-O-B angle are considered. To smoothly switch on and off the angular terms, the following procedure is chosen. The angular potential, according to equation (6.1), is multiplied by a smoothing function with the functional form, according to (3.13). However, the inter-particle distance r is substituted by a mean distance $\bar{r}$, leading to the following functional form:

$$V_{ijk}^{\text{Smooth}}(\mathbf{r}_i,\mathbf{r}_j,\mathbf{r}_k) = V_{ijk}^{\text{Gauss}}(\Phi(\mathbf{r}_i,\mathbf{r}_j,\mathbf{r}_k))\, G(\bar{r}_{ijk}(\mathbf{r}_i,\mathbf{r}_j,\mathbf{r}_k)), \tag{6.2}$$

$$\Leftrightarrow V_{ijk}^{\text{Smooth}}(\mathbf{r}_i,\mathbf{r}_j,\mathbf{r}_k) = V_{ijk}^{\text{Gauss}}(\Phi(\mathbf{r}_i,\mathbf{r}_j,\mathbf{r}_k))\exp\left[-\frac{d^{\text{ang}}}{\left(\bar{r}_{ijk}(\mathbf{r}_i,\mathbf{r}_j,\mathbf{r}_k)-r_c^{\text{ang}}\right)^2}\right] \tag{6.3}$$

$$\bar{r}_{ijk}(\mathbf{r}_i,\mathbf{r}_j,\mathbf{r}_k) = \sqrt[N]{r_{ij}^N + r_{kj}^N}, \quad r_{ij} = |\mathbf{r}_i-\mathbf{r}_j|,\ r_{kj} = |\mathbf{r}_k-\mathbf{r}_j|. \tag{6.4}$$

In the limit of $N \to \infty$, the value of $\bar{r}_{ijk}$ is equivalent to the maximum of r_{ij} and r_{jk}. The potential energy according to equation (6.2) is only added to the total potential energy of the system $V(\{\mathbf{r}_i(t)\})$ if both inter-atomic distances r_{ij} and r_{jk} are smaller than the cutoff distance r_c^{ang}. Otherwise, the additional 3-body term is set to $V_{ijk}^{\text{Smooth}} = 0$. The smooth decay to zero of $G(\bar{r}_{ijk})$ for $\bar{r}_{ijk} \to r_c^{\text{ang}}$ ensures that the potential V_{ijk}^{Smooth} is smoothly switched on if the value of $\bar{r}_{ijk}$ gets smaller than r_c^{ang} during the simulation run (meaning in the situation when

both relevant distances r_{ij} and r_{jk} get smaller than the cutoff radius r_c^{ang}). Choosing a finite, but rather high value of the parameter N, causes $V_{ijk}^{Smooth}(\mathbf{r}_i, \mathbf{r}_j, \mathbf{r}_k)$ (see equation (6.2)) to be continuously differentiable with respect to the atomic positions $\{\mathbf{r}_i(t)\}$, but still decaying reasonably fast to 0 at r_c^{ang}. In appendix A, the differentiation with respect to the atomic coordinates $\mathbf{r}_i$, $\mathbf{r}_j$ and $\mathbf{r}_k$ is carried out, leading to the functional form of the additional forces on the corresponding atoms (see equations (A.1), (A.16) and (A.17)).

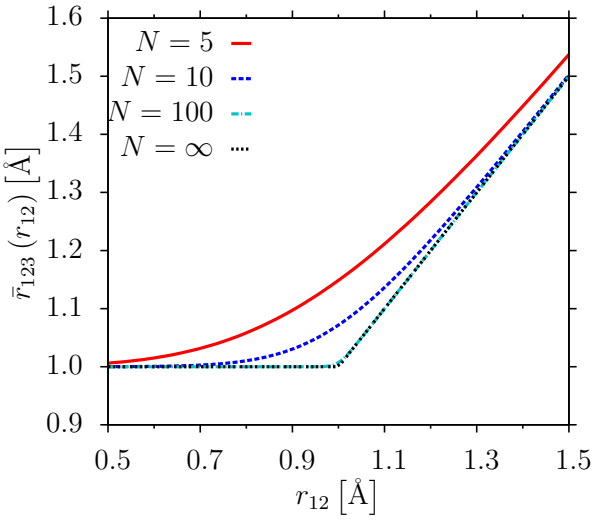

FIGURE 6.15: $\bar{r}_{123}(r_{12})$ for $N = 5$, 10, 100 and ∞ and $r_{23} = 1.0$ Å.

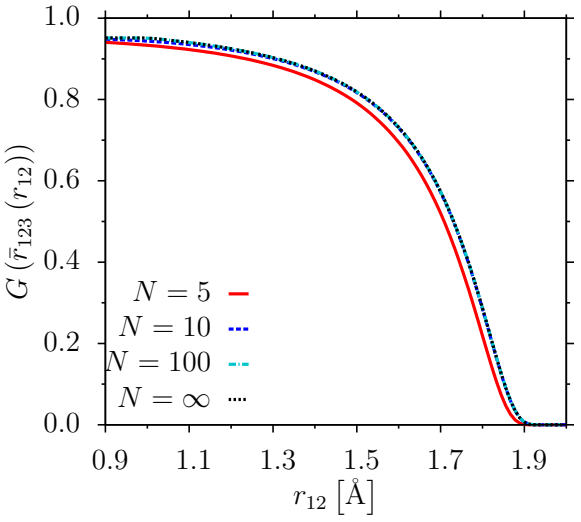

FIGURE 6.16: $G(\bar{r}_{123}(r_{12}))$ for $N = 5$, 10, 100 and ∞ and $r_{23} = 1.0$ Å with $r_c^{ang} = 2$ Å and $d^{ang} = 0.05$ Å^2.

The calculation of the (additional) potential energy and (additional) forces on the atoms, according to $V_{ijk}^{Smooth}(\mathbf{r}_i, \mathbf{r}_j, \mathbf{r}_k)$, is implemented in a new pair style of the LAMMPS software package [60, 61], called "gauss/smooth". So far, only the case is implemented where the atom with index i is of the same type as the atom with index k. The pair coefficients of this new pair style (pair_coeff command of the LAMMPS software package) are K_{ijk}, σ_{ijk}, $\Phi_{0,ijk}$, d^{ang} and N. The parameter r_c^{ang} is determined by means of the cutoff radius when invoking the pair style. The atom types of the central atom j and the two neighboring atoms i and k are determined by the first and the second atom type when invoking the pair style. When the pair style is included, at each time step of the simulation run, the potential energy term, according to equations (6.2) to (6.4), is evaluated and the forces on the atoms i, j and k are calculated, according to equations (A.1), (A.16) and (A.17), in the case of both r_{ij} and r_{jk} being smaller than r_c^{ang}.

In Fig. 6.15, the functional form of $\bar{r}_{123}$ is depicted with respect to the distance between atoms 1 and 2, r_{12}, for a triplet of atoms with a fixed inter-atomic distance of $r_{23} = 1.0$ Å. It can be seen that in in case of $N = \infty$, the function value is equal to 1.0 for $r_{12} < 1.0$ and for $r_{12} > 1.0$ it increases linearly with increasing r_{12}. For finite N, this transition is smoothed. In Fig. 6.16, the smoothing function $G(\bar{r}_{123})$ is displayed with respect to r_{12} for a fixed $r_{23} = 1.0$ Å, a cutoff radius of $r_c^{ang} = 2$ Å and $d^{ang} = 0.05$ Å^2. It can be seen that, in all cases, it decays smoothly to zero for $r_{12} \to r_c^{ang}$. The decay gets slightly steeper with increasing N.

Next, structural fits are carried out, including angular terms, according to equations (6.2) to (6.4). In all cases, a value of $N = 100$ is chosen, a cutoff radius of $r_c^{ang} = 2\,\text{Å}$ and $d^{ang} = 0.05\,\text{Å}^2$. A value of $r_c^{ang} = 2\,\text{Å}$ corresponds to the position of the first minimum of $g_{BO}(r)$, according to the ab initio MD run at 2300 K. Structural fits including angular terms are only carried out at the lowest temperature accessed by ab liquid ab initio MD runs, namely 2300 K. This is motivated by the fact that the liquid structure at this temperature is the one closest to the glass structure and the number of 3-membered rings starts to increase again at this temperature (see section 6.2). Also, the 2-body fit at 3600 K shows a slight irregularity at low distances r in $g_{OO}(r)$, which is not apparent for the parameter fits at 2300 K.

Following the work of [97], in a first attempt, structural fits are carried out with the additional 3-body term applied only to the O-B-O correlation. In a second attempt, the 3-body term is applied to the B-O-B correlation, as well as the O-B-O correlation. The 2-body interactions are chosen to be the same as described above, meaning the shifted and smoothed pair potential of the Buckingham type with Coulomb interactions and a harmonic substitution for small distances r, according to equation (4.3). Again, the B-B interaction is chosen to be purely electrostatic and the initial parameter set is the start parameter set, according to Table 6.5. The start parameters for the 3-body term are chosen as $K_{OBO} = K_{BOB} = 0.3\,\text{eV}$ and $\sigma_{OBO} = \sigma_{BOB} = 0.01\,^{\circ -2}$.

parameters	units	3-body O-B-O	3-body O-B-O and B-O-B fit 1	3-body O-B-O and B-O-B fit 2
q_B	[e]	0.979987	1.005560	0.996922
A_{BB}	[eV]	-	-	-
b_{BB}	$[\text{Å}^{-1}]$	-	-	-
C_{BB}	$[\text{eV}\,\text{Å}^6]$	-	-	-
A_{BO}	[eV]	86093.78125	335996.8125	236849.265625
b_{BO}	$[\text{Å}^{-1}]$	8.205286	9.461655	9.101221
C_{BO}	$[\text{eV}\,\text{Å}^6]$	13.519357	11.320659	12.766488
A_{OO}	[eV]	2191.408203	2635.602051	1405.565063
b_{OO}	$[\text{Å}^{-1}]$	3.37808	3.629571	2.967662
C_{OO}	$[\text{eV}\,\text{Å}^6]$	74.013123	-	127.219231
K_{OBO}	[eV]	0.235306	0.269162	0.299261
σ_{OBO}	$^{\circ -2}$	0.003204	0.001113	0.001170
K_{BOB}	[eV]	-	0.268771	0.267305
σ_{BOB}	$^{\circ -2}$	-	0.001656	0.001458

TABLE 6.7: Different parametrizations of the pair potential (see equation (3.122)) and 3-body potentials (see equation (6.1)) for B_2O_3. Comparison of different parametrizations after structural fits at 2300 K.

Again, structural fits are carried out, applying the Levenberg-Marquardt scheme, described in detail in section 3.5. As in the case of pure 2-body interactions, the structural fits are carried out with respect to the partial pair correlation functions and the relevant angular distributions,

meaning the parameters χ^2 are calculated, according to equation (3.128). This means, parameter sets of $M = 9$ to $M = 11$ parameters are optimized, namely q_B, A_{BO}, b_{BO}, C_{BO}, A_{OO}, b_{OO}, C_{OO}, K_{OBO}, σ_{OBO}, K_{BOB} and σ_{BOB}. As described above, this requires the conduction of $2\,M + 1$ classical MD runs per iteration step of the Levenberg-Marquardt procedure. These classical MD runs are carried out in exactly the same way as in case of the parameter fits for the pure 2-body potentials described above. The parameters ϵ_{a_i} for the 2-body terms are the same as described above and the values of the additional ϵ_{a_i} are chosen to be $\epsilon_{K_{OBO}} = \epsilon_{K_{BOB}} = 0.0\bar{6} \cdot K_{OBO} = 0.02\,\text{eV}$ and $\epsilon_{\sigma_{OBO}} = \epsilon_{\sigma_{BOB}} = 0.05 \cdot \sigma_{OBO} = 0.0005\,^{\circ -2}$. Again, the Levenberg-Marquardt procedures are carried out with an initial parameter of $\lambda = 0.01$, continuing in the same way as described above for the pure 2-body potentials. In the case of applying 3-body terms to the O-B-O, as well as the B-O-B correlation, two different fits are carried out, as in case of the 2-body fits at 2300 K. In the second one, the O-O interaction is chosen to be purely repulsive, meaning a fixed value of $C_{OO} = 0\,\text{eV}\,\text{Å}^6$ is chosen. In this case a set of $M = 10$ parameters is optimized. The final values of χ^2 after all iterations of the parameter optimizations are $\chi^2 = 46.08730$ (3-body terms for the O-B-O correlation) and $\chi^2 = 11.732140$ (3-body terms for the O-B-O and B-O-B correlation and $C_{OO} = 0\,\text{eV}\,\text{Å}^6$) and $\chi^2 = 10.961948$ (3-body terms for the O-B-O and B-O-B correlation and $C_{OO} \neq 0\,\text{eV}\,\text{Å}^6$) at 2300 K.

The optimized parameter sets are displayed in table 6.7. As in the 2-body case, a main effect of the structure matching scheme is to reduce the charge of the boron atoms q_B (and as a consequence also the charge of the oxygen atoms q_O). In all cases, the charges of the boron atoms are about $q_B = 1\,\text{e}$. Again, this value agrees quite well with the ones of the two most-promising classical force fields, according to [44] ($q_B = 1.2\,\text{e}$ (C1) and $q_B = 0.9\,\text{e}$ (C2)). The parameters of the 3-body interactions in all cases are pretty similar.

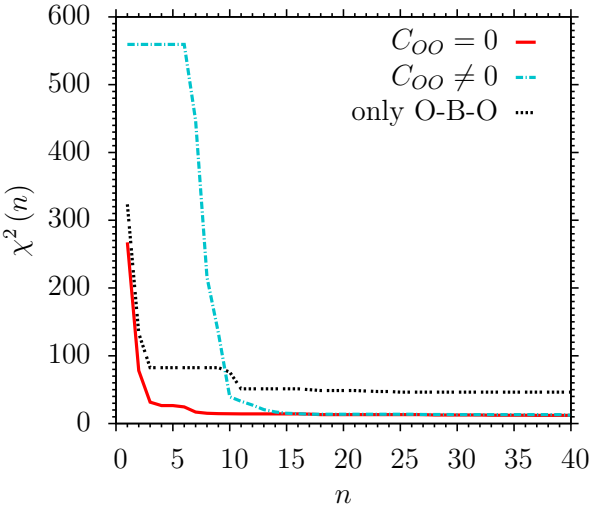

FIGURE 6.17: χ^2 with respect to iteration step. Parameter fitting of potentials including 3-body terms for B_2O_3 at 2300 K.

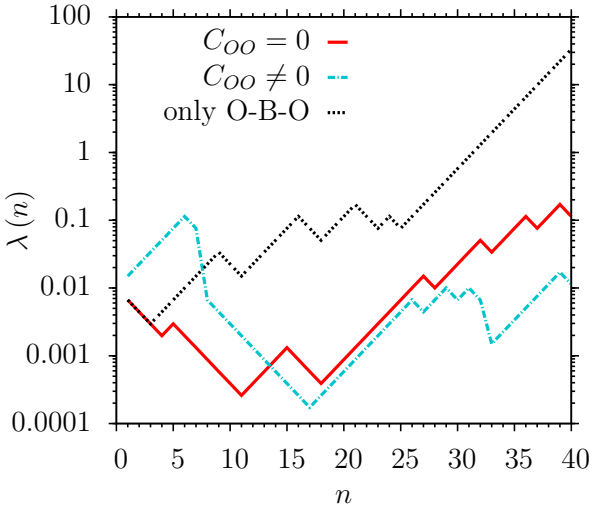

FIGURE 6.18: λ with respect to iteration step. Parameter fitting of potentials including 3-body terms for B_2O_3 at 2300 K.

In Figs. 6.17 and 6.18, the evolution of χ^2 (see equation (3.128)) and λ are displayed with respect to the iteration steps n for the first $n = 40$ steps of the structural fit. In case of the application of

3-body terms to the O-B-O and the B-O-B correlation and $C_{OO} \neq 0\,\text{eV}\,\text{Å}^6$, the displayed values of χ^2 and λ are a composition of three consecutive iteration runs, as the Levenberg-Marquardt procedure has been aborted twice due to the crash of the compute node. It has been restarted, first, with an initial value of $\lambda = 0.01$ at the 8^{th}, and, second, with an initial value of $\lambda = 0.001$ at the 33^{th} iteration step. Both, the developments of χ^2, as well as λ, show a similar behavior as in the case of the pair interactions, as described above.

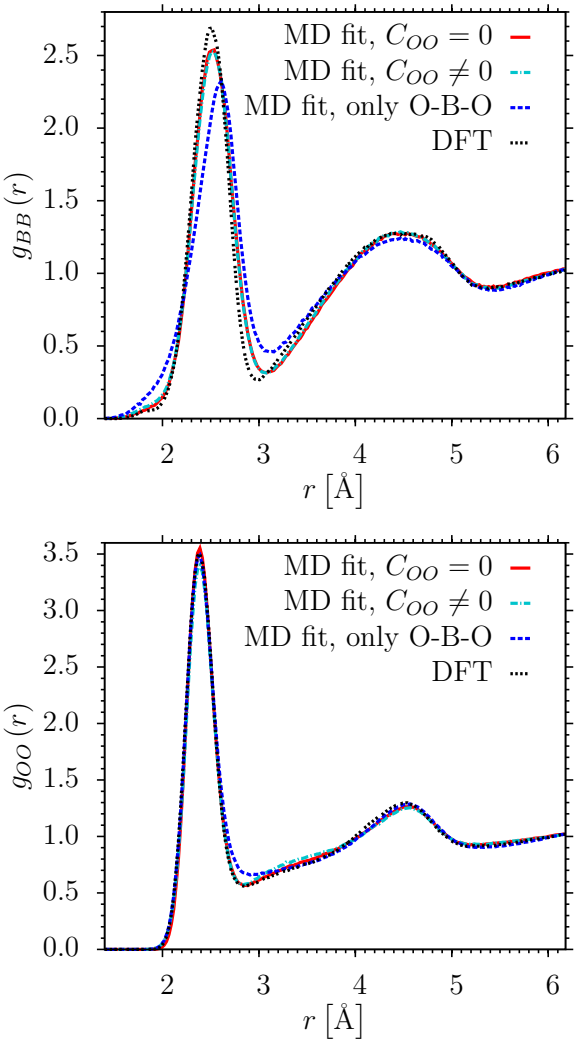

FIGURE 6.19: $g_{BB}(r)$ and $g_{OO}(r)$. Results of parameter fitting of potentials including 3-body terms for B_2O_3 at 2300 K.

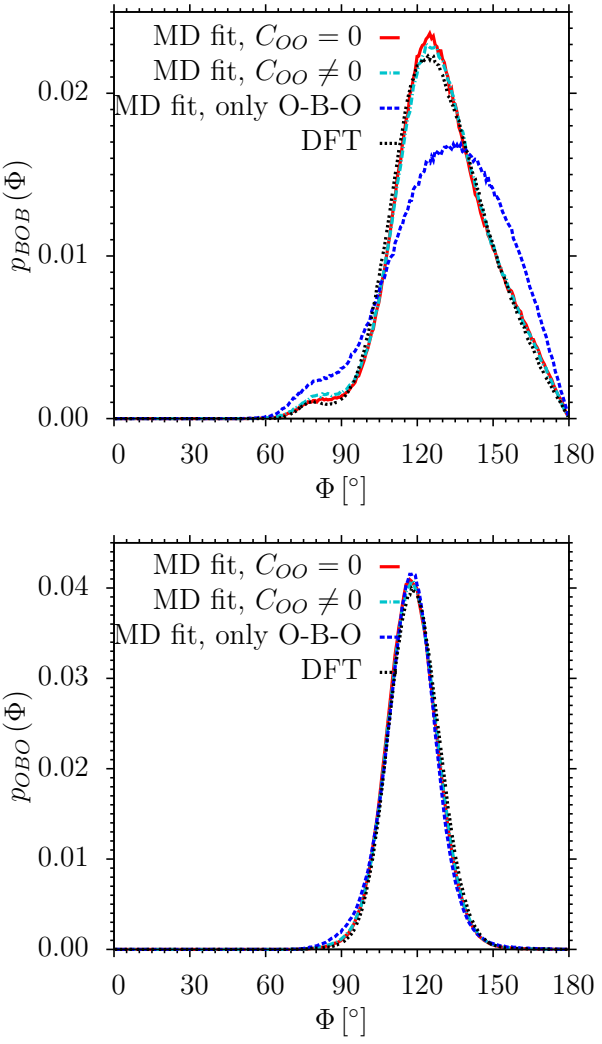

FIGURE 6.20: $p_{BOB}(\Phi)$ and $p_{OBO}(\Phi)$. Results of parameter fitting of potentials including 3-body terms for B_2O_3 at 2300 K.

In Figs. 6.19 and 6.20, the partial pair correlation functions $g_{BB}(r)$ and $g_{OO}(r)$ and the angular distributions $p_{BOB}(\Phi)$ and $p_{OBO}(\Phi)$ are displayed. The curves, according to the structural fits at $T = 2300\,\text{K}$ including 3-body terms, are compared to the curves based on the last 20000ts of the ab initio MD trajectory at the same temperature. As in case of the pure 2-body interactions, the curves of the two different fits with both 3-body terms ($C_{OO} \neq 0\,\text{eV}\,\text{Å}^6$ and $C_{OO} = 0\,\text{eV}\,\text{Å}^6$) have a pretty similar shape. It can be seen that the curves of the parameter sets with 3-body terms for the O-B-O, as well as the B-O-B interaction show an enhanced agreement with the

curves of the ab initio MD run. The curves of the parameter set with 3-body terms only for the O-B-O correlation show a similar behavior as the ones of the 2-body fits. Here, the agreement of $g_{OO}(r)$ and $p_{OBO}(\Phi)$ with the ab initio curves is pretty good. However, the positions of the main peaks in $g_{BB}(r)$ and $p_{BOB}(\Phi)$ are shifted to larger values by about 0.1 Å and 10°, as in case of the 2-body fits.

The results of the structural fitting procedure encourage to examine the two different parameter sets, including 3-body terms for the O-B-O and the B-O-B interaction, in detail. This is done in the next section with respect to the liquid properties. In sections 6.5 and 6.6, the structural and vibrational properties of B_2O_3 glass configurations, generated by this two force fields, are compared to the properties of the glass configurations, generated by full ab initio quenches and the original parameter set [97].

6.4 Liquid properties by means of classical MD simulations

In this section, the properties of liquid B_2O_3, according to the two most-promising force fields after the structural fit (see section 6.3), are studied. On the one hand, the structural and dynamical properties are compared to the ones of the ab initio MD simulations (see section 6.2) at the corresponding temperatures. On the other hand, the temperature dependence of certain structural and dynamical properties is examined. All classical simulations are carried out based on the two force fields, including 3-body interactions with fixed $C_{OO} = 0\,\text{eV}\,\text{Å}^6$ and $C_{OO} \neq 0\,\text{eV}\,\text{Å}^6$ (see Table 6.7). Again, all simulations are carried out with the LAMMPS software package [60, 61], in this case, employing the new pair style "gauss/smooth".

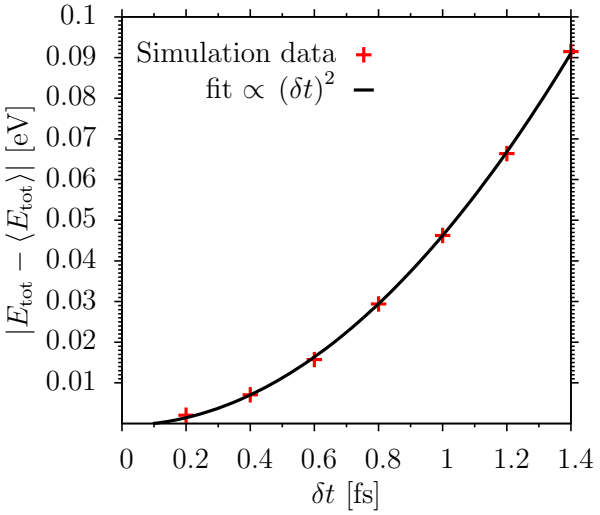

FIGURE 6.21: Test of relation $|E_{\text{tot}} - \langle E_{\text{tot}} \rangle| \propto (\delta t)^2$ for potential including 3-body terms and $C_{OO} = 0\,\text{eV}\,\text{Å}^6$.

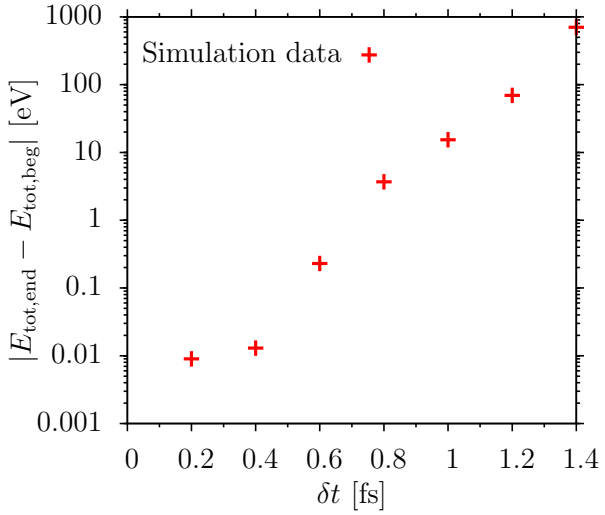

FIGURE 6.22: $|E_{\text{tot,end}} - E_{\text{tot,beg}}|$ in micro-canonical production run for potential including 3-body terms and $C_{OO} = 0\,\text{eV}\,\text{Å}^6$.

Simulations are carried out for two system sizes, namely 150 atoms and 1200 atoms. In the case of 150 atoms, all simulations are carried out at the fixed system density of $\rho = 1.83\,\text{g/cm}^3$

($L_{\text{Box}} = 12.375\,\text{Å}$), as in the previous chapter. In the case of 1200 atoms, simulations are carried out at constant external pressure of $p = 0$ to study the dependence of the system density ρ on the temperature. This system size is large enough to avoid significant finite size effects and the external pressure of $p = 0$ is a reasonable assumption for normal conditions ($p = 1\,\text{atm} \simeq 0.1\,\text{MPa}$), as the magnitude of relevant pressures in solids is in the order of GPa.

To test the implementation of the new pair style ("gauss/smooth"), a series of test runs is conducted, similar to the test runs in the case of SiO_2, described in subsection 4.1.1. The test runs are performed for the parameter set with fixed $C_{OO} = 0\,\text{eV}\,\text{Å}^6$. After a random initialization (see subsection 4.1.1), the system is equilibrated at 3600 for 200000 ts, using a time step of 0.6 fs. The equilibration run is done in a NVT ensemble, again using a chain of 3 Nosé-Hoover thermostats (see subsection 3.1.2) with a damping parameter of 60 fs, integrating the equations of motions, according to [68]. Again, at the end of the equilibration run, 10000 configurations are stored. As a starting point of the microcanonical test runs, the configuration is chosen with a total energy $E_{\text{tot}} = E_{\text{kin}} + E_{\text{pot}}$ closest to the mean total energy of the preceding equilibration run.

To test the relation $|E_{\text{tot}} - \langle E_{\text{tot}} \rangle| \propto (\delta t)^2$ (see equation (3.11)), short microcanonical runs of $1 \cdot 10^5$ ts are carried out with different time steps from $\delta t = 0.2\,\text{fs}$ to $\delta t = 1.4\,\text{fs}$. Again, the amplitude of fluctuations is determined by computing half of the mean difference between neighboring maxima and minima of E_{tot} in the microcanonical runs. The neighboring maxima and minima are only taken into account if there is a time difference of 10 time steps in between. In Fig. 6.22, $|E_{\text{tot}} - \langle E_{\text{tot}} \rangle|$ is displayed with respect to the time step δt. It can be seen that in this range of time steps δt, the relation $\delta E_{\text{tot}} \propto \delta t^2$ is fulfilled.

To examine the drift of the total energy, microcanonical test runs of 10 ns are carried out, again with different time steps from $\delta t = 0.2\,\text{fs}$ to $\delta t = 1.4\,\text{fs}$. In Fig. 6.22, the absolute difference of the total energy between the end and the beginning of the test runs is shown on a logarithmic scale. It can be seen that the energy difference $|E_{\text{tot,end}} - E_{\text{tot,beg}}|$ increases by orders of magnitude with increasing time step δt. As in case of the model glass former SiO_2 (see subsection 4.1.1), it seems to be a good compromise between computational efficiency and accuracy, to chose a time step of $\delta t = 0.6\,\text{fs}$. In the following, this time step is applied at all temperatures and system sizes.

To study the liquid properties at different temperatures, all systems are first randomly initialized and then pre-relaxed with Lennard-Jones potentials, as explained in subsection 4.1.1. Afterwards, they are equilibrated at 3600 K and then cooled down in different steps to 1000 K. The equilibration times are tabulated in Table 6.9. The 150 systems are equilibrated in NVT runs, using a chain of 3 Nosé-Hoover thermostats with a damping parameter of 60 fs (100 ts). The 1200 systems first are equilibrated in NpT runs in the isothermal-isobaric ensemble at $p = 0$ external pressure. In both cases, the equations of motions are integrated, according to [68]. Simulations are carried out using a Nosé-Hoover type barostat with a damping parameter of 600 fs (1000 ts), meaning the system volume is allowed to fluctuate and the pressure of the system is relaxed to the target pressure in a timespan of 1000 time steps. A chain of 3 Nosé-Hoover

temperature	# time steps	simulation time	δt
3600 K	$2 \cdot 10^5$ ts	120 ps	0.6 fs
3300 K	$2 \cdot 10^5$ ts	120 ps	0.6 fs
3000 K	$2 \cdot 10^5$ ts	120 ps	0.6 fs
2700 K	$4 \cdot 10^5$ ts	240 ps	0.6 fs
2500 K	$6 \cdot 10^5$ ts	360 ps	0.6 fs
2300 K	$1 \cdot 10^6$ ts	600 ps	0.6 fs
2100 K	$2 \cdot 10^6$ ts	1.2 ns	0.6 fs
1800 K	$3 \cdot 10^6$ ts	1.8 ns	0.6 fs
1500 K	$1 \cdot 10^7$ ts	6 ns	0.6 fs
1200 K	$2 \cdot 10^7$ ts	12 ns	0.6 fs
1000 K	$4 \cdot 10^7$ ts	24 ns	0.6 fs
800 K ($C_{OO} = 0\,\text{eV}\,\text{Å}^6$)	$8 \cdot 10^7$ ts	48 ns	0.6 fs
800 K ($C_{OO} \neq 0\,\text{eV}\,\text{Å}^6$)	$2 \cdot 10^8$ ts	120 ns	0.6 fs

TABLE 6.9: Cooling procedure of liquid B_2O_3 with number of time steps and equilibration times at each temperature.

thermostats is coupled to the barostat with a damping parameter of 60 fs (see subsection 3.1.2). Subsequently, at each temperature, a second equilibration run is conducted in the canonical ensemble at fixed system density, corresponding to the mean density of the preceding equilibration run at constant external pressure ($p = 0$). Again, a chain of 3 Nosé-Hoover thermostats with a damping parameter of 60 fs is employed. Afterwards, in each case, microcanonical production runs are carried out at the mean total energy of the preceding equilibration runs. In the case of the 1200 atom systems, the highest examined temperatures are 2500 K ($C_{OO} = 0\,\text{eV}\,\text{Å}^6$) and 3000 K ($C_{OO} \neq 0\,\text{eV}\,\text{Å}^6$). At higher temperatures, a simulation in the NpT ensemble was not possible, as a strong expansion of the simulation box occurred. Also, the lowest considered temperature for the 1200 atom systems is 1000 K. In each case, the properties of the 150 atom systems are averaged over 10 independent simulation runs and the properties of the 1200 atom systems are averaged over 3 independent runs.

In section 6.3, already $g_{BB}(r)$, $g_{OO}(r)$, $p_{BOB}(\Phi)$ and $p_{OBO}(\Phi)$ of the classical potentials including 3-body terms have been compared to the corresponding curves of the ab initio MD simulations at 2300 K. In this section, this comparison is continued in the whole temperature range, ab initio MD simulations have been carried out. Here, only the curves of the classical potential with $C_{OO} \neq 0\,\text{eV}\,\text{Å}^6$ are displayed as in the temperature range between 2300 K and 3600 K, the dynamical and structural properties of the two different parametrizations ($C_{OO} = 0\,\text{eV}\,\text{Å}^6$ and $C_{OO} \neq 0\,\text{eV}\,\text{Å}^6$) are nearly identical, in case of 150 atom simulations at constant density.

In Figs. 6.23 and 6.24, the incoherent intermediate scattering functions $F_{\text{S},B}(k,t)$ (see equation (3.100)) and the mean square displacements $\left\langle r_B^2(t) \right\rangle$ (see equation (3.98)) of the classical MD simulations are compared to the curves of the ab initio MD simulations at 3600 K and 2300 K. The incoherent intermediate scattering functions are evaluated at $k = 1.68\,\text{Å}^{-1}$. This is about the k-value of the first sharp diffraction peak (FSDP), visible in the partial static structure

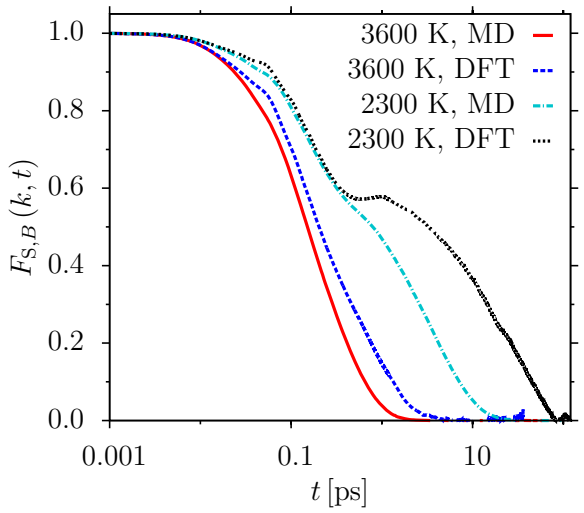

FIGURE 6.23: $F_{S,B}(k,t)$ at 2300 K and 3600 K. Comparison of classical potential including 3-body terms with ab initio MD.

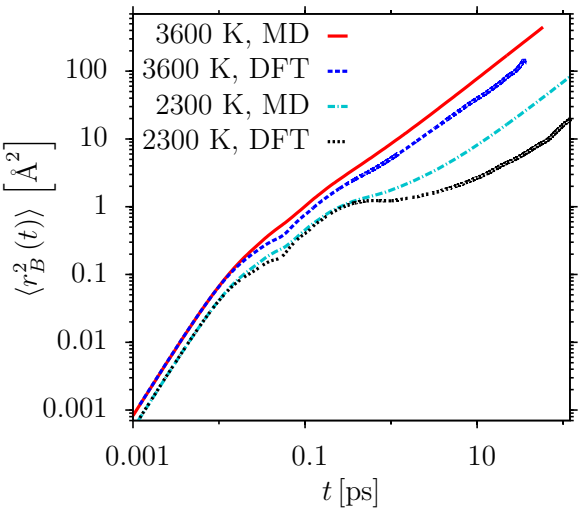

FIGURE 6.24: $\langle r_B^2(t)\rangle$ at 3600 K and at 2300 K. Comparison of classical potential including 3-body terms with ab initio MD.

factors (see section 6.2). It should be noted that the curves of the ab initio MD simulations are evaluated with respect to the MD runs in the canonical ensemble, meaning the dynamics is influenced by the Nosé thermostat (see subsection 3.1.2). At 2300 K, both curves show a two-step decay with an intermediate plateau. However, the characteristics of a two-step decay is much more pronounced in case of the ab initio MD simulations. At 3600 K, the two-step process is not yet apparent. The α-relaxation time at 3600 K is about 2-times smaller in case of the classical MD simulation as in case of the ab initio MD simulation. This ratio increases to about one order of magnitude at 2300 K. In principle, the dynamics of the oxygen atoms (not shown here) exhibits the same behavior. However, in the incoherent intermediate scattering functions of the boron atoms (see Fig. 6.24) a small shoulder is visible at a simulation time of about $50-60$ fs, which is not apparent in the curves of the oxygen atoms. So far, no clear explanation of the origin of this shoulder can be given.

In Figs. 6.25 and 6.26, the partial pair correlation functions $g_{BB}(r)$, $g_{OO}(r)$ and angular distributions $p_{BOB}(\Phi)$ and $p_{OBO}(\Phi)$ are shown at 3600 K and 2300 K. Reflecting the faster dynamics of the classical MD simulations, the peaks of $g_{BB}(r)$ are significantly lower. This already is described in section 6.3 at the temperature of 2300 K and is apparent, as well, at 3600 K. In $g_{BO}(r)$ (not shown here), this behavior is not visible at both temperatures and the agreement in both cases is very good. In the case of $g_{OO}(r)$, the curves of the classical MD and the ab initio MD simulations are nearly identical at the temperature of 2300 K, where the parameter fits are carried out. At 3600 K, the peak height of the classical MD simulation is significantly lower. Regarding $p_{BOB}(\Phi)$ and $p_{OBO}(\Phi)$, the agreement between the classical MD and the ab initio MD results is pretty good at both temperatures. The peak heights increase with decreasing temperature and the observed shoulder at about 80° in $p_{BOB}(\Phi)$ is visible in the classical, as well as in the ab initio MD curves.

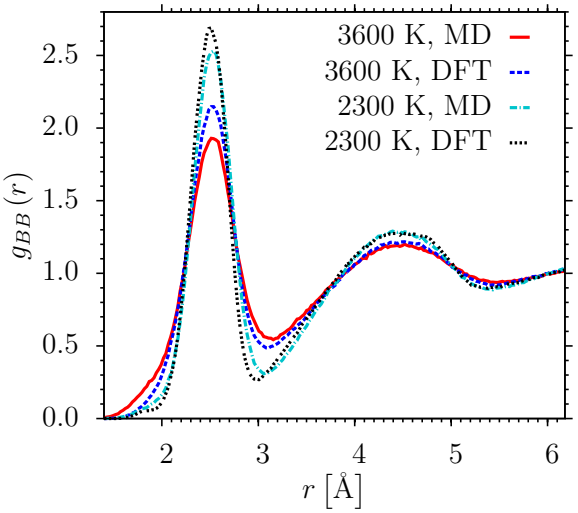

FIGURE 6.25: $g_{BB}(r)$ and $g_{OO}(r)$ at 3600 K and at 2300 K. Comparison of classical potential including 3-body terms with ab initio MD.

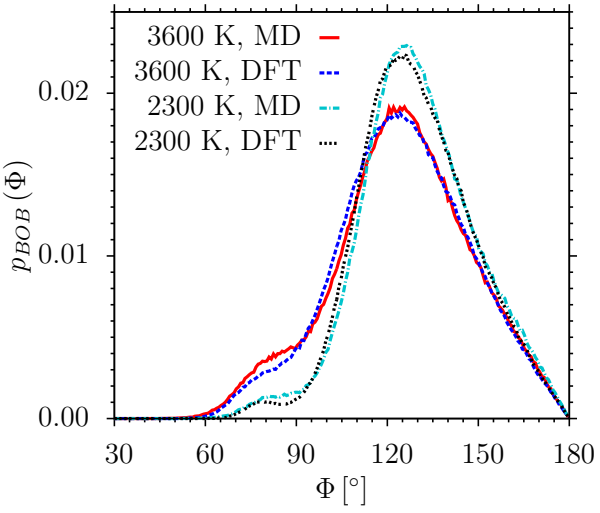

FIGURE 6.26: $p_{BOB}(\Phi)$ and $p_{OBO}(\Phi)$ at 3600 K and at 2300 K. Comparison of classical potential including 3-body terms with ab initio MD.

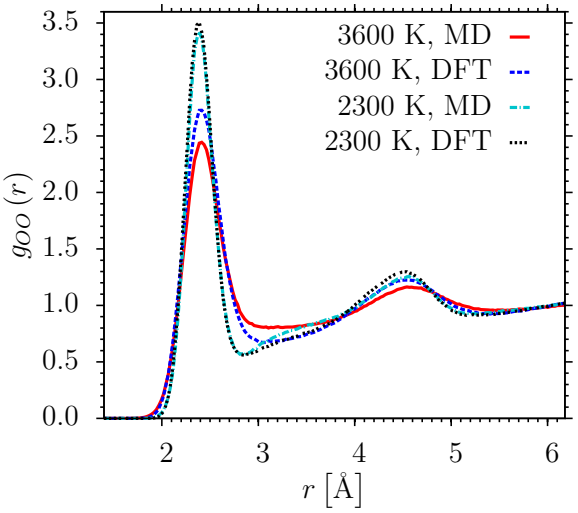

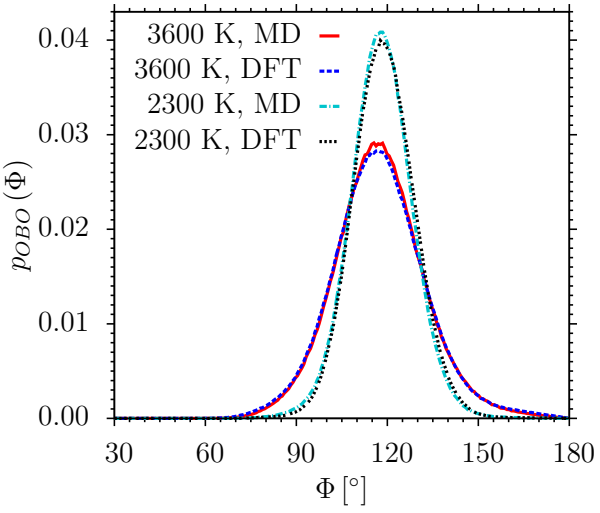

In Fig. 6.27, the probability that a B atom is member of a ring of size n is shown at 3600 K and 2300 K. Regarding $p_B(n)$, the classical MD simulations and the ab initio MD runs show some differences. At 3600 K, the most dominant ring size is $n = 7$ in both cases. However, the probability of a B atom to be in a ring of size $n = 1$ is significantly higher in case of the classical MD simulation. A ring size of $n = 1$ reflects the case of so-called non-bridging oxygen atoms, connected only to one boron atom. At 2300 K, the most dominant ring size is $n = 7$ in case of the classical MD simulation and $n = 8$ in case of the ab initio MD simulation. Again, the probability of a B atom to be in a ring of size $n = 1$ is significantly higher in case of the classical MD simulation. Also, the ab initio curve shows an increased probability of $p_B(n = 3)$, with respect to $p_B(n = 2)$ and $p_B(n = 4)$. This is not apparent in the classical MD curve. Overall, the number of small rings with $n \leq 4$ is larger in case of the classical MD simulations, at all examined temperatures. This behavior is reflected in Fig. 6.28, which shows the angular distributions of the B-B-B correlation. As already explained in section 6.2, the additional peak

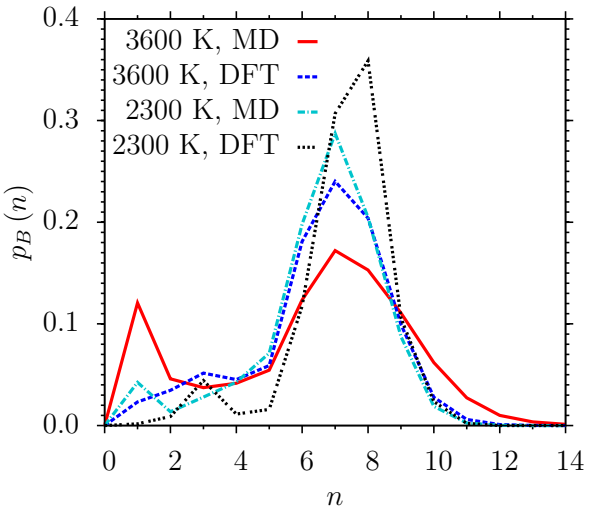

FIGURE 6.27: $p_B(n)$ at 3600 K and at 2300 K. Comparison of classical potential including 3-body terms with ab initio MD.

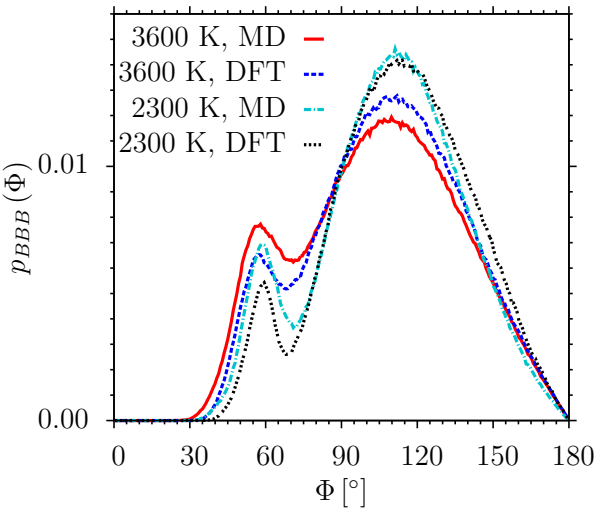

FIGURE 6.28: $p_{BBB}(\Phi)$ at 3600 K and at 2300 K. Comparison of classical potential including 3-body terms with ab initio MD.

at approximately 58° is connected to these small ring sizes with $n \leq 4$. At 3600 K, as well as 2300 K, this additional peak is slightly higher in case of the classical MD simulations. Overall, the agreement between the classical and the ab initio curves is slightly better at the temperature of the parameter fitting of 2300 K, compared to 3600 K.

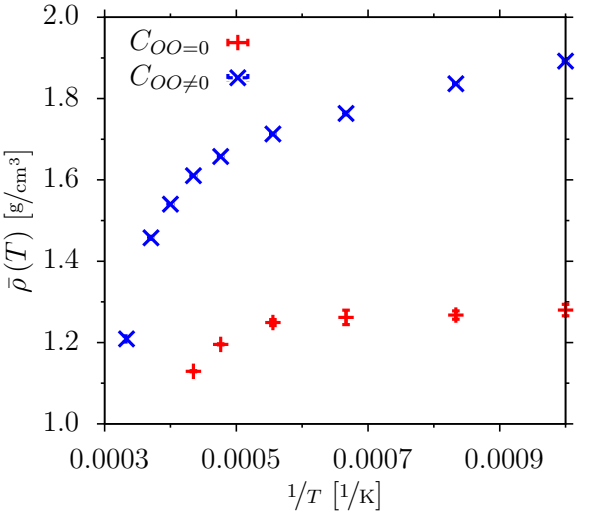

FIGURE 6.29: Mean system density $\bar{\rho}$ with respect to T at constant external pressure $p = 0$ for 1200 atom systems. Classical potentials including 3-body terms.

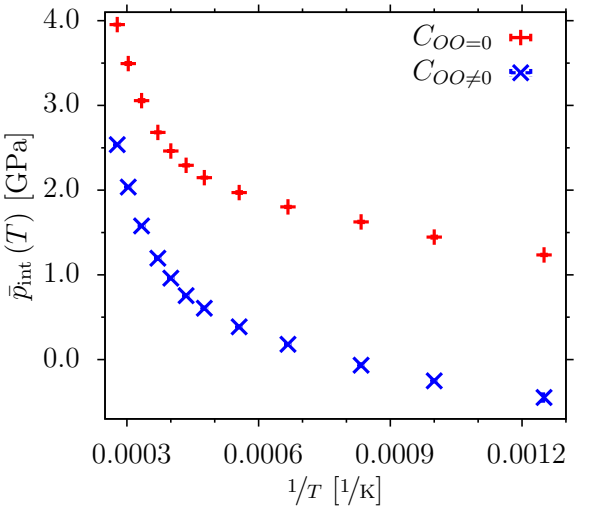

FIGURE 6.30: Mean internal pressure $\bar{p}_{\text{int}}$ with respect to T for 150 atom systems at constant density $\rho = 1.83\,\text{g/cm}^3$. Classical potentials including 3-body terms.

After the comparison with the results from the ab initio simulations, the properties of liquid B_2O_3, according to the 150 atom simulations at constant density of $\rho = 1.83\,\text{g/cm}^3$, are compared to the ones, according to the 1200 atom simulations at constant external pressure of $p = 0$. In Fig. 6.29, the temporal development of the mean system densities is compared for the two different classical potentials $C_{OO} = 0\,\text{eV}\,\text{Å}^6$ and $C_{OO} \neq 0\,\text{eV}\,\text{Å}^6$, according to the 1200

atom simulations. Despite the nearly identical dynamic and structural properties of the 150 atom system in the temperature range between 3600 K and 2300 K, the temporal development of the system densities between 3000 K and 1000 K ($C_{OO} \neq 0\,\text{eV}\,\text{Å}^6$) and 2500 K and 1000 K ($C_{OO} = 0\,\text{eV}\,\text{Å}^6$) shows significant differences. In the case of $C_{OO} = 0\,\text{eV}\,\text{Å}^6$, the mean system density increases from about $\bar{\rho} = 0.97 \pm 0.002\,\text{g/cm}^3$ at 2500 K to about $\bar{\rho} = 1.280 \pm 0.014\,\text{g/cm}^3$ at 1000 K. For $C_{OO} \neq 0\,\text{eV}\,\text{Å}^6$, $\bar{\rho}$ increases from about $\bar{\rho} = 1.209 \pm 0.008\,\text{g/cm}^3$ at 3000 K to about $\bar{\rho} = 1.892 \pm 0.003\,\text{g/cm}^3$ at 1000 K. The latter is pretty close to the experimental glass density of $\rho = 1.83\,\text{g/cm}^3$ [159]. Regarding this behavior, the potential with attractive O-O interactions ($C_{OO} \neq 0\,\text{eV}\,\text{Å}^6$) is preferable to the one with purely repulsive O-O interactions ($C_{OO} = 0\,\text{eV}\,\text{Å}^6$). In Fig. 6.29, the temporal development of the mean internal pressure (see equation (3.33)) is compared, according to simulations of the two different classical potentials for the 150 atom systems in the canonical ensemble. Reflecting the behavior of the system densities, the internal pressure decreases from about $p_{\text{int}} = 3.954 \pm 0.004\,\text{GPa}$ at 3600 K to about $p_{\text{int}} = 1.117 \pm 0.015\,\text{GPa}$ at 800 K ($C_{OO} = 0\,\text{eV}\,\text{Å}^6$) and from about $p_{\text{int}} = 2.537 \pm 0.005\,\text{GPa}$ at 3600 K to about $p_{\text{int}} = -0.447 \pm 0.042\,\text{GPa}$ at 800 K ($C_{OO} \neq 0\,\text{eV}\,\text{Å}^6$). In all cases, the depicted statistical errors are the standard deviations of the mean, with respect to the N independent simulation runs, $\overline{\sigma} = \frac{\sigma}{\sqrt{N}}$. Apparently, the additional attractive force between two neighboring oxygen atoms in the case of $C_{OO} \neq 0\,\text{eV}\,\text{Å}^6$ has a significant effect on the internal pressure of the system.

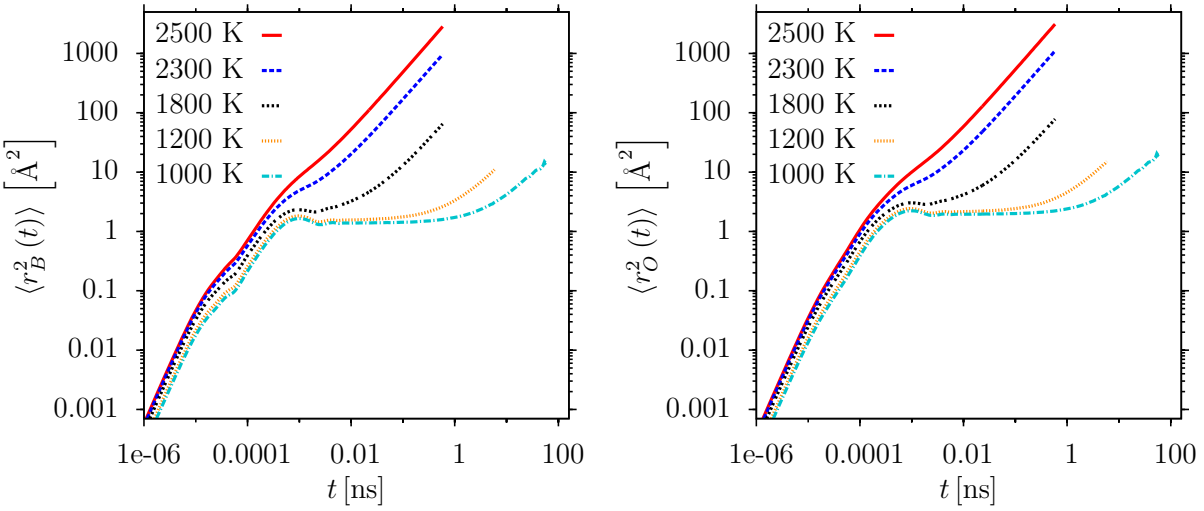

FIGURE 6.31: $\langle r_\alpha^2(t)\rangle$, $\alpha \in \{B, O\}$, at different temperatures for 1200 atom system at constant external pressure $p = 0$. Classical potential with 3-body terms and $C_{OO} = 0\,\text{eV}\,\text{Å}^6$.

Next, the dynamical properties are discussed for all examined cases, namely the two different classical potentials and the two different system sizes. In case of the mean square displacements (see equation (3.98)), the curves of the boron and the oxygen atoms are discussed separately. In case of the incoherent intermediate scattering functions (see equation (3.100)), only selected curves of the boron atoms are displayed.

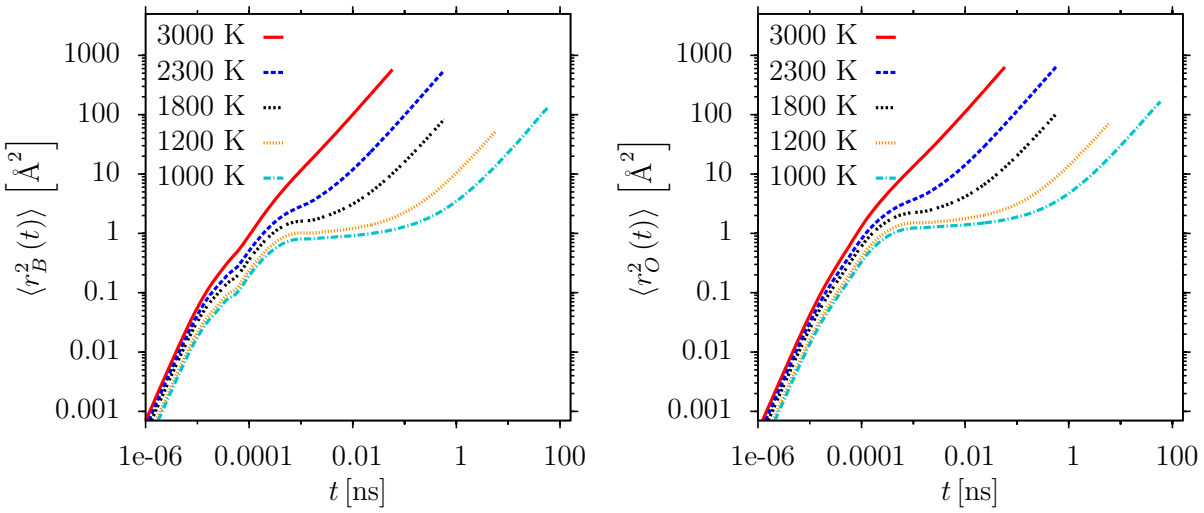

FIGURE 6.32: $\langle r_\alpha^2(t)\rangle$, $\alpha \in \{B, O\}$, at different temperatures for 1200 atom system at constant external pressure $p = 0$. Classical potential with 3-body terms and $C_{OO} \neq 0\,\text{eV}\,\text{Å}^6$.

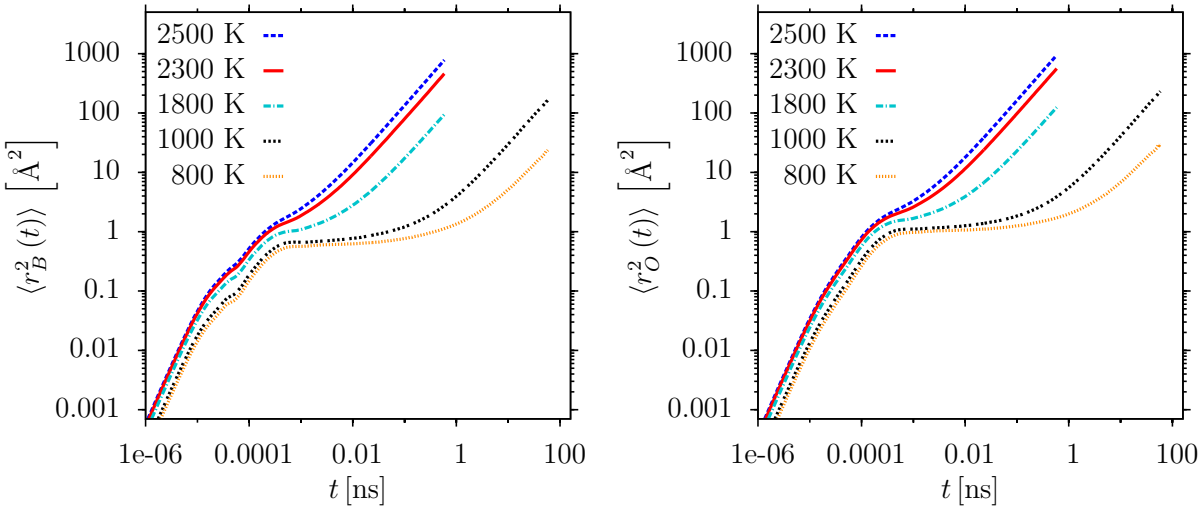

FIGURE 6.33: $\langle r_\alpha^2(t)\rangle$, $\alpha \in \{B, O\}$, at different temperatures for 150 atom system at constant density $\rho = 1.83\,\text{g/cm}^3$. Classical potential with 3-body terms and $C_{OO} = 0\,\text{eV}\,\text{Å}^6$.

In Figs. 6.31 and 6.32, the mean square displacements $\langle r_\alpha^2(t)\rangle$, $\alpha \in \{B, O\}$, are shown for the 1200 atom simulations at constant external pressure of $p = 0$ for temperatures between 2500 K and 1000 K ($C_{OO} = 0\,\text{eV}\,\text{Å}^6$) and 3000 K and 1000 K ($C_{OO} \neq 0\,\text{eV}\,\text{Å}^6$). In both cases, this corresponds to the entire examined temperature range. As expected, the emergence of a 2-step process with an intermediate plateau can be observed with decreasing temperature, coming along with an increase of the α-relaxation times by about 4 to 5 orders of magnitude. The height of the intermediate plateau decreases slightly with decreasing temperature, in all cases. The increase of the α-relaxation times is significantly larger for the classical potential with $C_{OO} = 0\,\text{eV}\,\text{Å}^6$. This slowing down of the dynamics can be explained by the significantly lower system density in the low-temperature range ($\bar{\rho} = 1.280 \pm 0.014\,\text{g/cm}^3$ at 1000 K), compared to $C_{OO} \neq 0\,\text{eV}\,\text{Å}^6$ ($\bar{\rho} = 1.892 \pm 0.003\,\text{g/cm}^3$ at 1000 K). This is the main difference in the dynamics at constant

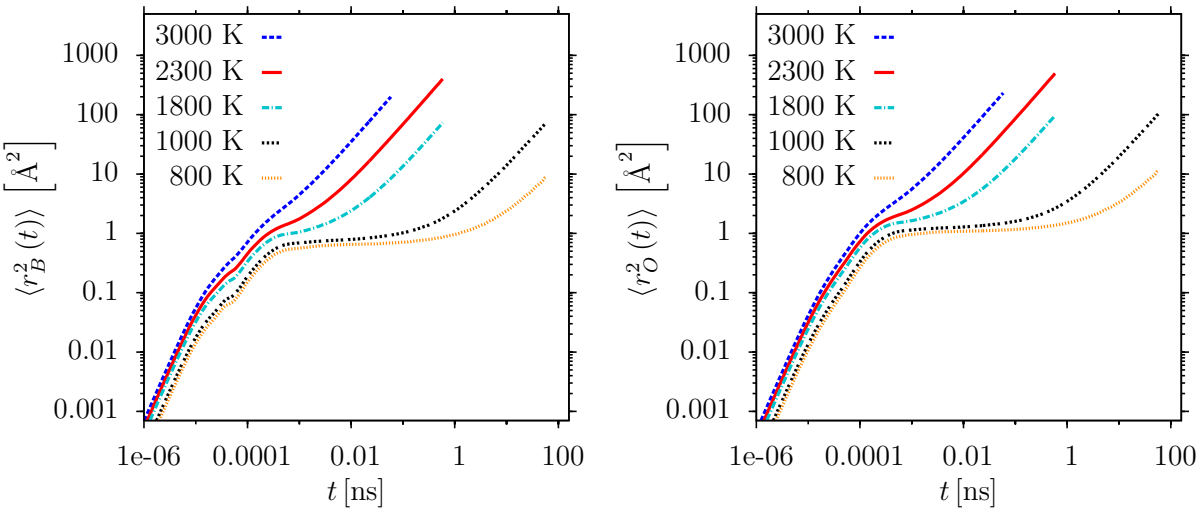

FIGURE 6.34: $\langle r_\alpha^2(t)\rangle$, $\alpha \in \{B, O\}$, at different temperatures for 150 atom system at constant density $\rho = 1.83\,\mathrm{g/cm^3}$. Classical potential with 3-body terms and $C_{OO} \neq 0\,\mathrm{eV\,Å^6}$.

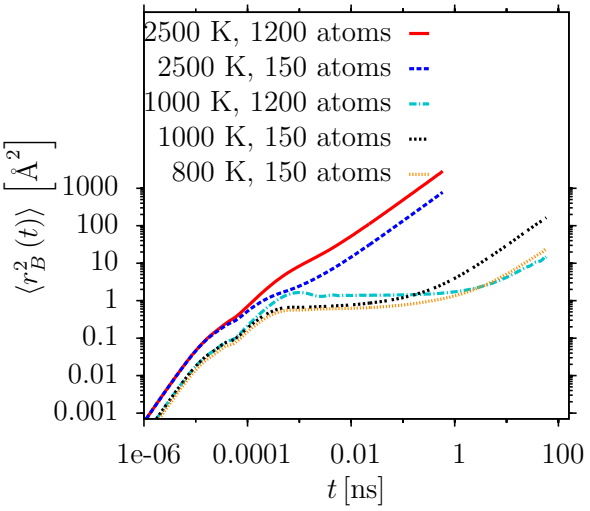

FIGURE 6.35: $\langle r_B^2(t)\rangle$. Comparison of 1200 ($p = 0$) and 150 ($\rho = 1.83\,\mathrm{g/cm^3}$) atom system. Classical potential with 3-body terms and $C_{OO} = 0\,\mathrm{eV\,Å^6}$.

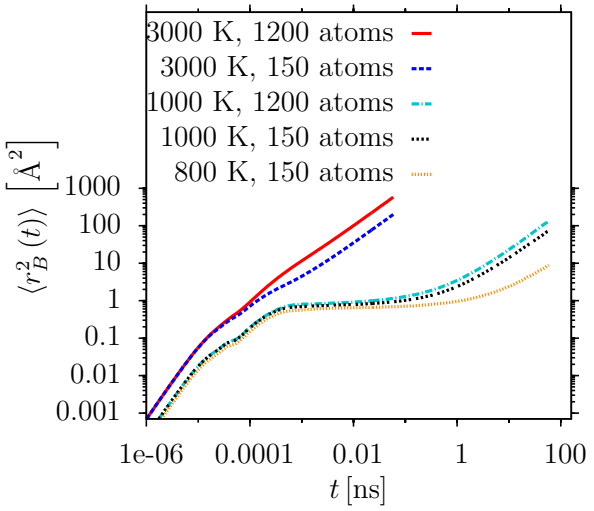

FIGURE 6.36: $\langle r_B^2(t)\rangle$. Comparison of 1200 ($p = 0$) and 150 ($\rho = 1.83\,\mathrm{g/cm^3}$) atom system. Classical potential with 3-body terms and $C_{OO} \neq 0\,\mathrm{eV\,Å^6}$.

external pressure $p = 0$ of the two different classical potentials. Regarding the differences of the oxygen and the boron dynamics, the dynamics of the oxygen atoms is slightly faster. However this difference is much less pronounced as in case of the model glass former SiO_2 (see subsection 4.1.3). The main difference is the emergence of a shoulder of unknown origin at a simulation time of about $50 - 60\,\mathrm{fs}$ in the boron curves, as already discussed in section 6.2.

In Figs. 6.33 and 6.34, the mean square displacements $\langle r_\alpha^2(t)\rangle$, $\alpha \in \{B, O\}$, are shown for the 150 atom simulations at constant density of $\rho = 1.83\,\mathrm{g/cm^3}$. Here, the same temperature range is examined as in case of the 1200 atom simulations at constant external pressure of $p = 0$, extended by the temperature of 800 K. In principle, the curves show show the same

characteristics as in case of the 1200 atom simulations, including the shoulder in $\langle r_B^2(t)\rangle$ at about $50-60\,\mathrm{fs}$. However, the 150 atom simulations show a significantly slower dynamics as the 1200 atom simulations in the high temperature regime for both examined potentials. This can be explained as a finite size effect and corresponds to the behavior observed for the model glass former SiO_2 (see subsection 4.1.2). In contrast to this, the dynamics of the 150 atom system is significantly faster than the one of the 1200 atom system in the low-temperature regime, in case of the classical potential with $C_{OO} = 0\,\mathrm{eV\,\AA^6}$. This effect is not observed, in case of the classical potential with $C_{OO} \neq 0\,\mathrm{eV\,\AA^6}$. Here, the dynamics of the 150 atom system is slower than the one of the 1200 atom system at all examined temperatures. As discussed above, this can be explained by the significantly lower system density in the low-temperature range ($\bar{\rho} = 1.280 \pm 0.014\,\mathrm{g/cm^3}$ at 1000 K), in the case of $C_{OO} = 0\,\mathrm{eV\,\AA^6}$.

In Figs. 6.35 and 6.36, the mean square displacements $\langle r_B^2(t)\rangle$ of the different system sizes (150 atoms at constant $\rho = 1.83\,\mathrm{g/cm^3}$ and 1200 atoms at constant external pressure $p = 0$) are directly compared to each other for the two different classical potentials ($C_{OO} = 0\,\mathrm{eV\,\AA^6}$ and $C_{OO} \neq 0\,\mathrm{eV\,\AA^6}$). Here, the curves of the boron atoms are exemplarily shown at the highest and lowest examined temperatures. The differences in the dynamics of the different system sizes, discussed above, are clearly visible in this direct comparison.

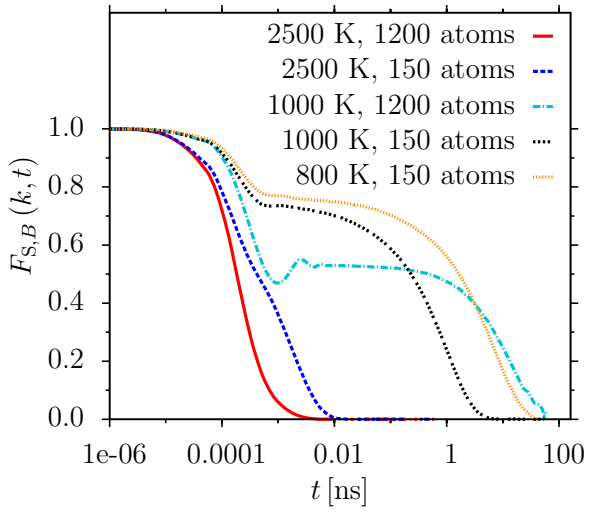

FIGURE 6.37: $F_{S,B}(k,t)$. Comparison of 1200 ($p = 0$) and 150 ($\rho = 1.83\,\mathrm{g/cm^3}$) atom system. Classical potential with 3-body terms and $C_{OO} = 0\,\mathrm{eV\,\AA^6}$.

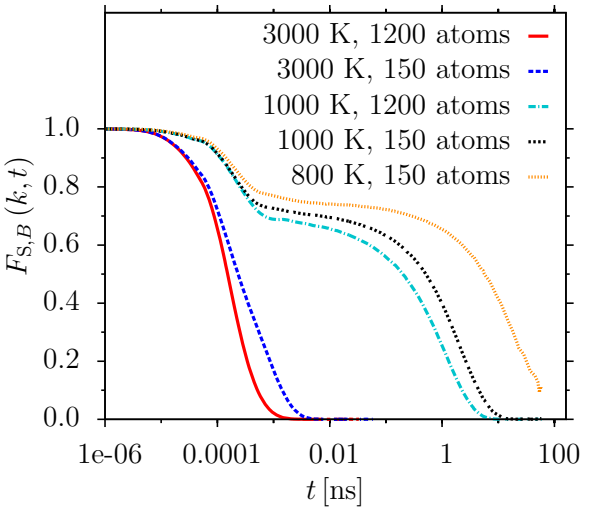

FIGURE 6.38: $F_{S,B}(k,t)$. Comparison of 1200 ($p = 0$) and 150 ($\rho = 1.83\,\mathrm{g/cm^3}$) atom system. Classical potential with 3-body terms and $C_{OO} \neq 0\,\mathrm{eV\,\AA^6}$.

In Figs. 6.37 and 6.38, the incoherent intermediate scattering functions $F_{S,B}(k,t)$ are displayed, comparing exactly the same simulation runs to each other, as in case of the mean square displacements in Figs. 6.35 and 6.36. The curves are evaluated at k-values between $k = 1.68\,\mathrm{\AA^{-1}}$ and $k = 1.68\,\mathrm{\AA^{-1}}$, depending on the system size. As explained above, this is about the k-value of the corresponding first sharp diffraction peak (FSDP). The depicted curves reflects the behavior of the mean square displacements. Regarding the classical potential with $C_{OO} = 0\,\mathrm{eV\,\AA^6}$, at 2500 K, the α-relaxation time is significantly lower, in case of the 1200 atom system compared to

the 150 atom system and no two-step process is visible. At 1000 K, the α-relaxation time of the 1200 atom system is over an order of magnitude larger, which can be explained in terms of the significantly lower system density ($\bar{\rho} = 1.280 \pm 0.014\,\mathrm{g/cm^3}$ at 1000 K), in case of the 1200 atom simulation. Regarding the classical potential with $C_{OO} \neq 0\,\mathrm{eV\,\AA^6}$, the α-relaxation time of the 150 atom system is about 2-3 times longer, as in case of the 1200 atom systems. As mentioned above, this can be explained as a finite size effect. Another interesting aspect is that, in all cases, the height of the intermediate plateau is significantly lower, in case of the 1200 atom systems. Focusing on the 150 atom simulations at constant $\rho = 1.83\,\mathrm{g/cm^3}$, the α-relaxation times are about the same at 2500 K for the two different potentials. However, at the lowest considered temperature of 800 K, the α-relaxation time is about 4-times larger for the potential including O-O attractions ($C_{OO} \neq 0\,\mathrm{eV\,\AA^6}$). This can be explained in terms of the higher internal pressure ($p_{\mathrm{int}} = 1.117 \pm 0.015\,\mathrm{GPa}$ at 800 K) of the system with purely repulsive O-O interactions ($C_{OO} = 0\,\mathrm{eV\,\AA^6}$), compared to the one ($p_{\mathrm{int}} = -0.447 \pm 0.042\,\mathrm{GPa}$ at 800 K) of the system with additional attractive force between two neighboring oxygen atoms ($C_{OO} \neq 0\,\mathrm{eV\,\AA^6}$). The plateau heights of the 150 atom systems are nearly identical for the two different potentials, in all cases.

Next, the structural properties of the different system sizes and potential sets are compared. In Figs. 6.41 and 6.42, the partial pair correlation functions $g_{BB}(r)$ and $g_{OO}(r)$ are displayed for the two different potentials, again comparing the 1200 atom (constant pressure) with the 150 atom (constant volume) simulations at the same temperatures as the dynamical properties. Comparing the curves of the same system size at different temperatures, the peak heights increase with decreasing temperature, as expected. Regarding the potential with $C_{OO} = 0\,\mathrm{eV\,\AA^6}$, the curves of the two different system sizes show significant differences in the whole temperature range. At 2500 K, as well as 1000 K, the peak height of the first neighbor peaks is increased for the 1200 atom system, in both cases. Regarding $g_{BB}(r)$, the first neighbor peaks are also slightly broader in the 1200 atom case and the second-neighbor peaks are shifted to slightly larger distances. This can be attributed to the significantly lower system density in the 1200 atom case. Regarding the potential with $C_{OO} \neq 0\,\mathrm{eV\,\AA^6}$, the increased peak height of the 1200 atom system is only observed at 3000 K. At 1000 K, the curves of the 1200 atom and the 150 atom simulations are nearly identical. This holds for $g_{BB}(r)$, as well as for $g_{OO}(r)$.

In Figs. 6.41 and 6.42, the angular distributions are displayed for the B-B-B, B-O-B and the O-B-O correlation, again comparing the different potentials and system sizes at the same temperatures as above. Regarding the O-B-O correlation, the curves of the different system sizes do not show significant differences in all cases. The peak heights increase with decreasing temperature and the mean O-B-O angles are between 118° and 120° in all cases. Regarding the B-O-B correlation, in case of $C_{OO} = 0\,\mathrm{eV\,\AA^6}$, at 2500 K, as well as 1000 K, the peak positions of main peaks of the 1200 atom curves are shifted to larger angles by about 2°. In case of $C_{OO} \neq 0\,\mathrm{eV\,\AA^6}$, this shift to slightly larger angles for the 1200 atom curve can only be observed at 3000 K. At 1000 K the curves of the 150 atom and the 1200 atom simulations are nearly identical. Regarding the B-B-B correlation, in case of $C_{OO} = 0\,\mathrm{eV\,\AA^6}$, the peak positions of the main peaks of the 1200 atom simulations are shifted to larger angles by about 5° (2500 K) to 4° (1000 K). The peak

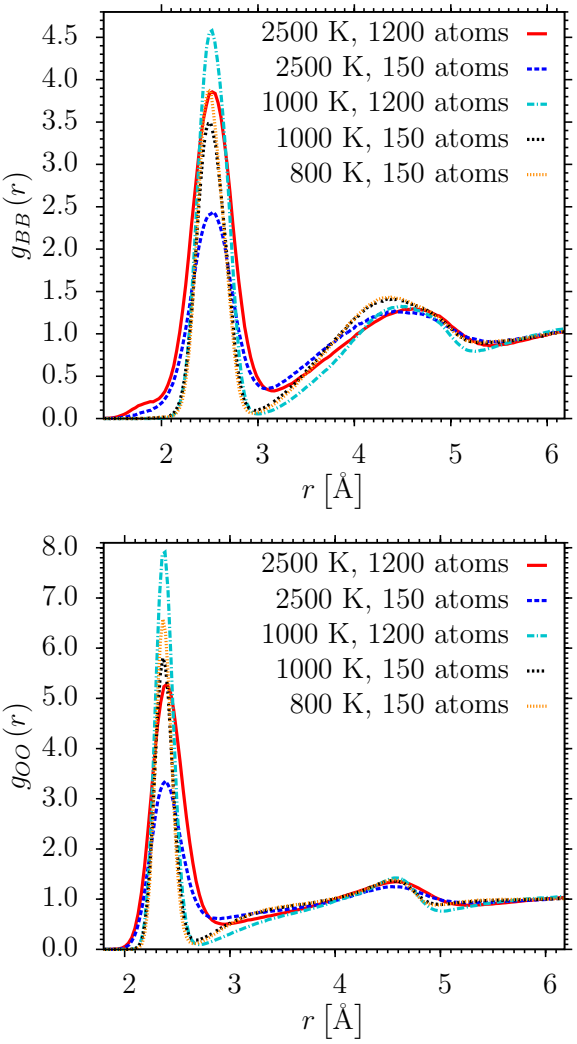

FIGURE 6.39: $g_{BB}(r)$ and $g_{OO}(r)$. Comparison of 1200 ($p = 0$) and 150 ($\rho = 1.83\,\mathrm{g/cm^3}$) atom system. Classical potential with 3-body terms and $C_{OO} = 0\,\mathrm{eV\,Å^6}$.

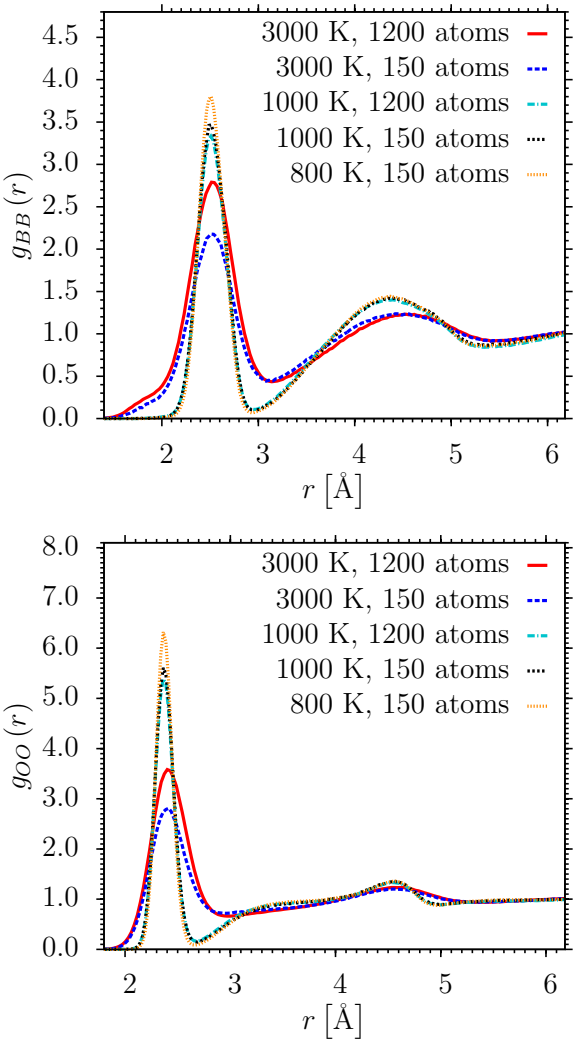

FIGURE 6.40: $g_{BB}(r)$ and $g_{OO}(r)$. Comparison of 1200 ($p = 0$) and 150 ($\rho = 1.83\,\mathrm{g/cm^3}$) atom system. Classical potential with 3-body terms and $C_{OO} \neq 0\,\mathrm{eV\,Å^6}$.

height of the additional peak at about 58° is nearly identical for both system sizes at 2500 K. At 1000 K, the peak height is slightly reduced for the larger system size. As already explained in section 6.2, this peak is mainly connected to smaller ring sizes $n \leq 4$. In case of $C_{OO} \neq 0\,\mathrm{eV\,Å^6}$, the peak position of the main peak of the 1200 atom simulation is shifted to larger angles by about 3° at 3000 K. At 1000 K, the curves of the different system sizes are nearly identical. At both temperatures, the peak heights of the 58°-peak are pretty similar for both system sizes.

To further study the liquid properties of the different system sizes in the examined temperature range, in Figs. 6.43 and 6.44, the probabilities of a B atom to be in a ring of size n, $p_B(n)$, are displayed. Regarding the 150 atom simulations, in all cases the most dominant ring size is $n = 7$, as already explained above. The probability $p_B(n = 7)$ increases with decreasing temperature for both potentials and the probabilities $p_B(n \leq 4)$ decrease with decreasing temperature. A slight difference between the two potentials is that the probabilities $p_B(n = 7)$ and $p_B(n = 3)$

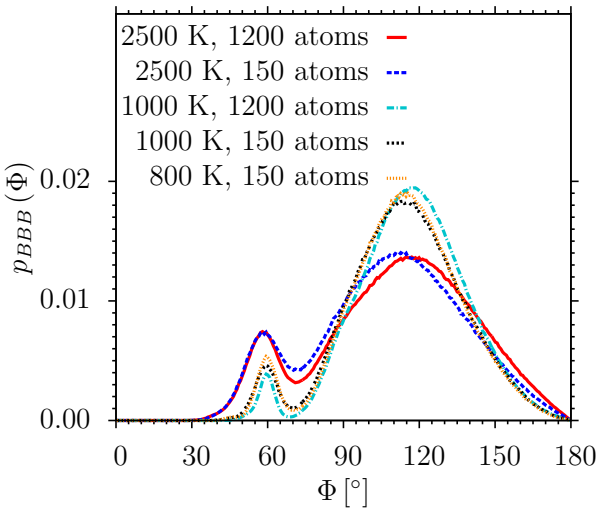

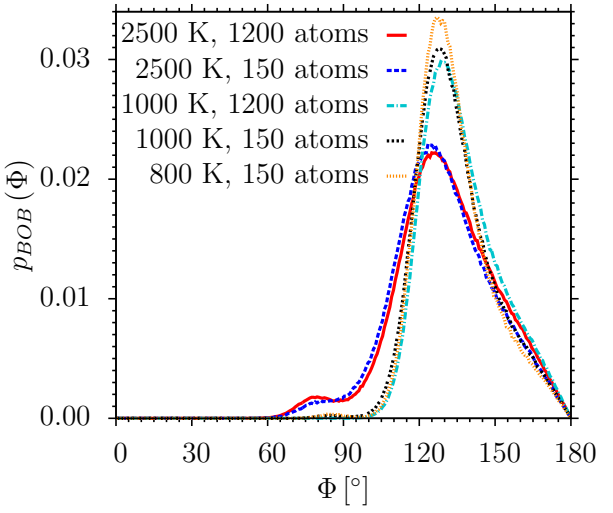

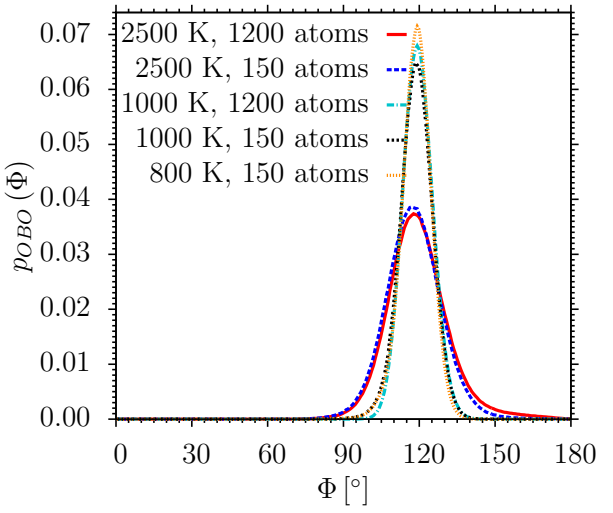

FIGURE 6.41: $p_{\alpha\beta\gamma}(\Phi), \alpha, \beta, \gamma \in \{B, O\}$. Comparison of 1200 ($p = 0$) and 150 ($\rho = 1.83\,\mathrm{g/cm^3}$) atom system. Classical potential with 3-body terms and $C_{OO} = 0\,\mathrm{eV\,\AA^6}$.

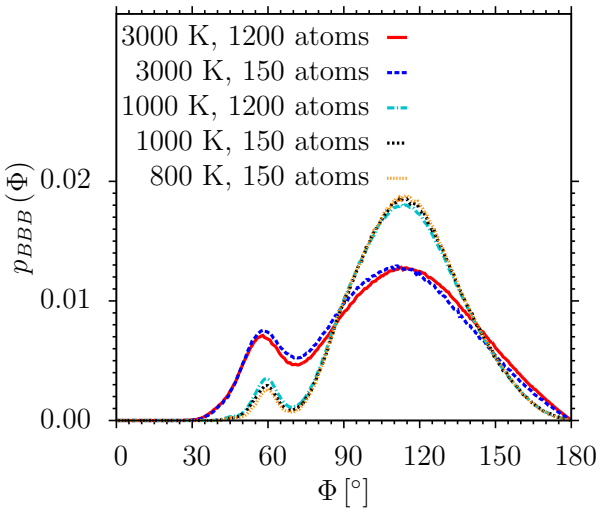

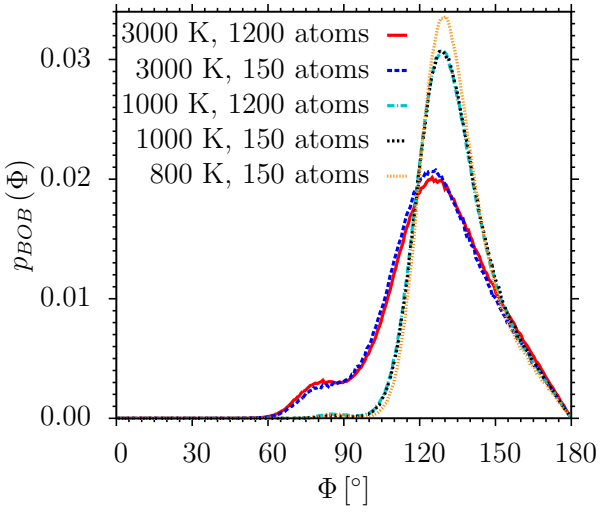

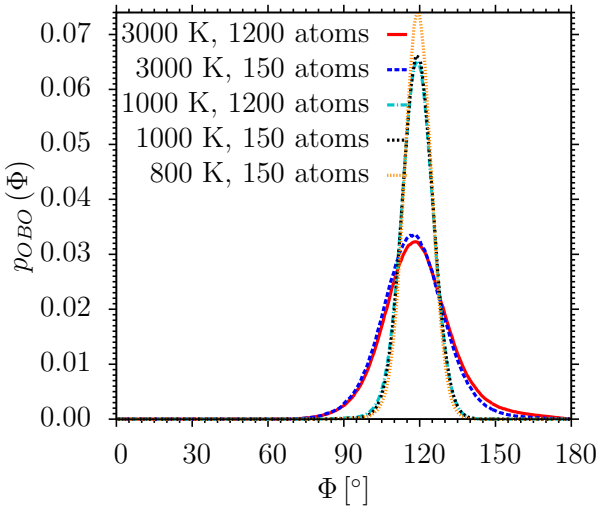

FIGURE 6.42: $p_{\alpha\beta\gamma}(\Phi), \alpha, \beta, \gamma \in \{B, O\}$. Comparison of 1200 ($p = 0$) and 150 ($\rho = 1.83\,\mathrm{g/cm^3}$) atom system. Classical potential with 3-body terms and $C_{OO} \neq 0\,\mathrm{eV\,\AA^6}$.

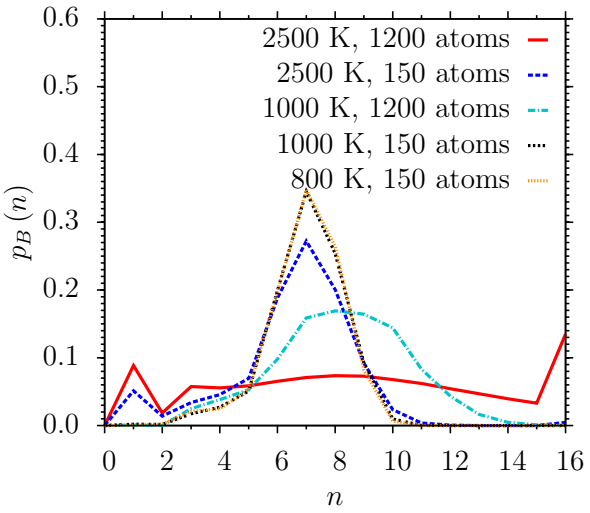

FIGURE 6.43: $p_B(n)$. Comparison of 1200 ($p = 0$) and 150 ($\rho = 1.83\,\mathrm{g/cm^3}$) atom system. Classical potential with 3-body terms and $C_{OO} = 0\,\mathrm{eV\,\AA^6}$.

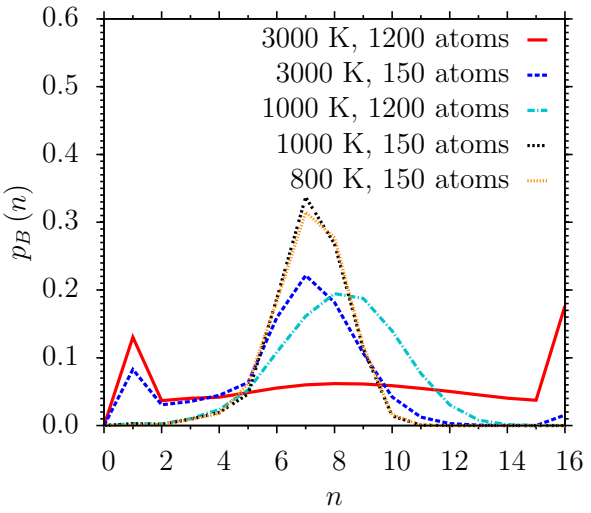

FIGURE 6.44: $p_B(n)$. Comparison of 1200 ($p = 0$) and 150 ($\rho = 1.83\,\mathrm{g/cm^3}$) atom system. Classical potential with 3-body terms and $C_{OO} \neq 0\,\mathrm{eV\,\AA^6}$.

are slightly higher at 800 K than at 1000 K in the case of $C_{OO} = 0\,\mathrm{eV\,\AA^6}$ and slightly lower in the case of $C_{OO} \neq 0\,\mathrm{eV\,\AA^6}$. Regarding the simulations of the 1200 atom systems, in all cases, the most dominant ring size is $n = 8$. In the case of $C_{OO} = 0\,\mathrm{eV\,\AA^6}$, the probabilities $p_B(n \leq 4)$ are increased for the 1200 atom system at the highest examined temperature of 2500 K. Also the distribution $p_B(n)$ is rather flat in the latter case with only a small maximum at $n = 8$ and a rather high probability of $p_B(n = 16)$. This stands for the probability of a B atom to be in a ring of size $n \geq 16$. At 1000 K, the agreement between the 150 and the 1200 atom distributions is better for lower ring sizes n. Overall, the distribution in the 1200 atom case is broader with a significant amount of rings with size $n \geq 10$, not apparent in the 150 atom case. Regarding the case of $C_{OO} \neq 0\,\mathrm{eV\,\AA^6}$, the behavior at the highest examined temperature of 3000 K is comparable to the behavior in the case of $C_{OO} = 0\,\mathrm{eV\,\AA^6}$ at 2500 K and the behavior at 1000 K is also quite similar. Here, the 150 and the 1200 atom distributions are nearly identical for $n \leq 4$. The lack of rings with $n \geq 10$ in the 150 atom simulations clearly is a finite size effect, due to the rather small simulation box with $L_{\mathrm{Box}} = 12.375\,\mathrm{\AA}$ in the 150 atom case. The broad distribution at high temperatures in the 1200 atom case can be explained by the rather low system densities of $\bar{\rho} = 0.97 \pm 0.002\,\mathrm{g/cm^3}$ ($C_{OO} = 0\,\mathrm{eV\,\AA^6}$, 2500 K) and ($\bar{\rho} = 1.209 \pm 0.008\,\mathrm{g/cm^3}$ ($C_{OO} \neq 0\,\mathrm{eV\,\AA^6}$, 3000 K).

In the following, the dependence of several quantities on the temperature is compared for all different cases, namely ab initio MD simulations of the 150 atom system and classical MD simulations of the 150 atom systems at constant density $\rho = 1.83\,\mathrm{g/cm^3}$ and the 1200 atom systems at constant external pressure $p = 0$.

First, the dependence of the self-diffusion constants D_α, $\alpha \in \{B, O\}$, on the temperature is examined. As explained in subsection 4.1.3, they are determined by means of the slope of a linear fit to the corresponding mean square displacements at large simulation times, where the Einstein

relation $D_\alpha = \lim_{t\to\infty} \frac{\langle r_\alpha^2(t)\rangle}{6t}$ [15] holds (see equation (3.99)). In all cases, $D_\alpha(T)$, $\alpha \in \{B, O\}$, are plotted on a logarithmic scale with respect to the inverse temperatures $1/T$. In case of the classical MD simulations, the displayed statistical errors are the standard deviations of the mean, with respect to the N independent simulation runs, $\overline{\sigma} = \frac{\sigma}{\sqrt{N}}$. In case of the ab initio MD simulations, no statistical errors are shown, as only one simulation run is carried out at each examined temperature.

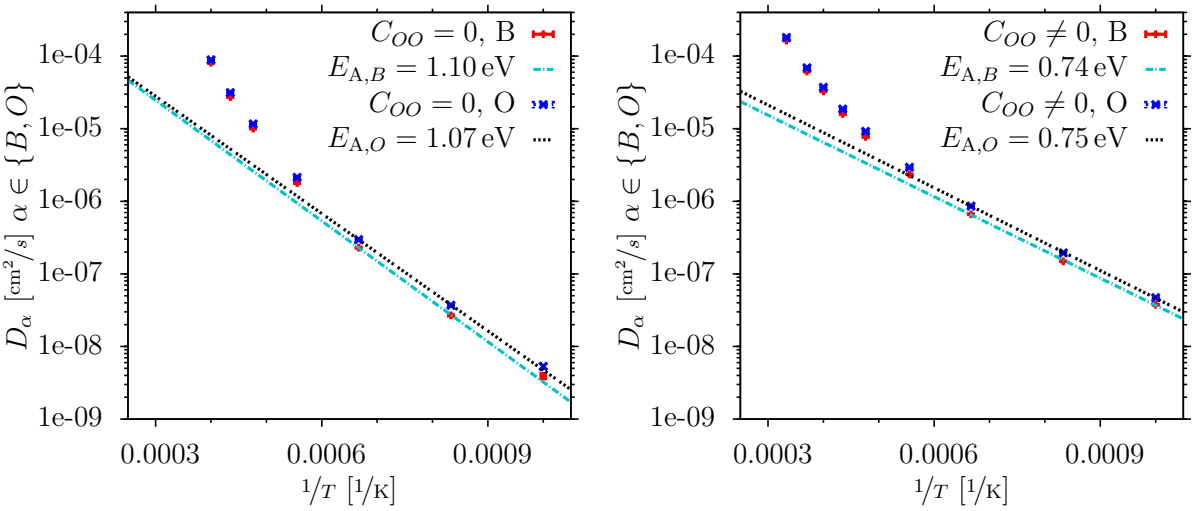

FIGURE 6.45: Arrhenius plot of self diffusion constants for B and O at different temperatures for 1200 atom systems at constant external pressure $p = 0$. Different classical potentials with 3-body terms.

In Fig. 6.45, $D_\alpha(T)$, $\alpha \in \{B, O\}$, of the 1200 atom simulations at constant external pressure $p = 0$ are analyzed for both classical potentials ($C_{OO} = 0\,\text{eV}\,\text{Å}^6$ and $C_{OO} \neq 0\,\text{eV}\,\text{Å}^6$). As expected, in both cases, the diffusion constants decrease by orders of magnitude with decreasing temperature. Regarding the differences of the oxygen and the boron dynamics, at each temperature, the self-diffusion constants of the oxygen atoms are slightly larger than the ones of the boron atoms in agreement with the behavior of the mean square displacements. However, this difference is much less pronounced as in case of the model glass former SiO_2 (see subsection 4.1.3). In principle, the temperature dependence of $D_\alpha(T)$, $\alpha \in \{B, O\}$, follows an Arrhenius behavior (see equation (4.4)). However, in all cases the slope of the exponential decrease of $D_\alpha(T)$ with respect to $1/T$ is significantly lower at temperatures below about 1800 K, leading to a different activation energy $E_{A,\alpha}$ at low than at high temperatures. This difference in activation energies at low and high temperatures has not been observed in case of the model glass former SiO_2 (see subsection 4.1.3) and so far is not clearly understood. It could be connected to a different diffusion mechanism at low temperatures. The decrease of the slope at low temperatures is less pronounced in case of the classical potential with $C_{OO} = 0\,\text{eV}\,\text{Å}^6$, leading to lower self-diffusion constants at low temperatures. As in case of the longer α-relaxation times, this can be explained in terms of the significantly lower system density ($\bar{\rho} = 1.280 \pm 0.014\,\text{g/cm}^3$ at 1000 K) for $C_{OO} = 0\,\text{eV}\,\text{Å}^6$, compared to $\bar{\rho} = 1.892 \pm 0.003\,\text{g/cm}^3$ at 1000 K for $C_{OO} \neq 0\,\text{eV}\,\text{Å}^6$. As in case of the model glass former SiO_2 (see subsection 4.1.3), the activation energies $E_{A,\alpha}$, $\alpha \in \{B, O\}$, are extracted by

means of an Arrhenius fit (see equation (4.4)). Here, the temperature range of $T \leq 1500\,\mathrm{K}$ is taken into account and the given errors are the asymptotic standard errors of the least-squares fit with gnuplot [101, 106]. The values are: $E_{\mathrm{A},B} \simeq 1.10 \pm 0.03\mathrm{eV}$, $E_{\mathrm{A},O} \simeq 1.07 \pm 0.02\mathrm{eV}$ ($C_{OO} = 0\,\mathrm{eV\,\AA^6}$) and $E_{\mathrm{A},B} \simeq 0.74 \pm 0.02\mathrm{eV}$, $E_{\mathrm{A},O} \simeq 0.75 \pm 0.01\mathrm{eV}$ ($C_{OO} \neq 0\,\mathrm{eV\,\AA^6}$).

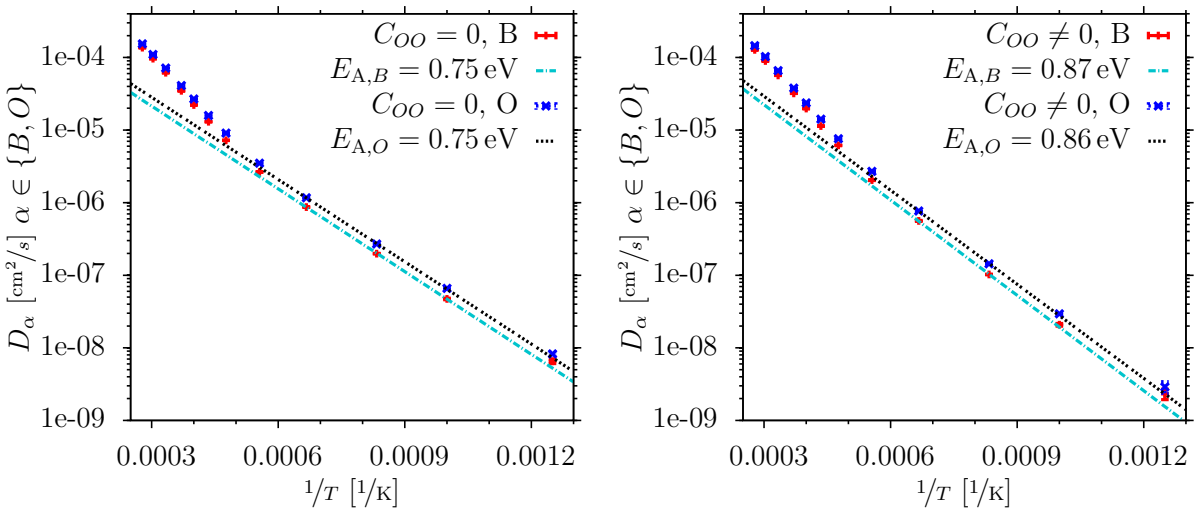

FIGURE 6.46: Arrhenius plot of self diffusion constants for B and O at different temperatures for 150 atom systems at constant density $\rho = 1.83\,\mathrm{g/cm^3}$. Different classical potentials with 3-body terms.

In Fig. 6.46, $D_\alpha(T)$, $\alpha \in \{B, O\}$, of the 150 atom simulations at constant density of $\rho = 1.83\,\mathrm{g/cm^3}$ are displayed for both classical potentials ($C_{OO} = 0\,\mathrm{eV\,\AA^6}$ and $C_{OO} \neq 0\,\mathrm{eV\,\AA^6}$). The overall temporal behavior of the self-diffusion constants is the same as in case of the 1200 atom simulations at constant external pressure of $p = 0$. Again, at each temperature, the values of D_O are slightly larger than the values of D_B, in agreement with the behavior of the mean square displacements. Also, the temperature dependence of $D_\alpha(T)$, $\alpha \in \{B, O\}$, follows an Arrhenius behavior (see equation (4.4)) with a significantly lower slope of the exponential decrease of $D_\alpha(T)$ with respect to $1/T$ at temperatures below about 1800 K. As explained above, this behavior is not clearly understood. In this case, additional equilibration runs have been carried out at 1200 K and 1000 K with significant longer equilibration times as the ones displayed in Table 6.9, to check the influence of the equilibration time on the diffusive behavior. The corresponding equilibration times are 42 ns at 1200 K and 600 ns at 100 K ($C_{OO} = 0\,\mathrm{eV\,\AA^6}$) and 54 ns at 1200 K and 600 ns at 100 K ($C_{OO} \neq 0\,\mathrm{eV\,\AA^6}$). However, the mean square displacements and self-diffusion constants of the subsequent microcanonical measure runs are nearly identical to the runs with the shorter equilibration times displayed in Table 6.9. This indicates that the change of the diffusive behavior at low temperatures is no artifact of a too short equilibration time. Here, the decrease of the slope at low temperatures is less pronounced in case of the classical potential with $C_{OO} \neq 0\,\mathrm{eV\,\AA^6}$, leading to lower self-diffusion constants at low temperatures. As in case of the longer α-relaxation times, this can be explained in terms of the significantly higher internal pressure ($p_{\mathrm{int}} = 1.117 \pm 0.015\,\mathrm{GPa}$ at 800 K) of the system with purely repulsive O-O interactions ($C_{OO} = 0\,\mathrm{eV\,\AA^6}$), compared to the one ($p_{\mathrm{int}} = -0.447 \pm 0.042\,\mathrm{GPa}$ at 800 K) of the system with additional attractive force between two neighboring oxygen atoms ($C_{OO} \neq 0\,\mathrm{eV\,\AA^6}$).

Again, the activation energies $E_{\mathrm{A},\alpha}$, $\alpha \in \{B, O\}$ are extracted by means of an Arrhenius fit (see equation (4.4)) for temperatures $T \leq 1500\,\mathrm{K}$, leading to the values of $E_{\mathrm{A},B} \simeq 0.75 \pm 0.01\mathrm{eV}$, $E_{\mathrm{A},O} \simeq 0.75 \pm 0.01\mathrm{eV}$ ($C_{OO} = 0\,\mathrm{eV\,\AA^6}$) and $E_{\mathrm{A},B} \simeq 0.87 \pm 0.02\mathrm{eV}$, $E_{\mathrm{A},O} \simeq 0.86 \pm 0.01\mathrm{eV}$ ($C_{OO} \neq 0\,\mathrm{eV\,\AA^6}$).

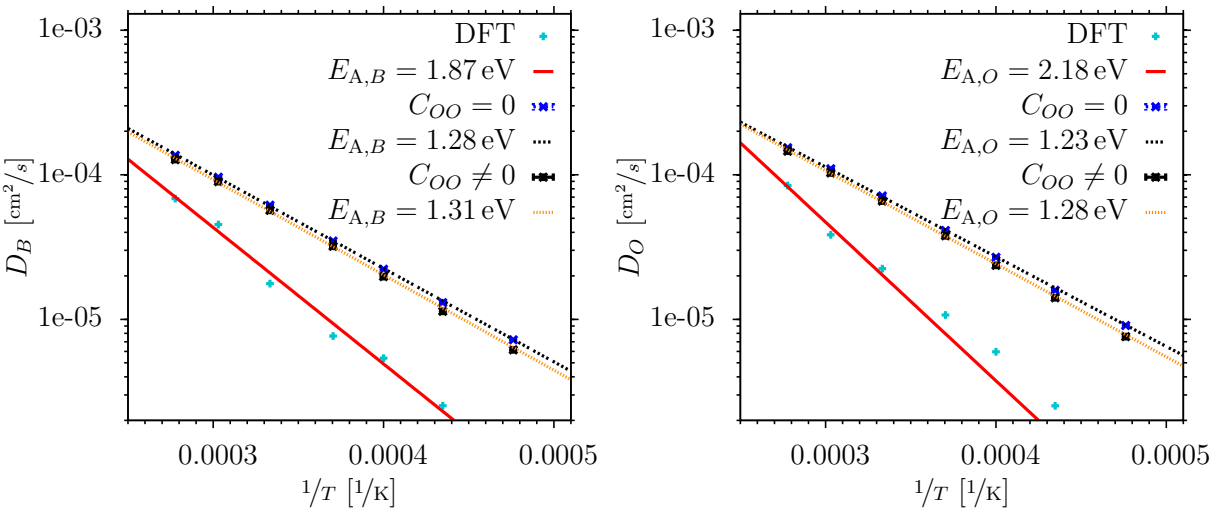

FIGURE 6.47: Arrhenius plot of self diffusion constants for B and O at different temperatures for 150 atom systems at constant density $\rho = 1.83\,\mathrm{g/cm^3}$. Comparison of different classical potentials with 3-body terms with ab initio MD simulations.

In Fig. 6.47, $D_\alpha(T)$, $\alpha \in \{B, O\}$, of the 150 atom simulations with both parameter sets ($C_{OO} = 0\,\mathrm{eV\,\AA^6}$ and $C_{OO} \neq 0\,\mathrm{eV\,\AA^6}$) at constant density of $\rho = 1.83\,\mathrm{g/cm^3}$ are compared to the ones of the ab initio MD simulations. Here, the temperature range is shown, in which the ab initio runs could still be equilibrated (see section 6.2). In contrast to the classical MD simulations, no change of the slope of the exponential decrease of $D_\alpha(T)$, $\alpha \in \{B, O\}$, with respect to $1/T$ is visible in case of the ab initio MD simulations. However, in the temperature range, the ab initio MD simulations can be equilibrated, this change of slope is not observed in the classical MD simulations, as well. In all cases, the diffusion constants of the ab initio MD simulations are significantly smaller than the ones of the classical MD simulations, in agreement with the significantly slower dynamics observed in the curves of $F_{\mathrm{S},B}(k,t)$ and $\langle r_B^2(t)\rangle$ (see Figs. 6.23 and 6.24). Also, the slope of the exponential decrease of $D_\alpha(T)$, $\alpha \in \{B, O\}$, is significantly steeper in case of the ab initio MD simulations, compared to the classical MD simulations with both parameter sets ($C_{OO} = 0\,\mathrm{eV\,\AA^6}$ and $C_{OO} \neq 0\,\mathrm{eV\,\AA^6}$). Again, the activation energies $E_{\mathrm{A},\alpha}$, $\alpha \in \{B, O\}$, are extracted by means of an Arrhenius fit (see equation (4.4)). Here, the temperature range of $T \geq 2300\,\mathrm{K}$ is taken into account, leading to different values of the activation energies of the classical MD simulations as in the low temperature range of $T \leq 1500\,\mathrm{K}$. The corresponding values are: $E_{\mathrm{A},B} \simeq 1.87 \pm 0.16\mathrm{eV}$, $E_{\mathrm{A},O} \simeq 2.18 \pm 0.19\mathrm{eV}$ (ab initio MD), $E_{\mathrm{A},B} \simeq 1.28 \pm 0.01\mathrm{eV}$, $E_{\mathrm{A},O} \simeq 1.23 \pm 0.01\mathrm{eV}$ ($C_{OO} = 0\,\mathrm{eV\,\AA^6}$) and $E_{\mathrm{A},B} \simeq 1.31 \pm 0.02\mathrm{eV}$, $E_{\mathrm{A},O} \simeq 1.28 \pm 0.02\mathrm{eV}$ ($C_{OO} \neq 0\,\mathrm{eV\,\AA^6}$). As explained above, it should be taken into account that the analysis of the ab initio MD runs is carried out with respect to NVT runs in contrast to the microcanonical runs of the classical MD simulations. Also, the underlying data is from a single simulation run only due to the huge computational effort. As a consequence, one

has to be careful when interpreting the displayed curves. However, the temporal development of $D_\alpha(T)$, $\alpha \in \{B, O\}$, give an indication about dynamics of the system at the examined temperatures.

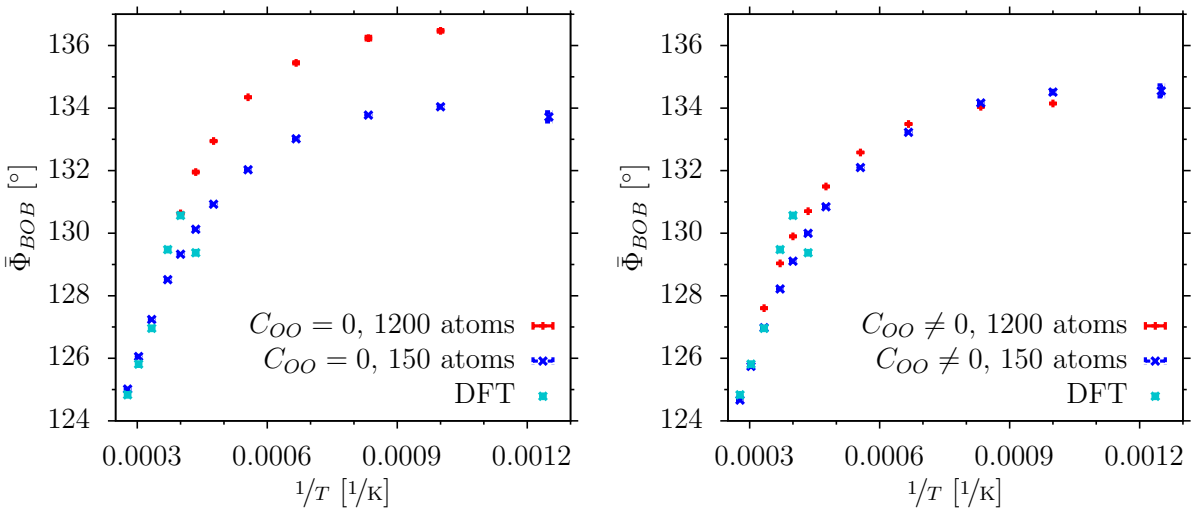

FIGURE 6.48: Temporal development of mean B-O-B angle. Comparison of different classical potentials with 3-body terms with ab initio MD simulations.

Next, the temporal development of the mean B-O-B angle is displayed for all studied cases (see Fig. 6.48). Again, the statistical errors are calculated in terms of the standard deviation of the mean, $\overline{\sigma} = \frac{\sigma}{\sqrt{N}}$, with respect to the independent simulation runs. In general, the agreement of the classical MD simulations of the 150 atom systems and the ab initio MD simulations is quite good in the temperature range, the latter still can be equilibrated. In all cases, the mean B-O-B angle increases initially with decreasing temperature. Regarding the classical MD simulations, the initial increase with decreaseing temperature is followed by a plateau at about $\bar{\Phi}_{BOB} \simeq 134°$ ($C_{OO} = 0\,\mathrm{eV\,\AA^6}$, 150 atoms and $C_{OO} \neq 0\,\mathrm{eV\,\AA^6}$, 150 atoms and 1200 atoms) and about $\bar{\Phi}_{BOB} \simeq 136°$ ($C_{OO} = 0\,\mathrm{eV\,\AA^6}$, 1200 atoms) in the temperature range between aprroximately 1200 K to 800 K. In the case of $C_{OO} = 0\,\mathrm{eV\,\AA^6}$, 150 atoms, a slight decrease of $\bar{\Phi}_{BOB}$ is visible at $T = 800\,\mathrm{K}$, compared to $T = 1000\,\mathrm{K}$. Regarding the ab initio MD simulations, the initial increase of $\bar{\Phi}_{BOB}$ with decreasing temperature is followed by a slight decrease at $T = 2300\,\mathrm{K}$.

Other interesting quantities to study, are the mean coordination numbers of the B-B and the B-O correlation (see Fig. 6.49). Regarding the B-B correlation, $\bar{n}_{BB}$ shows a decrease from $\bar{n}_{BB} \simeq 3.5$ at $T = 3600\,\mathrm{K}$ (classical MD simulations, 150 atoms) to $\bar{n}_{BB} \simeq 3.2$ ($C_{OO} = 0\,\mathrm{eV\,\AA^6}$, 150 atoms) and $\bar{n}_{BB} \simeq 3.1$ ($C_{OO} \neq 0\,\mathrm{eV\,\AA^6}$, 150 atoms) at $T = 800\,\mathrm{K}$. Here, the agreement to the ab initio MD simulations is less pronounced. The latter show a decrease from about $\bar{n}_{BB} \simeq 3.4$ ($T = 3600\,\mathrm{K}$) to $\bar{n}_{BB} \simeq 3.15$ ($T = 2300\,\mathrm{K}$). In contrast to the 150 simulations, the classical MD simulations of the 1200 atom systems show an initial increase of $\bar{n}_{BB}$, followed by a subsequent decrease. This is connected to the significantly lower system density at high temperatures (see Fig. 6.29). The value of $\bar{n}_{BB}$ is significantly lower in the case of $C_{OO} = 0\,\mathrm{eV\,\AA^6}$. Again, this can be explained by the significantly lower system density. Regarding the B-O correlation,

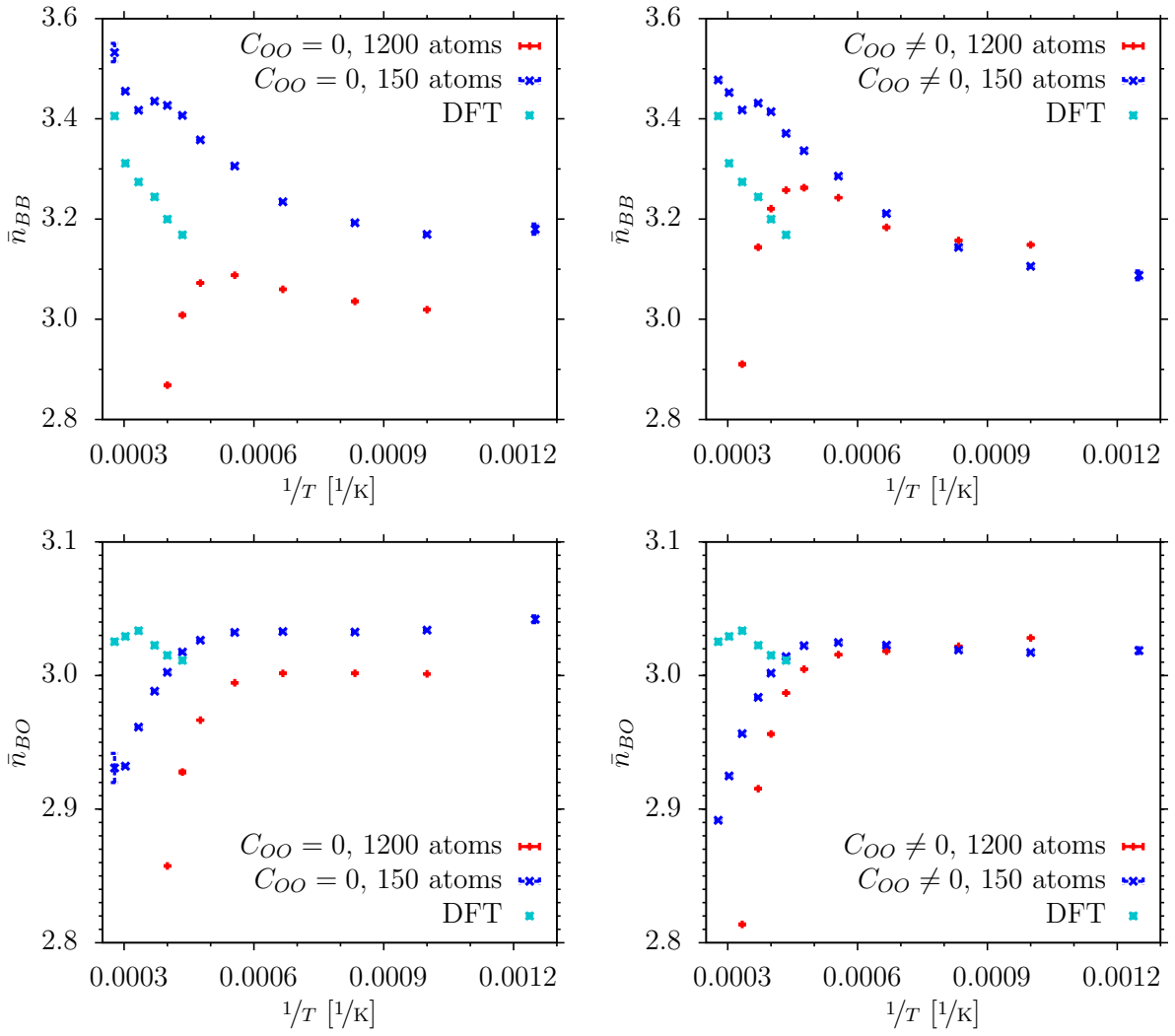

FIGURE 6.49: Temporal development of mean B-B and B-O coordination. Comparison of different classical potentials with 3-body terms with ab initio MD simulations.

all classical MD simulations show an initial increase with decreasing temperature, followed by a transition to a plateau at about $T = 1800\,\mathrm{K}$. The plateau values are about $\bar{n}_{BO} \simeq 3.03$ ($C_{OO} = 0\,\mathrm{eV\,\AA^6}$, 150 atoms), $\bar{n}_{BO} \simeq 3.00$ ($C_{OO} = 0\,\mathrm{eV\,\AA^6}$, 1200 atoms) and $\bar{n}_{BO} \simeq 3.02$ ($C_{OO} \neq 0\,\mathrm{eV\,\AA^6}$, 150 and 1200 atoms). Again, the ab initio MD simulations show a slightly different behavior with a slight initial increase to $\bar{n}_{BO} \simeq 3.03$ at $T = 3000\,\mathrm{K}$, followed by a decrease to $\bar{n}_{BO} \simeq 3.01$ at $T = 2300\,\mathrm{K}$.

Last, the temporal development of the probability of a B atom to be in a ring of size $p_B\,(n = 3)$, $p_B\,(n = 4)$, $p_B\,(n = 7)$ and $p_B\,(n = 8)$ is studied (see Fig. 6.50). In case of the classical MD simulations, a ring size of $p_B\,(n = 7)$ corresponds to the maximum value of $p_B\,(n)$ of the 150 atom simulations and a and ring size of $p_B\,(n = 8)$ corresponds to the maximum value of $p_B\,(n)$ of the 1200 atom simulations (see Figs. 6.43 and 6.44). In case of the ab initio MD simulations, a ring size of $p_B\,(n = 7)$ corresponds to the maximum value of $p_B\,(n)$, as well. Only at $T = 2700\,\mathrm{K}$ and $T = 2300\,\mathrm{K}$, the probability of $p_B\,(n = 8)$ is higher than $p_B\,(n = 7)$ (see Fig. 6.7). Regarding $n = 3$, $p_B\,(n = 3)$, in all cases, shows an initial decrease with decreasing temperature and the

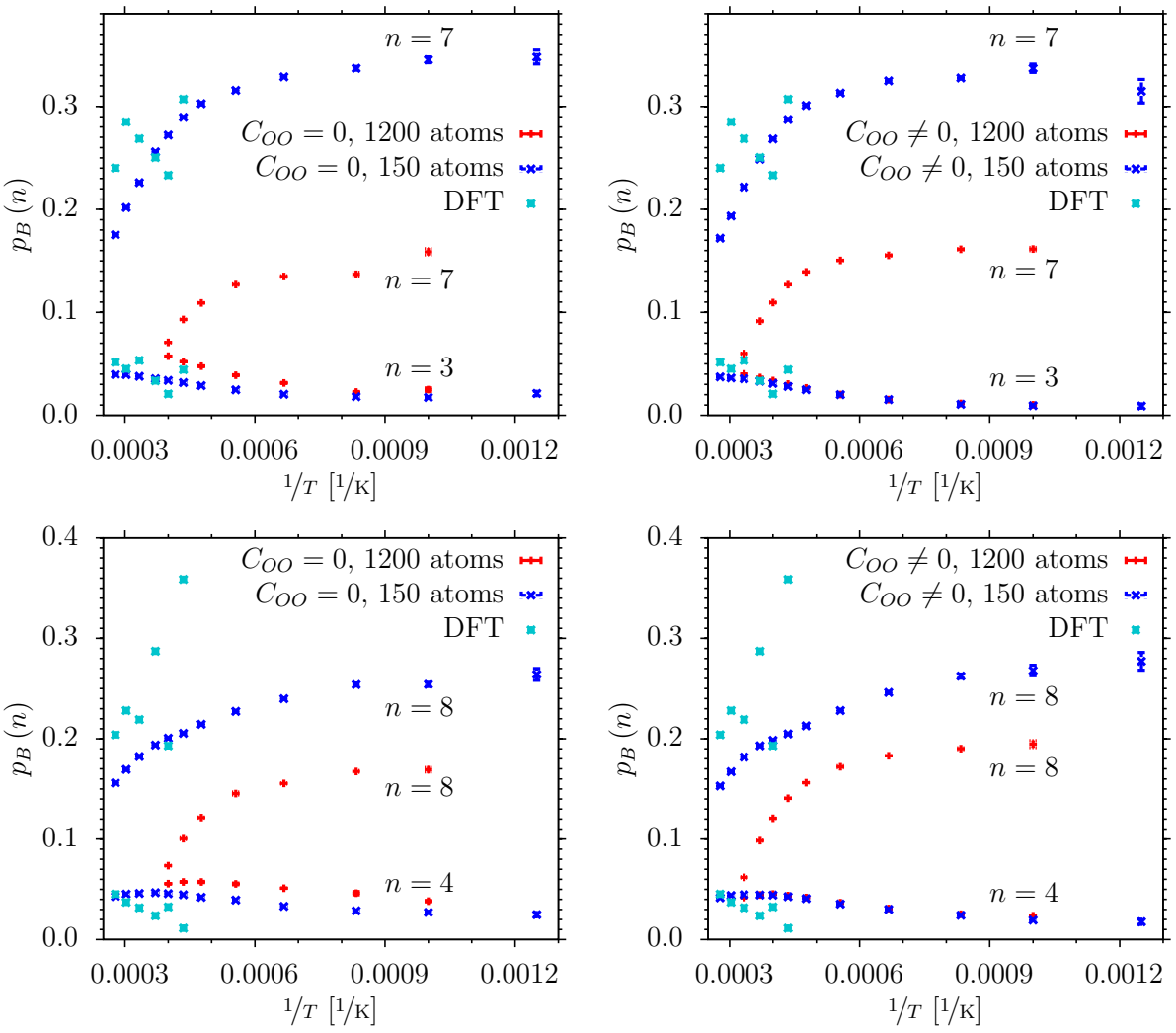

FIGURE 6.50: Temporal development of probability of B atom to be in a ring of size n, $p_B(n)$, for $n = 3$, $n = 4$, $n = 7$ and $n = 8$. Comparison of different classical potentials with 3-body terms with ab initio MD simulations.

agreement of the 150 atom and the 1200 atom simulations is quite good. In case of the ab initio MD simulations, a significant increase of $p_B(n = 3)$ is visible from $T = 2500\,\mathrm{K}$ to $T = 2300\,\mathrm{K}$ (compare Fig. 6.7). In case of the classical MD simulations, a slight increase of $p_B(n = 3)$ can be observed from $T = 1000\,\mathrm{K}$ to $T = 800\,\mathrm{K}$ in the 150 atom simulation with $C_{OO} = 0\,\mathrm{eV\,\AA^6}$. In all other cases, $p_B(n = 3)$ shows a steady decrease with decreasing temperature in the whole examined temperature range. Looking at $n = 4$, the classical MD simulations show a slight initial increase of $p_B(n = 4)$ with decreasing temperature, followed by a steady decrease with decreasing temperature. In contrast to this, the ab initio MD simulations show an initial decrease of $p_B(n = 4)$ with decreasing temperature, followed by an increase of $p_B(n = 4)$ from $T = 2700\,\mathrm{K}$ to $T = 2500\,\mathrm{K}$ and a subsequent decrease from $T = 2500\,\mathrm{K}$ to $T = 2300\,\mathrm{K}$. Regarding $n = 7$, the classical MD simulations show an initial increase of $p_B(n = 7)$ with decreasing temperature that gets less pronounced at lower temperatures. Only in case of the 150 atom simulation with $C_{OO} \neq 0\,\mathrm{eV\,\AA^6}$, the value of $p_B(n = 7)$ starts to decreases again at $T \leq 1000\,\mathrm{K}$. Here, the ab

initio MD simulations show a different behavior. An initial increase of $p_B\,(n=7)$ is followed by a decrease of $p_B\,(n=7)$ from $T = 3300\,\mathrm{K}$ to $T = 2500\,\mathrm{K}$ and an increase at $T = 2300\,\mathrm{K}$. Finally, looking at $n = 8$, a steady increase of $p_B\,(n=8)$ with decreasing temperature is observed in all classical MD simulations. The ab initio MD simulations show an unsteady temporal development of $p_B\,(n=8)$, reflecting the fact that the maximum of $p_B\,(n)$ is observed at $n = 8$ at $T = 2700\,\mathrm{K}$ and $T = 2300\,\mathrm{K}$ and at $n = 7$ at all other temperatures (see Fig. 6.7). In general, the temporal development of $p_B\,(n)$ reflects the decrease of defects (small ring sizes) with decreasing temperature and the narrowing of the distribution of $p_B\,(n)$ with decreasing temperature (compare Figs. 6.7, 6.27, 6.43 and 6.44). An exception is the rather strong increase of $p_B\,(n=3)$ at $T = 2300\,\mathrm{K}$, in case of the ab initio MD simulations.

6.5 Glass structure

After examining the properties of the model glass former B_2O_3 in the liquid state, in this section the structural properties of the vitreous state are examined. The glass structures investigated in this section are generated in different ways. However, in all cases systems of 150 atoms are regarded at the experimental glass density of $\rho = 1.83\,\mathrm{g/cm^3}$ [159]. As in case of the model glass former SiO_2 (see section 4.2), this is a reasonable system size in terms of balancing between the influence of finite size effect and computational feasibility for quantum mechanical DFT calculations.

In one approach, the glass configurations are generated by a quench from the melt with classical molecular dynamics simulations after an initial random initialization, as described in subsection 4.1.1. Here, in all cases, 10 independent simulation runs are carried out in the NVT ensemble, using a chain of 3 Nosé-Hoover thermostats (see subsection 3.1.2) with a damping parameter of 100 ts (see section 6.3). First, 10 independent glass configurations are generated with the original potential parameters before the structural fit [97], according to Table 6.5, again choosing the B-B interaction to be purely electrostatic. After an equilibration at 3600 K for 240 ps ($ts = 1.2\,\mathrm{fs}$), the configurations are cooled linearly down to 300 K with a cooling rate of $\Gamma = 1 \cdot 10^{11}\,\mathrm{K/s}$. After annealing at 300 K for 240 ps, the configurations are quenched down to 0 K. Next, glass configurations are generated with the two different parameter sets of the classical force field, including 3-body terms, as displayed in Table 6.7. This is done in two different ways. On the one hand, the configurations are equilibrated at 2300 K for 300 ps ($ts = 0.6\,\mathrm{fs}$), followed by a quench to 300 K with a cooling rate of $\Gamma = 1 \cdot 10^{11}\,\mathrm{K/s}$. On the other hand, the configurations are quenched down to 300 K after the stepwise cooling procedure down to 800 K and equilibration at 800 K, according to Table 6.9. In both cases, the configurations are quenched down to 0 K after annealing at 300 K for 600 ps. The first procedure is only applied in the case of $C_{OO} = 0\,\mathrm{eV\,\AA^6}$. The second one is applied for both classical potentials.

In another approach, glass configurations are generated by quenches from the melt with ab initio MD simulations. Here, two different cases are studied. First, the system is equilibrated at 3600 K for 36 ps (30000 ts, $\delta t = 1.2\,\mathrm{fs}$), as described in section 6.2. To generate two independent

glass samples, one quench is started after the first 20000 K time steps of this equilibration run, continuing the simulation at 3600 K for another 3000 ts. Another quench is started at the end of the 30000 ts equilibration run. Second, the system is equilibrated at 2300 K for 124.2 ps (103500 ts, $\delta t = 1.2$ fs, as described in section 6.2. Here, one quench is started after the first 72000 ts of this equilibration run and the second quench is started at the end of the 103500 ts equilibration run, to generated two independent glass samples. In all four cases, the systems are linearly quenched to 300 K and afterwards to 0 K with a cooling rate of $\Gamma = 1.\overline{6} \cdot 10^{14}$ K/s. In addition, in all four cases, Born-Oppenheimer MD runs at 300 K are carried out for 5000 ts (6 ps). In the following, the structural quantities at 300 K refer to the last 3 ps of these Born-Oppenheimer runs. All ab initio MD simulations are carried out with the VASP package [78, 79], using exactly the same parameters as for the ab initio MD simulations in section 6.2.

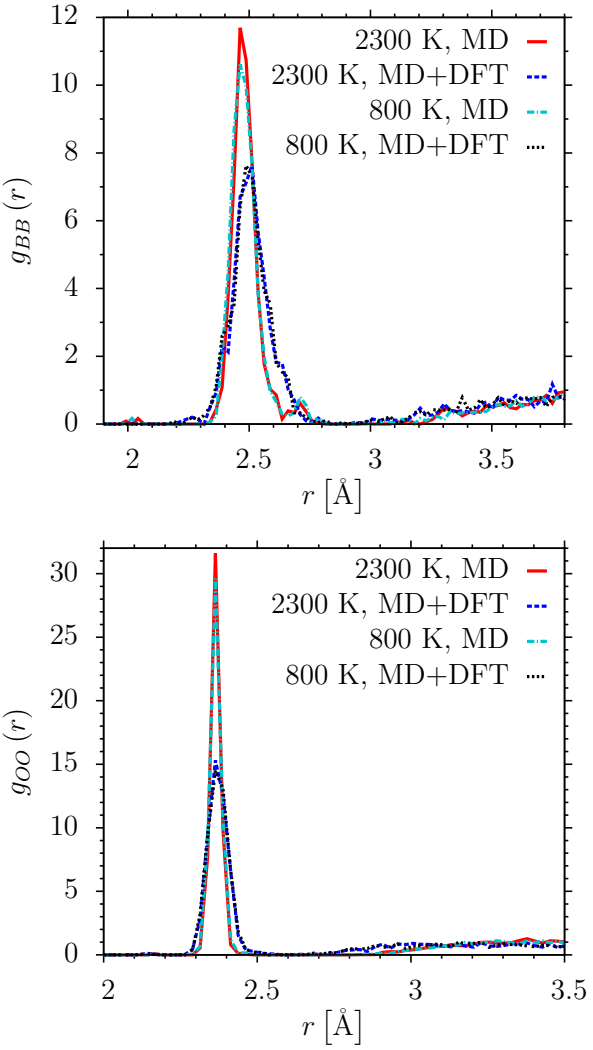

FIGURE 6.51: $g_{BB}(r)$ and $g_{OO}(r)$ at 0 K, before and after structural relaxation. 3-body potential with $C_{OO} = 0\,\text{eV}\,\text{Å}^6$, different equilibration temperatures.

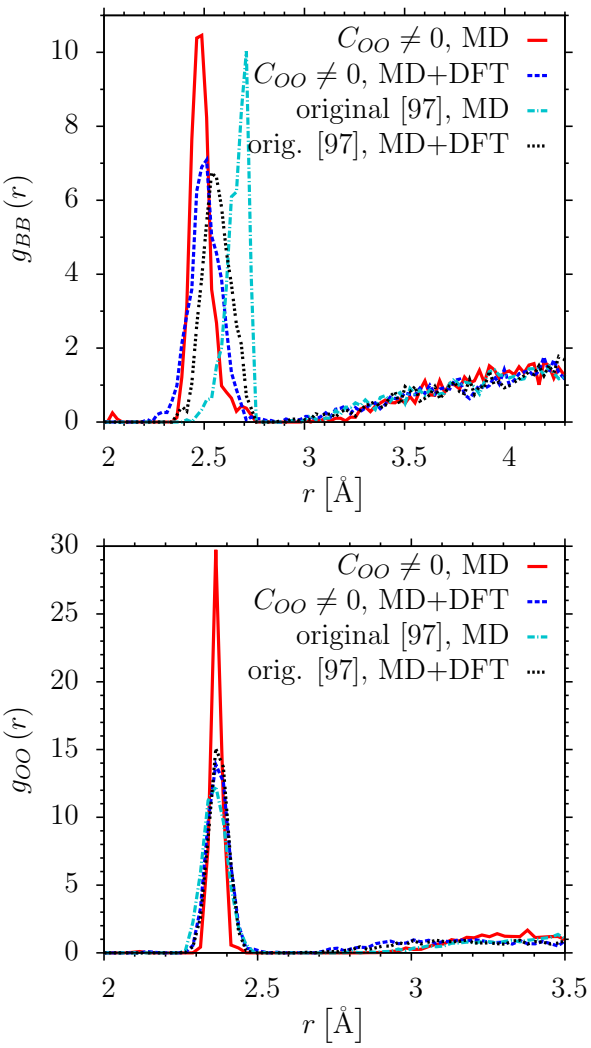

FIGURE 6.52: $g_{BB}(r)$ and $g_{OO}(r)$ at 0 K, before and after structural relaxation. Original potential [97] and 3-body potential with $C_{OO} \neq 0\,\text{eV}\,\text{Å}^6$.

These glass structures are compared to one model glass structure, not generated by a quench

from the melt, but in terms of an alternative method [131–133] where $f = 75\%$ of the boron atoms are located within boroxol rings.

After employing the different quenching schemes to 0 K, all glass configurations are structurally relaxed at constant volume by a conjugate gradient method [111]. This is done in the same way, as described in section 4.2 about the model glass former SiO_2. Again, the structural relaxation is stopped when all forces on the atoms are smaller than $5 \cdot 10^{-4}\, eV/\mathring{A}$, accurate VASP precision is applied and the break condition for the electronic relaxation is a relative energy difference of 10^{-8}.

Next, the structural changes before and after the quantum mechanical relaxation at 0 K are studied for the glass samples generated by means of the classical MD simulations.

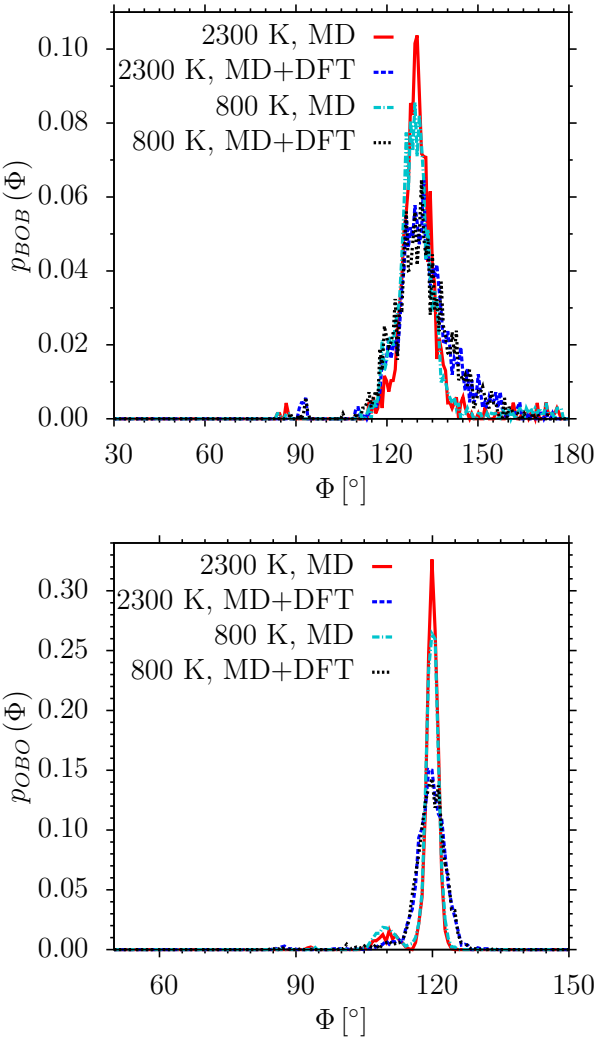

FIGURE 6.53: $p_{BOB}(\Phi)$ and $p_{OBO}(\Phi)$ at 0 K, before and after structural relaxation. 3-body potential with $C_{OO} = 0\,\text{eV}\,\mathring{\text{A}}^6$, different equilibration temperatures.

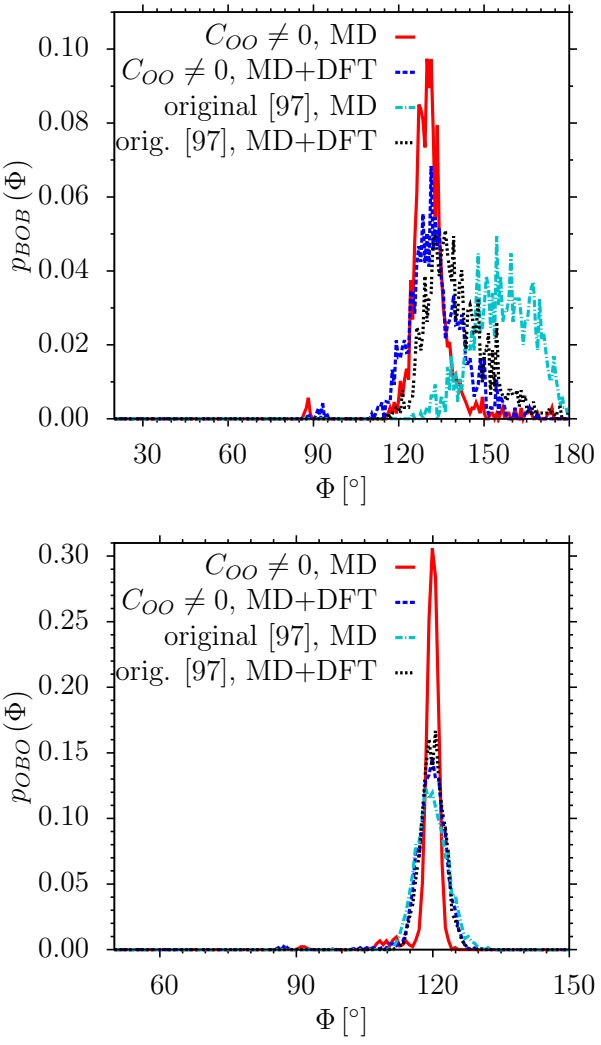

FIGURE 6.54: $p_{BOB}(\Phi)$ and $p_{OBO}(\Phi)$ at 0 K, before and after structural relaxation. Original potential [97] and 3-body potential with $C_{OO} \neq 0\,\text{eV}\,\mathring{\text{A}}^6$.

In Figs. 6.51 and 6.52, the partial pair correlation functions for the B-B and O-O correlations are shown before and after the structural relaxation for all considered classical potentials. These are the correlations that show the most significant differences before and after the structural relaxation. For the classical potential with 3-body terms and $C_{OO} = 0\,\mathrm{eV\,\AA^6}$, the cases of the quenches from 2300 K and 800 K are distinguished. Regarding the 3-body potentials after the fitting procedure (see section 6.3), the main effect of the structural relaxation is the slight increase of all mean first neighbor distances by about 0.01 Å to 0.02 Å. In addition, all first neighbor peaks of the partial pair correlation functions are slightly broadened and the peak heights are decreased. Regarding the original parameter set, the structural change is more pronounced. Here, the average first neighbor B-B distance is decreased by about 0.1 Å and the first neighbor B-O and O-O distances are slightly increased by about 0.01 Å. Here, the peak heights of the first neighbor peak is slightly decreased in case of $g_{BB}(r)$ and slightly increased in case of $g_{OO}(r)$.

In Figs. 6.53 and 6.54, the angular distributions of the B-O-B and the O-B-O correlations are exemplarily shown. Regarding $p_{BBB}(\Phi)$, not shown here, no significant differences can be observed before and after the structural relaxation, in all cases. As in case of the model glass former SiO_2 (see section 4.2), this indicates that the medium-range structure of the network is not altered significantly. Regarding the 3-body potentials after the fitting procedure (see section 6.3), the main effect of the structural relaxation is a slight increase of the mean B-O-B angle by about 1° to 2°, in combination with a broadening of the main peaks and the decrease of the peak heights in $p_{BOB}(\Phi)$ and $p_{OBO}(\Phi)$. The mean O-B-O angle is not altered significantly. Regarding $p_{OBO}(\Phi)$, a small secondary peak is visible at about 109.5° which diminishes in size after the structural relaxation. This is connected to a small percentage of boron atoms with 4 oxygen neighbors, as further explained below. Regarding the original parameter set, the main structural change is the decrease of the mean B-O-B angle by about 16°. This reflects the decrease of the mean B-B distance, described above. Again, the mean O-B-O angle is not altered significantly. The main peak in $p_{OBO}(\Phi)$ gets slightly higher and narrower. Here, no secondary peak at approximately 109.5° is visible.

Next, the effect of the structural relaxation on the distribution of coordination numbers $p_{\alpha\beta}(n)$, $\alpha, \beta \in \{B, O\}$, is studied. In Table 6.11, the probabilities of boron atoms to be 3-fold coordinated with respect to neighboring boron and oxygen atoms and the probabilities of oxygen atoms to be 2-fold coordinated with respect to neighboring boron atoms and 4-fold coordinated with respect to neighboring oxygen atoms are depicted. These are the configurations of an "ideal" glass structure without defects. It can be seen that all probabilities are close to 100 % and that they increase during the structural relaxation procedure. In all cases, the partial coordination numbers are equal to 0 for less atomic neighbors n of the respective atom type, as displayed in Table 6.11. However, in all cases a certain number of overcoordinated atoms exist. Regarding the classical quenches from 800 K, in all cases, the probabilities shown in Table 6.11 are close to the corresponding values of the 150 atom simulations at 800 K as shown at the end of section 6.4. In case of the original potential [97], all boron atoms have $n = 3$ boron and oxygen neighbors and all oxygen atoms have $n = 2$ boron and $n = 4$ oxygen neighbors.

	$C_{OO} = 0\,\text{eV}\,\text{Å}^6$ 2300 K		$C_{OO} = 0\,\text{eV}\,\text{Å}^6$ 800 K		$C_{OO} \neq 0\,\text{eV}\,\text{Å}^6$ 800 K	
	quench	relaxation	quench	relaxation	quench	relaxation
$p_{BB}\,(n=3)$	0.89	0.93	0.85	0.92	0.94	0.96
$p_{BO}\,(n=3)$	0.96	0.97	0.94	0.97	0.98	0.98
$p_{OB}\,(n=2)$	0.97	0.98	0.96	0.98	0.98	0.99
$p_{OO}\,(n=4)$	0.90	0.93	0.86	0.92	0.94	0.96

TABLE 6.11: Probabilities $p_{\alpha\beta}\,(n)\,,\ \alpha,\beta \in \{B,O\}$, of having the exact number of atomic neighbors n of an "ideal" glass configuration. Glass structures after classical classical quench with 3-body potentials and structural relaxation. In case of $C_{OO} = 0\,\text{eV}\,\text{Å}^6$, quenches from the melt at two different temperatures.

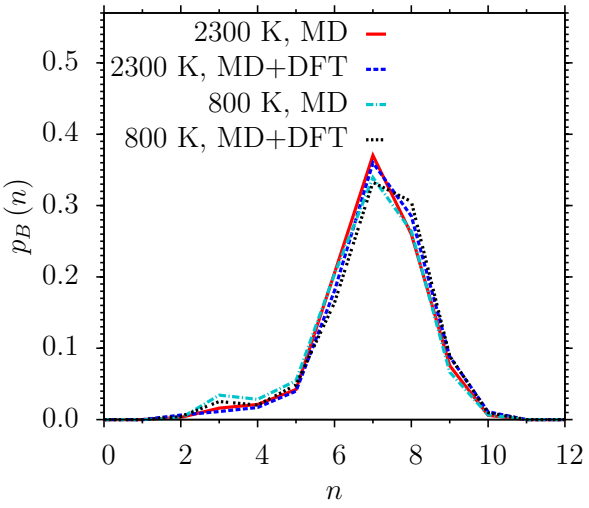

FIGURE 6.55: $p_B\,(n)$ at 0 K, before and after structural relaxation. 3-body potential with $C_{OO} = 0\,\text{eV}\,\text{Å}^6$, different equilibration temperatures.

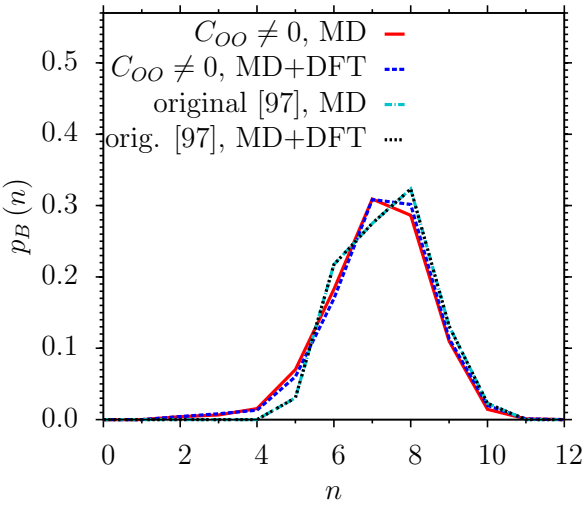

FIGURE 6.56: $p_B\,(n)$ at 0 K, before and after structural relaxation. Original potential [97] and 3-body potential with $C_{OO} \neq 0\,\text{eV}\,\text{Å}^6$.

In Figs. 6.55 and 6.56, the probability that a boron atom is member of a ring of size n is shown before and after the structural relaxation for all considered classical potentials. In contrast to the model glass former SiO_2, slight changes in $p_B\,(n)$ are observed in case of the classical potentials including 3-body terms. However, the curves after the classical quenches are similar to the ones for the 150 atom simulations at 800 K (see section 6.4). The most dominant ring size, in all cases, is $n = 7$ and the probability of a boron atom to be in a ring of size $n = 3$ is lower in case of $C_{OO} \neq 0\,\text{eV}\,\text{Å}^6$ than in the case of $C_{OO} = 0\,\text{eV}\,\text{Å}^6$. In case of $C_{OO} = 0\,\text{eV}\,\text{Å}^6$, the probability of a boron atom to be in a ring of size $n \leq 5$, $p_B\,(n \leq 5)$, is slightly higher for the quench from 800 K than for the quench from 2300 K. In all cases, the effect of the structural relaxation is the slight decrease of the probabilities $p_B\,(n = 7)$ and $p_B\,(n \leq 5)$ and the slight increase of $p_B\,(n = 8)$. In contrast to this, the distribution of ring sizes is not altered after the structural relaxation, in case of the classical quench with the original parameter set. Here, the

dominant ring size is $n = 8$ and rings with size $n \leq 4$ are not apparent at all.

Despite the inclusion of 3-body terms, the probability of a B atom to be in a ring of size $n = 3$ is still lower than 2.6% in the glass structures after the classical quenches and the quantum mechanical relaxation. However, in the glass structures after the classical quench with the original parameter set [97], no rings of size $n = 3$ are apparent at all.

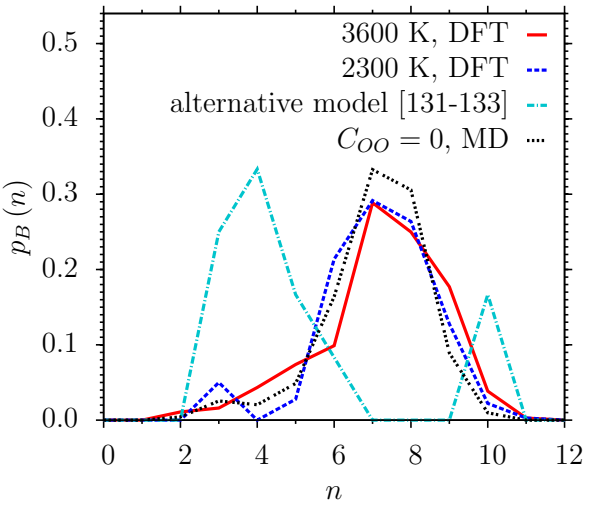

FIGURE 6.57: $p_B(n)$ at 0 K. Comparison of full ab initio quenches (different equilibration temperatures) with one classical quench after structural relaxation ($C_{OO} = 0\,\text{eV}\,\text{Å}^6$, equilibration at 800 K) and model glass structure with $f = 75\%$ [131–133].

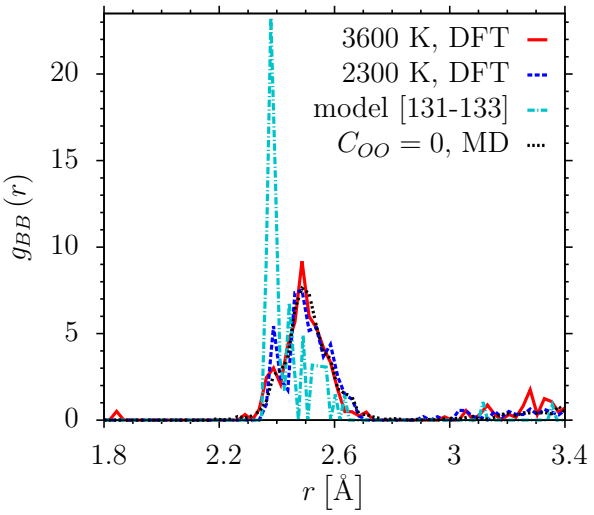

FIGURE 6.58: $g_{BB}(r)$ at 0 K. Comparison of full ab initio quenches (different equilibration temperatures) with one classical quench after structural relaxation ($C_{OO} = 0\,\text{eV}\,\text{Å}^6$, equilibration at 800 K) and model glass structure with $f = 75\%$ [131–133].

Next, the structural properties of the glass configurations generated by the full ab initio quenches from 3600 K and 2300 K are studied. In Fig. 6.57, the probability that a boron atom is member of a ring of size n is shown. The curves of the ab initio quenches are compared to the ones, according to the classical quench with subsequent quantum mechanical relaxation with the largest amount of 3-membered rings ($C_{OO} = 0\,\text{eV}\,\text{Å}^6$, equilibration at 800 K), and the model glass structure with $f = 75\%$ of the boron atoms located within boroxol rings, scaled to the experimental density of $\rho = 1.83\,\text{g/cm}^3$. The structure file of this configuration has been provided by the first author of [133], G. Ferlat. The curves of the ab initio quenches, in each case, are averaged over two independent runs. The distributions of ring sizes show significant differences with respect to the starting temperatures of the full ab initio quenches. In both cases, the most dominant ring size is $n = 7$. However, in case of the quench from 3600 K, the probability $p_B(n \geq 9)$ is higher than in all other quenched glass structures. Also, the respective curve shows a depletion of rings with size $n = 6$ and an increased amount of rings with size $n \leq 5$ with respect to all other quenched glass configurations, except for $p_B(n = 3)$, which is only about $p_B(n = 3) = 0.016$. Regarding the quench from 2300 K, the probabilities $p_B(n \geq 9)$, $p_B(n = 6)$ and $p_B(n = 5)$ are similar to the ones of the classical quenches with 3-body potentials after the structural relaxation. The probabilities $p_B(n = 7)$ and $p_B(n = 8)$ are slightly lower than the ones of the latter and slightly higher than the ones of the ab initio quench from 3600 K. The most pronounced difference to

all other quenched configurations is that $p_B\,(n=4) = p_B\,(n \leq 2) = 0$ in combination with a probability of $p_B\,(n=3) = 0.05$, which is higher than in all other cases of glass structures, quenched from the melt. Regarding the model glass structure of G. Ferlat, the distribution of ring sizes looks completely different. In contrast to all glass structures, generated in this work, rings of size $n = 7$, $n = 8$ and $n = 9$ are not apparent at all. The probability $p_B\,(n \leq 5)$ is much higher compared to the configurations, quenched from the melt. It is remarkable that the probability of a B atom to be in a ring of size $n = 4$, $p_B\,(n=4) = 0.\bar{3}$, is higher than $p_B\,(n=3) = 0.25$.

Regarding the distribution of coordination numbers, in case of the full ab initio quench from 2300 K, all boron atoms have $n = 3$ boron and oxygen neighbors and all oxygen atoms have $n = 2$ boron and $n = 4$ oxygen neighbors. The same holds for the structure file from G. Ferlat [133]. In case of the quench from 3600 K, the probabilities are $p_{BB}\,(n=3) = 0.95$, $p_{BO}\,(n=3) = 0.98$, $p_{OB}\,(n=2) = 0.99$ and $p_{OO}\,(n=4) = 0.96$. In contrast to the classical quenches, the differences to 100% are not only due to overcoordinated atoms. In case of the B-B correlation, the probability $p_{BB}\,(n=2) = 0.01\bar{6}$. This can be assigned to a defect structure of two edge-sharing BO_3 triangles apparent in one of the two quenched samples.

To further illustrate the structural properties of the ab initio quenches, in Fig. 6.58, the curves of $g_{BB}\,(r)$ are shown for the same glass configurations investigated in Fig. 6.57. As in case of the classical quenches, this is the correlation with the most distinct differences between the different glass configurations. The peak positions and shapes of the main peak of both curves, according to the ab initio quenches, are pretty similar to the ones after the classical quenches with the 3-body potentials after the structural relaxation. However, in both ab initio curves a small secondary peak is visible at inter-atomic distances of about $r = 2.39$ Å which can be attributed to boron atoms within boroxol rings, which is more pronounced in case of the 2300 K quench. In case of the 3600 K quench, also a small peak at about $r = 1.84$ Å is visible, which can be attributed to the above-mentioned defect structure of two edge-sharing BO_3 triangles. Regarding the model glass structure of G. Ferlat, the shape of the main peak is completely different. Here, a sharp peak is visible at approximately $r = 2.38$ Å, connected to the B atoms within boroxol rings. The curves of $g_{BO}\,(r)$ and $g_{OO}\,(r)$, not shown here, show less distinct variations between the different glass configurations.

As mentioned above, in case of the ab initio quenches also 5000 ts (6 ps) NVT runs are carried out at 300 K. As in case of the model glass former SiO_2, the distribution of ring sizes is exactly the same at 300 K compared to 0 K, implying that the medium range structure remains unchanged between 300 K and 0 K. Also the local structure remains unchanged in the sense that the average first neighbor distances and average angles do not show any significant differences between 300 K and 0 K.

As already mentioned above, the highest amount of boroxol rings in the glass structures is apparent in the ab initio glass samples quenched from 2300 K. Here, the mean number of 3-membered rings is 3.0 ± 1.0, corresponding to a fraction of $f = 15 \pm 5\%$ of the boron atoms located in 3-membered rings. In the ab initio samples quenched from 3600 K, the average number of

	$C_{OO} = 0\,\text{eV}\,\text{Å}^6$ 2300 K	$C_{OO} = 0\,\text{eV}\,\text{Å}^6$ 800 K	$C_{OO} \neq 0\,\text{eV}\,\text{Å}^6$ 800 K	original parameters [97]
$\overline{r}_{BB}$ [Å]	2.5115 ± 0.0029	2.5092 ± 0.0038	2.5104 ± 0.0039	2.5672 ± 0.0038
$\overline{r}_{BO}$ [Å]	1.3735 ± 0.0012	1.3747 ± 0.0014	1.3721 ± 0.0014	1.3707 ± 0.0002
$\overline{r}_{OO}$ [Å]	2.3728 ± 0.0007	2.3737 ± 0.0008	2.3724 ± 0.0010	2.3731 ± 0.0003
$p_{BOB}\,(\Phi)$ [°]	132.57 ± 0.41	131.94 ± 0.15	132.87 ± 0.40	140.27 ± 0.50
$p_{OBO}\,(\Phi)$ [°]	119.34 ± 0.16	119.25 ± 0.19	119.58 ± 0.18	119.964 ± 0.002
	Ab initio 3600 K	Ab initio 2300 K	Alternative Model [131–133]	Experiment [29]
$\overline{r}_{BB}$ [Å]	2.4935 ± 0.0003	2.5077 ± 0.0032	2.44	$2.364/2.474 \pm 0.07$
$\overline{r}_{BO}$ [Å]	1.3729 ± 0.0016	1.3694 ± 0.0004	1.37	1.365 ± 0.043
$\overline{r}_{OO}$ [Å]	2.3742 ± 0.0001	2.3708 ± 0.0008	2.37	2.364 ± 0.07
$p_{BOB}\,(\Phi)$ [°]	130.75 ± 0.57	133.61 ± 0.07	126.4	120/130
$p_{OBO}\,(\Phi)$ [°]	119.60 ± 0.35	119.96 ± 0.01	120.0	120

TABLE 6.13: Mean first neighbor distances and average angles of B_2O_3 for all examined glass configurations after the structural relaxation at 0 K. Comparison with experimental results [29].

3-membered rings is 1.0 ± 1.0, meaning $f = 5 \pm 5\%$. In both cases, all boron atoms within these rings are 3-fold coordinated with respect to neighboring oxygen atoms and all oxygen atoms are 2-fold coordinated with respect to neighboring boron atoms. The same holds for the model glass structure of G. Ferlat [131–133], with a boroxol ring fraction of $f = 75\%$. In case of the glass structures after the classical quenches and the subsequent quantum mechanical relaxation, the boroxol ring fraction is $f = 0\%$ in case of the original parameter set [97] before the structural fit, as already stated above. In case of the 3-body potentials, the glass structures contain an average number of 0.7 ± 0.3 and 1.6 ± 0.5 3-membered rings ($C_{OO} = 0\,\text{eV}\,\text{Å}^6$, quenches from 2300 K and 800 K) and 0.5 ± 0.2 3-membered rings ($C_{OO} \neq 0\,\text{eV}\,\text{Å}^6$, quench from 800 K), corresponding to fractions of B atoms located in 3-membered rings of $f = 3.5 \pm 1.5\%$, $f = 8 \pm 2.3\%$ and $f = 2.5 \pm 1.1\%$. The statistical errors shown, in each case, are the standard deviation of the mean with respect to the N independent quenches from the melt, $\overline{\sigma} = \frac{\sigma}{\sqrt{N}}$. However, here not all 3-membered rings of the classical quenches are boroxol rings in a sense that all boron atoms in the ring are 3-fold coordinated with respect to neighboring oxygen atoms and all oxygen atoms are 2-fold coordinated with respect to neighboring boron atoms [31]. In case of the potential $C_{OO} = 0\,\text{eV}\,\text{Å}^6$ and the quench from 2300 K, the respective proportion of atoms is about 76% in case of boron and 81% in case of oxygen. Only 3 out of the 7 three-membered rings contained in the 10 independent glass structures, in total, are boroxol rings. In case of the quench from 800 K, the proportion of 3-fold coordinated B atoms is about 63% and the proportion of 2-fold coordinated O atoms is about 65%. Only 4 out of the 16 three-membered rings contained in the 10 independent glass structures, in total, are boroxol rings. In case of the potential $C_{OO} \neq 0\,\text{eV}\,\text{Å}^6$ and the quench from 800 K, the proportion of 3-fold coordinated B atoms is 80% and the proportion of 2-fold coordinated O atoms is 80%, as well. Here, only 3 out of the 5 three-membered rings contained in the 10 independent glass structures, in total, are boroxol rings.

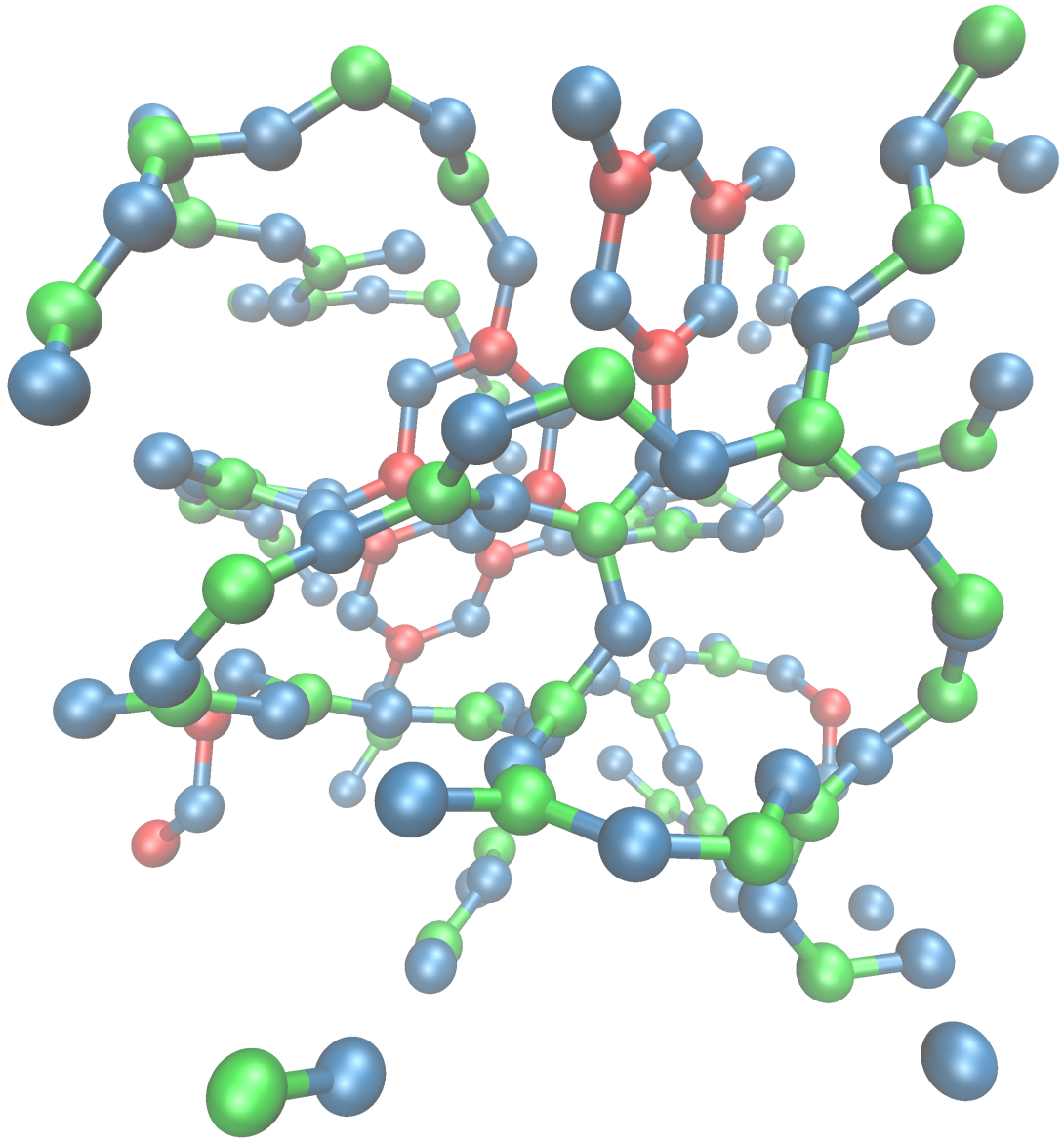

FIGURE 6.59: Snapshot of the glass structure of a 150 atom system $B2O_3$ containing 4 boroxol rings. Configuration of one full ab initio quench from 2300 K. B atoms outside of boroxol rings are displayed green and B atoms inside of boroxol rings are displayed red. O atoms are displayed blue.

In Fig. 6.59, a snapshot of a 150 atom glass structure of B_2O_3 is shown. Here the glass structure with the highest boroxol ring fraction is chosen, containing 4 boroxol rings. This is one of the 2 glass structures generated by a full ab initio quench from 2300 K. (The second one contains only 2 boroxol rings). It can be seen that the glass structure consist of interconnected BO_3 triangles. Also, the 4 boroxol rings are clearly visible.

In Table 6.13, the mean first neighbor distances and mean B-O-B and O-B-O angles are displayed for all examined glass configurations after the structural relaxation. Again, the statistical errors shown, are the standard deviation of the mean with respect to the N independent quenches from the melt. Therefore, the values of the alternative model [131–133] are shown without the

specification of an error. The mean first neighbor distances are compared to experimental results from neutron diffraction at room temperature [29]. As in case of the model glass former SiO_2 (see section 4.2), the experimental data is extracted from the real space correlation function $T(r)$, which basically is the Fourier transform of the interference function, assuming a certain structural model. In this model, a certain fraction f of B atoms is localized within boroxol rings with an O-B-O, as well as an B-O-B angle of 120°. The B-O-B angle for boron atoms outside a boroxol group is assumed to be 130°. This value is found to give a good fit to X-ray data, according to [139]. The displayed experimental errors are the root mean square of the Gaussian fits of the peaks in $T(r)$. The two different experimental first neighbor B-B distances refer to the two cases of B atoms localized within and outside a boroxol ring. The displayed values of the first neighbor distances agree within the statistical errors to previous values from neutron scattering [140] and X-ray scattering [139]. For all glass configurations, except the one generated with the original parameter set before the structural fit, the mean first neighbor distances agree nearly perfectly with the experimental results in the case of boron atoms localized outside a boroxol group. This can be understood, as the highest fraction of boron atoms within boroxol rings in all generated glass structures is $f = 0.15$. In case of the original parameter set, the agreement of the mean B-B distance and mean B-O-B angle is inferior compared to the other glass samples.

As in case of the model glass former SiO_2 (see section 4.2), the total energies E_0 and the total energies per atom E_0/N of the different glass structures are compared. In case of the classical quenches, the corresponding values after the structural relaxation by means of the DFT calculation are $E_0 = -1244.3362 \pm 0.1583\,\text{eV}$ and $E_0/N = -8.2956 \pm 0.\,0.0011\,\text{eV}$ ($C_{OO} = 0\,\text{eV}\,\text{Å}^6$, quench from 2300 K), $E_0 = -1243.9831 \pm 0.2858\,\text{eV}$ and $E_0/N = -8.2932 \pm 0.\,0.0019\,\text{eV}$ ($C_{OO} = 0\,\text{eV}\,\text{Å}^6$, quench from 800 K), $E_0 = -1244.0339 \pm 0.2828\,\text{eV}$ and $E_0/N = -8.2936 \pm 0.\,0.0019\,\text{eV}$ ($C_{OO} \neq 0\,\text{eV}\,\text{Å}^6$, quench from 800 K) and $E_0 = -1244.1764 \pm 0.2332\,\text{eV}$ and $E_0/N = -8.2945 \pm 0.\,0.0016\,\text{eV}$ (original parameter set, quench from 3600 K). The values in case of the full ab initio quenches are $E_0 = -1245.2646 \pm 0.4383\,\text{eV}$ and $E_0/N = -8.3018 \pm 0.\,0.0029\,\text{eV}$ (quench from 2300 K) and $E_0 = -1243.5606 \pm 1.0604\,\text{eV}$ and $E_0/N = -8.2904 \pm 0.\,0.0071\,\text{eV}$ (quench from 3600 K). In case of the alternative model structure [131–133], consisting of 80 atoms, the values are $E_0 = -665.3687\,\text{eV}$ and $E_0/N = -8.3171\,\text{eV}$. The depicted errors are the standard deviation of the mean with respect to the N independent quenches. Regarding the mean total energies after the structural relaxation of the classical quenches, no significant differences between the different potentials are visible. It is remarkable that, despite the significantly larger mean first neighbor B-B distance and mean B-O-B angle of the glass structures generated with the original parameter set, no difference in the mean total energy per atom E_0/N is visible with respect to the glass structures of the 3-body potentials. An explanation could be that the energetic cost of defects (overcoordinated atoms in case of the 3-body potentials, see Table 6.11) in average cancels out the energetic gain of the improved mean B-B distances and the existence of boroxol rings.

Regarding the ab initio quenches, the mean per atom energy of the quench from 3600 K is about $0.003 - 0.005\,\text{eV}$ higher than in case of the classical quenches. On the other hand, the mean per

atom energy of the quench from 2300 K is about 0.006−0.009 eV lower than in case of the classical quenches. The picture is becoming clearer, when looking at the total energies of the 4 different ab initio quenches, individually, as the content of boroxol rings in the individual quenches varies from 0 to 4 rings. The corresponding values are $E_0 = -1242.5002\,\text{eV}$, $E_0/N = -8.2833\,\text{eV}$ (3600 K quench, 0 boroxol rings), $E_0 = -1244.6209\,\text{eV}$, $E_0/N = -8.2975\,\text{eV}$ (3600 K quench, 2 boroxol rings), $E_0 = -1244.8263\,\text{eV}$, $E_0/N = -8.2988\,\text{eV}$ (2300 K quench, 2 boroxol rings) and $E_0 = -1245.7029\,\text{eV}$, $E_0/N = -8.3047\,\text{eV}$ (2300 K quench, 4 boroxol rings). In [133], the average energetic gain per boroxol ring is given by about $6.6 \pm 1\,\text{kcal/mol} \hat{=} 0.2862 \pm 0.0430\,\text{eV}$ from DFT calculations, compared to an experimental value of $6.4 \pm 0.4\,\text{kcal/mol} \hat{=} 0.2775 \pm 0.0174\,\text{eV}$ from Raman measurements [166]. Two times this value is about the order of the energy difference of the two structures, quenched from 2300 K. In case of the 3600 K quenches, the energy difference is larger. This can be attributed to the existence of a defect structure of two edge-sharing BO_3 triangles in the first structure, containing 0 boroxol rings. Also, the difference of the mean per atom energy of the alternative model structure with respect to the mean per atom energies of the glass structures, generated in this work, can be explained in terms of the energy gain per boroxol ring.

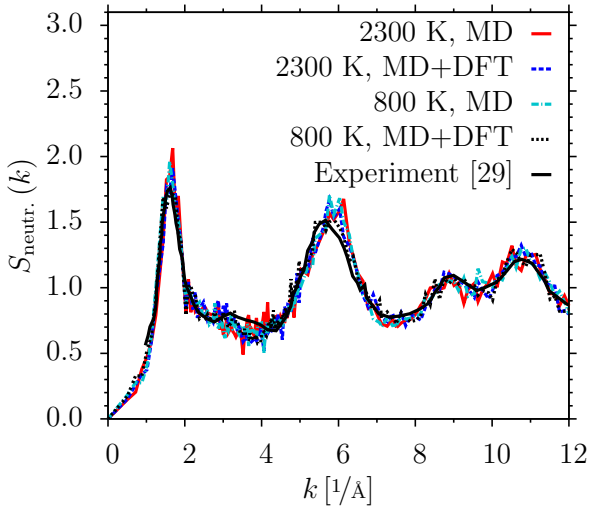

FIGURE 6.60: $S_{\text{neutr.}}(k)$ at 0 K, before and after structural relaxation. 3-body potential with $C_{OO} = 0\,\text{eV Å}^6$, different equilibration temperatures. Comparison with experimental results [29], taken from [141].

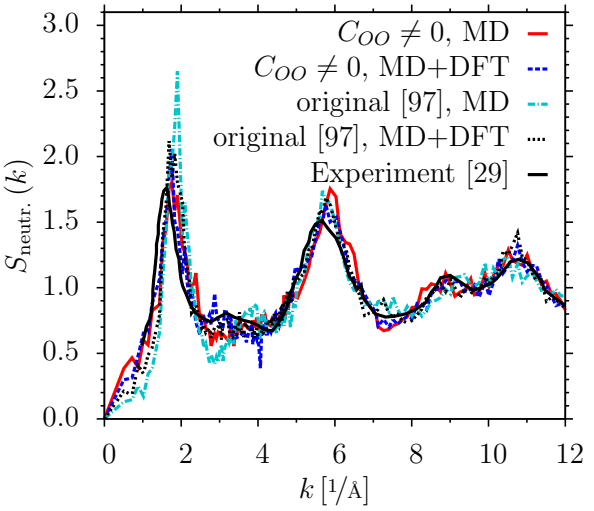

FIGURE 6.61: $S_{\text{neutr.}}(k)$ at 0 K, before and after structural relaxation. Original potential [97] and 3-body potential with $C_{OO} \neq 0\,\text{eV Å}^6$. Comparison with experimental results [29], taken from [141].

Next, the total neutron structure factor $S_{\text{neutr.}}(k)$ is examined. As explained in section 3.3, it is obtained by weighting the partial static structure factors $S_{\alpha\beta}(k)$, $\alpha, \beta \in \{B, O\}$, with the B and O neutron scattering lengths (see equation (3.95)). The curves are compared to experimental data, according to the same experimental results, the mean first neighbor distances are extracted [29] from. Here, the glass samples contain 99.57% ^{11}B, in contrast to 80% natural abundance. Regarding this, the respective neutron scattering length of ^{11}B is chosen, meaning $b_B = 6.65\,\text{fm}$ and $b_O = 5.803\,\text{fm}$ [89]. In Figs. 6.61 and 6.61, the total neutron structure factor is compared to the experimental one for all classical quenches before and after the structural relaxation. It

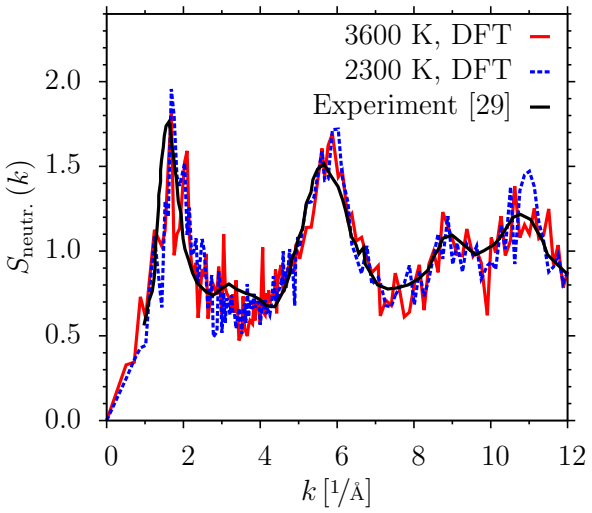

FIGURE 6.62: $S_{\text{neutr.}}(k)$ at 0 K. Comparison of full ab initio quenches with experimental results [29], taken from [141].

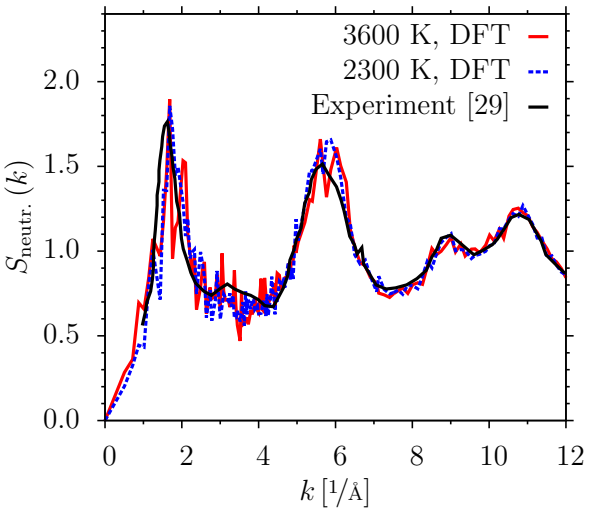

FIGURE 6.63: $S_{\text{neutr.}}(k)$ at 300 K. Comparison of full ab initio quenches with experimental results [29], taken from [141].

can be seen that the overall agreement is quite good. In case of the 3-body potentials after the structural fit, the curves before and after the structural relaxation at 0 K are nearly identical. The biggest differences before and after the structural relaxation are visible in the case of the original parameter set. In Figs. 6.62 and 6.63, the curves of the ab initio quenches are compared to the experimental ones. Here, the curves at 0 K and at 300 K are depicted. Again, the overall agreement is quite good. Also, no significant difference is visible between the curves at 0 K and 300 K. The agreement of the static structure factor, despite the reduced number of boroxol rings in the simulated glass structures $f \leq 0.15$, shows that this is not a sufficient condition for the agreement of the glass structures, as well. This is in agreement with [141] and [133]. Here, model glass structures generated by ab initio quenches from the melt with a boroxol ring fraction of $f = 0.094$ and $f = 0.22$ show a good accordance of $S_{\text{neutr.}}(k)$ with experimental results, as well.

6.6 Vibrational properties

In this section, different vibrational properties of the model glass former B_2O_3 are examined and compared with experimental results, following the approach of section 4.3. As in case of the model glass former SiO_2, the glass structures are treated as a crystalline structure with a large unit cell containing all 150 atoms and the so-called "frozen phonon" method is used, based on the harmonic approximation.

Again, the vibrational properties of the quantum mechanical forces are compared to the ones of the classical forces. Here, the classical force fields after the structural fit including 3-body terms (see section 6.3) and the original parameter set [97] are employed. The basis for calculating the vibrational properties, according to the DFT forces, are the glass samples at 0 K after the classical quenches and the full ab initio quenches, followed by a structural relaxation with

quantum mechanical forces, as explained in section 6.5. To calculate the vibrational spectra of the classical interaction potentials, also a structural relaxation of the configurations at 0 K is performed with respect to the classical forces, again, employing a conjugate gradient algorithm [111]. Afterwards, all atoms $i \in \{1, N\}$ are displaced by $\Delta r_{\alpha;i} = \pm 0.02\,\mathring{A}$, $\alpha\,\{1, 2, 3\}$ and the forces on all atoms $F_{\alpha;i}\,(\Delta r_{\beta;j})$ are computed. Again, all DFT calculations are conducted with the VASP package, using the same DFT parameters as in section 6.5 for the structural relaxation, and the forces on the atoms are the Hellman-Feynman forces [112].

In all cases, the vibrational properties are calculated by means of the open source package Phonopy [90, 91]. As in case of the model glass former SiO_2 (see section 4.3), the input parameters are the forces with respect to all atomic displacements $F_{\alpha;i}\,(\Delta r_{\beta;j})$. Again, the force constants $\Phi_{\alpha\beta;i,j}$ are computed by means of a slightly modified form of the so-called original Parlinski-Li-Kawazoe method [118] and the dynamical matrix $D_{\alpha\beta;i,j}\,(\mathbf{k})$ is evaluated on a fixed mesh of k-points within the Brillouin-zone with a mesh-grid of 5 points along each of the $\mathbf{k}$-axes. In each case, the phonon density of states $g\,(\nu)$ (see equation (3.109)) is evaluated, according to the eigenfrequencies of $D_{\alpha\beta;i,j}\,(\mathbf{k})$ at the specific k-points $\nu_n\,(\mathbf{k})$, $n \in \{1, \ldots, 3N\}$ (see equation (3.108)), and Gaussian smearing is applied with a smearing width of 0.1 THz.

Regarding the pure ab initio quenches from 3600 K to 0 K and from 2300 K to 0 K, in each case, the curves are averaged over the 2 independent glass configurations. In case of the classical quenches with the potentials including 3-body terms and the subsequent quantum mechanical relaxation, the vibrational properties, according to the DFT forces, in each case, are averaged over 5 independent glass samples. Regarding the classical quench with the original potential before the structural fit, the curves, according to the quantum mechanical forces, are averaged over 2 independent configurations. All curves with respect to the different classical potentials are averaged over 10 different configurations.

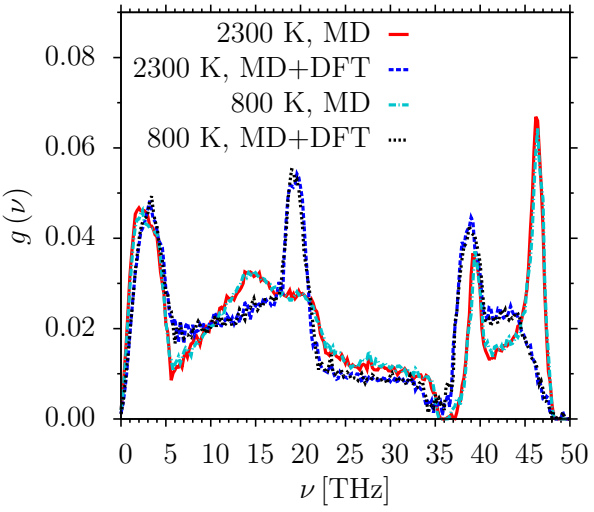

FIGURE 6.64: $g\,(\nu)$ of $B2O_3$, classical quench. Comparison of classical with quantum mechanical forces. 3-body potential with $C_{OO} = 0\,\text{eV}\,\mathring{\text{A}}^6$, different equilibration temperatures.

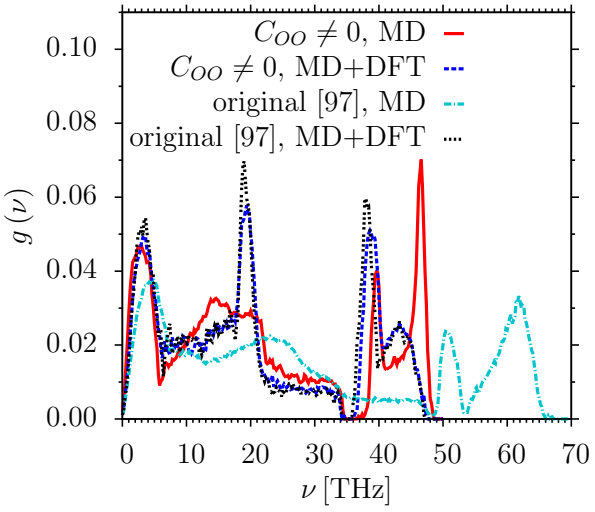

FIGURE 6.65: $g\,(\nu)$ of $B2O_3$, classical quench. Comparison of classical with quantum mechanical forces. Original potential [97] and 3-body potential with $C_{OO} \neq 0\,\text{eV}\,\mathring{\text{A}}^6$.

In Figs. 6.64 and 6.65, the phonon densities of states $g(\nu)$, according to the quantum mechanical forces after the classical quench and the structural relaxation are compared to the ones, according to the classical forces. In case of the force field including 3-body terms with $C_{OO} = 0\,\mathrm{eV\,\AA^6}$, the different quenches from 2300 K and from 800 K are distinguished. Regarding the phonon densities of states of the classical potentials with 3-body terms, the shape of the different curves is nearly identical. In all cases, a low-frequency peak at about 1 - 5 THz is observed followed by a rather broad double peak between about 12 and 22 THz and a high-frequency doublet at about 38 - 48 THz. The vibrational spectra, according to the quantum mechanical forces also all have a pretty similar shape, in all cases. Here, the main features are a low-frequency peak at approximately 1.5 - 5 THz, followed by a rather distinct peak at approximately 18 - 21 THz. In the high-frequency regime, a distinct peak is visible at about 37 - 40 THz, followed by a shoulder at approximately 43 - 45 THz. The biggest differences to the phonon densities of states, according to the classical forces with 3-body terms, are the rather distinct peak at intermediate frequencies (about 18 - 21 THz) in contrast to the broader one in the classical curves and differences in the high-frequency regime (single peak with shoulder in contrast to double peak). Also this high-frequency pattern of the DFT curves is shifted to slightly lower frequencies with respect to the classical curves. According to [134], the distinct peak at intermediate frequencies is connected to symmetric stretching modes within a BO_3 triangle, where the oxygen atoms are vibrating together in phase with respect to the central boron atom and to so-called out-of-plane deformations of the BO_3 triangle. The high-frequency peak (about 37 - 40 THz) and the shoulder (about 43 - 45 THz) are also connected to vibrational modes localized within the BO_3 triangles [26]. According to [134], the high-frequency modes are connected to anti-symmetric stretching modes, where two oxygen atoms move towards the central boron atom and the other oxygen atom moves away. Regarding this, the data suggest that the forces between neighboring boron and oxygen atoms are slightly larger in the classical case leading to this shift of the local vibrational modes. In contrast to the model glass former SiO_2 (see section 4.3), the accordance of the classical curves with the DFT curves in the low-frequency range of the spectrum which is connected to the more delocalized vibrational modes is quite good. This comparison does not hold for $g(\nu)$, according to the original parameters. In this case, the differences to the DFT curve are much more distinct. The classical $g(\nu)$ shows a peak at about 2 - 6 THz, a rather broad peak at about 20 - 27 THz and a high-frequency doublet at approximately 50 - 64 THz. This means that the corresponding vibrational modes are shifted to higher frequencies with respect to all other cases. An explanation could be the much stronger inter-atomic forces compared to the other models, connected to the increased Coulomb interactions due to the significantly higher partial charges of the boron and the oxygen atoms (see Tables 6.5 and 6.7).

In Fig. 6.66, the phonon densities of states of the glass structures after the classical quenches, followed by a structural relaxation, are compared to the ones after the full ab initio quenches and to the one of the alternative model structure [131–133]. In all cases, DFT forces are employed. Regarding the glass structures generated in this work, all vibrational spectra have a nearly identical shape. The biggest difference with respect to the other curves is visible in case of the glass samples generated with the original parameter set. Here, the peak heights of all

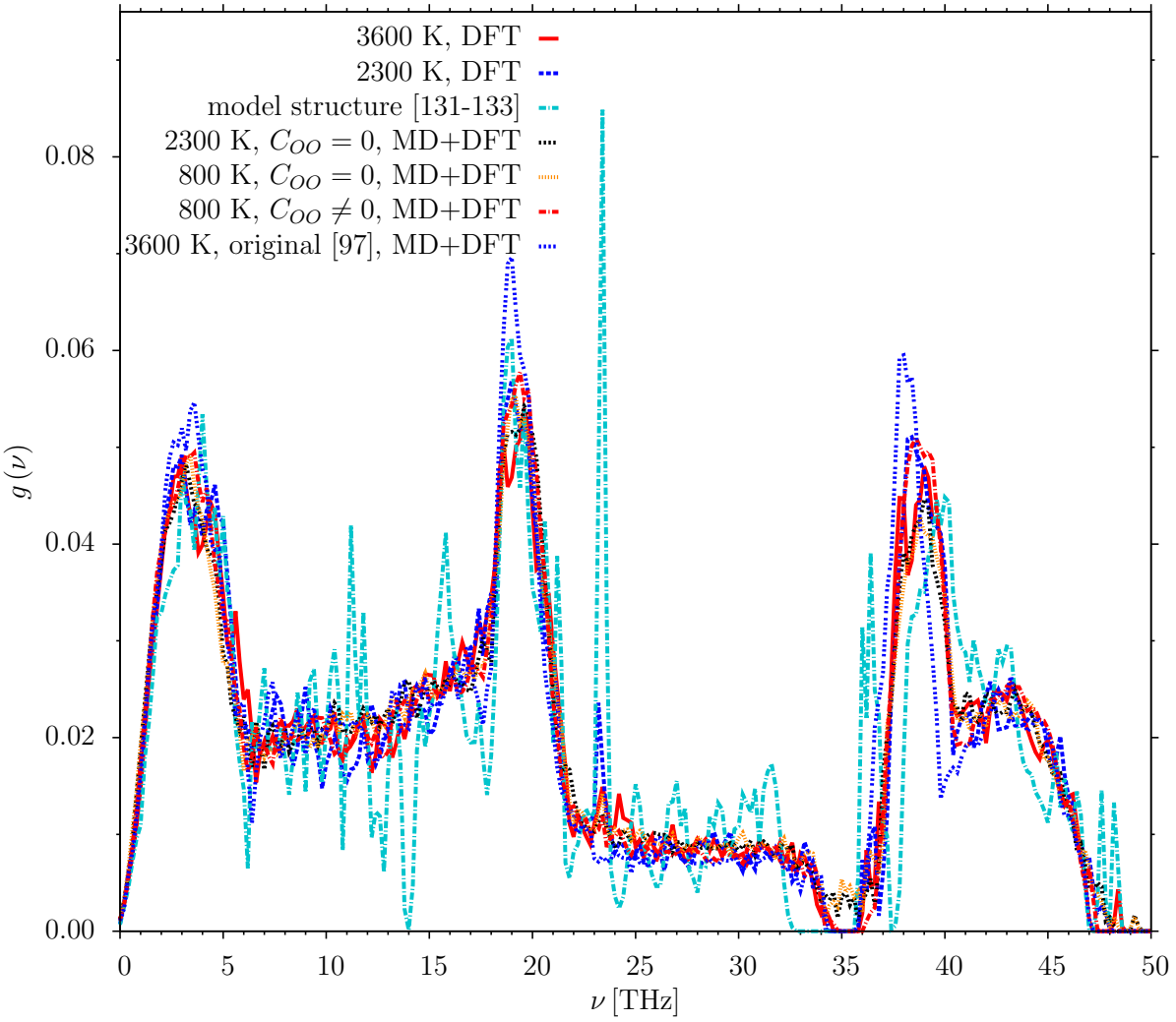

FIGURE 6.66: $g(\nu)$ of $B2O_3$, DFT forces. Comparison of classical quenches with subsequent structural relaxation to full ab initio quenches and alternative model structure [131–133].

peaks are slightly higher with respect to the other cases. In addition, the position of the high-frequency peak (about 37 - 40 THz) is shifted to slightly lower frequencies. The main structural differences with respect to the other glass structures are the slightly larger first neighbor B-B distances (about 0.06Å to 0.08Å) and the slightly larger mean B-O-B angle (about 8° 10°), as displayed in Table 6.13. As explained above, the high frequency pattern is connected to the vibrational modes within the BO_3 triangles [26]. This implies that the arrangement of the BO_3 units also has a slight effect on the vibrational modes within the BO_3 triangles, connected to the strength of the bonding forces between neighboring boron and oxygen atoms. Regarding the alternative model structure, the overall shape of the vibrational spectrum is similar to the ones according to the glass samples generated in this work. There are distinct differences in the high-frequency pattern (about 38 to 48 THz). Again, this can be explained in terms of the differences in the inter-connection of the BO_3 triangles. As already explained in section 6.5, in this model structure $f = 75\%$ of the B atoms are localized within boroxol rings, connected to a B-O-B angle of 120°. Besides the differences in the high-frequency range, the most noticeable

feature of this model structure is the very prominent peak at about 23.2 to 23.4 THz. This peak can be assigned to the breathing mode of the boroxol ring [26, 30]. Also a second distinct peak at approximately 36 to 36.4 THz is visible in this $g(\nu)$, which is a boroxol ring signature, as well [30]. As examined in section 6.5, the ratio of B atoms localized in 3-membered rings varies from about $f = 2.5\%$ (classical potential with 3-body terms, $C_{OO} \neq 0\,\text{eV}\,\text{Å}^6$) to $f = 15\%$ (full ab initio quench from 2300 K). In all cases, a small distinct peak is visible at about 23.2 to 23.4 THz, increasing in size with increasing ratio f. Also, in all cases, a small pattern at approximately 36 to 36.4 THz is visible. However, this is not as pronounced as the distinct peak at about 23.2 to 23.4 THz. In case of the model glass structure with $f = 0\%$ (classical potential with original parameter set) this peak is clearly missing. Regarding once again the vibrational spectra according to the classical forces (see Figs. 6.64 and 6.65), this signature is missing as well. As explained in section 6.5, the distribution of ring sizes is only altered insignificantly by the structural relaxation. This means that the value of f is about the same in the respective glass structures. In the vibrational spectra of the classical force fields with 3-body interactions, a small feature is visible between about 27.5 and 28.5. This could be connected to vibrations within the 3-membered rings.

Next, the so-called effective neutron scattering cross sections $G(\nu) = C(\nu)\ g(\nu)$ are compared to experimental results from inelastic neutron scattering [30, 134]. Here, only the case of DFT forces is studied. As in case of the model glass former SiO_2 (see section 4.3), the correction function $C(\nu)$ is calculated using the incoherent approximation, according to [121]. This means that the functional form of $C(\nu)$ is equal to the one of equation (4.5), substituting Si with B. As in case of the static neutron structure factor [29], the glass samples, according to [30], contain 99.57% of the isotope ^{11}B, in contrast to 80% natural abundance. In [134], the isotope composition is not stated. However, the authors of [134] are also authors of the corresponding publications [29] and [30]. Having this in mind and the enhanced absorption of neutrons of ^{11}B, it is assumed that also in the latter case a ^{11}B sample is used. Regarding this, the respective neutron scattering length of ^{11}B is chosen, meaning $b_B = 6.65\,\text{fm}$ and $b_O = 5.803\,\text{fm}$ [89] and the atomic mass of the isotope ^{11}B is chosen, meaning $m_B = 11.0093\,\text{amu}$ and $m_O = 15.9994\,\text{amu}$. This means that in equation (4.5) (Si substituted with B), $\langle m \rangle = 14.00336\,\text{amu}$ is the mean atomic mass of the system, $\left\langle b^2 \right\rangle = N^{-1} \sum_i b_i^2 = 37.8938854\,\text{fm}^2$ is the mean squared neutron scattering length, $g(\nu)$ is the full phonon density of states and $g_\alpha(\nu), \alpha \in \{B, O\}$, are the partial phonon densities of states. As in case of the model glass former SiO_2, a Debye-Waller factor $\exp\left[-k^2 \left\langle u_\alpha^2 \right\rangle / 3\right] \simeq 1$, $\alpha \in \{B, O\}$, is assumed [92] which is a good assumption at low temperature. Comparing the curves in Figs. 6.67 and 6.68 with the ones in Fig. 6.66, it can be seen that the main effect of $C(\nu)$ is the slight increase of the height of the peaks at intermediate (about 18 - 21 THz) and high frequencies (about 37 - 40 THz) and a slight reduction of the peak height of the low-frequency peak (about 1.5 - 5 THz). In [134], the experimental spectrum is composed of two parts, a low- and a high-frequency part, measured at two different spectrometers and temperatures of 15 K and 300 K, respectively. In [30], the full spectrum is measured in a single scattering experiment at 20 K with an incident neutron energy of $E_0 = 250\,\text{meV} \mathrel{\hat{=}} 60.45\,\text{THz}$. Here, the experimental

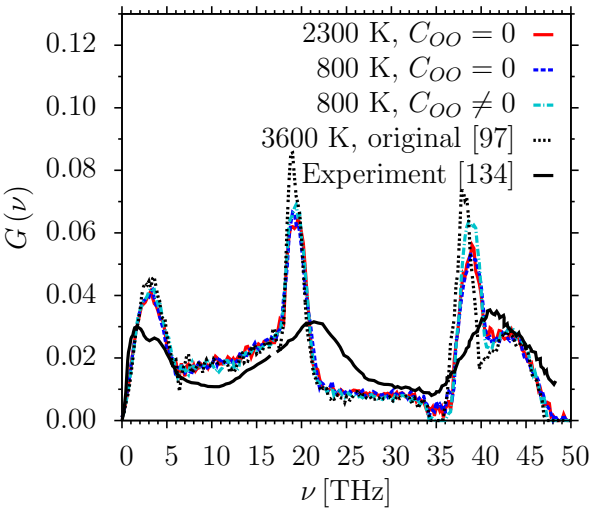

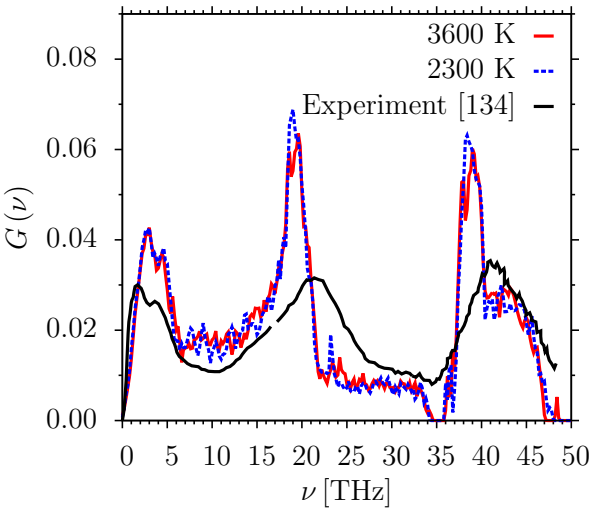

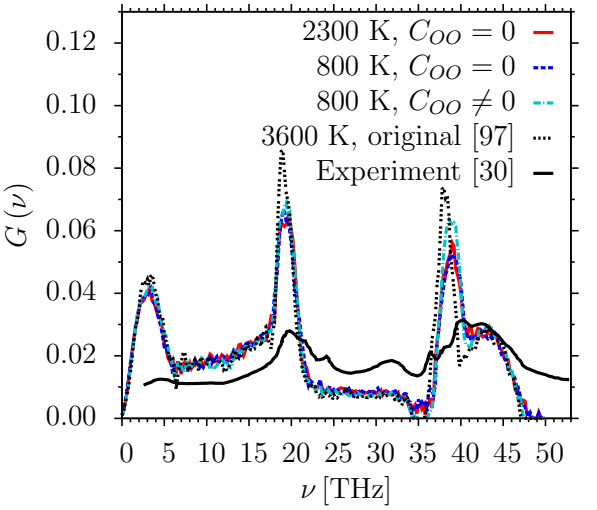

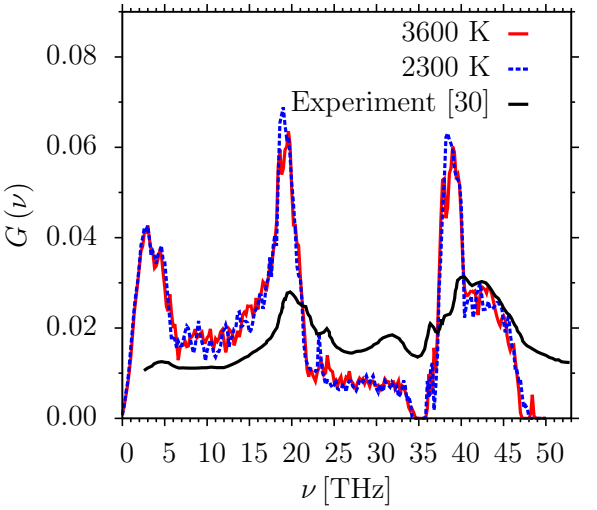

FIGURE 6.67: $G(\nu)$ of $B2O_3$ according to quantum mechanical forces. Different classical quenches. Comparison with inelastic neutron scattering [30, 134].

FIGURE 6.68: $G(\nu)$ of $B2O_3$ according to quantum mechanical forces. Ab initio quenches, different equilibration temperatures. Comparison with inelastic neutron scattering [30, 134].

resolution is increased compared to [134] in the intermediate and high-frequency range. However, the low-frequency peak is not resolved.

In Figs. 6.67 and 6.68, all curves are normalized to $\int G(\nu) = 1$. It can be seen that the overall agreement between the calculated $G(\nu)$ and the experimental ones is quite good. Regarding [134], all three peaks are apparent in the quantum mechanical curves, as discussed above. In [30], two distinct peaks are visible at 24.2 THz and 36.5, assigned to the boroxol rings. As discussed above, these two patterns are also visible in the generated glass structures containing boroxol rings. However, they are shifted to slightly lower frequencies (about 23.2 to 23.4 THz and about 36 to 36.4 THz). This shift to slightly lower frequencies is also apparent, regarding the intermediate frequency peak (about 18 - 21 THz) and the high frequency pattern (about 37 to 47 THz). As explained in section 4.3, a reason for this can be the tendency to overestimate bond-lengths and to underestimate vibrational frequencies in case of the applied exchange-correlation

functional (PBEsol) [81]. In addition to the shift, the peaks of the calculated $G(\nu)$ are higher than the experimental ones. This is connected to the experimental resolution.

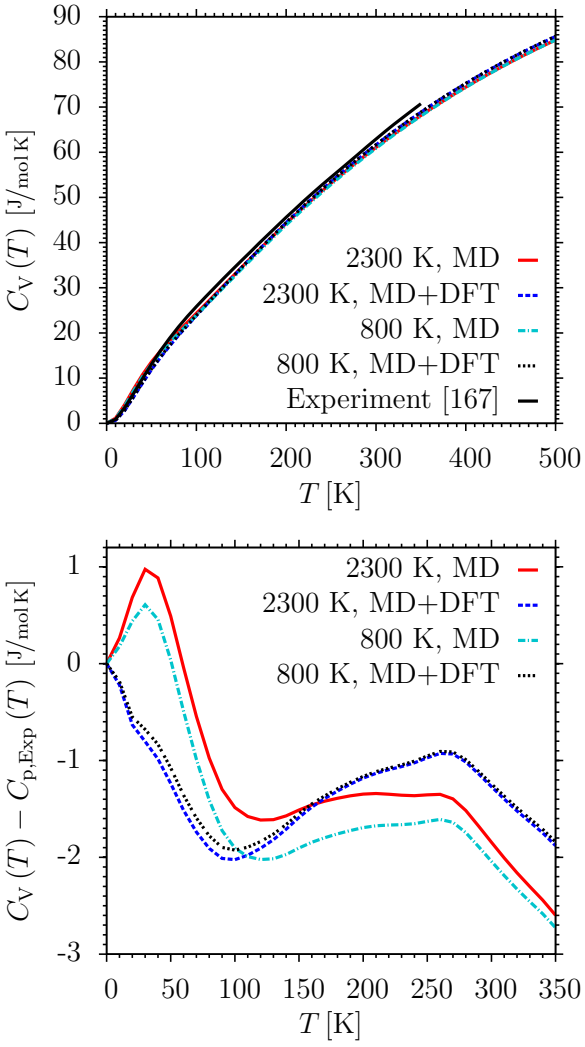

FIGURE 6.69: $C_V(T)$ of B_2O_3, according to classical and quantum mechanical forces. 3-body potential with $C_{OO} = 0\,\text{eV}\,\text{Å}^6$, different equilibration temperatures. Comparison with experimental results of $C_p(T)$ [167]

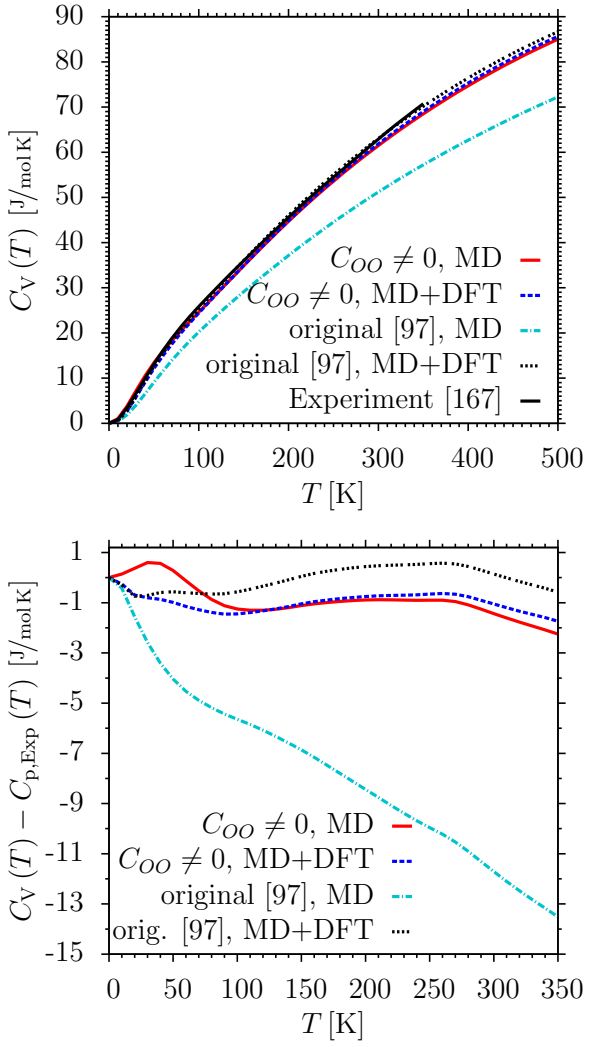

FIGURE 6.70: $C_V(T)$ of B_2O_3, according to classical and quantum mechanical forces. Original potential [97] and 3-body potential with $C_{OO} \neq 0\,\text{eV}\,\text{Å}^6$. Comparison with experimental results of $C_p(T)$ [167]

Next, the specific heat at constant volume $C_V(T)$ is calculated, according to equation (3.121), multiplied by the factor $\frac{N_A}{N_{units}}$ to obtain the values in units of [J/mol]. Again, N_A is the Avogadro constant and N_{units} is the number of structural units in the configuration, which is 30 B_2O_3 units in the case of a 150 atom system of B_2O_3. As in case of the model glass former SiO_2 (see section 4.3), the calculation is based on the eigenfrequencies $\nu_n(\mathbf{k})$, $n \in \{1, \ldots, 3N\}$, on a k-mesh with 15 points along each of the $\mathbf{k}$-axes. In Figs. 6.69, 6.70 and 6.71, the curves of $C_V(T)$, according to the quantum mechanical and the classical forces, are compared to $C_p(T)$ from calorimetric measurements [167] for all considered cases. In [167], $C_p(T)$ is measured in a temperature range from 5 K to 350 K. The reported results are in good agreement with the ones of [168] for temperatures greater than 20 K. In the temperature range between 10 K and

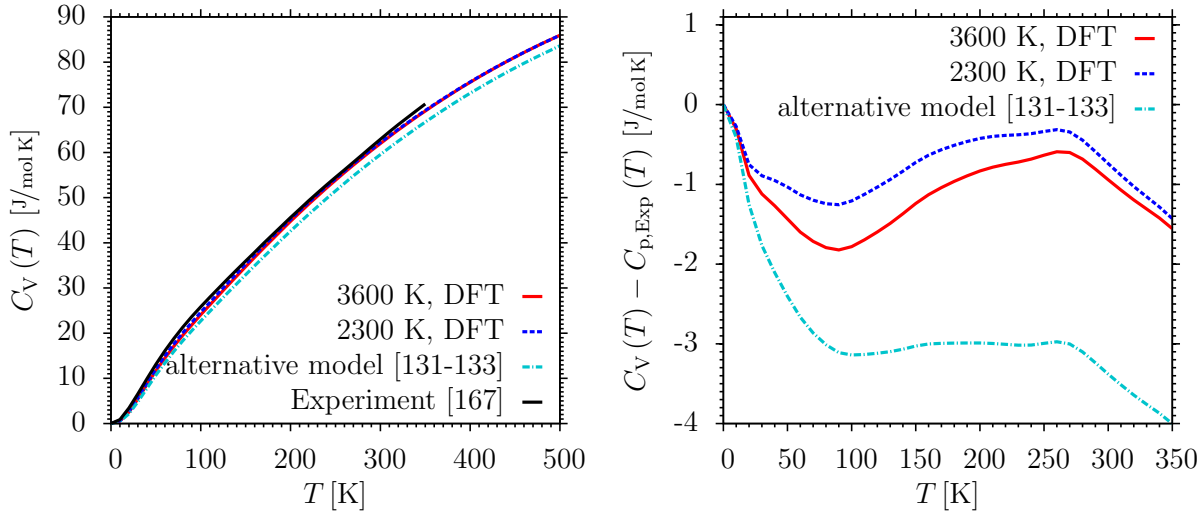

FIGURE 6.71: $C_V(T)$ of B_2O_3, according to quantum mechanical forces. Ab initio quenches at different equilibration temperatures and alternative model structure [131–133]. Comparison with experimental results of $C_p(T)$ [167]

20 K, the measured values of $C_p(T)$, according to [168], are about 3% lower, which is within the error bars of the techniques. However, the reason for the difference could be the different thermal histories of the glass samples. As stated in section 4.3, the difference between C_V and C_p per mol is expressed by the thermodynamic relation of equation (4.7), according to [124]. Again, M is the molar mass, ρ the density, α_V the volumetric coefficient of thermal expansion at constant pressure and K the bulk modulus at constant temperature. In case of B_2O_3, the values at room temperature are $M = 69.6182\,\mathrm{g/mol}$ (molar mass of one B_2O_3 unit), $\rho = 1.83\,\mathrm{g/cm^3}$ [159], $\alpha_V \simeq 3 \times \alpha_L \simeq 3 \times 1.545 \cdot 10^{-5} K^{-1}$ and $K \simeq 13\,\mathrm{GPa}$. To calculate the value of the molar mass of a B_2O_3 unit, in this case, an atomic mass of $m_B = 10.81\,\mathrm{amu}$ is assumed, according to the natural abundance of ^{11}B of 80%. The values of α_L and K are given in [168]. This leads to a difference between C_p and C_V of about $C_p - C_V = 1.06 \cdot 10^{-3} \frac{\mathrm{J}}{\mathrm{K^2\,mol}} T\,[K]$. This value is more than 2 magnitudes higher than in case of the model glass former SiO_2 (see section 4.3), due to the significantly larger linear expansion coefficient α_L at room temperature (about 28 times). However, also in this case the difference between C_p and C_V is only about $C_p - C_V = 0.37\,\mathrm{J/mol\,K}$ at the largest considered temperature of 350 K.

In Figs. 6.69, 6.70 and 6.71 it can be seen that the agreement between the theoretical and the experimental curves is good in all cases, except for the curve based on $\nu_n(\mathbf{k})$, $n \in \{1, \ldots, 3N\}$, according to the classical forces of the original parameter set. Here, the theoretical curve of $C_V(T)$ is significantly below the experimental one of $C_p(T)$ with a deviation of about $C_p - C_V \simeq -13.5\,\mathrm{J/mol\,K}$ at 350 K. This is related to the shift of the respective vibrational patterns to higher frequencies and therefore, to a reduced number of vibrational modes in the low and intermediate frequency-range. In contrast to the model glass former SiO_2, the curves, according to the quantum mechanical forces, and the ones, according to the classical forces, do not show a significant difference for both classical force fields with 3-body terms. This is related to the fact that the classical and quantum mechanical vibrational spectra $g(\nu)$ are in better agreement

with each other in the low and intermediate frequency range as observed in case of SiO_2 for the BKS and the CHIK potential (see Figs. 6.64 and 6.65). In addition, there are also no significant differences visible in $C_V(T)$ of the glass samples after the classical quench and subsequent quantum mechanical relaxation and the ab initio quenches. Here, the highest differences between the theoretical and the experimental values at 350 K are about $C_p - C_V \simeq -2.8\,\mathrm{J/mol\,K}$. In case of the alternative model structure [131–133], the agreement is slightly inferior with a deviation of about $C_p - C_V \simeq -4\,\mathrm{J/mol\,K}$ at 350 K.

In this chapter, the simulation results of the model glass former B_2O_3 are summarized. First, an overview over different experimental results is given, supporting the special feature of about $60\% - 80\%$ of the boron atoms located in planar, 3-membered boroxol rings in vitreous B_2O_3. In addition, a summary over previous classical molecular dynamics studies of boron oxide is presented. Next, the results of ab initio molecular dynamics (MD) simulations of 150 atom systems at the experimental density of $\rho = 1.83\,\mathrm{g/cm^3}$ are depicted in a temperature range, the systems still can be equilibrated, namely between 3600 K and 2300 K. At 2300 K, an increased amount of 3-membered rings is observed, compared to the liquid structures at 2500 K and 2700 K. This motivates to take the latter as a basis for the development of a new interaction potential for classical MD simulations of liquid B_2O_3. The parameter fits are carried out, using a modified form of the structural fitting procedure, presented in [43]. Starting with the parameter set, according to [97], the differences in the pair correlation functions and the angular distributions of the classical and the ab initio MD simulation are minimized, using a Levenberg-Marquardt procedure. The best results are obtained, including 3-body angular interactions for the O-B-O and the B-O-B angles. A new angular potential type is introduced, namely an inverse Gaussian potential that is smoothly switched on and off, depending on the inter-atomic distances (see equations (6.1) to (6.4)). This potential type is implemented into a new LAMMPS pair style, called "gauss/smooth". Classical MD simulations of 150 are atom systems are carried out at the experimental glass density of $\rho = 1.83\,\mathrm{g/cm^3}$ in a temperature range between 3600 K and 800 K, using two different parametrizations of the 3-body potential, with ($C_{OO} \neq 0\,\mathrm{eV\,\AA^6}$) and without ($C_{OO} = 0\,\mathrm{eV\,\AA^6}$) O-O attractions. The main difference between these simulation runs and the ab initio MD simulations are reduced peak heights and $2-10$ times shorter α-relaxation times in the classical MD simulations. In addition, classical MD simulations of 1200 atom systems at constant external pressure $p = 0$ are presented. Here, the parametrization with O-O attractions leads to a system density comparable to the experimental one at low temperatures ($\bar{\rho} = 1.892 \pm 0.003\,\mathrm{g/cm^3}$ at 1000 K), whereas the parametrization without O-O attractions leads to a significantly lower system density at low temperatures ($\bar{\rho} = 1.280 \pm 0.014\,\mathrm{g/cm^3}$ at 1000 K). Regarding the temperature dependence of the self-diffusion constants D_α, $\alpha \in \{B, O\}$, in principle, an Arrhenius behavior can be observed (see equation (4.4)). However, the slope of the exponential decrease of $D_\alpha(T)$ with respect to $1/T$ significantly decreases at temperatures below about 1800 K, leading to a different activation energy $E_{A,\alpha}$, $\alpha \in \{B, O\}$, at low than at high temperatures. So far, this behavior is not clearly understood. It could be connected to a different diffusion mechanism at low temperatures. Finally, glass structures are generated in different ways, namely by quenches from the melt with classical MD and ab initio

MD simulations with a subsequent structural relaxation with quantum mechanical forces. The main improvement of the glass structures, generated by the new 3-body potentials, are a slightly smaller B-B distance and the occurrence of some boroxol rings, compared to the ones generated by the original parameter set before the structural fit. However, the boroxol ring fraction is still small ($f = 2.5 \pm 1.1\%$ to $f = 8 \pm 2.3\%$). The ab initio quenches show slightly larger boroxol ring fractions of $f = 5 \pm 5\%$ (3600 K quench) and $f = 15 \pm 5\%$ (2300 K quench). Regarding the vibrational properties, the phonon densities of state, according to the quantum mechanical forces show an acceptable agreement with results from inelastic neutron scattering [30, 134]. However, the peak height of the peak, assigned to boroxol rings, is significantly lower than in case of an alternative model structure with a boroxol ring fraction of $f = 75\%$. The vibrational spectra, according to the classical forces of the new 3-body potentials, show an acceptable agreement with experimental results, as well.

Chapter 7

Discussion and Conclusions

In this work, computer simulations of the model glass formers SiO_2 and B_2O_3 are carried out by means of classical molecular dynamics (MD) simulations with the LAMMPS software package [60, 61] and quantum mechanical calculations, based on density functional theory (DFT) with the VASP software package [77–79].

Regarding the model glass former SiO_2, the structural and dynamical properties of the liquid state are studied at different temperatures between 4300 K and 2700 K by classical MD simulations (see section 4.1). First, different system sizes of 114, 165, 256 and 1152 are compared at constant density of $\rho = 2.37\,\mathrm{g/cm^3}$, which is slightly larger than the experimental density of vitreous SiO_2 of $\rho = 2.2\,\mathrm{g/cm^3}$ [98] (see subsection 4.1.2). These studies are carried out using a slightly modified form of the BKS potential [22], leading to an overall smooth pair potential. As already reported in [104], the main finite size effect is a dynamical slowing down, visible the mean square displacements $\left\langle r_\alpha^2(t)\right\rangle$ and the incoherent intermediate scattering functions $F_{\mathrm{S},\alpha}(k,t)$. Regarding the structural quantities, nearly no dependence on the system size is found in the static structure factors $S_{\alpha\beta}(k)$, pair correlation functions $g_{\alpha\beta}(r)$ and angular distributions $p_{\alpha\beta\gamma}(\Phi)$ ($\alpha,\beta,\gamma \in \{Si,O\}$). The distribution of ring sizes shows a reduced probability $p_{Si}(n)$ for rings of size $n > 6$ in the small system sizes. Finite size effects are significantly larger for the 114 atom than for the 165 atom system, justifying the choice of the latter system size in the following considerations. In subsection 4.1.3, the structural and dynamical properties of the BKS [22] and the CHIK [43] potential are compared to each other for the system size of 165 atoms, again, in the temperature range between 4300 K and 2700 K. Here, simulations are carried out at $\rho = 2.2\,\mathrm{g/cm^3}$. In agreement to [43], the structural relaxation times τ_α of the CHIK potential are about $3-10$ times shorter at the same temperature than in case of the BKS potential. Regarding the structural quantities $S_{\alpha\beta}(k)$, $g_{\alpha\beta}(r)$ and $p_{\alpha\beta\gamma}(\Phi)$, the peak heights of the CHIK potential are slightly lower and the mean Si-O-Si angles are slightly smaller by approximately $2^\circ - 3^\circ$ at all examined temperatures. This is in agreement with [43]. The activation energies $E_{\mathrm{A},\alpha}$, $\alpha \in \{Si,O\}$, are determined by means of the temperature dependence of the self-diffusion constants D_α. In case of the BKS potential, they are about 1.9 eV (Si) to 1.6 eV (O) larger than the ones reported in [42] for simulations of 8016 atoms at $\rho = 2.37\,\mathrm{g/cm^3}$ and about 1.4 eV (O)

larger than the ones reported in [107, 108] for simulations of 99 atoms at $\rho = 2.30\,\mathrm{g/cm^3}$. These differences can be understood in terms of effects of the system size and the system density, as the activation energies increase with decreasing system size and decreasing system density. In case of the CHIK potential, the activation energies are approximately 0.8 eV (Si) to 0.9 eV (O) larger than the ones reported in [43] for simulations of 1152 atoms at $\rho = 2.2\,\mathrm{g/cm^3}$. Here, the differences are due to the different system sizes.

In section 4.2, glass structures are generated by quenches from the melt from 4300 K to 0 K with a cooling rate of $\Gamma = 1 \cdot 10^{11}\,K/s$. The BKS and CHIK potential are employed and the glass configurations at 0 K are structurally relaxed in terms of a quantum mechanical DFT calculation. The main effect of the structural relaxation, in both cases, is the decrease of the mean Si-O-Si angle by about $4° - 6°$, in agreement with [10]. After the structural relaxation, no significant differences are visible in the glass structures generated with the BKS potential and the CHIK potential. These glass structures are compared to the one of a full ab initio quench from the melt from 3600 K to 0 K with $\Gamma = 1.\overline{6} \cdot 10^{14}\,K/s$. A good agreement is observed. However, the latter shows a slightly smaller mean Si-O-Si angle by approximately $2° - 3°$. All mean first neighbor distances and mean angles of the different glass structures are in good agreement with experimental results of neutron and X-ray scattering [113, 114]. This aspect has not been investigated so far for the CHIK potential. The mean total energies per atom of the glass structures generated with the BKS and the CHIK potential are comparable ($E_0/N = -8.1811 \pm 0.\,0.0016$ eV and $E_0/N = -8.1778 \pm 0.\,0.0010$ eV) and slightly lower than the value of the full ab initio quench ($E_0/N = -8.1663$ eV). In section 4.3, the vibrational properties are calculated using the so-called "frozen phonon" method, based on the harmonic approximation. All vibrational spectra, according to the DFT forces, show excellent accordance with experimental results from inelastic neutron scattering [99, 100], in agreement with [11, 28, 119, 120]. The accordance with experimental results is clearly improved, compared to the classical forces. Also the specific heat $C_V(T)$ shows a significantly improved agreement with the experimental curve at constant pressure [123] in the DFT case, compared to both classical force fields.

In chapter 5, the thermal expansion of vitreous silica is calculated, based on the vibrational properties of glass structures, generated in section 4.2, at different system densities. The applied method is the so-called quasi-harmonic approximation [125]. It is based on the dependence of the Helmholtz free energy $F(T, V)$ on the volume of the system, due to the volume dependence of the eigenfrequencies $\nu_n(\mathbf{k}; V)$. The calculated curves of the linear expansion coefficients $\alpha_L(T)$ show the striking result of a change of sign in $\alpha_L(T)$ and a temperature range of negative thermal expansion, both, using quantum mechanical and classical forces for all but one examined glass configuration. To my knowledge this has not been reported before. The temperature range of negative thermal expansion is below approximately 140 K to 160 K, in case of the DFT forces. In fact, the DFT curves are in good agreement with experimental results [32, 33] at temperatures below approximately 200 K. At higher temperatures, however, the calculated curves of $\alpha_L(T)$ are significantly higher than the experimental ones. The linear expansion coefficients, according to the classical forces of the BKS and the CHIK potential, show a negative sign at temperatures below about 290 K to 325 K. Here, the agreement with experimental results is less pronounced, as

in case of the DFT forces. The change of sign in the linear thermal expansion coefficient $\alpha_L(T)$, in all cases, can be explained in terms of negative microscopic mode Grüneisen parameters γ_n at low eigenfrequencies.

In chapter 6, the model glass former B_2O_3 is studied. In vitreous B_2O_3, about $60\% - 80\%$ of the boron atoms are localized within 3-membered boroxol rings (see section 6.1). A 3-membered ring is called boroxol ring when the participating boron atoms are all 3-fold coordinated with respect to the oxygen atoms and the oxygen atoms are all 2-fold coordinated with respect to the boron atoms [31]. Therefore, these 3-membered rings are of special interest in the study of B_2O_3. First, the structural and dynamical properties of liquid B_2O_3 are studied by means of ab initio Born-Oppenheimer MD simulations of a 150 atom system in a temperature range between 3600 K and 2300 K at the experimental glass density of $\rho = 1.83\,\mathrm{g/cm^3}$ [159] (see section 6.2). Regarding the dynamical properties, the structural relaxation time increases by about the factor 30 from 3600 K to 2300 K. The pair correlation functions $g_{\alpha\beta}(r)$ at 2500 K are compared to the ones in [162] at a system density of $1.92\,\mathrm{g/cm^3}$, showing an acceptable agreement. In principle, $p_B(n=3)$ decreases with decreasing temperature. However, at 2300 K, the probability $p_B(n=3)$ starts to increase again, reflecting the emergence of new 3-membered rings.

In section 6.3, a set of new force field parameters is obtained by means of a structural fit to $g_{\alpha\beta}(r)$ and $p_{\alpha\beta\gamma}(\Phi)$ of the ab initio MD trajectory at 2300 K. Here, the structural fitting routine of A. Carré is applied [43, 51], extended in terms of including the relevant angular distributions $p_{\alpha\beta\gamma}(\Phi)$ into the fitting procedure. Starting with the parameter set of the force field of C. R. Trott [97], the agreement of the structural quantities of the MD simulation with the ones of the ab initio MD trajectory can be significantly improved. One effect, is the reduction of the partial charge of the boron atom to approximately $q_B = 1\,\mathrm{e}$, in all cases. The best agreement is obtained in the case of including 3-body angular interactions for the O-B-O and the B-O-B angles, in addition to the pair potential of a slightly modified form of the Buckingham type [94] with Coulomb interactions. In this course, a new angular potential type is introduced, namely an inverse Gaussian potential that is smoothly switched on and off, depending on the inter-atomic distances. It is implemented into a new LAMMPS pair style, called "gauss/smooth". This leads to an overall smooth interaction potential. The main improvement of the additional angular terms is a reduction of the mean B-B distance and mean B-O-B angle. Trials of the structural fitting procedure at 3600 K lead to inferior results.

In section 6.4, the static and dynamic properties of the two parameter sets with angular interactions are calculated in a temperature range between 3600 K and 800 K. In one case, the O-O interaction is purely repulsive ($C_{OO} = 0\,\mathrm{eV\,\AA^6}$). The results of 150 atom simulations at constant experimental glass density $\rho = 1.83\,\mathrm{g/cm^3}$ [159] are compared to the ones of the ab initio MD simulations, in the temperature range the latter can still be equilibrated, namely between 3600 K and 2300 K. In general, the agreement is acceptable. The main differences are the $2-10$ times shorter α-relaxation times τ_α and the reduced peak heights in case of the classical MD simulations. In contrast to the ab initio MD simulations, the probability for a B atom to be in a 3-membered ring $p_B(n=3)$ is smaller than $p_B(n=3)$ in the classical MD simulations. In

addition, NpT MD simulations at $p = 0$ external pressure are carried out for a system size of 1200 atoms, where finite size effects play a less significant role. Here, distinct differences between the two different parameter sets are visible. The parameter set with $C_{OO} = 0\,\text{eV}\,\text{Å}^6$ shows a significantly too low system density of approximately $\bar{\rho} = 1.280 \pm 0.024 \text{g/cm}^3$ at 1000 K. The corresponding value of the potential with $C_{OO} \neq 0\,\text{eV}\,\text{Å}^6$ is about $\bar{\rho} = 1.892 \pm 0.005 \text{g/cm}^3$ at 1000 K. This is in quite good agreement with the experimental glass density of $\rho = 1.83\,\text{g/cm}^3$ [159]. Regarding the dynamical properties, at high temperatures, the structural relaxation times of the 1200 atom simulations are significantly lower than the ones of the 150 atom simulations, in both cases. The same holds for all other examined temperatures, in case of the potential with $C_{OO} \neq 0\,\text{eV}\,\text{Å}^6$. This is due to finite size effects. In the case of $C_{OO} = 0\,\text{eV}\,\text{Å}^6$, τ_α is over an order of magnitude larger for the 1200 than for the 150 atom system at 1000 K. This can be explained in terms of the significantly lower system density of the 1200 simulation at this temperature. Regarding the structural properties, the most significant difference between the large and the small systems is seen in the distribution of ring sizes. The distribution is much broader in case of 1200 atom simulations and the 150 atom simulations show a lack of ring sizes with $n \geq 10$, in both cases. As in case of SiO_2, the temperature dependence of the self-diffusion constants D_α is studied, in all cases. Here, the slope of the exponential decrease of $D_\alpha(T)$, $\alpha \in \{B, O\}$, with respect to $1/T$ significantly decreases at temperatures below approximately 1800 K, leading to different activation energies $E_{\text{A},\alpha}$, $\alpha \in \{B, O\}$ at low than at high temperatures. So far, this behavior is not clearly understood. It could be connected to a different diffusion mechanism at low temperatures. To exclude effects of insufficient equilibration, in case of the 150 atom systems, additional equilibration runs are carried out at 1200 K and 1000 K with significant longer equilibration times. The activation energies at low temperatures are between $E_{\text{A},B} \simeq 0.74 \pm 0.02\text{eV}$ and $E_{\text{A},B} \simeq 1.10 \pm 0.03\text{eV}$ and $E_{\text{A},O} \simeq 0.75 \pm 0.01\text{eV}$ and $E_{\text{A},O} \simeq 1.07 \pm 0.02\text{eV}$. The respective values at high temperatures are between $E_{\text{A},B} \simeq 1.28 \pm 0.01\text{eV}$ and $E_{\text{A},B} \simeq 1.31 \pm 0.02\text{eV}$ and $E_{\text{A},O} \simeq 1.23 \pm 0.02\text{eV}$ and $E_{\text{A},O} \simeq 1.28 \pm 0.02\text{eV}$ for the classical potentials, compared to the values of $E_{\text{A},B} \simeq 1.87 \pm 0.16\text{eV}$ and $E_{\text{A},O} \simeq 2.18 \pm 0.19\text{eV}$, extracted from the ab initio MD runs.

In section 6.5, glass structures, generated by quenches from the melt with classical MD simulations and subsequent quantum mechanical relaxations, are compared to the ones, generated by pure ab initio quenches. In the first case, the quench rate is $\Gamma = 1 \cdot 10^{11}\,K/s$ and the starting temperatures of the quenches are 2300 K ($C_{OO} = 0\,\text{eV}\,\text{Å}^6$) and 800 K (both parameter sets). In addition, classical quenches from 3600 K are studied with the original parameter set before the structural fit. In the second case, the quench rate is $\Gamma = 1.\overline{6} \cdot 10^{14}\,\text{K/s}$ and the starting temperatures of the quenches are 3600 K and 2300 K. Regarding the different glass configurations, the mean first neighbor B-O and O-O distances show a very good agreement with experimental results [29], in all cases. In contrast to this, the mean B-B distances and the number of boroxol rings show significant differences between the different glass samples. In case of the original parameter set, all atoms show "ideal" coordination numbers. However, no boroxol rings are present in the structures and the mean B-B distance is significantly larger by about 0.06 Å than in all other cases. In case of the 3-body potentials after the structural fit, between 4% and 7% of the

boron atoms are overcoordinated with respect to B atoms and approximately 3% and 4% of the B atoms are overcoordinated with respect to O atoms, after the structural relaxation. However, the mean first neighbor B-B distances show an acceptable agreement with experimental results [29] for the B atoms, not located in boroxol rings. These glass structures have a boroxol ring fraction of approximately $f = 2.5 \pm 1.1\%$ to $f = 8 \pm 2.3\%$, which is significantly lower than the experimentally predicted value of about $f = 60\%$ to $f = 80\%$. In case of the glass structures generated by means of ab initio MD simulations, the corresponding values are $f = 5 \pm 5\%$ (3600 K quench) and $f = 15 \pm 5\%$ (2300 K quench) and the mean first neighbor distances show an acceptable agreement with experimental results, as well. Here, the first neighbor peak in $g_{BB}(r)$ shows clearly a second maximum attributed to B atoms within a boroxol ring. As in case of SiO_2, the mean total energies per atom of the different glass structures are studied. Regarding the classical quenches and subsequent structural relaxations, the values are of comparable size in all cases, namely between $E_0/N = -8.2956 \pm 0.\,0.0011$ eV and $E_0/N = -8.2932 \pm 0.\,0.0019$ eV. An explanation is that the energetic cost of defects (overcoordinated atoms in case of the 3-body potentials) in average cancels out the energetic gain of the improved mean B-B distances and the existence of boroxol rings, with respect to the original parameter set [97]. Comparing the 4 different full ab initio quenches, the energies per atom are in a range between $E_0/N = -8.3047$ eV one (2300 K quench with 4 boroxol rings) and $E_0/N = -8.2833$ eV (one 3600 K quench with 0 boroxol rings). These value (regarding the total energy of the whole 150 atom systems, namely $E_0/N \cdot 150$) fit to the average energetic gain per boroxol ring of about 0.2862 ± 0.0430 eV [133], in addition to the defect energy of two edge-sharing BO_3 triangles in the one 3600 K quench without boroxol rings.

In section 6.6, the vibrational properties of the glass structures are examined in terms of classical and DFT forces, again using the so-called "frozen phonon" method. Regarding the 3-body potentials after the structural fit, the classical spectra show an improved agreement to quantum mechanical spectra, compared to the one, according to the classical forces of the original parameter set [97]. Overall, the agreement of the quantum mechanical spectra with results from inelastic neutron scattering [30, 134] is acceptable. Also the boroxol ring signature is visible for all glass structures containing boroxol rings. The corresponding sharp peak is shifted to slightly lower frequencies as in the experimental curves (23.2 to 23.4 THz in contrast to 24.2 THz). However, the peak heights of the boroxol ring signatures are significantly lower as in case of the alternative model structure with $f = 0.75$. In addition, the specific heat $C_V(T)$ shows good agreement with the experimental curve at constant pressure [167]. In contrast to SiO_2, the agreement, according to the DFT forces, is comparable to the one, according to the classical forces of the new 3-body potentials after the structural fit.

Summarizing the above results, it is possible to generate glass structures by quenches from the melt with classical MD simulations and a subsequent quantum mechanical relaxation that are comparable to the ones generated by quenches from the melt with ab initio MD calculations. The requirement is to employ a classical force field that leads to glass structures which are close to the ones obtained from pure ab initio quenches. No general statement can be given, which method leads to a glass structure that is in better agreement with the "real" one obtained by a

quench from the melt in a laboratory experiment. On the one hand, in case of the classical MD simulations, the system can be equilibrated at lower temperatures and slower quench rates by about 3 - 4 orders of magnitude are possible. On the other hand, in ab initio MD simulations the inter-atomic forces are described much more realistically. In case of the model glass former SiO_2, both methods lead to comparable results. Regarding the mean total energy per atom, the MD quenches lead to a slightly lower value after the structural relaxation. In case of the model glass former B_2O_3, the best results with the lowest energies per atom (and also containing the largest amount of boroxol rings) are obtained by full ab initio quenches from 2300 K. In case of the glass structures after the classical quench and the structural relaxation, the accordance of the mean B-B distances and B-O-B angles is improved applying new force field parameters, including 3-body terms. Regarding the significantly improved agreement of the structural and dynamical properties of liquid B_2O_3 with ab initio MD results, the structural differences of the generated glass structures are less than expected, compared to the original parameter set [97]. This is reflected in nearly identical mean total energies per atom. The existence of boroxol rings in the glass structures generated with the new parameter sets goes along with approximately 2% to 3% overcoordinated B atoms with respect to the next nearest O atoms. In principle, the structure matching scheme according to a liquid ab initio MD trajectory, developed by A. Carré [43] for the model glass former SiO_2, is proven to be successfully also in case of the model glass former B_2O_3. In the latter case (at least) angular terms have to be included. The perspective is to apply this fitting scheme to more complicated systems as alkaline borate or alkaline borosilicate glasses.

Appendix A

Calculation of forces for new 3-body interaction term

Here, the differentiation of the total smooth potential $V_{ijk}^{\text{smooth}} = V_{ijk}(\Phi)^{\text{Gauss}}\, G(\bar{r}_{ijk})$ (see equation (6.2) in combination with equations (6.1), (6.3) and (6.4)) is carried out with respect to the atomic coordinates of the three atoms forming an angle: $\mathbf{r}_i$, $\mathbf{r}_j$ and $\mathbf{r}_i$. Due to Newton's third theorem, the force on atom j, $\mathbf{F}_j$ is equal to:

$$\mathbf{F}_j = -\mathbf{F}_i - \mathbf{F}_k. \tag{A.1}$$

Therefore, it is sufficient to calculate the forces on atoms i and k:

$$\mathbf{F}_i = \left[-\nabla_{\mathbf{r}_i} V_{ijk}(\Phi)\right] G(\bar{r}_{ijk}) - V_{ijk}(\Phi)\left[\nabla_{\mathbf{r}_i} G(\bar{r}_{ijk})\right] \tag{A.2}$$

$$\text{and} \quad \mathbf{F}_k = \left[-\nabla_{\mathbf{r}_k} V_{ijk}(\Phi)\right] G(\bar{r}_{ijk}) - V_{ijk}(\Phi)\left[\nabla_{\mathbf{r}_k} G(\bar{r}_{ijk})\right]. \tag{A.3}$$

Using the notation

$$\mathbf{r}_{ij} = \mathbf{r}_i - \mathbf{r}_j, \quad \mathbf{r}_{kj} = \mathbf{r}_k - \mathbf{r}_j, \quad r_{ij} = |\mathbf{r}_{ij}|, \quad r_{kj} = |\mathbf{r}_{kj}|, \tag{A.4}$$

the cosine of the angle formed by the atoms i, j and k can be expressed as

$$\cos\left[\Phi(\mathbf{r}_i, \mathbf{r}_j, \mathbf{r}_k)\right] = \frac{\mathbf{r}_{ij} \cdot \mathbf{r}_{kj}}{r_{ij}\, r_{kj}}. \tag{A.5}$$

With

$$\nabla_{\mathbf{r}_{i,k}} \cos\left[\Phi(\mathbf{r}_i, \mathbf{r}_j, \mathbf{r}_k)\right] = -\sin\left[\Phi(\mathbf{r}_i, \mathbf{r}_j, \mathbf{r}_k)\right] \nabla_{\mathbf{r}_{i,k}} \Phi(\mathbf{r}_i, \mathbf{r}_j, \mathbf{r}_k), \tag{A.6}$$

the derivative of the angle Φ with respect to the coordinates $\mathbf{r}_i$ and $\mathbf{r}_i$ can be written as:

$$\nabla_{\mathbf{r}_{i,k}} \Phi(\mathbf{r}_i, \mathbf{r}_j, \mathbf{r}_k) = -\frac{1}{\sin\left[\Phi(\mathbf{r}_i, \mathbf{r}_j, \mathbf{r}_k)\right]} \nabla_{\mathbf{r}_{i,k}} \frac{\mathbf{r}_{ij} \cdot \mathbf{r}_{kj}}{r_{ij}\, r_{kj}}. \tag{A.7}$$

The last term in equation (A.7) is evaluated exemplarily for atom i as:

$$\frac{\partial}{\partial \mathbf{r}_{i,\alpha}} \frac{\mathbf{r}_{ij} \cdot \mathbf{r}_{kj}}{r_{ij}\, r_{kj}} = \left(\frac{\partial}{\partial \mathbf{r}_{i,\alpha}} \frac{\mathbf{r}_{ij}}{r_{ij}} \right) \cdot \frac{\mathbf{r}_{kj}}{r_{kj}} = \left(\frac{\hat{\mathbf{e}}_\alpha}{r_{ij}} + \mathbf{r}_{ij} \frac{-\mathbf{r}_{ij,\alpha}}{r_{ij}\, r_{ij}^2} \right) \cdot \frac{\mathbf{r}_{kj}}{r_{kj}} \tag{A.8}$$

$$\Leftrightarrow \frac{\partial}{\partial \mathbf{r}_{i,\alpha}} \frac{\mathbf{r}_{ij} \cdot \mathbf{r}_{kj}}{r_{ij}\, r_{kj}} = \frac{\mathbf{r}_{kj,\alpha}}{r_{ij}\, r_{kj}} - \cos\left[\Phi\right] \frac{\mathbf{r}_{ij,\alpha}}{r_{ij}^2}. \tag{A.9}$$

The evaluation for atom k leads to the same results, exchanging i with k. Finally, the derivative of the angle $\Phi\left(\mathbf{r}_i, \mathbf{r}_j, \mathbf{r}_k\right)$ with respect to $\mathbf{r}_i$ and $\mathbf{r}_k$ can be written as:

$$\nabla_{\mathbf{r}_i} \Phi\left(\mathbf{r}_i, \mathbf{r}_j, \mathbf{r}_k\right) = -\frac{1}{\sin\left[\Phi\left(\mathbf{r}_i, \mathbf{r}_j, \mathbf{r}_k\right)\right]} \left(\frac{\mathbf{r}_k - \mathbf{r}_j}{r_{ij}\, r_{kj}} - \cos\left[\Phi\left(\mathbf{r}_i, \mathbf{r}_j, \mathbf{r}_k\right)\right] \frac{\mathbf{r}_i - \mathbf{r}_j}{r_{ij}^2} \right) \tag{A.10}$$

$$\text{and} \quad \nabla_{\mathbf{r}_k} \Phi\left(\mathbf{r}_i, \mathbf{r}_j, \mathbf{r}_k\right) = -\frac{1}{\sin\left[\Phi\left(\mathbf{r}_i, \mathbf{r}_j, \mathbf{r}_k\right)\right]} \left(\frac{\mathbf{r}_i - \mathbf{r}_j}{r_{ij}\, r_{kj}} - \cos\left[\Phi\left(\mathbf{r}_i, \mathbf{r}_j, \mathbf{r}_k\right)\right] \frac{\mathbf{r}_k - \mathbf{r}_j}{r_{kj}^2} \right). \tag{A.11}$$

The derivative of the angular potential of the inverse gaussian form (see equation (6.1)) with respect to the angle Φ can be written as:

$$\frac{\partial}{\partial \Phi} V_{ijk}^{\text{Gauss}}\left(\Phi\right) = 2\, K_{ijk}\, \sigma_{ijk}\, \left(\Phi - \Phi_{0,ijk}\right) \exp\left[-\sigma_{ijk}\, \left(\Phi - \Phi_{0,ijk}\right)^2\right]. \tag{A.12}$$

Finally, the derivative of the smoothing function $G\left(\bar{r}_{ijk}\right)$ (see equations (6.2) and (6.3)) with respect to the atom positions $\mathbf{r}_i$ and $\mathbf{r}_i$ can be decomposed into

$$\frac{\partial}{\partial \bar{r}_{ijk}} G\left(\bar{r}_{ijk}\right) = \frac{2\, d^{\text{ang}}}{\left(\bar{r}_{ijk} - r_{\text{c}}^{\text{ang}}\right)^3} \exp\left[-\frac{d^{\text{ang}}}{\left(\bar{r}_{ijk} - r_{\text{c}}^{\text{ang}}\right)^2}\right] \tag{A.13}$$

and (see equation (6.4))

$$\frac{\partial \bar{r}_{ijk}}{\partial r_{ij}} \nabla_{\mathbf{r}_i} r_{ij} = r_{ij}^{(N-1)} \left(r_{ij}^N + r_{kj}^N\right)^{\left(\frac{1}{N}-1\right)} \frac{\mathbf{r}_i - \mathbf{r}_j}{r_{ij}}, \tag{A.14}$$

$$\frac{\partial \bar{r}_{ijk}}{\partial r_{kj}} \nabla_{\mathbf{r}_k} r_{kj} = r_{kj}^{(N-1)} \left(r_{ij}^N + r_{kj}^N\right)^{\left(\frac{1}{N}-1\right)} \frac{\mathbf{r}_k - \mathbf{r}_j}{r_{kj}}. \tag{A.15}$$

Combining equations (A.10), (A.11), (A.12), (A.13), (A.14) and (A.15), the total force acting on atom i and k due to the smoothed angular potential $V_{ijk}^{\text{smooth}}\left(\Phi\left(\mathbf{r}_i, \mathbf{r}_j, \mathbf{r}_k\right)\right)$ (see equation (6.2) in combination with equations (6.1), (6.3) and (6.4)) can be written as:

$$\begin{aligned}
\mathbf{F}_i = {} & 2\, K_{ijk}\, \sigma_{ijk}\, \left(\Phi - \Phi_{0,ijk}\right) \mathrm{e}^{-\sigma_{ijk}\left(\Phi - \Phi_{0,ijk}\right)^2} \frac{1}{\sin\left[\Phi\right]} \left(\frac{\mathbf{r}_k - \mathbf{r}_j}{r_{ij}\, r_{kj}} - \cos\left[\Phi\right] \frac{\mathbf{r}_i - \mathbf{r}_j}{r_{ij}^2} \right) \mathrm{e}^{-\frac{d^{\text{ang}}}{\left(\bar{r}_{ijk} - r_{\text{c}}^{\text{ang}}\right)^2}} \\
& + K_{ijk}\, \mathrm{e}^{-\sigma_{ijk}\left(\Phi - \Phi_{0,ijk}\right)^2} \frac{2\, d^{\text{ang}}}{\left(\bar{r}_{ijk} - r_{\text{c}}^{\text{ang}}\right)^3} \mathrm{e}^{-\frac{d^{\text{ang}}}{\left(\bar{r}_{ijk} - r_{\text{c}}^{\text{ang}}\right)^2}} r_{ij}^{(N-1)} \left(r_{ij}^N + r_{kj}^N\right)^{\left(\frac{1}{N}-1\right)} \frac{\mathbf{r}_i - \mathbf{r}_j}{r_{ij}}
\end{aligned} \tag{A.16}$$

and

$$\mathbf{F}_k = 2\,K_{ijk}\,\sigma_{ijk}\,\left(\Phi-\Phi_{0,ijk}\right)\,\mathrm{e}^{-\sigma_{ijk}\left(\Phi-\Phi_{0,ijk}\right)^2}\,\frac{1}{\sin\left[\Phi\right]}\,\left(\frac{\mathbf{r}_i-\mathbf{r}_j}{r_{ij}\,r_{kj}}-\cos\left[\Phi\right]\,\frac{\mathbf{r}_k-\mathbf{r}_j}{r_{kj}^2}\right)\,\mathrm{e}^{-\frac{d^{\mathrm{ang}}}{\left(\bar{r}_{ijk}-r_{\mathrm{c}}^{\mathrm{ang}}\right)^2}}$$
$$+\,K_{ijk}\,\mathrm{e}^{-\sigma_{ijk}\left(\Phi-\Phi_{0,ijk}\right)^2}\,\frac{2\,d^{\mathrm{ang}}}{\left(\bar{r}_{ijk}-r_{\mathrm{c}}^{\mathrm{ang}}\right)^3}\,\mathrm{e}^{-\frac{d^{\mathrm{ang}}}{\left(\bar{r}_{ijk}-r_{\mathrm{c}}^{\mathrm{ang}}\right)^2}}\,r_{kj}^{(N-1)}\,\left(r_{ij}^N+r_{kj}^N\right)^{\left(\frac{1}{N}-1\right)}\,\frac{\mathbf{r}_k-\mathbf{r}_j}{r_{kj}}. \tag{A.17}$$

Bibliography

[1] Schott & Genossen. Glastechnisches Laboratorium, Genossenschaft, in Jena. Verfahren zur Herstellung von Verbund-Hartglas. *Patent, Kaiserliches Patentamt*, April 5, 1891.

[2] Properties of DURAN® from DURAN Group GmbH [Online]. *http://www.duran-group.com/en/about-duran/duran-properties.html*, April 2, 2015.

[3] R. Brüning. On the glass transition in vitreous silica by differential thermal analysis measurements. *J. Non-Cryst. Solids*, 330:13–22, 2003.

[4] A. K. Varshneya. *Fundamentals of inorganic glasses*. The Society of Glass Technology, Sheffield, UK, 2nd edition, 2006.

[5] R. Brüning and K. Samwer. Glass transition on long time scales. *Phys. Rev. B*, 46:11318–11322, 1992.

[6] W. H. Zachariasen. The atomic arrangement in glass. *J. Am. Chem. Soc.*, 54:3841–3851, 1932.

[7] D. Frenkel and B. Smit. *Understanding molecular simulations*. Academic Press, Inc., San Diego, CA, USA, 2nd edition, 2002.

[8] K. Binder and D. W. Heermann. *Monte Carlo simulations in statistical physics*. Springer, Berlin, Heidelberg, DE, 5th edition, 2010.

[9] P. Hohenberg and W. Kohn. Inhomogeneous electron gas. *Phys. Rev.*, 136:B864–B871, 1964.

[10] M. Benoit, S. Ispas, P. Jund, and R. Jullien. Model of silica glass from combined classical and ab initio molecular-dynamics simulations. *Eur. Phys. J. B*, 13:631–636, 2000.

[11] M. Benoit and W. Kob. The vibrational dynamics of vitreous silica: Classical force fields vs. first principles. *Europhys. Lett.*, 60:269–275, 2002.

[12] C. A. Angell. Formation of glasses from liquids and biopolymers. *Science*, 267:1924–1935, 1995.

[13] L. Berthier and G. Biroli. Theoretical perspective on the glass transition and amorphous materials. *Rev. Mod. Phys.*, 83:587–645, 2011.

[14] D. Sidebottom, R. Bergman, L. Börjesson, and L. M. Torell. Two-step relaxation decay in a strong glass former. *Phys. Rev. Lett.*, 71:2260–2263, 1993.

[15] K. Binder and W. Kob. *Glassy materials and disordered solids: An introduction to their statistical mechanics.* World Scientific, Singapore, 1st edition, 2005.

[16] J. E. Shelby. *Introduction to glass science and technology.* The Royal Society of Chemistry, Cambridge, UK, 2nd edition, 2005.

[17] T. V. Tropin, J W. P. Schmelzer, and C. Schick. On the dependence of the properties of glasses on cooling and heating rates II: Prigogine–Defay ratio, fictive temperature and fictive pressure. *J. Non-Cryst. Solids*, 357:1303–1309, 2011.

[18] C. T. Moynihan and et. al. Structural relaxation in vitreous materials. *Ann. N.Y. Acad. Sci.*, 279:15–35, 1976.

[19] C. B. Carter and M. G. Norton. *Ceramic materials.* Springer, Berlin, Heidelberg, DE, 1st edition, 2007.

[20] K. Vollmayr, W. Kob, and K. Binder. Cooling-rate effects in amorphous silica: A computer-simulation study. *Phys. Rev. B*, 54:15808–15827, 1996.

[21] A. Takada and A. N. Cormack. Computer simulation models of glass structure. *Phys. Chem. Glasses: Eur. J. Glass Sci. Technol. B*, 49:127–135, 2008.

[22] B. W. H. van Beest, G. J. Kramer, and R. A. van Santen. Force fields for silicas and aluminophosphates based on ab initio calculations. *Phys. Rev. Lett.*, 64:1955–1958, 1990.

[23] W. Kauzmann. The nature of the glassy state and the behavior of liquids at low temperatures. *Chem. Rev.*, 43:219–256, 1948.

[24] W. Götze. *Complex dynamics of glass-forming liquids: A mode-coupling theory.* Oxford University Press, Oxford, UK, 1st edition, 2009.

[25] F. L. Galeener. Planar rings in glasses. *Solid State Commun.*, 44:1037–1040, 1982.

[26] F. L. Galeener, G. Lucovsky, and J. C. Mikkelsen Jr. Vibrational spectra and the structure of pure vitreous B_2O_3. *Phys. Rev. B*, 22:3983–3990, 1980.

[27] F. L. Galeener, R. A. Barrio, E. Martinez, and R. J. Elliot. Vibrational decoupling of rings in amorphous solids. *Phys. Rev. Lett.*, 53:2429–2432, 1984.

[28] A. Rahmani, M. Benoit, and C. Benoit. Signature of small rings in the Raman spectra of normal and compressed amorphous silica: A combined classical and ab initio study. *Phys. Rev. B*, 68:184202, 2003.

[29] A. C. Hannon, D. I. Grimley, R. A. Hulme, A. C. Wright, and R. N. Sinclair. Boroxol groups in vitreous boron oxide: new evidence from neutron diffraction and inelastic neutron scattering studies. *J. Non-Cryst. Solids*, 177:299–316, 1994.

[30] R. N. Sinclair, C. E. Stone, A. C. Wright, I. G. Polyakova, N. M. Vedishcheva, B. A. Shakhmatkin, S. A. Feller, B. C. Johanson, P. Venhuizen, R. B. Williams, and A. C. Hannon. Inelastic neutron scattering studies of superstructural units in borate glasses and crystalline phases. *Phys. Chem. Glasses*, 41:286–289, 2000.

[31] J. Goubeau and H. Keller. Raman-Spektren und Struktur von Boroxol-Verbindungen. *Z. anorg. allg. Chem.*, 272:303–312, 1953.

[32] W. P. Reed. Standard Reference Material 739. Fused-silica thermal expansion. Revision of certificate dated 5-12-71. *National Institute of Standards and technology, Gaithersburg, MD*, 20899, 1991.

[33] G. K. White. Thermal expansion of reference materials: copper, silica and silicon. *J. Phys. D: Appl. Phys.*, 6:2070–2078, 1973.

[34] C. A. Angell and H. Kanno. Density maxima in high-pressure supercooled water and liquid silicon dioxide. *Science*, 193:1121–1122, 1976.

[35] J. Kieffer. Understanding the anomalous behaviours of B_2O_3 glass. *Phys. Chem. Glasses: Eur. J. Glass Sci. Technol. B*, 50:294–300, 2009.

[36] A. K. Hassan, L. M. Torell, L. Börjesson, and H. Doweidar. Structural changes of B_2O_3 through the liquid-glass transition range: A Raman-scattering study. *Phys. Rev. B*, 45:12797–12805, 1992.

[37] R. E. Youngman, J. Kieffer, J. D. Bass, and L. Duffrene. Extended sturcutral integriy in network glasses and liquids. *J. Non-Cryst. Solids*, 222:190–198, 1997.

[38] L. Huang and J. Kieffer. Amorphous-amorphous transitions in silica glass. I. Reversible transitions and thermomechanical anomalies. *Phys. Rev. B*, 69:224203, 2004.

[39] R. J. Bell and P. Dean. The stucture of vitreous silica: Validity of the random network theory. *Philos. Mag.*, 25:1381–1398, 1972.

[40] M. P. Allen and D. J. Tildesley. *Computer simulation of liquids*. Oxford Science Publications, Oxford, UK, 1st edition, 1999.

[41] M. Born and B. Oppenheimer. Zur Quantentheorie der Molekeln. *Ann.Phys.*, 84:457–484, 1927.

[42] J. Horbach and W. Kob. Static and dynamic properties of viscious silica melt. *Phys. Rev. B*, 60:3169–3181, 1999.

[43] A. Carré, J. Horbach, S. Ispas, and W. Kob. New fitting scheme to obtain effective potential from Car-Parrinello molecular-dynamics simulations: Application to silica. *Europhys. Lett.*, 82:17001, 2008.

[44] A. Takada, C. R. A. Catlow, and G. D.. Price. Computer modelling of B_2O_3. I. New interatomic potentials, crystalline phases and predicted polymorphs. *J. Phys.: Condens. Matter*, 7:8659–8693, 1995.

[45] A. Takada, C. R. A. Catlow, and G. D.. Price. Computer modelling of B_2O_3. II. Molecular dynamics simulations of vitreous structures. *J. Phys.: Condens. Matter*, 7:8693–8722, 1995.

[46] R. Fernández-Perea, F. J. Bermejo, and M. L. Senent. Importance of rings on the microscopic properties of a strong glass. *Phys. Rev. B*, 54:6039–6042, 1996.

[47] E. Kashchieva, B. Shivachev, and Y. Dimitriev. Molecular dynamics studies of vitreous boron oxide. *J. Non-Cryst. Solids*, 351:1158–1161, 2005.

[48] L. Huang and J. Kieffer. Thermomechanical anomalies and polyamorphism in B_2O_3 glass: A molecular dynamics simulation study. *Phys. Rev. B*, 74:224107, 2006.

[49] J. K. Maranas, Y. Chen, D. K. Stillinger, and F. H. Stillinger. Polarization interactions and boroxol ring formation in boron oxide: A molecular dynamics study. *J. Chem. Phys.*, 115:6578–6589, 2001.

[50] A. Zeidler, K. Wezka, D. A. J. Whittaker, P. S. Salmon, A. Baroni, S. Klotz, H. E. Fischer, M. C. Wilding, C. L. Bull, M. G. Tucker, M. Salanne, G. Ferlat, and M. Micoulaut. Density-driven structural transformations in B_2O_3 glass. *Phys. Rev. B*, 90:024206, 2014.

[51] A. Carré. *Development of empirical potentials for amorphous silica.* PhD thesis, Johannes Gutenberg-Universität Mainz, 2007.

[52] David P. Landau and K. Binder. *A Guide to Monte Carlo simulations in statistical physics.* Cambridge University Press, Cambride, UK, 1st edition, 2002.

[53] L. Verlet. Computer "experiments" on classical fluids. I. Thermodynamical properties of Lennard-Jones molecules. *Phys. Rev.*, 159:98–103, 1967.

[54] W. C. Swope, H. C. Andersen, P. H. Berens, and K. R. Wilson. A computer simulation method for the calculation of equilibrium constants for the formation of physical clusters of molecules: Application to small water clusters. *J. Chem. Phys.*, 76:637–649, 1982.

[55] B. Leimkuhler. *Simulating Hamiltonian dynamics.* Cambridge University Press, Cambride, UK, 1st edition, 2005.

[56] P. P. Ewald. Die Berechnung optischer und elektrostatischer Gitterpotentiale. *Ann.Phys.*, 64:253–287, 1921.

[57] A. Winkler. *Molekulardynamik-Untersuchungen zur atomistischen Struktur und Dynamik von binären Mischgläsern $(Na_2O)(x \cdot SiO_2)$ und $(Al_2O_3)(2 \cdot SiO_2)$.* PhD thesis, Johannes Gutenberg-Universität Mainz, 2002.

[58] J. J. Benedetto and G. Zimmermann. Sampling multipliers and the poisson summation formula. *J. Fourier Anal. Appl.*, 3:505–523, 1997.

[59] M. Abramowitz and I. A. Stegun. *Handbook of mathematical functions.* Dover Publications, New York, NY, USA, 9th Dover print, 1970.

[60] Large-scale Atomic/Molecular Massively Parallel Simulator (LAMMPS) [Online]. *http://lammps.sandia.gov/*, April 2, 2015.

[61] S. J. Plimpton. Fast parallel algorithms for short-range molecular dynamics. *J. Comput. Phys.*, 117:1–19, 1995.

[62] Message Passing Interface Forum. *MPI: A Message-Passing Interface Standard, Version 3.0.* Höchstleistunsrechenzentrum Stuttgart, HLRS, Stuttart, DE, 2012.

[63] J. Honerkamp. *Statistical Physics: An advanced approach with applications.* Springer, Berlin, Heidelberg, DE, 2nd edition, 2002.

[64] S. Nosé. A unified formulation of the constant temperature molecular dynamics methods. *J. Chem. Phys.*, 81:511–519, 1984.

[65] H. Okumura. Nosé Thermostat and Nosé-Hoover Thermostat [Online]. *University Lecture, Rutgers University, New Jersey, USA, http://www.biomaps.rutgers.edu/nose_hoover_notes.pdf*, 2008, website from April 2, 2015.

[66] W. G. Hoover. Canonical dynamics: Equilibrium phase-space distributions. *Phys. Rev. A*, 31:1695–1697, 1985.

[67] G. J. Martyna, D. J. Klein, and M. L. Klein. Constant pressure molecular dynamics algorithms. *J. Chem. Phys.*, 101:4177–4189, 1994.

[68] W. Shinoda, M. Shiga, and M. Mikami. Rapid estimation of elastic constants by molecular dynamics simulation under constant stress. *Phys. Rev. B*, 69:134103, 2004.

[69] M. Parrinello and A. Rahman. Polymorphic transitions in single crystals: A new molecular dynamics method. *J. Appl. Phys.*, 52:7182–7190, 1981.

[70] K. Burke and L. O. Wagner. DFT in a nutshell. *Int. J. Quant. Chem.*, 113:96–101, 2013.

[71] V. Fock. Näherungsmethode zur Lösung des quantenmechanischen Mehrkörperproblems. *Z. Phys.*, 61:126–148, 1930.

[72] J. C. Slater. The theory of complex spectra. *Phys. Rev.*, 136:B864–B871, 1929.

[73] S. Rix. *Radiation-induced defects in calcium fluoride and their influence on material properties under 193 nm laser irradiation.* PhD thesis, Johannes Gutenberg-Universität Mainz, 2011.

[74] W. Kohn and L. J. Sham. Self-consistent equations including exchange and correlation effects. *Phys. Rev.*, 140:A1133–A1138, 1965.

[75] K. Burke. Perspective on density functional theory. *J. Chem. Phys.*, 136:150901, 2012.

[76] F. Bloch. Über die Quantenmechanik der Elektronen in Kristallgittern. *Z. Phys.*, 52:555–600, 1929.

[77] Vienna Ab-initio Simulation Package (VASP) [Online]. *http://www.vasp.at/, http://cms.mpi.univie.ac.at/vasp/vasp/*, April 2, 2015.

[78] G. Kresse and J. Furthmueller. Efficiency of ab-initio total energy calculations for metals and semiconductors using a plane-wave basis set. *Comp. Mater. Sci.*, 6:15–50, 1996.

[79] G. Kresse and J. Furthmueller. Efficient iterative schemes for ab initio total-energy calculations using a plane-wave basis set. *Phys. Rev. B*, 54:11169 – 11186, 1996.

[80] J. P. Perdew and Y. Wang. Accurate and simple analytic representation of the electron-gas correlation energy. *Phys. Rev. B*, 45:13244–13249, 1992.

[81] M. De La Pierre, R. Orlando, L. Maschio, K. Doll, P. Ugliengo, and R. Dovesi. Performance of six functionals (LDA, PBE, PBESOL, B3LYP, PBE0, and WC1LYP) in the simulation of vibrational and dielectric properties of crystalline compounds. The case of forsterite Mg_2SiO_4. *J. Comput. Chem.*, 32:1775–1784, 2011.

[82] J. P. Perdew, K. Burke, and M. Ernzerhof. Generalized gradient approximation made simple. *Phys. Rev. Lett.*, 77:3865–3868, 1996.

[83] J. P. Perdew, K. Burke, and M. Ernzerhof. Generalized gradient approximation made simple [Phys. Rev. Lett. 77, 3865 (1996)]. *Phys. Rev. Lett.*, 78:1396, 1997.

[84] J. P. Perdew, A. Ruzsinszky, G. I. Csonka, O. A. Vydrov, G. E. Scuseria, L. Constantin, X. Zhou, and K. Burke. Restoring the density-gradient expansion for exchange in solids and surfaces. *Phys. Rev. Lett.*, 100:136406, 2008.

[85] D. Vanderbilt. Soft self-consistent pseudopotentials in a generalized eigenvalue formalism. *Phys. Rev. B*, 41:7892–7895, 1990.

[86] P. E. Blöchl. Projector augmented-wave method. *Phys. Rev. B*, 50:17953–17979, 1994.

[87] G. Kresse and D. Joubert. From ultrasoft pseudopotentials to the projector augmented-wave method. *Phys. Rev. B*, 59:1758–1775, 1999.

[88] P. Ganster, M. Benoit, J.-M. Delay, and W. Kob. Structural and vibrational properties of a calcium aluminosilicate glass: classical force fields vs. first-principles. *Mol. Simulat.*, 33:1093–1103, 2007.

[89] National Institute of Standards and Technology (NIST), NIST center for neutron research [Online]. *www.ncnr.nist.gov/resources/n-lengths/elements*, April 2, 2015.

[90] Phonopy software package [Online]. *http://phonopy.sourceforge.net/*, April 4, 2015.

[91] A Togo, F Oba, and I Tanaka. First-principles calculations of the ferroelastic transition between rutile-type and $CaCl_2$-type SiO_2 at high pressures. *Phys. Rev. B*, 78:134106, 2008.

[92] M. Dove. *Introduction to lattice dynamics*. Cambridge University Press, Cambride, UK, 1st edition, 1993.

[93] J. Sólyom. *Fundamentals of the physics of solids. Volume 1 - structure and dynamics*. Springer, Berlin, Heidelberg, DE, 1st edition, 2007.

[94] R. A. Buckingham. The classical equation of state of gaseous helium, neon and argon. *Proc. R. Soc. Lond. A*, 168:264–283, 1938.

[95] J. E. Jones. On the determination of molecular fields. II. From the equation of state of a gas. *Proc. R. Soc. Lond. A*, 106:463–477, 1924.

[96] P. M. Morse. Diatomic molecules according to the wave mechanics. II. Vibrational levels. *Phys. Rev.*, 34:57–64, 1929.

[97] C. R. Trott. *$LAMMPS_{CUDA}$ - A new GPU accelerated molecular dynamics simulations pacakge and its application to ion-conducting glasses*. PhD thesis, Technische Universitaet Ilmenau, 2011.

[98] O. V. Mazurin, M. V. Streltsina, and T. P. Shvaiko-Shvaikovskaya. *Handbook of glass data, Part A. Silica glass and binary silicate glasses (physical sciences data)*, volume 15. Elsevier, Amsterdam, NL, 1983.

[99] J. M. Carpenter and D. L. Price. Correlated motions in glasses studied by coherent inelastic neutron scattering. *Phys. Rev. Lett.*, 54:441–443, 1985.

[100] U. Buchenau, M. Prager, N. Nuecker, A. J. Dianoux, N. Ahmad, and W. A. Phillips. Low-frequency modes in vitreous silica. *Phys. Rev. B*, 34:5665–5673, 1986.

[101] P. Deuflhard and A. Hohmann. *Numerische Mathematik: Eine algorithmisch orientierte Einführung*. de Gruyter, Berlin, DE, 1st edition, 1991.

[102] D. Wolff and W. G. Rudd. Tabulated potentials in molecular dynamics simulations. *Comput. Phys. Commun.*, 120:20–32, 1999.

[103] A. Saksaengwijit and A. Heuer. Finite-size effects in silica: a landscape perspective. *J. Phys.: Condens. Matter*, 19:205143, 2007.

[104] J. Horbach, W. Kob, K. Binder, and C. A. Angell. Finite size effects in simulations of glass dynamics. *Phys. Rev. E*, 54:R5897–R5900, 1996.

[105] J. Kärger, P. Heitjans, and R. Haberlandt. *Diffusion in condensed matter*. Vieweg, Braunschweig, Wiesbaden, DE, 1st edition, 1998.

[106] P. Young. Everything you wanted to know about data analysis and fitting but were afraid to ask. *arXiv:1210.3781v3 [physics.data-an]*, 2014.

[107] A. Saksaengwijit, J. Reinisch, and A. Heuer. Origin of the fragile-to-strong crossover in liquid silica as expressed by its potential-energy landscape. *Phys. Rev. Lett.*, 93:235701, 2004.

[108] A. Saksaengwijit and A. Heuer. Dynamics of liquid silica as explained by properties of the potential energy landscape. *Phys. Rev. E*, 73:061503, 2006.

[109] G. Brebec, R. Sequin, C. Sella, J. Bevenot, and J. C. Martin. Diffusion du silicium dans la silice amorphe. *Acta Metall.*, 28:327–333, 1980.

[110] J. C. Mikkelsen Jr. Self-diffusivity of network oxygen in vitreous SiO_2. *Appl. Phys. Lett.*, 45:1187–1189, 1984.

[111] W. H. Press, S. A. Teukolsky, W. T. Vetterling, and B. P. Flannery. *Numerical recipes: The art of scientific computing.* Cambridge University Press, Cambride, UK, 2007.

[112] R. P. Feynman. Forces in molecules. *Phys. Rev.*, 56:340–343, 1939.

[113] P. A. V. Johnson, A. C. Wright, and R. N. Sinclair. Neutron scattering from vitreous silica II. Twin-axis diffraction experiments. *J. Non-Cryst. Solids*, 58:109–130, 1983.

[114] J. Neuefeind and K.-D. Liss. Bond angle distribution in amorphous germania and silica. *Ber. Bunsenges. Phys. Chem.*, 100:1341–1349, 1996.

[115] S. Susman, J. Volin, D. L. Price, M. Grimsditch, J. P. Rino, R. K. Kalia, P. Vashishta, G. Gwanmesia, Y. Wang, and R. C. Liebermann. Intermediate-range order in permanently densified vitreous SiO_2: A neutron-diffraction and molecular-dynamics study. *Phys. Rev. B*, 43:1194–1197, 1991.

[116] K. Parlinski, Z. Q. Li, and Y. Kawazoe. First-principles determination of the soft mode in cubic ZrO_2. *Phys. Rev. Lett.*, 78:4063–4066, 1997.

[117] MedeA® software package of Materials Design, including MedeA® Phonon [Online]. *http://www.materialsdesign.com/medea, http://www.materialsdesign.com/medea/phonon*, April 5, 2015.

[118] L. Chaput, A. Togo, I. Tanaka, and G. Hug. Phonon-phonon interactions in transition metals. *Phys. Rev. B*, 84:094302, 2011.

[119] A. Pasquarello, J. Sarnthein, and R. Car. Dynamic structure factor of vitreous silica from first principles: Comparison to neutron-inelastic-scattering experiments. *Phys. Rev. B*, 57:14133–14140, 1998.

[120] L. Giacomazzi, P. Umari, and A. Pasquarello. Medium-range structure of vitreous SiO_2 obtained through first-principles investigation of vibrational spectra. *Phys. Rev. B*, 79:064202, 2009.

[121] S. N. Taraskin and S. R. Elliot. Connection between the true vibrational density of states and that derived from inelastic neutron scattering. *Phys. Rev. B*, 55:117–123, 1997.

[122] Properties of Lithosil®, synthetic fused silica from Schott Lithotec® [Online]. *http://itos.de/dateien/fusedsilicia/lithotec_fused_silica_jan2009.pdf*, Jan 2009, website from April 2, 2015.

[123] P. Richet, Y. Bottinga, L. Denielou, J. P. Petite, and C. Tequi. Thermodynamic properties of quartz, cristobalite and amorphous SiO_2: drop calorimetry measurements between 1000 and 1800 K and a review from 0 to 2000 K. *Geochim. cosmochim. acta*, 46:2639–2658, 1982.

[124] J. Horbach, W. Kob, and K. Binder. Specific heat of amorphous silica within the harmonic approximation. *J. Phys. Chem. B*, 103:4104–4108, 1999.

[125] A Togo, L. Chaput, I Tanaka, and G. Hug. First-principles phonon calculations of thermal expansion in Ti_3SiC_2, Ti_3AlC_2, and Ti_3GeC_2. *Phys. Rev. B*, 81:174301, 2010.

[126] F. D. Murnaghan. The compressibility of media under extreme pressures. *Proc. Natl. Acad. Sci. USA*, 30:244–247, 1944.

[127] F. Birch. Finite Elastic Strain of Cubic Crystals. *Phys. Rev.*, 71:809–824, 1947.

[128] P. Vinet, J. H. Rose, J. Ferrante, and J. R. Smith. Universal features of the equation of state of solids. *J. Phys.: Condens. Matter*, 1:1941–1963, 1989.

[129] T. H. K. Barron, J. F. Collins, T. W. Smith, and G. K. White. Thermal expansion, Grüneisen functions and static lattice properties of quartz. *J. Phys. C:Solid State Phys.*, 15:4311–4326, 1982.

[130] G. K. White. Thermal expansion of silica at low temperatures. *Cryogenics*, 4:2–7, 1964.

[131] A. Takada, C. R. A. Catlow, and G. D. Price. 'Computer synthesis' of B_2O_3 polymorphs. *Phys. Chem. Glasses*, 44:147–149, 2003.

[132] A. Takada. Molecular dynamics study of pressure induced structural changes in B_2O_3. *Phys. Chem. Glasses*, 45:156–159, 2004.

[133] G. Ferlat, T. Charpentier, A. P. Seitsonen, A. Takada, M. Lazzeri, L. Cormier, G. Calas, and F. Mauri. Boroxol Rings in Liquid and Vitreous B_2O_3 from First Principles. *Phys. Rev. Lett.*, 101:065504, 2008.

[134] A. C. Hannon, R. N. Sinclair, and A. C. Wright. The vibrational modes of vitreous B_2O_3. *Physica A*, 201:375–380, 1993.

[135] J. Krogh-Moe. The structure of vitreous and liquid boron oxide. *J. Non-Cryst. Solids*, 1:269–284, 1969.

[136] G. E. Jellison Jr., L. W. Panek, P. J. Bray, and G. B. Rouse Jr. Determinations of structure and bonding in vitreous B_2O_3 by means of ^{10}B, ^{11}B and ^{17}O NMR. *J. Chem. Phys.*, 66:802–812, 1977.

[137] R. E. Youngman and J. W. Zwanziger. Multiple boron sites in borate glass detected with dynamic angle spinning nuclear magnetic resonance. *J. Non-Cryst. Solids*, 168:293–297, 1994.

[138] R. E. Youngman, S. T. Haubrich, J. W. Zwanziger, M. T. Janicke, and B. F. Chmelka. Short-and intermediate-range structural ordering in glassy boron oxide. *Science*, 269:1416–1420, 1995.

[139] R. L. Mozzi and B. E. Warren. The structure of vitreous boron oxide. *J. Appl. Cryst.*, 3:251–257, 1970.

[140] P. A. V. Johnson, A. C. Wright, and R. N. Sinclair. A neutron diffraction investigation of the structure of vitreous boron trioxide. *J. Non-Cryst. Solids*, 50:281–311, 1982.

[141] P. Umari and A. Pasquarello. Fraction of boroxol rings in vitreous boron oxide from a first-principles analysis of Raman and NMR spectra. *Phys. Rev. Lett.*, 95:137401, 2005.

[142] R. Car and M. Parrinello. Unified approach for molecular dynamics and density-functional theory. *Phys. Rev. Lett.*, 55:2471–2474, 1985.

[143] J. Krogh-Moe and M. Ihara. The crystal structure of caesium enneaborate, $Cs_20.9B_2O_3$. *Acta Cryst.*, 23:427–430, 1967.

[144] T. F. Soules. A molecular dynamic calculation of the structure of B_2O_3 glass. *J. Chem. Phys.*, 73:4032–4036, 1980.

[145] Q. Xu, K. Kawamura, and T. Yokokawa. Molecular dynamics calculations for boron oxide and sodium borate glasses. *J. Non-Cryst. Solids*, 104:261–272, 1988.

[146] W. Soppe, C. van der Marel, W. F. Gunsteren, and H. W. den Hartog. New insights into the structure of B_2O_3 glass. *J. Non-Cryst. Solids*, 103:201–209, 1988.

[147] W. Soppe and H. W. den Hartog. A molecular dynamics study of $(B_2O_3)_{1-x-y}$ $(Li_2O)_x$ $(Li_2Cl_2)_y$ and $(B_2O_3)_{1-x-y}$ $(Li_2O)_x$ $(Cs_2O)_y$. *J. Non-Cryst. Solids*, 108:260–268, 1989.

[148] H. Inoue, N. Aoki, and I. Yasui. Molecular dynamics simulation of the structure of borate glasses. *J. Am. Ceram. Soc.*, 70:622–627, 1987.

[149] A. H. Verhoef and H. W. den Hartog. A molecular dynamics study of B_2O_3 glass using different interaction potentials. *J. Non-Cryst. Solids*, 146:267–278, 1992.

[150] A. Takada. Modelling of B_2O_3 glass structure by coupled MD/MC simulation. *Phys. Chem. Glasses: Eur. J. Glass Sci. Technol. B*, 47:493–496, 2006.

[151] B. Park, E. Bylaska, and L. R. Corrales. Energy dependence of vitreous B_2O_3 on boroxol ring concentration. *Phys. Chem. Glasses*, 44:174–177, 2003.

[152] A. N. Cormack and B. Park. Molecular dynamics simulations of borate glasses. *Phys. Chem. Glasses*, 41:272–277, 2000.

[153] D. C. Anderson, J. Kieffer, and S. Klarsfeld. Molecular dynamic simulations of the infrared dielectric response of silica structures. *J. Chem. Phys.*, 98:8978–8986, 1993.

[154] R. Fernández-Perea, F. J. Bermejo, and E. Enciso. Molecular dynamics on a realistic model for a strong glass. *Phys. Rev. B*, 53:6215–6224, 1996.

[155] L. Huang and J. Kieffer. Molecular dynamics study of cristobalite silica using a charge transfer three-body potential: Phase transformation and structural disorder. *J. Chem. Phys.*, 118:1487–1498, 2003.

[156] L. Huang, J. Nicholas, J. Kieffer, and J. Bass. Polyamorphic transitions in vitreous B_2O_3 under pressure. *J. Phys.: Condens. Matter*, 20:075107, 2008.

[157] S. K. Fullerton and J. K. Maranas. A molecular interpretation of vitreous boron oxide dynamics. *J. Chem. Phys.*, 121:8562–8570, 2004.

[158] V. V. Brazhkin, Y. Katayama, K. Trachenko, O. B. Tsiok, A. G. Lyapin, E. Artacho, M. Dove, G. Ferlat, Y. Inamura, and H. Saitoh. Nature of the structural transformations in B_2O_3 glass under high pressure. *Phys. Rev. Lett.*, 101:035702, 2008.

[159] P. B. Macedo, W. Capps, and T. A. Litovitz. Two-state model for the free volume of vitreous B_2O_3. *J. Chem. Phys.*, 44:3357–3364, 1965.

[160] S. Ohmura and F. Shimojo. Mechanism of atomic diffusion in liquid B_2O_3: An ab initio molecular dynamics study. *Phys. Rev. B*, 78:224206, 2008.

[161] S. Ohmura and F. Shimojo. Anomalous pressure dependence of self-diffusion in liquid B_2O_3: An ab initio molecular dynamics study. *Phys. Rev. B*, 80:020202(R), 2009.

[162] S. Ohmura and F. Shimojo. Ab initio molecular-dynamics study of structural, bonding, and dynamic properties of liquid B_2O_3 under pressure. *Phys. Rev. B*, 81:014208, 2010.

[163] J. P. Perdew, K. Burke, and M. Ernzerhof. Generalized gradient approximation made simple. *Phys. Rev. Lett.*, 77:3865–3868, 1996.

[164] J. Habasaki and I. Okada. Molecular dynamics simulation of alkali silicates based on the quantum mechanical potential surfaces. *Mol. Simul.*, 9:319–326, 1992.

[165] D. Li and W. Y. Ching. Electronic structures and optical properties of low- and high-pressure phases of crystalline B_2O_3. *Phys. Rev. B*, 54:13616–13622, 1996.

[166] G. E. Walrafen, S. R. Samanta, and P. N. Krishnan. Raman investigations of vitreous and molten boric oxide. *J. Chem. Phys.*, 72:113–120, 1980.

[167] P. Richet, D. de Ligny, and E. F. Westrum Jr. Low-temperature heat capacity of GeO_2 and B_2O_3 glasses: thermophysical and structural implications. *J. Non-Cryst. Solids*, 315:20–30, 2003.

[168] G. K. White, S. J. Collocott, and J. S. Cook. Thermal expansion and heat capacity of vitreous B_2O_3. *Phys. Rev. B*, 29:4778–4781, 1984.

Acknowledgements

Aus Datenschutzgründen entfernt.